



Luis Carlos Neto Martins

**Composite Materials for Electromagnetic  
Shielding: Experimental and Theoretical  
Analysis**

**Universidade do Minho**  
Escola de Engenharia







**Universidade do Minho**

Escola de Engenharia

Luís Carlos Neto Martins

**Composite Materials for Electromagnetic  
Shielding: Experimental and Theoretical  
Analysis**

Tese de Doutoramento

Programa Doutoral em  
Ciência e Engenharia de Polímeros e Compósitos

Trabalho efetuado sob a orientação do

**Professor Doutor António José Vilela Pontes**

**Professor Doutor Nuno Miguel Machado Reis Peres**

Maio de 2024

## **DIREITOS DE AUTOR E CONDIÇÕES DE UTILIZAÇÃO DO TRABALHO POR TERCEIROS**

Este é um trabalho académico que pode ser utilizado por terceiros desde que respeitadas as regras e boas práticas internacionalmente aceites, no que concerne aos direitos de autor e direitos conexos.

Assim, o presente trabalho pode ser utilizado nos termos previstos na licença abaixo indicada.

Caso o utilizador necessite de permissão para poder fazer um uso do trabalho em condições não previstas no licenciamento indicado, deverá contactar o autor, através do RepositóriUM da Universidade do Minho.

### ***Licença concedida aos utilizadores deste trabalho***



**Atribuição  
CC BY**

<https://creativecommons.org/licenses/by/4.0/>

# ACKNOWLEDGEMENTS

*We are not alone in this world...*

This work was accomplished with the contribution of several individuals to whom I am immensely grateful, and I extend my genuine thanks for their invaluable support.

Jaime E. Santos, a guiding light in many moments that occurred during the development of the thesis. Your immense generosity and unwavering availability were fundamental on this journey. You were always there as a mentor, making a significant contribution to the development of my knowledge and the execution of the thesis. Your profound wisdom enriched not only my academic journey but my entire life experience. Thank you for turning those challenging moments into something that was worth it in the end.

My supervisors, Professor António J. Pontes, and Professor Nuno M. R. Peres, were always patient, available, and supportive, guiding me throughout this work. Without them, this research would not have been possible.

I would like to extend my heartfelt thanks to all the associates from the Department of Polymers Engineering, the Department of Physics (especially Professor Bernardo Almeida), PIEP, Bosch Car Multimedia (including Susana Silva, Carlos Barbosa, and José Viana), Graphenest (particularly Bruno Figueiredo), and the DONE Lab. Your active involvement in this research, as well as your contributions in terms of facilities and resources, were indispensable. Thanks for your assistance and the valuable friendship that I hold dear.

My beloved Eva Silva, my parents, my sister, my brother, my parents-in-law, brothers-in-law, and other family members and friends: you are the most important people in my life, always there to provide comfort and a good-natured kick in the head when needed. Please continue being your wonderful selves.

The execution of this thesis received financial support from three R&D projects, including the Portuguese Incentive System for Research and Technological Development under Project no 36265/2013 (HMIEXCEL), the European Regional Development Fund (ERDF) within the Operational Competitiveness and Internationalization Programme (COMPETE 2020) under Project n° 002797 (Funding Reference: POCI-01-0247-FEDER-002797), and under Project No. 47108, known as "SIFA" (Funding Reference: POCI-01-0247-FEDER-047108).

To all of you, a huge thank you.

## DECLARAÇÃO DE INTEGRIDADE

Declaro ter atuado com integridade na elaboração do presente trabalho académico e confirmo que não recorri à prática de plágio nem a qualquer outra forma de utilização indevida ou falsificação de informações ou resultados em nenhuma das etapas conducente à sua elaboração.

Mais declaro que conheço e respeitei o Código de Conduta Ética da Universidade do Minho.

Universidade do Minho, \_\_\_/\_\_\_/\_\_\_\_\_

Nome completo: Luís Carlos Neto Martins

Assinatura: \_\_\_\_\_

# RESUMO

Inovações recentes em materiais poliméricos e processos de fabricação têm impulsionado alternativas aos materiais metálicos para caixas de dispositivos eletrônicos. Estas caixas, feitas de polímeros leves e resistentes à corrosão com reforços condutores, são essenciais para proteção contra ESD (descargas eletrostáticas) e isolamento EMI (interferência eletromagnética). No entanto, desafios surgem devido à limitada caracterização e à natureza anisotrópica da moldação por injeção. Esta tese investiga a eficácia de blindagem eletromagnética (EMSE) de compósitos termoplásticos, visando apoiar o design e a fabricação de chassis poliméricos.

A investigação revelou que estes materiais apresentam uma ampla gama de EMSE, revelando variações significativas de 20 dB a 100 dB. Influenciados por fatores como natureza, concentração, comprimento e orientação das cargas condutoras, a combinação de fibras de carbono e aço inoxidável destacaram-se com uma excepcional blindagem superior a 60 dB em múltiplas frequências. A análise dos parâmetros de moldação por injeção revelou resultados notáveis, destacando o impacto positivo do aumento da temperatura de fusão. Estabeleceu-se uma relação entre EMSE e condutividade elétrica, seguindo uma tendência exponencial, principalmente devido ao mecanismo de absorção da blindagem. Além disso, o estudo demonstrou a viabilidade de representar compostos poliméricos heterogêneos teoricamente usando propriedades anisotrópicas, emergindo um modelo teórico baseado na matriz de transferência dos índices de refração de um meio homogêneo definido por uma impedância equivalente como uma abordagem precisa para estimar a blindagem eletromagnética nesses agregados poliméricos.

A técnica de extrusão de material com fibra de carbono contínua foi utilizada para produzir compósitos com blindagem eletromagnética até 70 dB, superando em 22 vezes o desempenho do composto de poliamida sem fibra de carbono. A versatilidade deste processo permite personalização da estrutura interna da peça, com diferentes camadas de fibras resultando numa EMSE de 40 a 70 dB, sendo a absorção o seu principal mecanismo.

A utilização de grafeno FLG e MLG para revestir substratos de silicone foi investigada como solução para EMSE. Revestimentos com espessuras de 100 a 300 micrômetros e resistência de 50 a 100 Ohm/sq resultaram em blindagem abaixo de 15 dB, sendo necessário aumentar significativamente a espessura do revestimento ou melhorar a condutividade da tinta de grafeno para alcançar uma blindagem satisfatória, na ordem dos 30 dB.

**Palavras-chave:** blindagem eletromagnética, compostos termoplásticos, condutividade elétrica, moldagem por injeção, polímeros condutores, fabricação aditiva

# ABSTRACT

Recent innovations in polymer materials and manufacturing processes have driven alternatives to metallic materials for electronic device enclosures. These enclosures, made from lightweight and corrosion-resistant polymers with conductive reinforcements, are essential for protection against ESD (electrostatic discharge) and EMI (electromagnetic interference) shielding. However, challenges arise due to limited characterisation and the anisotropic nature of injection moulding. This thesis investigates the electromagnetic shielding effectiveness (EMSE) of thermoplastic composites, aiming to support the design and manufacture of polymer chassis.

The research revealed that these materials exhibit a wide range of EMSE, with significant variations from 20 dB to 100 dB. Influenced by factors such as the nature, concentration, length, and orientation of conductive fillers, the combination of carbon fibres and stainless steel stood out with exceptional shielding above 60 dB at multiple frequencies. The analysis of injection moulding parameters showed notable results, highlighting the positive impact of increasing the melting temperature. A relationship between EMSE and electrical conductivity was established, following an exponential trend, primarily due to the absorption mechanism of the shielding. Furthermore, the study demonstrated the feasibility of theoretically representing heterogeneous polymer composites using anisotropic properties, with a theoretical model based on the transfer matrix of refractive indices of a homogeneous medium defined by an equivalent impedance as an accurate approach to estimate the electromagnetic shielding in these polymeric aggregates.

The material extrusion technique with continuous carbon fibre was used to produce composites with electromagnetic shielding up to 70 dB, outperforming the polyamide composite without carbon fibre by 22 times. The versatility of this process allows customisation of the internal structure of the part, with different fibre layers resulting in an EMSE of 40 to 70 dB, with absorption being the primary mechanism.

The use of FLG and MLG graphene to coat silicone substrates was investigated as a solution for EMSE. Coatings with thicknesses of 100 to 300 micrometres and resistance of 50 to 100 Ohm/sq resulted in shielding below 15 dB, necessitating a significant increase in coating thickness or improvement in graphene ink conductivity to achieve satisfactory shielding in the order of 30 dB.

**Keywords:** electromagnetic shielding, thermoplastic compounds, electrical conductivity, conducting polymers.



# CONTENTS

<b>Acknowledgements</b> .....	<b>i</b>
<b>Resumo</b> .....	<b>iii</b>
<b>Abstract</b> .....	<b>iv</b>
<b>Contents</b> .....	<b>v</b>
<b>list of figures</b> .....	<b>viii</b>
<b>List of Tables</b> .....	<b>xi</b>
<b>list of abbreviations</b> .....	<b>xiii</b>
<b>list of publications from this work</b> .....	<b>xiv</b>
<b>1. Introduction</b> .....	<b>1</b>
1.1. Contextualization and motivation .....	2
1.2. Research questions .....	3
1.3. Objectives .....	3
1.4. Thesis outline.....	4
<b>2. EM Shielding concept</b> .....	<b>5</b>
2.1. Introduction to EM shielding .....	6
2.2. Theoretical formalism.....	10
2.2.1. Plane waves in lossless and lossy media: dispersion relations.....	10
2.2.2. Reflection and transmission at the interface between a lossless and lossy medium .....	12
2.2.3. Power relations at the interface .....	14
<b>3. Thermoplastic compounds processed by injection moulding</b> .....	<b>16</b>
3.1 Introduction .....	17
3.2 Literature review .....	18
3.3 Work methodology.....	23
3.3.1. Materials and samples .....	24
3.3.2. EM Shielding procedure .....	24
3.3.3. Electrical conductivity.....	27

3.3.4. Electrical permittivity and frequency dependent conductivity .....	30
3.3.5. Theoretical models.....	32
3.4    First approach onto SE of thermoplastic compounds .....	38
3.4.1. Materials .....	39
3.4.2. Experimental procedure .....	39
3.4.3. Results and discussion.....	42
3.4.4. Concluding remarks.....	44
3.5    Effect of injection moulding conditions on the materials electromagnetic shielding and electrical conductivity .....	45
3.5.1. Materials .....	46
3.5.2. Experimental procedure .....	47
3.5.3. Results and discussion.....	52
3.5.4. Concluding remarks.....	68
3.6    An improved assessment on the relationship between the injection process, the EMSE and the frequency dependent properties .....	71
3.6.1. Materials .....	72
3.6.2. Experimental procedure .....	74
3.6.3. Results and discussion.....	81
3.6.4. Concluding remarks.....	96
<b>4.    New developments of advanced materials .....</b>	<b>99</b>
4.1    Introduction .....	100
4.2    Additive manufacturing .....	101
4.2.1. Literature review .....	101
4.2.2. Materials and methods.....	104
4.2.3. Results and discussion.....	109
4.2.4. Concluding remarks.....	118
4.3    Graphene based coatings.....	120
4.3.1. Literature review .....	120
4.3.2. Materials and methods.....	124
4.3.3. Results and discussion.....	127
4.3.4. Concluding remarks.....	131
<b>5.    Conclusions .....</b>	<b>133</b>

5.1	General conclusion .....	134
5.2	Future research opportunities .....	137
<b>References .....</b>		<b>138</b>
<b>Appendices .....</b>		<b>146</b>
	Appendix A. Supplementary information regarding the EM shielding apparatus. ....	147
	Appendix B. Supplementary information for the theoretical model. ....	149
	Appendix C. Codes build in <i>Mathematica 10.2</i> software. ....	150
	Appendix D. Supplementary results to chapter 3.5. ....	155
	Appendix E. Supplementary results to chapter 3.6. ....	167
	Appendix G. Supplementary results to chapter 4.2. ....	179
	Appendix H. Supplementary results to chapter 4.3. ....	183

# LIST OF FIGURES

Figure 1. Common aspects and tests for EMC.....	6
Figure 2. Shielding mechanisms. ....	8
Figure 3. Work plan. ....	23
Figure 4. Schematic of the experimental apparatus. ....	25
Figure 5. Illustration of reference and load samples [97]. ....	26
Figure 6. Electrodes schematic to measure the longitudinal electrical resistance.....	28
Figure 7. Electrodes schematic to measure the transversal electrical resistance.....	29
Figure 8. Picture of the E4991A impedance analyzer with dielectric test fixture 16454A. source: Keysight Technologies .....	31
Figure 9. Equivalent LCR circuit diagram.....	31
Figure 10. Workflow adopted in the first study. ....	40
Figure 11. Injection moulding specimens: a) generic dimensions; b) 3D representation.....	41
Figure 12. Disk shaped samples for EM shielding.....	41
Figure 13. EM Shielding for the tested materials.....	42
Figure 14. Experimental SE and fitted theoretical modelling.....	44
Figure 15. Workflow adopted in the second study. ....	47
Figure 16. Injection moulding samples: a) Generic dimensions; b) sample picture .....	48
Figure 17. EMSE samples layout: a) load sample; b) reference sample .....	50
Figure 18. Virtual and physical electrodes models: a) and c) show the general dimensions, b) and d), show only one electrode to enable the visualization of plastic samples in position. ....	51
Figure 19. Samples general dimensions (in mm) and cutting operation scheme at both near and opposite gate locations: A – sample for perpendicular measurements; B – sample for parallel measurements; C – sample for transversal measurements.....	51
Figure 20. EM Shielding measured for the M7 Compound.....	53
Figure 21. EM Shielding measured for the M8 Compound.....	54
Figure 22. EM Shielding measured for the M9 Compound.....	54
Figure 23. Effect of processing conditions on the EM shielding for the M7 compound. ....	56
Figure 24. Effect of processing conditions on the EM shielding for the M7 compound. ....	56
Figure 25. Effect of processing conditions on the EM shielding for the M7 compound. ....	56

Figure 26. Average shielding measured for the three injected compounds at each experimental condition. .....	60
Figure 27. Normalized shielding for the three injected compounds at each experimental condition. ....	60
Figure 28. Specific shielding calculated for the three compounds at each experimental condition. ....	61
Figure 29. Measured conductivity in the parallel (top left), perpendicular (top right) and transversal (bottom) directions. Results belong to compound M7 and are shown in function of the applied compression force for different processing conditions and sample locations.....	62
Figure 30. Measured conductivity in the parallel (top left), perpendicular (top right) and transversal (bottom) directions. Results belong to compound M8 and are shown in function of the applied compression force for different processing conditions and sample locations.....	63
Figure 31. Measured conductivity in the parallel (top left), perpendicular (top right) and transversal (bottom) directions. Results belong to compound M9 and are shown in function of the applied compression force for different processing conditions and sample locations.....	64
Figure 32. Electrical conductivity at 200 N compression force. Results for M7 (top left), M8 (top right) and M9 (bottom) at different processing conditions, sample locations and measurement direction.....	65
Figure 33. EMSE relation with both experimental (parallel, perpendicular, and transversal to flow) and theoretical EC. EC axis is plotted with a logarithmic scale. ....	68
Figure 34. Fibres length histogram.....	74
Figure 35. Workflow adopted in the third study.....	75
Figure 36. Injection moulding samples: a) and b) sprue gate; c) and d) side edge gate.....	76
Figure 37. Samples drawing for EMSE test: a) load sample; b) reference sample. ....	77
Figure 38. Virtual model for the longitudinal conductivity test cell: a) electrical schematic; c) bottom electrode conceptual model, b) and d) shows the assembly of the complete test cell, with accessories. .....	78
Figure 39. Virtual model for the transversal conductivity test cell: a) electrical schematic; c) bottom electrode conceptual model, b) and d) shows the assembly of the complete test cell, with accessories. .....	79
Figure 40. Samples general dimensions in millimetres and cutting operation scheme: A – sample for perpendicular measurements; B – sample for parallel measurements; C – sample for transversal measurements; D – sample for impedance measurements. ....	80
Figure 41. Average thickness measured in the material samples injected under each experimental condition (A, B, C and D). A and C used the sprue gate while B and D used the lateral edge gate.....	83

Figure 42. Density measured in the materials injected under each experimental condition (A, B, C and D). A and C used the sprue gate while B and D used the lateral edge gate. ....	83
Figure 43. Average EMSE at 1 GHz for each fibre-filled compound (CF or SSF) injected under each experimental condition (A, B, C and D). A and C used the sprue gate while B and D used the lateral edge gate. ....	84
Figure 44. Effect of the CF or SSF fibre weight (wt) concentration on the EM shielding .....	85
Figure 45. Average specific SE at 1 GHz for each fibre-filled compound (CF or SSF). Experimental conditions A and C used the sprue gate while B and D used the lateral edge gate. ....	86
Figure 46. EM Shielding by absorption for the produced specimens. Values measured at 1 GHz. ....	87
Figure 47. EM Shielding by reflection for the produced specimens. Values measured at 1 GHz. ....	87
Figure 48. Electrical conductivity estimation to achieve the measured EM shielding. Transfer matrix theoretical model is based on a constant and isotropic conductivity. ....	88
Figure 49. Theoretical estimation for effect of the CF concentration on the compound's electrical conductivity. ....	89
Figure 50. Measured conductivity in the perpendicular (a), parallel (b) and transversal (c) directions. Properties are shown for each material and experimental condition (A, B, C and D). d) shows relative the ratio between the longitudinal and transversal properties. ....	90
Figure 51. Effect of the CF percentages of the measured conductivity in the perpendicular (a), parallel (b) and transversal (c) directions. d) shows the longitudinal to transversal ratio. ....	91
Figure 52. Linear impedance and respective phase angle for the 15wt% CF-filled specimens. ....	92
Figure 53. Equivalent impedance fitted to the initial linear impedance provided by the apparatus. ....	93
Figure 54. Complex permittivity for the 15% CF-filled material produced by each experimental condition. ....	93
Figure 55. Real values for the frequency-dependent conductivity characterized for the 15wt% CF-filled material in both transversal ( $\sigma'Z$ ) and longitudinal ( $\sigma'XY$ ) directions. ....	94
Figure 56. EM shielding theoretical estimations according to the LCR model. Results correspond to the experimental condition A, for 10% CF (a), 15% CF (b) and 30% CF (c). ....	95
Figure 57. (a) CAD representation of the printed load and reference specimens; and (b) build platform depicting with specimens positioning for manufacturing, image from software Eiger™ 3D Printing Software from <i>Markforged</i> . ....	105

Figure 58. Printing patterns, established by the <i>Eiger™</i> 3D Printing Software, for <i>Onyx™</i> (white) and carbon fibre (blue): <i>Onyx™</i> with (a) -45° pattern; (b) 45° pattern; and CF with (c) -45° pattern; and (d) 45° pattern. ....	105
Figure 59. Experimental and theoretical values for: (a) part weight; and (b) part density. ....	111
Figure 60. Microscopy of specimen's cross-section. ....	111
Figure 61. a) EMSE for all specimens as function of frequency; b) Average EMSE as function of CF layers. ....	113
Figure 62. a) Total shielding ( $SE_{t}$ ) along the frequency range; b) Absorption shielding ( $SE_{a}$ ) along the frequency range; c) Reflection shielding ( $SE_{r}$ ) along the frequency range; d) Average ratio for each shielding mechanism. ....	114
Figure 63. EM shielding and resistivity relation. EMSE is expected to decrease for higher resistivities by power law. ....	116
Figure 64. Normalized shielding effectiveness for the specimen's thickness (t) and per added CF layer (CFt).....	117
Figure 65. Specific EM Shielding for each composite formulation.....	118
Figure 66. Schematic of a conventional manual spray gun. ....	125
Figure 67. Normal plane wave incidence scattering along a heterogeneous specimen. Geometry of a thin layer of conducting material of thickness d covering a silicone dielectric of thickness D. ....	126
Figure 68. EM shielding measured at 1 GHz to the six graphene-based inks painted on silicone. ....	128
Figure 69. Theoretical estimate for the effect of electrical conductivity on EM shielding for graphene-based conductive coatings. ....	129
Figure 70. Effect of the number of graphene layers on the EM shielding. ....	129
Figure 71. Effect of the graphene layer thickness on the EM shielding. Results show similar characteristics to the theoretical estimations. ....	130

## LIST OF TABLES

Table 1. Thermoplastic compounds with respective electrical properties. ....	39
Table 2. Datasheet properties of the injection moulding compounds. ....	46
Table 3. Injection moulding experiment plan. ....	48
Table 4. Injection moulding conditions. ....	49

Table 5. Specimens' physical properties. ....	52
Table 6. Datasheet properties of the injection moulding compounds. ....	73
Table 7. Average fibre length and diameter. ....	73
Table 8. Experimental plan for the injection of disk-shaped samples. ....	76
Table 9. Design layout for the produced specimens. O is <i>Onyx™</i> and CF is carbon fibre. ....	106
Table 10. Load specimens' characteristics. ....	107
Table 11. Specimen's average physical dimensions. ....	110
Table 12. Measured electrical resistivity for filaments and printed specimens. ....	115



# LIST OF ABBREVIATIONS

<b>Abbreviation</b>	<b>Meaning</b>	<b>Abbreviation</b>	<b>Meaning</b>
2D	Two dimensional	LCR	Inductive-Capacitive-Resistive
3D	Three dimensional	LNCCF	Long Nickel-Coated Carbon Fibre
A	Absorption	LOM	Laminated Object Manufacturing
ABS	Acrylonitrile Butadiene Styrene	ME	Material Extrusion
AM	Additive Manufacturing	MLG	Multi-Layer Graphene
C	Capacitance	MR	Multiple internal reflections
CB	Carbon Black	MWCNT	Multi-walled carbon nanotubes
C-C	Carbon-carbon bond	n	Refractive index
CEM	Computational Electromagnetics	NCCF	Nickel-Coated Carbon Fibre
CF	Carbon Fibres	NCG	Nickel-coated graphite
CFR	Carbon Fibre Reinforcement	NDA	Non-Discharge Agreement
CNC	Computed Numerical Control	O	Onyx
CNF	Carbon nanofibre	OEM	Original electronic equipment
CNT	Carbon nanotubes	PBT	Polybutylene terephthalate
CT	Computed Tomography	PC	Polycarbonate
CVD	Chemical Vapour Deposition	PLA	Poly(lactic) acid
dB	Decibel	PP	Polypropylene
DC	Direct current	PS	Polystyrene
E	Electric field	R	Reflection
EC	Electrical Conductivity	RF	Radiofrequency
EM	Electromagnetic	S	Electrode surface area
EMC	Electromagnetic Compatibility	SE	Shielding Effectiveness
EMI	Electromagnetic Interference	SE <sub>a</sub>	Shielding by absorption
EMSE	Electromagnetic Shielding Effectiveness	SE <sub>r</sub>	Shielding by reflection
ESD	Electrostatic Dissipative	SE <sub>t</sub>	Shielding by transmission
FCSH	Flanged Coaxial Sample Holder	SI	International System of Units
G	Electrical conductance	SS	Stainless Steel
Gr	Graphene	SSF	Stainless Steel Fibre
H	Magnetic field	T	Thickness
LCF	Long Carbon Fibres	Z	Impedance

# LIST OF PUBLICATIONS FROM THIS WORK

## International Journal Publications

**Martins, L.C.**, & Pontes, A.J. (2022). Fiber reinforced thermoplastics compounds for electromagnetic interference shielding applications. *Journal of Reinforced Plastics and Composites*, 41(5–6), 206–214.

<https://doi.org/10.1177/07316844211051732>

**Martins, L.C.**, Barbosa, C.N., Silva, S., Bernardo, P., Dias, G.R., Pontes, A.J. (2021). *Polym. Eng. Sci.*, 61 (10), 2576. <https://doi.org/10.1002/pen.25784>

Alexandre, B.S.C., **Martins, L.C.**, Santos, J.E., Pontes A.J., Peres, N.M.R. (2020). Fresnel polarisation of infra-red radiation by elemental bismuth. *Eur. Phys. J. B*, 93, 119.

<https://doi.org/10.1140/epjb/e2020-10090-9>

**Martins, L.C.**; Silva, C.S.; Fernandes, L.C.; Sampaio, Á.M.; Pontes, A.J. Evaluating the Electromagnetic Shielding of Continuous Carbon Fiber Parts Produced by Additive Manufacturing. *Polymers* 2023, 15, 4649. <https://doi.org/10.3390/polym15244649>

## Oral communications

Campos, R., **Martins, L.C.**, Ribeiro, C., Dias, G.R., Pontes, A.J. (2016). “Polymeric chassis for multimedia products”. *Jornadas de Polímeros 2016*, Centro Cultural Vila Flor, Guimarães, Portugal, 1-2 July.

**Martins, L.C.**, & Pontes, A.J. (2016). “Reinforced thermoplastics compounds for EMI shielding applications”. 7<sup>th</sup> bi-annual International Conference on Polymers and Moulds Innovations, Ghent, Belgium, 21-23 September.

**Martins, L.C.**, Barbosa, C.N., Silva, S., *et al.* (2018). “Electrical conductive thermoplastic compounds for electromagnetic shielding applications”. FEMS Junior EUROMAT 2018 Conference, Budapest, Hungary, 8-12 July.

**Martins, L.C.**, Barbosa, C.N., Silva, S., *et al.* (2018). “Effect of processing conditions on electric resistivity of injection molded PBT compounds”. 8<sup>th</sup> bi-annual International Conference on Polymers and Moulds Innovations, Guimarães, Portugal, 19-21 September.

**Martins, L.C.**, Pinho, J., Santos J.E., Pontes, A.J., Peres, N.M. (2018). “Thermoplastic compound’s electrical and electromagnetic characterization and their mutual relation”. 8<sup>th</sup> bi-annual International Conference on Polymers and Moulds Innovations, Guimarães, Portugal, 19-21 September.

**Martins, L.C.**, Santos J.E., Peres, N.M., Pontes, A.J., (2021). “Carbon fiber reinforced polycarbonate for electromagnetic shielding: Experimental and theoretical approach”. 1<sup>st</sup> International Polymer Process Innovation Conference, Online, 15-16 December.

**Martins, L.C.**, Fernandes, L., Sampaio, A.M., Pontes, A.J. (2022). “Continuous carbon fiber composites produced by additive manufacturing: electromagnetic shielding case study”. 2<sup>nd</sup> International Polymer Process Innovation Conference, Lavrion, Greece, 15-16 September.

### **Posters**

**Martins, L.C.**, Peres, N.M., Pontes, A.J. (2017). “Thermoplastic compounds for electromagnetic shielding”. Jornadas de Polímeros 2017, Guimarães, Portugal, 30 June to 1 July.

### **Patents**

Freitas R.M.D., Sá R.F., Gomes M.V.P., et al. Conductive polymeric housing for electronic component. PCT/IB2015/054879, Portugal, 2017.

<https://patents.google.com/patent/WO2017001888A1/en>

# **1. INTRODUCTION**

## 1.1. Contextualization and motivation

This thesis was developed within the agenda of a couple of technological and innovation projects established in a collaboration between the University of Minho, the academic and scientific counterpart, and two industrial partners (*Bosch Car Multimedia Portugal, S.A.* and *Graphenest, S.A.*) as lead technological owners. These agendas had the goal of developing processes, tools, or materials to address the market requirements and future trends. One of the goals encompassed the development of polymeric materials and processes to produce new solutions of enclosures for electronic devices. Such innovative product can allow the replacement of metallic materials, as being lightweight, having better corrosion resistance, improved structure with fitted stiffness and part consolidation, assembly simplicity and faster manufacturing time, while being compliant with all the mechanical, thermal, and electromagnetic requirements.

Throughout the research and development of polymer-based housings, a series of challenges, notably in the realm of electromagnetic compatibility (EMC), became evident. One significant challenge revolved around the production and/or selection of suitable compounds for the housing product. This process was intricate due to the lack of comprehensive data (including electric, magnetic, and electromagnetic shielding properties) available in the datasheets provided by suppliers.

Furthermore, the heterogeneous nature of the reinforced polymeric aggregates and their properties' dependence on processing conditions required in-depth understanding. To scale up production for industrial purposes and achieve cost-efficiency, the polymer-based housing had to be manufactured through injection moulding. However, it is widely acknowledged that the injection process can introduce anisotropic properties to the polymeric components.

In addition to polymer housing manufacturing, another technical challenge lay in the measurement procedures to characterize the anisotropic properties of polymeric composites. These encompassed the need for an enhanced measurement method for electrical conductivity under constant current and an improved approach to measure frequency-dependent conductivity, ultimately to establish a robust relationship between conductivity and electromagnetic shielding. This comprehensive characterization of conductivity and its connection to shielding holds the potential to supply ample data for developing or refining theoretical models capable of predicting shielding behaviour for specific materials or products.

## 1.2. Research questions

Based on the points outlined earlier, the principal research questions established for the study of polymeric compounds processed by injection moulding encompass:

- EM shielding efficiency of polymeric compounds: What is the effectiveness of thermoplastics in blocking electromagnetic waves?
- Impact of injection moulding parameters: How do injection moulding parameters influence fibre orientation, concentration, and subsequent properties of a specimen, ultimately leading to optimal EM shielding performance?
- Relationship between conductivity, dielectric Function, and EM shielding: How are the electrical conductivity and dielectric function interconnected with the electromagnetic shielding properties of polymer aggregates?
- Accurate measurement of anisotropic conductivity and dielectric function: How can the anisotropic conductivity and dielectric function of these heterogeneous composites be precisely measured?
- Theoretical modelling of electromagnetic properties: How can the electromagnetic properties of these polymeric compounds be theoretically evaluated to forecast the performance of a given product?

Since there have been significant discoveries and advancements in new advanced materials and new processing technologies, two complementary research question were appended to this research:

- Innovative additive manufacturing process: Can the additive manufacturing of continuous carbon fibre be an effective fabrication technology for developing products capable of blocking electromagnetic waves?
- EM shielding of graphene: How efficient is the EM shielding provided by the graphene-based solutions?

## 1.3. Objectives

This doctoral project aims to address the research question by conducting both experimental and theoretical characterizations of the electromagnetic shielding effectiveness (EMSE) of thermoplastic composites. This analysis seeks to develop engineering tools and methodologies that can predict the EM shielding properties of materials, supporting product design and manufacturing processes. The traditional

method for evaluating material shielding effectiveness relies on a costly trial-and-error approach, both in terms of time and economic expenses. Therefore, the creation of a predictive model is of significant interest to the industry, as it can reduce development cycles and costs.

Throughout this thesis, the following objectives are anticipated to be achieved:

- Characterization of the shielding performance of injection-moulded thermoplastic compounds and advanced composite materials, all of which are reinforced with materials such as carbon fibre, graphene, and other fillers.
- Development of an experimental methodology for the proper characterization of anisotropic conductivity and dielectric function, encompassing both electrical and dielectric anisotropic properties (constant and frequency-dependent), and establishing their correlation with EM shielding.
- Examination of the influence of processing-induced properties due to fibre orientation and concentration and their relation to EM shielding performance.
- Formulation of theoretical models designed to characterize the EM shielding of composite materials with heterogeneous microstructures and anisotropic properties.

### **1.4. Thesis outline**

The thesis is organized as follows:

Chapter 2. Provides a concise introduction to the concept of electromagnetic (EM) shielding, detailing the theoretical expressions derived from Maxwell's equations to describe the dispersion relations within various media.

Chapter 3. Presents an investigation into the electromagnetic properties of thermoplastic compounds processed through injection moulding. This investigation comprises three consecutive studies, focusing on both the experimental and theoretical analysis of the EMSE of the materials produced.

Chapter 4. Discusses the findings from the investigation of innovative additive manufacturing processing methods and the application of graphene-based solutions for EM shielding purposes.

Chapter 5. Summarizes the principal conclusions and offers suggestions for future research.

At the end of the document, we highlight the work references and some attachments that can be used to aid in the analysis.

## **2. EM SHIELDING CONCEPT**



## 2.1. Introduction to EM shielding

The rapid evolution of electronic technology and telecommunications has introduced a multitude of electromagnetic interference (EMI) sources, contributing to what can be termed modern environmental pollution. This pollution has the potential to disrupt the performance of electronic systems and even pose health concerns [1]. Consequently, the development and application of electronic technology have become subject to strict regulations and monitoring, like those highlighted in Figure 1. The aim is to ensure the safe and efficient operation of electronic systems and to guarantee that a particular system functions as intended within its designated electromagnetic environment, in which it involves preventing interference with other devices and protecting against susceptibility to radiation from external sources [2], [3].

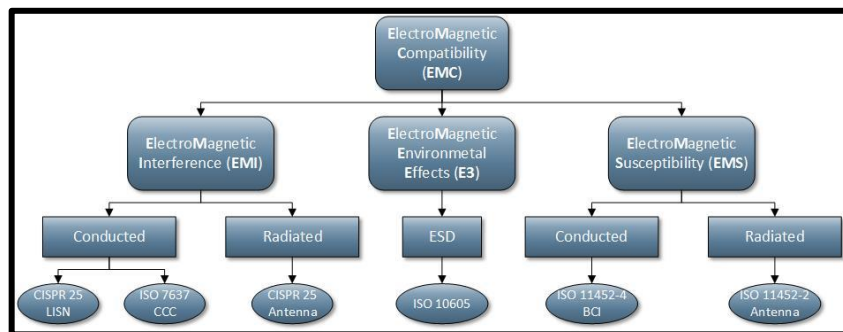


Figure 1. Common aspects and tests for EMC.

EMC is a field within science and engineering that seeks to establish guidelines for the design and operation of electrical and electronic devices. The primary objective of EMC is to control and manage the level of EMI generated by these devices. These guidelines ensure that the device functions correctly within its intended electromagnetic environment, without causing interference to other devices, avoiding self-interference, and being resilient to external factors such as radiation from other devices or electrostatic discharge (ESD) [2], [4].

Within the realm of EMC standards, the management of radiated signals in both directions, whether they are emissions or susceptibilities, takes precedence. EMI, and Radiofrequency Interference (RFI) are common issues encountered in electronic devices. EMI refers to the process where disruptive electromagnetic energy is transferred from one electronic device to another through either radiated or conducted paths, or a combination of both. This phenomenon involves three essential components: a source or emitter of interference, a receptor or victim of interference, and a propagation or coupling path connecting the source and the receptor through which energy is transmitted. To effectively manage EMI, a suppression process is employed, typically involving the use of shielding or filtering. EMI shielding is a

fundamental and highly effective approach within EMC design. It operates by reducing or eliminating EMI energy by obstructing its propagation path through the use of an EMI impermeable material (shield), thereby creating what is known as a Faraday cage [4].

An EMC-compliant device does not cause interference to other devices, avoids self-interference, and remains resilient against radiation from other devices [2], [3]. To achieve this, all electronic devices need protection from electromagnetic interference, typically through an enclosure. This enclosure serves a dual purpose by providing mechanical support and electromagnetic shielding, effectively forming a Faraday cage [3], [5], [6]. A well-designed shield should effectively block both incoming and outgoing EMI, preventing noise, malfunctions, and the risk of electrical circuit and component damage [2], [3], [7].

The principles and concepts of EMC and EMI shielding are well-documented in both theoretical and practical physics [2], [4], [7]. Shielding effectiveness (SE) quantifies the ability of an enclosure or shield to attenuate EMI radiation. It is expressed as the ratio of electromagnetic field strength between the source and the receptor and is typically measured in decibels (dB) [8]–[10]. Commercial electronic devices often require an EMI/RFI shielding effectiveness within the range of 40 to 60 dB, indicating a 99.99% to 99.999% reduction in EMI power [5], [6]. However, for many applications, an SE of 30 dB (equivalent to 99.9% attenuation) is considered adequate [11], [12].

When assessing EM shielding in terms of electric (E) or magnetic (H) field attenuation, the shielding effectiveness of a material can be defined as:

$$SE = 20 \log \left( \frac{E_0}{E_1} \right) = 20 \log \left( \frac{H_0}{H_1} \right) \quad (1)$$

where  $E_0$ ,  $H_0$  is the intensity of the incident field, and  $E_1$ ,  $H_1$  is the intensity of the transmitted field.

EMI SE of an enclosure is a complex problem that depends on the source type, distance, frequency of interference, waveform, shield thickness, apertures design and shield material EM properties (electric conductivity –  $\sigma$ , electric permittivity –  $\epsilon$  and magnetic permeability –  $\mu$ ) [2], [3], [10], [13].

One straightforward approach to assess the shielding effectiveness (SE) of a homogeneous material is to employ Schelkunoff and Schultz's shielding theory for a plane wave transmission line. This model is particularly suitable for lossy materials, such as good conductors, and it characterizes shielding in a homogeneous material with infinitely wide boundaries. It breaks down the SE into three components:

reflection (R), absorption (A), and multiple internal reflections (MR), as depicted in Figure 2 [9], [12]–[16].

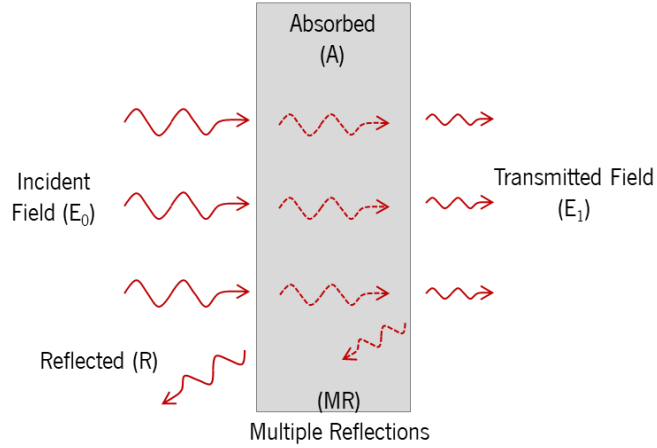


Figure 2. Shielding mechanisms.

This theory is well-suited to describe the shielding of electromagnetic plane waves in the far-field region when they interact with the boundaries of lossy materials. One of the advantages of this model is that it only relies on three material characteristics to describe shielding over a broad frequency range ( $\omega$ ): intrinsic impedance ( $Z_s$ ), skin-depth ( $\delta$ ), and thickness ( $t$ ) [3], [15].

Reflection loss ( $SE_R$ ) is the primary mechanism of shielding, and it is related to an impedance mismatch between the shield's surface and propagating wave at free space ( $Z_0 \approx 377 \Omega$ ), and it can be mathematically described by Equation 2. This effect is promoted by the free charge carriers presented in the conductive material. Therefore, a high electrical conductivity will increase the reflection loss component.

$$SE_R = 20 \log_{10} \frac{(Z_0 + Z_s)^2}{4Z_0 Z_s} \quad [dB] \quad (2)$$

$$Z_s = \sqrt{\frac{j\omega \cdot \mu}{\sigma + j\omega \cdot \epsilon}} \quad [\Omega] \quad (3)$$

Where  $\sigma$  is the conductivity,  $\mu$  is the permeability, and  $\epsilon$  is the permittivity of the material.

Absorption loss ( $SE_A$ ) is the secondary mechanism of shielding, and it happens due to magnetization and electric polarization processes in the medium. The electromagnetic energy is absorbed across the material and converted into other forms, such as heat or molecular vibrations. This component exponentially increases with the material thickness. The absorption loss is proportional to the material

thickness and its skin-depth, which is defined as the depth below the material's surface at which the current density has fallen to approximately 37% (1/e). The formula for the Absorption loss and the material skin-depth is presented in Equation 4 and Equation 5, respectively.

$$SE_A = 20 \log_{10} e^{t/\delta} \text{ [dB]} \quad (4)$$

$$\delta = \sqrt{\frac{2}{\omega \cdot \mu \cdot \sigma}} \text{ [m]} \quad (5)$$

The multiple internal reflections are the third mechanism of shielding, and it happens by the wave reflects back and forth between boundaries of two different medium. For practical purposes, this mechanism can be neglected when  $SE_a > 10$  dB [15], [17], [18].

According to the described methodology, the total shielding effectiveness for a given material can be estimated by Equation 6.

$$SE = SE_R + SE_A = 20 \log_{10} \frac{(Z_0 + Z_S)^2}{4Z_0Z_S} + 20 \log_{10} e^{t/\delta} \text{ [dB]} \quad (6)$$

SE is proportional to the material electrical conductivity and that's the reason that conducting metals such as aluminium, copper, steel or silver are broadly used as reflecting EMI shielding materials. However, the high density, poor mechanical flexibility, low resistance to chemicals and high reflectance constricts the use of these metallic materials. Because of these reasons, metallic shields are being replaced by flexible hybrid shields made by metamaterials [19], [20], intrinsically conducting polymers [8], [15], [21] or thermoplastic composites [11], [22]–[24].

The use of thermoplastics composites reinforced with carbon allotropes, such as carbon nanotubes (CNT), carbon black (CB), carbon fibres (CF) or graphene (Gr) is very appealing for EMI shielding [8], [9], [25]. Their low density, easy processability and resistance to corrosion and oxidation allows many improvements over traditional conductive materials, such as more complex, flexible and lightweight enclosures, made in a sole part which reduce or eliminate seams, preventing EM radiation leakage and SE dropping [10], [26], [27]. Current market trends for lightweight and innovative products stimulate a redesign and manufacture of electronic enclosures fully made of thermoplastic-based materials. These plastic enclosures need to encompass the right combination of material properties with specific design

for mechanical, thermal, and electrical performance, maintaining or improving the EMC. Such solution must comply with the applicable norms and requirements of the targeted multimedia system and surpass the traditional metal-based solution by reducing the product weight and lowering the cost.

### 2.2. Theoretical formalism<sup>1</sup>

The propagation of electromagnetic (EM) waves is a fundamental concern within the realms of electromagnetism and optics. One of the most basic scattering problems involving EM waves relates to the phenomenon of refraction at a planar interface that separates two dielectric media with distinct electrical and/or magnetic properties [28]–[30]. More intricate scenarios are studied by considering the involvement of dissipative media [31]–[38], dispersive properties [39], and generalizing for the transmission of EM waves through multiple media [40], [41].

Frezza et al. [32] delve into the transmission of a plane wave between two lossy media and highlight the absence of total reflection in such systems. On the other hand, Kim et al. [34] explore the transmission of light from a transparent medium onto an absorbing substrate. Their work specifically provides an analytical solution for the pseudo Brewster's angle, which refers to the angle of incidence of the incoming wave at which one of the polarized components of the reflected wave exhibits a minimum of intensity. This is in contrast to the case of two dielectric media where such a minimum reaches zero intensity, referred to as a true Brewster's angle.

#### 2.2.1. Plane waves in lossless and lossy media: dispersion relations

In this section, the refraction of a plane EM wave at a plane interface is examined. This interface separates two distinct media: one is lossless and characterized by its relative permittivity ( $\epsilon_{1r}$ ) and relative permeability ( $\mu_{1r}$ ), while the other is lossy and possesses a relative permittivity ( $\epsilon_{2r}$ ), relative permeability ( $\mu_{2r}$ ), and a conductivity ( $\sigma_2$ ). The SI units are consistently used, and all the constants mentioned are assumed to be real.  $\epsilon_0$  and  $\mu_0$  represent the permittivity and permeability of vacuum, respectively. The chosen coordinate system aligns the interface with the  $z=0$  plane, with its normal directed along the  $z$ -axis.

The homogeneous Maxwell equations that describe the propagation of plane waves in each of these two media, in the frequency domain, are represented by the following equations.

---

<sup>1</sup> This subchapter is based on: Alexandre, B.S.C., Martins, L.C., Santos, J.E., Pontes A.J., Peres, N.M.R. (2020). Fresnel polarisation of infra-red radiation by elemental bismuth. *Eur. Phys. J. B*, 93, 119. <https://doi.org/10.1140/epjb/e2020-10090-9>

$$\nabla \cdot H = 0 \quad (7)$$

$$\nabla \times E = i\mu_0\mu_r\omega H \quad (8)$$

$$\nabla \cdot E = 0 \quad (9)$$

$$\nabla \times H = -i\varepsilon_0\varepsilon_c\omega E \quad (10)$$

Here,  $\mu_r$  varies depending on the medium,  $\varepsilon_c = \varepsilon_{1r}$  applying to medium 1, and  $\varepsilon_c = \varepsilon_{2r}(1 + i\tau_2)$  to medium 2. The loss tangent of medium 2 is denoted as  $\tau_2(\omega) = \frac{\sigma_2}{\omega\varepsilon_0\varepsilon_{2r}}$ . Given the problem's homogeneous nature, the presence of a conduction current in medium 2 can be incorporated into the description by considering a complex permittivity with the aforementioned structure [2].

To obtain a solution for Maxwell's equations, the approach involves considering plane waves with the typical forms of  $H(r) = H_0e^{ik \cdot r}$  and  $E(r) = E_0e^{ik \cdot r}$ . Subsequently, these expressions are substituted into the aforementioned equations, returning:

$$k \cdot H_0 = 0 \quad (11)$$

$$k \times E_0 = i\mu_0\mu_r\omega H_0 \quad (12)$$

$$k \cdot E_0 = 0 \quad (13)$$

$$k \times H_0 = -\varepsilon_0\varepsilon_{2c}\omega E_0 \quad (14)$$

The first and third equations convey the transverse nature of the fields, while the second and fourth equations establish the relationship between the amplitudes  $H_0$  and  $E_0$ . By substituting the expression for  $H_0$  and applying the transverse condition for the electric field, one can derive the dispersion equation for the waves, denoted as  $k \cdot k = \frac{\omega^2}{c^2}\mu_r\varepsilon_c$ . This equation represents the condition for the existence of non-zero solutions for the homogeneous Maxwell equations, with  $c = \frac{1}{\sqrt{\mu_0\varepsilon_0}}$ , signifying the speed of light in vacuum.

For medium 1,  $k_1 = \frac{\omega}{c}\sqrt{\mu_{1r}\varepsilon_{1r}}$  is a real wave vector, and this leads to the dispersion relation. However, in the case of medium 2, this equation implies that the wave vector  $k_2$  has both a real ( $k_2'$ ) and an imaginary ( $k_2''$ ) component, resulting in two equations. It's worth noting that while medium 1

exhibits a linear dispersion relation for plane waves, this is not the case for medium 2, even when considering a constant real conductivity, as  $\tau_2$  varies with frequency  $\omega$ .

The vector  $k_2'$  governs the phase variation of the wave, while  $k_2''$  determines the decay of its amplitude within the lossy medium, owing to dissipation. When these two vectors are parallel, the wave is referred to as a uniform damped wave, meaning that the planes of constant phase align with those of constant amplitude. If they are not parallel, it's termed a non-uniform damped wave.

It's important to note that a decaying non-uniform wave can exist even in a lossless medium. In such a scenario, the two vectors must be perpendicular. This solution characterizes an evanescent wave within the aforementioned lossless medium.

In the general case of a non-uniform wave, where the angle between the vectors  $k_2'$  and  $k_2''$  is represented as  $\zeta$ , the dispersion equation for  $k_2'$  is  $k_2'^4 - \frac{\omega^2 \mu_{2r} \epsilon_{2r}}{c^2} k_2'^2 - \frac{\omega^4 \mu_{2r}^2 \epsilon_{2r}^2 \tau_2^2}{4c^4 \cos^2 \zeta} = 0$ , with  $k_2'' = \frac{\omega^2 \mu_{2r} \epsilon_{2r} \tau_2}{2c^2 \cos \zeta k_2'}$ .

The analysis becomes simpler in the limiting case of a uniform wave. In the limit where  $\tau_2 \ll 1$ , we derive the penetration depth  $\delta_2 = \frac{2}{\sigma Z_2}$ , where  $Z_2$  represents the (real) impedance of the lossy medium. Conversely, if  $\tau_2 \gg 1$ ,  $\delta_2 = \sqrt{\frac{2}{\sigma \omega \mu_0 \mu_{2r}}}$ .

Considering that conductivity is a dimensionful property, the key factor in determining whether a medium can be classified as a conductor, or a dielectric is the dimensionless loss tangent. If  $\tau \gg 1$ , the medium can be regarded as a good conductor at the specific frequency it is being excited, while the opposite limit classifies it as a dielectric.

In situations where conductivity is a frequency-dependent complex function, these findings remain applicable. In this case,  $\epsilon_{2r}$  can be replaced with the real part of the dielectric function, and the loss tangent can be represented as the ratio of its imaginary part to the real part. It's important to note that if, in a specific region of the spectrum,  $\epsilon_2'(\omega)$  is less than zero, the analysis discussed above can be applied without any alterations.

### **2.2.2. Reflection and transmission at the interface between a lossless and lossy medium**

The scenario involves the refraction of a plane wave approaching the interface from the lossless medium at an angle  $\theta_i$  with respect to the normal to the interface. This results in a reflected wave within

the lossless medium, at an angle  $\theta_r$  relative to the normal, and a transmitted wave entering the lossy medium at an angle  $\theta_t$ .

For the sake of generality, it is assumed that the wavevectors of the incident and reflected waves are represented by  $k_i = q_i\hat{x} + u_i\hat{z}$  and  $k_r = q_r\hat{x} + u_r\hat{z}$ , signifying that the plane of incidence is the  $xz$  plane. Both of these vectors adhere to the dispersion relation.

The expressions for the electric field of the incident and reflected waves are denoted as

$$E_i(\mathbf{r}) = [E_{ip}(\cos\theta_i\hat{x} - \sin\theta_i\hat{z}) + E_{is}\hat{y}] \times e^{i(q_ix+u_iz)} \quad (15)$$

$$E_r(\mathbf{r}) = [-E_{rp}(\cos\theta_r\hat{x} - \sin\theta_r\hat{z}) + E_{rs}\hat{y}] \times e^{i(q_rx+u_rz)} \quad (16)$$

where the subscripts  $p$  and  $s$  represent, respectively, the components of the electric field in the plane of incidence and perpendicular to it. Both of these vectors adhere to the transversality condition. The amplitude  $E_{rp}$  is chosen with the same sign to ensure that the polarization axes of all three waves coincide in the limit of normal incidence.

In the case of the transmitted wave, the lossy nature of the medium results in its wave-vector,  $k_t$ , being composed of both a real and an imaginary part.

The electric field of the transmitted wave is represented as  $E_t(\mathbf{r}) = E_{t0}e^{ik_t\mathbf{r}}$ , and it's essential to emphasize that the involved angles are real parameters. These parameters must be appropriately selected to ensure that the transversality condition for  $E_t(\mathbf{r})$  is satisfied, particularly considering that the wave vector  $k_t$  is complex. It's worth noting that this parameterization differs from the conventional approach involving a complex refractive index and a complex transmission angle, as mentioned earlier.

The boundary conditions at the interface, which establish the relationships between the fields in media 1 and 2, can be derived from the integral form of the Maxwell equations. These conditions are expressed as

$$\hat{z} \cdot (\mu_{2r}H_2 - \mu_{1r}H_1)_{z=0} = 0 \quad (17)$$

$$\hat{z} \times (E_2 - E_1)_{z=0} = 0 \quad (18)$$

$$\hat{z} \cdot (\varepsilon_{2c}E_2 - \varepsilon_{1c}E_1)_{z=0} = 0 \quad (19)$$

$$\hat{z} \times (H_2 - H_1)_{z=0} = 0 \quad (20)$$



It's important to note that if we were considering refraction by a slab of lossy material, the field in medium 2 would also encompass a reflected component, and the third medium would be the one where only a transmitted component would exist.

Hence, based on this latest result, it can be inferred that only in the case of normal incidence, will the wave in medium 2 be uniform. Furthermore, it follows that  $\theta_r$ , which represents the angle of reflection, is equal to the angle of incidence, and that  $k'_t \sin \theta_t = \frac{\omega}{c} \sqrt{\mu_{1r} \epsilon_{1r}} \sin \theta_i$ , serving as the generalization of Snell's law, needs to be determined, with  $k'_t$  being a variable in this context. It's important to note that as  $k''_t$  is aligned along the z-axis,  $\zeta$  is equal to  $\theta_t$ , allowing for the determination of  $k'_t$  through this substitution. However, this approach yields an equation expressing  $\sin \theta_i$  in terms of  $\sin \theta_t$  and  $\cos \theta_t$ .

Utilizing this result, we ultimately derive

$$\sin \theta_t = \sqrt{2\mu_{1r}\epsilon_{1r} \sin \theta_i \{[(\mu_{2r}\epsilon_{2r} - \mu_{1r}\epsilon_{1r}\sin^2\theta_i)^2 + \mu_{2r}^2\epsilon_{2r}^2\tau_2^2(\omega)]^{1/2} + \mu_{2r}\epsilon_{2r} + \mu_{1r}\epsilon_{1r}\sin^2\theta_i\}^{-1/2}} \quad (21)$$

which is expressed in terms of  $\sin \theta_i$ . When  $\tau_2 = 0$ , it reduces to the familiar Snell's law. It's worth noting that this result can be loosely interpreted as if medium 2 had a refractive index that depends on the direction of incidence of the incoming wave.

It's important to observe that, in the previous equation, regardless of the ratio of  $\mu_{1r}\epsilon_{1r}$  to  $\mu_{2r}\epsilon_{2r}$ ,  $\sin \theta_t$  is always less than 1. This is in contrast to the scenario with two dielectrics, where  $\mu_{1r}\epsilon_{1r} > \mu_{2r}\epsilon_{2r}$ , leading to the phenomenon of total reflection for angles of incidence such that  $\sin \theta_i \geq \sqrt{\frac{\mu_{2r}\epsilon_{2r}}{\mu_{1r}\epsilon_{1r}}}$ . Additionally, it's noteworthy that at large  $\tau_2$ , the penetration depth  $\delta_2$  approaches zero.

### 2.2.3. Power relations at the interface

To analyse the power relationships at the interface, it is necessary to calculate the expressions for the averaged power of the field over a period of the incoming wave on each side of the interface. The Poynting vector of the EM field is represented as

$$P_1(r) = \frac{1}{2Z_1} (|E_{i0}|^2 \hat{k}_i + |E_{r0}|^2 \hat{k}_r) + \frac{1}{2\omega\mu_0\mu_{1r}} [Re(E_{i0} \cdot E_{r0}^*)(k_i + k_r) + Re(E_{i0} \cdot (k_i - k_r)E_{r0}^* - Re(E_{r0} \cdot (k_i - k_r)E_{i0}^*)] \quad (22)$$

where  $\hat{k}_i$  and  $\hat{k}_r$  are unit vectors in the direction of incidence for the incoming and reflected waves, respectively. It's worth noting that in this specific scenario, the Poynting vector remains independent of position, suggesting that no energy is absorbed by medium 1.

In medium 2,  $P_2(r) = \frac{e^{-2u_t''z}}{2\omega\mu_0\mu_{2r}} [k_t'|E_{t0}|^2 - iu_t''\hat{z} \times (E_{t0} \times E_{t0}^*)]$ . The decreasing Poynting vector with increasing distance from the interface signifies that energy is being absorbed within medium 2.

The coefficients  $\mathcal{R}$  and  $\mathcal{T}$  can be defined to represent the relative amounts of transmitted and reflected energy at the interface. It holds that  $\mathcal{T} + \mathcal{R} = 1$ , with  $\mathcal{R} = |r_p|^2 \cos^2 \xi + |r_s|^2 \sin^2 \xi$  and  $\mathcal{T} = \frac{\mu_{1r} \tan \theta_i}{\mu_{2r} \tan \theta_t} (|t_p|^2 \cos^2 \xi + |t_s|^2 \sin^2 \xi)$ , where  $\cos \xi = \frac{|E_{ip}|}{|E_{io}|}$  and  $\sin \xi = \frac{|E_{is}|}{|E_{io}|}$ , and the reflection and transmission coefficients are determined by

$$t_p = \frac{2\zeta_p \cos \theta_i}{\zeta_p \cos \theta_t + Z_1 \cos \theta_i} \quad (23)$$

$$r_p = \frac{\zeta_p \cos \theta_t - Z_1 \cos \theta_i}{\zeta_p \cos \theta_t + Z_1 \cos \theta_i} \quad (24)$$

$$t_s = \frac{2\zeta_s \cos \theta_i}{\zeta_s \cos \theta_i + Z_1 \cos \theta_t} \quad (25)$$

$$r_s = \frac{\zeta_s \cos \theta_i - Z_1 \cos \theta_t}{\zeta_s \cos \theta_i + Z_1 \cos \theta_t} \quad (26)$$

where  $Z_1 = \sqrt{\frac{\mu_0 \mu_{1r}}{\epsilon_0 \epsilon_{1r}}}$  is the impedance of medium 1,  $\zeta_p = \frac{u_t' + iu_t''}{\omega \epsilon_{2c} \epsilon_0 \cos \theta_t}$  and  $\zeta_s = \frac{\mu_0 \mu_{2r} \omega \cos \theta_t}{u_t' + iu_t''}$ . In the

case of normal incidence, there is only  $\mathcal{R} = |r|^2$  and  $\mathcal{T} = Z_1 \text{Re}(Z_{2c}^{-1}) |t|^2$ , with  $Z_{2c} = \sqrt{\frac{\mu_0 \mu_{2r}}{\epsilon_0 \epsilon_{2c}}}$ ,  $r =$

$$\frac{Z_{2c} - Z_1}{Z_{2c} + Z_1} \text{ and } t = \frac{2Z_{2c}}{Z_{2c} + Z_1}.$$

### **3. THERMOPLASTIC COMPOUNDS PROCESSED BY INJECTION MOULDING**

### **3.1 Introduction**

The use of engineering thermoplastic composites has garnered significant interest from original electronic equipment manufacturers (OEMs). These materials offer numerous advantages for the structural components of electronic devices, commonly known as housings or enclosures. Traditionally, these enclosures have been made from metallic materials like steel or aluminium. In the pursuit of enhancing product efficiency, manufacturing productivity, and aligning with environmental goals, OEMs are increasingly turning to thermoplastics. These materials are valued for their lightweight properties, ease of processing into complex shapes, and the ability to reduce the number of components, all of which help manufacturers remain competitive and in line with new legislation and environmental targets.

However, thermoplastic composites exhibit lower electrical conductivity compared to metals, and their anisotropic characteristics introduce complexity to their electrical properties and shielding effectiveness. Therefore, it is crucial to investigate and optimize their electrical properties to achieve adequate SE and EMC compliance for electronic devices. This chapter presents a comprehensive characterization of the shielding performance of injection-moulded thermoplastic compounds reinforced with carbon fibres, stainless steel, and other fillers. Alongside the experimental analysis, theoretical models were developed to describe the dielectric and electromagnetic shielding properties of the created specimens.

The work in this chapter unfolded in three sequential studies:

- First approach on the characterizing the electromagnetic (EM) shielding of fibre-reinforced thermoplastic compounds. Commercially available thermoplastics were used to create 2mm thick, disk-shaped specimens via injection moulding. The shielding effectiveness of these specimens was experimentally measured and characterized using simplified theoretical models.
- On a second phase, the study progressed to investigate two injection-moulded grades of carbon-fibre-reinforced polybutylene terephthalate (PBT). During this stage, the anisotropic conductivity was evaluated and correlated with the shielding effect. Additionally, the influence of specific injection moulding process conditions was considered.
- In the third and last phase of this chapter, the study delved into the shielding properties in correlation with frequency-dependent conductivity. This analysis was conducted on new materials filled with either carbon or stainless-steel fibres and processed under different

injection moulding conditions. In addition to the experimental investigation, a theoretical characterization was performed using an improved workflow and theoretical models.

This comprehensive research enhances the understanding of the electrical and shielding properties of thermoplastic composites, thereby facilitating advancements in electronic device enclosures and their electromagnetic compatibility performance.

## 3.2 Literature review

Traditionally, metals like steel or aluminium have been the preferred choice for producing electromagnetic interference shielding enclosures for electronic devices due to their high electrical conductivity. However, recent research efforts have focused on the development of polymer matrix composites with conductive fillers as an alternative to traditional metal structures [5], [6], [13], [24], [42]–[50].

Polymer composites with conductive fillers offer several advantages for EMI shielding. They have low density, making them lightweight, and are easily processable, particularly through methods like injection moulding. This ease of processing allows for the production of more complex and lightweight enclosures without seams, which is desirable for preventing electromagnetic radiation leakage and maintaining high shielding effectiveness [13]. Using injection moulding technology for conductive polymer composites in electronic enclosures enables cost-effective industrial production.

Researchers and institutions have invested considerable efforts in understanding and optimizing the electrical conductivity and electromagnetic shielding properties of plastic composites. These composites involve reinforcing the polymer matrix with dispersed electrically conductive fillers, such as various carbon materials (carbon fibres, carbon black, carbon nanotubes, graphene) or metallic particles or fibres (e.g., stainless steel, copper, or aluminium). This approach allows for the creation of composite materials with a wide range of properties, ranging from antistatic to conductive [8]–[10], [15], [21], [24], [51]–[60].

Reinforced thermoplastic composites offer flexibility in tailoring and controlling electrical properties, especially EM shielding, to meet specific requirements. Key factors that can be controlled include material composition (type of filler, its length or aspect ratio, and its volume fraction), part thickness, and processing parameters that influence filler dispersion and orientation. This flexibility makes them suitable for a wide range of applications [24], [61]–[63].

Researchers have conducted extensive studies on the EMI SE of polymer composites with various matrices and conductive fillers, resulting in a wide range of shielding performance. Commonly used fillers for these applications include carbon fibres, carbon nanotubes/fibres, nickel-coated carbon fibres, stainless steel fibres, and metallic particles. Stainless-steel and nickel-coated carbon fibres, owing to their ferromagnetic properties, enhance electromagnetic absorption, leading to increased composite SE. As a result, polymer composites with stainless steel fibres or nickel-coated carbon fibres exhibit superior shielding effectiveness [6], [9], [10], [17], [42], [64], [65].

The utilization of thermoplastic compounds reinforced with carbon fibres is highly attractive due to the numerous advantages they offer over traditional conductive materials used for enclosure components. These advantages include resistance to oxidation and corrosion, reduced weight, enhanced versatility, and improved processability. These features contribute to consolidating the housing structure and reducing or eliminating seams [9], [26].

Research by Al-saleh et al has focused on incorporating various carbon fillers into polymeric matrices. Their investigations have revealed a direct relationship between electrical conductivity and shielding properties. These properties are directly proportional to filler concentration and sample thickness [14], [66]–[69].

Chiu et al, investigated the addition of carbon fibres to a nylon matrix in or to shield a laser diode package and, besides founding that the electrical resistivity is lower with an increase of fibre loadings, they found that higher fibre lengths provided even lower resistivity. Lower resistivity led to higher electromagnetic shielding, as they verified. The SE at 1 GHz was almost 60 dB for a loading of 30% of long carbon fibres, while the same concentration of short carbon fibres only provided a 30 dB shielding [23].

Weber et al, verified that the electrical resistivity of polypropylene reinforced with nickel-coated graphite (NCG) fibres or stainless-steel (SS) fibres is anisotropic for both compression moulding, injection moulding and extrusion samples, being lowest in the main direction of fibre orientation. Additionally, besides checking that the distance to the injection gate influences the measured resistivity, they found that the resistivity decreases with an increase of fibre loading and that the SS fibres percolation threshold is lower than the NCG fibres but NCG fibres provided lower resistivities at ultimate loading [61].

Arjmand et al, studied the addition of MWCNT to polycarbonate and polystyrene, produced by compression or injection moulding. They found that the electrical resistivity is more anisotropic in injection

moulded samples, and resistivity decays with an increase of CNT loadings and a lower percolation threshold and for compression moulding samples. Furthermore, they measured the EM SE and found that shielding increased with an increase of injection moulding temperature and speed, but was lower than the shielding measured in compression moulded samples [46], [70].

Bryant studied the addition of long nickel-coated carbon fibre (LNCCF) to polycarbonate in comparison to standard nickel-coated carbon fibre (NNCF) and stainless-steel fibre (SSF) and discovered that at relatively low loading levels the addition of LNCCF resulted in an increase in the EM SE. Hence, LNCCF is an excellent filler to use in order to achieve higher SE with lower specific gravity. Nevertheless, at a loading of 20 wt% all of the fillers provided an excellent shielding above 80 dB for a 3 mm thick sample [6].

The synergic effect of the addition of multi-fillers was found to be beneficial to the electrical properties and SE of the hybrid composite. The addition of carbon filler, such as CNT or Carbon Black, to an existing loaded polymer can provide a decrease in resistivity and, hence, an increase in SE [5], [69], [71]–[75].

The processing parameters, specifically the injection moulding variables, can affect the performance of plastic part since the thermomechanical dynamics in the process will affect the filler dispersion and orientation. The melt temperature, Mold temperature, injection speed, holding pressure, back pressure, and screw speed are the most studied processing variables, but other parameters such as gate design and channel length. It was found, in correlation with the type of filler and concentration, that the melt temperature, holding pressure, injection speed and channel length can have significant effect on the electrical conductivity and EM shielding. These factors contribute significantly to the fillers dispersion and orientation along the sample leading to a good or bad conductive network from the fillers inside the polymer matrix [47], [56], [70], [76]–[83].

In a study by Bryant, a two-level partial factorial design of experiments was employed to analyse effect of five moulding parameters on the EMI shielding of a SSF filled polycarbonate (PC) compound. The results showed that the melt temperature was the most significant parameter, followed by the injection speed and screw speed, influencing the EMI shielding performance. Specifically, the melt temperature had a positive effect on shielding, while the injection speed had a negative effect [84].

Lee et al and Chen et al investigated the impact of fibre content and various injection moulding parameters, including melt temperature, mould temperature, and injection speed, on the EMI SE in SSF-filled ABS composites. The research findings indicate that fibre content significantly affects the EMI SE

performance of the parts, observing a logarithmic increase from 40 dB to 72 dB. Higher melt and mould temperatures enhance shielding effectiveness by promoting a more uniform and random fibre orientation. In contrast, higher injection velocities result in highly oriented and less uniform fibre distribution, leading to reduced shielding effectiveness [50], [85]. In a previous study aimed at producing carbon-filled PPS bipolar plates for fuel cells, Lee examined the correlation between specimen conductivity and fibre orientation and distribution resulting from the moulding process. His findings indicated that higher melt temperature, Mold temperature, and packing pressure promoted increased conductivity due to a more random fibre orientation that closely intertwined the carbon fibres. However, higher injection speed led to a higher fibre orientation, resulting in lower conductivity. Additionally, Lee also investigated the conductivity in different regions of the part and observed a sequence of conductivity values from highest to lowest as follows: far-gate regions > near-gate regions > centre regions. This variation can be attributed to the combined effects of fountain flow, frozen layer thickness, and gapwise melt front velocity [86].

Cheng et al investigated the EMI SE of injection-moulded polycarbonate composites filled with conductive nickel-coated carbon fibres was investigated. The research examined the effects of injection speed, melt temperature, mould temperature, and packing pressure on EMI SE using a Taguchi experimental design. The results indicate that packing pressure and mould temperature have the most significant impact on EMI shielding efficiency, followed by injection speed and melt temperature. The EMI SE of the specimens ranged from 12 dB to 19 dB, with injection speed negatively affecting it and packing pressure having a positive effect. Both melt and mould temperature induced variations, although without a clear trend [47].

Arjmand et al. conducted a study to examine the electrical resistivity and EMI SE properties of 15 wt.% multi-walled carbon nanotubes/polycarbonate (MWCNT/PC) composites under different injection conditions. They measured electrical resistivity in three different areas, for both parallel and perpendicular to the flow direction. The results revealed that areas inducing higher alignments exhibited higher resistivity and a percolation threshold. Furthermore, for samples with a random distribution of MWCNT created through compression moulding, both shielding by reflection and absorption increased with higher MWCNT concentration and greater thickness of the shielding material [46].

Mehdi et al.'s investigation emphasizes that both processing conditions and mould designs significantly impact the electrical conductivity and shielding performance of injection-moulded CNT-filled composites. They conducted a study to assess the effects of gate and runner designs and processing conditions, including mould temperature, melt temperature, packing pressure, and injection velocity, on



the volume resistivity of the composites in both the thickness and in-flow directions. The experiments revealed that volume resistivity could be varied by up to 7 orders of magnitude by altering the processing conditions and that EMI SE decreased with an increase in the alignment of the injection-moulded MWCNTs in the polystyrene matrix [87].

As discussed, there is a substantial body of knowledge concerning the electrical and electromagnetic properties of polymers reinforced with electrically conductive fillers. However, these materials exhibit a complex behaviour and require precise control to optimize their final properties and production costs. Therefore, the goal of this research is to contribute valuable insights to the field of electrical conductivity and electromagnetic shielding in polymeric compounds reinforced with electrically conductive fibres. This investigation focuses specifically on the impact of injection moulding conditions on the anisotropic electrical conductivity and EMI SE of fibre-filled injection-moulded compounds.

When it comes to theoretically modelling the electromagnetic shielding behaviour of materials and complex structures, numerical tools dedicated to solving electrodynamics equations and simulating EM/RF environments and problems play a crucial role. These tools are invaluable for studying how EM waves scatter when interacting with a dissipative or conductive medium. They can be used to analyse the shielding performance of enclosure designs, including critical features such as seams and apertures, which is essential for early EMC pre-compliance [88].

These numerical tools enable the estimation of shielding effectiveness for various materials based on their electrical properties. However, it's important to note that simulated materials are typically metals with isotropic behaviour and well-defined properties that can be accurately represented in virtual models. Shielding for more complex materials, such as composites, has also been explored in previous research. However, these studies often focus on structured filler arrangements or multilayer systems [18], [89]–[95].

Paliotta et al. conducted a theoretical analysis of EM wave propagation through a shield composed of highly conductive multilayer graphene papers. Their analysis assumed constant and isotropic values for magnetic permeability, electrical conductivity, and dielectric permittivity, and encompassed the transmission line formalism using an equivalent impedance model [96]. This approach, similar to the one used in this work, yielded a good approximation to experimental measurements.

### 3.3 Work methodology

The adopted methodology comprised of three areas, two of them experimental and one theoretical, as show in the plan from Figure 3.

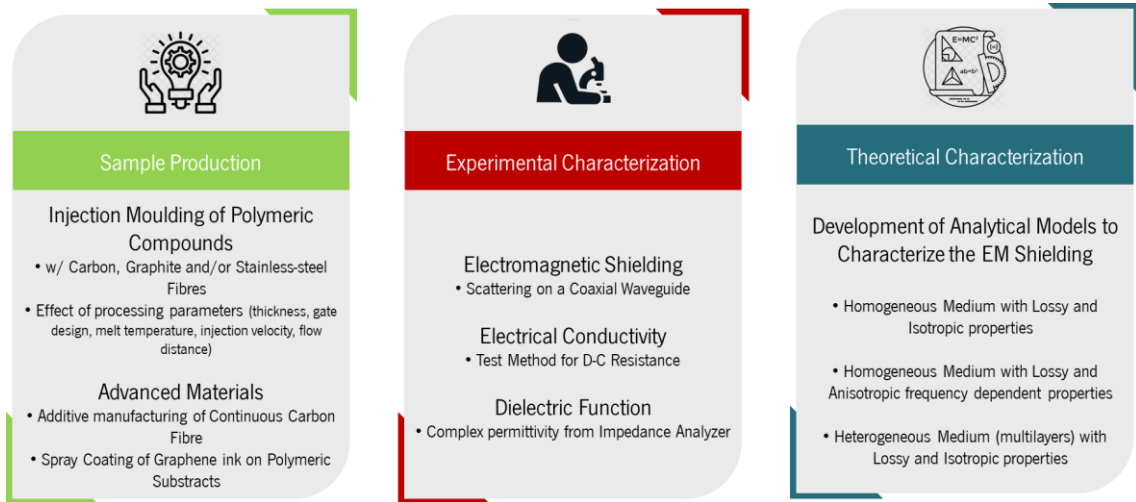


Figure 3. Work plan.

The first aspect of this working methodology involves the production of specimens for analysis. This phase includes selecting suitable thermoplastics that are reinforced with electrically conductive fillers, such as carbon fibres (CF), carbon black (CB), and/or stainless-steel fibres (SSF). Specimens are then manufactured using injection moulding technology. The selection of the aforementioned types of conductive fillers was based on their good conductive properties, ease of commercial availability, excellent compatibility with thermoplastic materials, and suitability for processing by injection moulding, which was the selected processing method due to its well-known industrial advantages.

Subsequently, the specimens undergo a comprehensive characterization process, which includes assessing their electromagnetic shielding, electrical conductivity, and permittivity. The goal is to establish correlations between these characteristics, as well as their relationship with the injection moulding parameters. In addition to these macroscopic properties, a comprehensive investigation of the morphological characteristics would be highly beneficial for fully understanding the properties of the produced specimens and for enhancing the scientific contribution of this work by establishing a relationship between processing, morphology, and properties. However, accurately assessing the distribution of conductive fillers is technically challenging and would significantly increase the complexity of the work. This level of detail is ultimately not essential for the primary objective of this study, which is to examine the relevant macroscopic properties that describe the electromagnetic shielding behaviour.

Successively, theoretical models were developed. These models are based on the transfer matrix approach, which is used to analyse the scattering of electromagnetic waves within a homogeneous medium. These models incorporate either arbitrary material properties or data collected during the experimental characterization. The primary objective of these theoretical models is to predict the shielding effectiveness of the polymeric compounds.

The following sub-chapters provide a more detailed description of each aspect of this working methodology.

### **3.3.1. Materials and samples**

Several commercially available thermoplastic compounds from different suppliers were identified and tested during in this investigation. These compounds are reinforced with electrically conductive fillers, such as carbon fibres (CF), carbon black (CB), and/or stainless-steel fibres (SSF). The material selection process was essentially based on their datasheet's electrical resistivity or SE if available. However, aspects such as stiffness, thermal stability, injection moulding suitability and costs were also considered.

Due to the diversity of studies carried out, the description of the material used will be made further down, and in the corresponding studies. However, the existence of a Non-Disclosure Agreements (NDA) with project owners and suppliers, restricts the sharing of some of the trade names and filler specifications. Nonetheless, some general properties will be provided.

Regarding the production of test specimens, flat disks or rectangular plates were produced in an injection moulding press (*Ferromatik Milacron K85-S/2F*). In this process, the thermoplastics pellets were hopped into the injection moulding barrel, heated, and injected into a one-cavity mould through specific feeding system. The generic dimensions of the mouldings, which are different to each study, and corresponding injection moulding conditions will be provided further down to each investigation. At the end of the injection cycle, and after at least 24 hours, some smaller specimens were cut from the mouldings to be used in the measuring apparatus for shielding, conductivity, and permittivity, following the respective procedures described below.

### **3.3.2. EM Shielding procedure**

EMSE measurements were performed with a test procedure that follows the ASTM D4935-99 Standard (Standard Test Method for Measuring the Electromagnetic Shielding Effectiveness of Planar

Materials)[97] wherein the sample is placed between two coaxial flanges which acts both as sample holder and TEM waveguide, as used by Hong (2003) [98], Sarto (2006)[99] and Vasquez (2009)[100].

The flanged coaxial sample holder (FCSH) is an enlarged coaxial transmission line, made in a Brass alloy, designed, and manufactured in our laboratory to support 60 mm diameter samples maintaining a characteristic impedance of  $50 \pm 0.28 \Omega$  throughout the entire length of the holder and a theoretical cut-off frequency of 5.78 GHz. The FCSH is connected to a Vector Network Analyzer (R&S®ZVL3) with the assistance of two 50  $\Omega$  coaxial cables and two 10 dB 50  $\Omega$  attenuators to improve the impedance matching, as show in Figure 4.

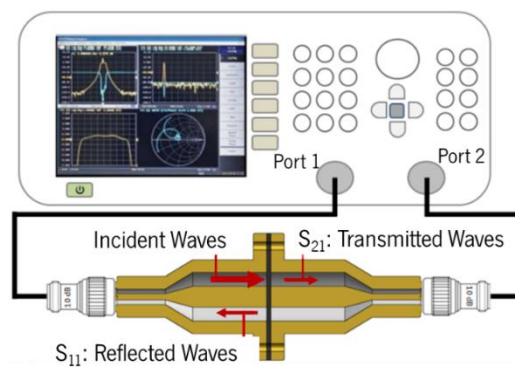


Figure 4. Schematic of the experimental apparatus.

Shielding Effectiveness (SE) was measured at the frequency range between 30 MHz and 3 GHz, which is a radio frequency spectrum common to automotive standards for electromagnetic compatibility (CISPR 25)[101], and is the VNA limit range. The VNA used an input power of 0 dBm, corresponding to 1 mW, to generate EM waves and recorded the scattering parameters S11 (reflection) and S21 (transmission) to determine the total EMSE and the respective shielding components according to the Equation 27 [102]–[106].

$$SE_T (dB) = SE_R + SE_A + SE_M \quad (27)$$

The shielding by reflection ( $SE_R$ ) and shielding by absorption ( $SE_A$ ) were calculated using Equation 28 and Equation 29, respectively. The microwave multiple internal reflections ( $SE_M$ ) can be negligible, since the  $SE_T$  is higher than 10 dB [103].

$$SE_R (dB) = -10 \log_{10}(1 - R) \quad (28)$$

$$SE_A (dB) = -10 \log_{10} \left( \frac{T}{1 - R} \right) \quad (29)$$

wherein the reflected coefficient (R) and transmission coefficient (T) were directly obtained as

$$R = |S_{11}|^2 \quad (30)$$

$$T = |S_{21}|^2 \quad (31)$$

As described in ASTM D4935 [97], can also be used to quantify the electromagnetic shielding across a given material thickness. This procedure determines the EM shielding by means of the insertion loss method between an EM signal generator and a receiver and can also be conveniently performed using only the vector network analyser transmission coefficient. Thereby, the resulting SE can be expressed by a ratio between the transmission scattering parameter S21 of a reference sample (S21ref) and a load sample (S21load), as shown in the Equation 32.

$$IL = SE = 20 \log_{10} \frac{S21_{ref}}{S21_{load}} \quad (32)$$

As state in the ASTM D 4935 standard, the reference and load samples must be of the same material and thickness. The load sample is a solid thick disk with diameter at least the size of the outer diameter of the flange holder, while the reference sample consists of two pieces of the same material obtained by removing a toroid shape area, corresponding to the air gap inside the flange holder where the EM waves propagate. Both sample's geometries are show in Figure 5.

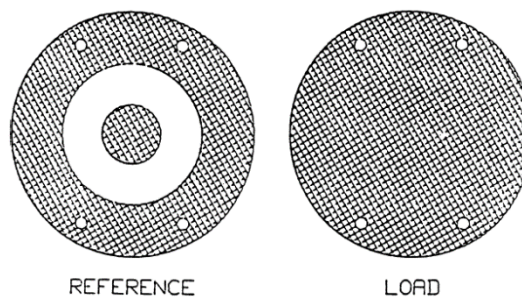


Figure 5. Illustration of reference and load samples [97].

As mentioned in chapter 2.1. Introduction to EM shielding, an experimental apparatus to measure the electromagnetic shielding effectiveness can be different depending on the type of characterization that is to be performed. In this way, in the course of this research an experimental system with multiples configurations was produced. This apparatus allows the measurement of the EM shielding according to

ASTM D4935, but it may also be used to evaluate the shielding to normally incident waves with the transverse electric ( $TE_{10}$ ) propagation mode. In the latter, one uses a rectangular waveguide which can analyse the shielding effectiveness of flat solid samples or samples with perforations, like ventilation grids. More information about the developed apparatus on Appendix A. Supplementary information regarding the EM shielding apparatus

### 3.3.3. Electrical conductivity

Electrical conductivity, denoted by the symbol “ $\sigma$ ”, is a material property that quantifies its ability to conduct electric current. It is the measure of the conductance (G) per unit length and per unit cross-sectional area of a material. The SI unit of conductivity is siemens per meter (S/m) and, in an ideal case of a uniform material it can be expressed by the Equation 33.

$$G = \sigma \frac{l}{A} \quad (33)$$

where G is the electrical conductance,  $\sigma$  is the electrical conductivity, A is the cross-sectional area of the material, and l is the length of the material.

Conversely to conductivity, the material electrical resistivity, is an intrinsic property that characterizes its resistance to the electric current flow. Resistivity can be measured more swiftly with common equipment used for this purpose, and the corresponding conductivity can be determined by the Equation 34.

$$\sigma = \frac{1}{\rho} \quad (34)$$

Electrical resistivity is the measure of the electrical resistance (R) per unit length and per unit cross-sectional area of a material. It is denoted by the symbol “ $\rho$ ” and is measured in ohm-meters ( $\Omega.m$ ). In an ideal case, a uniform material resistance is directly proportional to its length and inversely proportional to its cross-sectional area and expressed by Equation 35.

$$R = \rho \frac{l}{A} \quad (35)$$

In this work, the static (or DC) electrical resistance properties for the produced specimens was measured under ambient temperature conditions with two customized 4-point copper electrodes, which were designed and manufactured in house to characterize the anisotropic electrical properties for both longitudinal (in-plane) and transversal (through-plane, or through-thickness) directions of a given specimen. For both measurements, a test setup, which contain a power source and a multimeter, is used for voltage and current measurements following Ohm's law. This empirical relation is adequate to accurately describe the conductivity for most electrically conductive materials, and states that, for a given constant resistance, the electrical current through the material is directly proportional to the voltage across the measured points and described as

$$I = \frac{V}{R} \quad (36)$$

where  $I$  is the current through the conductor, expressed in Amperes (A),  $V$  is the voltage measured across the material, expressed in Volts (V) and  $R$  is the resistance of the material, expressed in Ohms ( $\Omega$ ).

The electrical resistance in the longitudinal direction was measured with 4-point electrodes which were designed based on ASTM D4496-87 (test method for DC resistance of moderately conductive materials) and ISO 3915:1981 (measurement of resistivity of conductive plastics). With this setup, there is a constant electric current ( $I$ ) passing through the specimen's length. The power source to induce the electrical current is applied on both edges to promote a constant current on the complete cross section of the specimen. The resulting voltage drop ( $V$ ) is measured at one of the surfaces with two sensors spaced by 10 mm and placed within the source electrodes. A schematic of this setup can be seen in Figure 6.

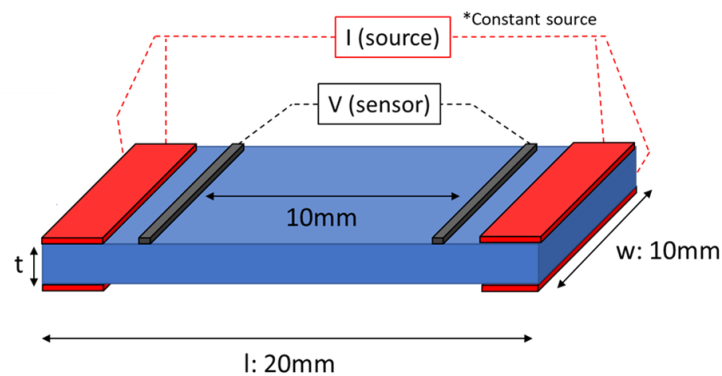


Figure 6. Electrodes schematic to measure the longitudinal electrical resistance.

For the transversal resistance, a capacitor-like geometry was manufactured with copper electrodes placed in the opposite faces of the specimen. With this setup, there is a constant electric current ( $I$ ) passing through the specimen's thickness. A constant current is applied on both sides of the specimens and the resulting voltage drop ( $V$ ) is measured by two sensors placed within the current electrodes on each face of the specimen. The schematic of this setup can be seen in Figure 7.

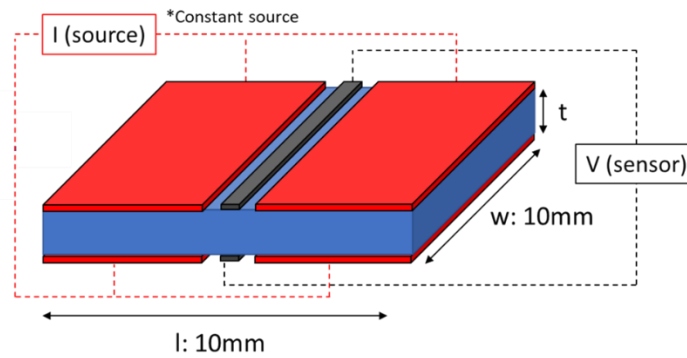


Figure 7. Electrodes schematic to measure the transversal electrical resistance.

For both setups, all four electrodes (current positive and negative pole, and voltage negative and positive pole) are independent to each other and connected to the power source (like a picoammeter, or sourcemeter) to supply direct current and to measure the resulting voltage. According to the Ohm's law fundamentals, and assuming a uniform material model, it's possible to quantify the static electrical resistance, and corresponding resistivity (longitudinal or transversal), with Equations 37, 38 and 39, respectively.

$$R = \frac{V}{I} \quad (37)$$

$$\rho_L = \frac{R \times (w \times t)}{l} \quad (38)$$

$$\rho_T = \frac{R \times (w \times l)}{t} \quad (39)$$

where  $R$  is the static electrical resistance (units in Ohm,  $\Omega$ ),  $V$  is the voltage drop (unit in Volt,  $V$ ),  $I$  is the electrical current (unit in Ampere,  $A$ ),  $w$  and  $l$  are the specimen's width and length, respectively,  $t$  is distance between the electrodes or sample thickness,  $\rho_L$  is the longitudinal resistivity (with units in Ohm/cm), and  $\rho_T$  is the transversal resistivity (with units in Ohm/cm).



### **3.3.4. Electrical permittivity and frequency dependent conductivity**

Electrical permittivity, also known as dielectric permittivity, is denoted by the symbol  $\epsilon$  (epsilon), and the corresponding SI unit is farads per meter (F/m). Permittivity is a fundamental property of a material that describes its ability to store electrical energy in an electric field. The characteristic of how easily an electric field can penetrate a material and how strongly it can affect the behaviour of the inner charges is an important parameter to understand the behaviour of dielectric materials, and electromagnetic wave propagation.

It's worth noting that permittivity is a complex quantity ( $\epsilon^*$ ), meaning it has both a real and imaginary part. The real part of permittivity ( $\epsilon'$ ), also called dielectric constant, represents the material's ability to store energy when an external electric field is applied, while the imaginary part ( $\epsilon''$ ) accounts for energy losses in the material. And it is represented by the Equation 40.

$$\epsilon_r^* = \epsilon_r' - i\epsilon_r'' \quad (40)$$

The permittivity of a material can be determined through various experimental methods. One common method is known as capacitance measurement, or parallel plate method, where the capacitance material of interest sandwiched between two electrodes is measured. The capacitance of a capacitor is directly related to the permittivity of the dielectric material between its plates. This method is straightforward to accurately measure the frequency dependent permittivity in low frequency spectrum for both thin sheets or liquid samples.

By measuring the capacitance (C) and knowing the geometric dimensions (A and t) of the material, one can calculate the permittivity with equations 41 and 42, for both the real and imaginary part, respectively.

$$\epsilon_r' = \frac{C t}{\epsilon_0 A} \quad (41)$$

$$\epsilon_r'' = \epsilon_r' \times \tan \delta = \frac{\sigma}{\epsilon_0 \omega} \quad (42)$$

Where C is the measured capacitance,  $\epsilon_r'$  is the real part of permittivity,  $\epsilon_0$  is the permittivity of free space,  $\tan \delta$  is the measured loss tangent,  $\sigma$  is the electrical conductivity,  $\omega$  is the angular frequency, A is the area of the capacitor electrode, and t is the thickness of the sample material.

The measurement system used in this research, is based on the parallel plate method, also called the three-terminal method in ASTM D150, with the *16453A Dielectric Material Fixture* connected to the *E4991A Impedance Analyzer*, both developed by *Keysight Technology, Inc.*

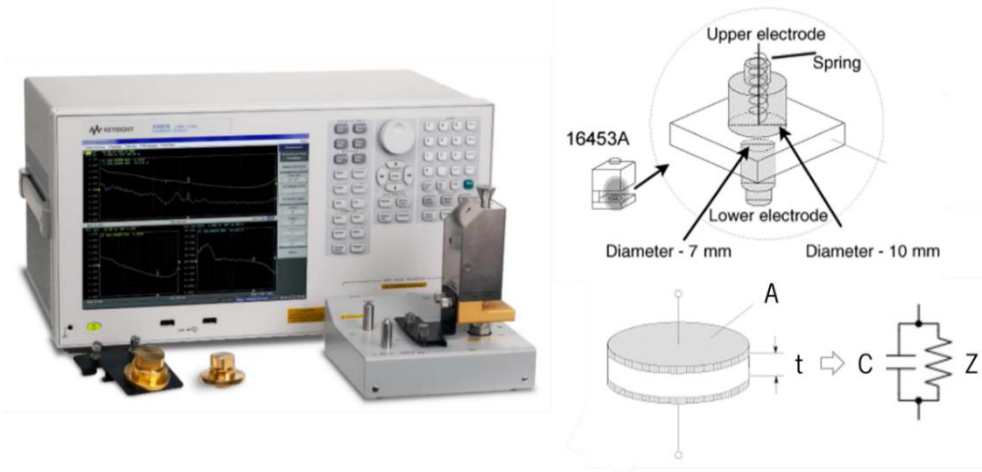


Figure 8. Picture of the E4991A impedance analyzer with dielectric test fixture 16454A. source: Keysight Technologies

With this setup, it is possible to directly measure the relative permittivity and its related parameters for solid dielectric materials in a wide frequency range between 1 MHz and 1 GHz, and at room temperature. Figure 8 shows an actual image for the E4991A impedance analyser and the 16453A accessory to measure permittivity according to the ASTM D150 “*Standard Test Methods for AC Loss Characteristics and Permittivity (Dielectric Constant) of Solid Electrical Insulation*”. Since the capacitor formed using the 16453A cell has a small capacity because of its large impedance, the common equivalent circuit for the apparatus consists of an equivalent parallel capacitance (C) and an equivalent parallel impedance (Z), as shown in Figure 8.

The adopted procedure provides the possibility to measure the electrical permittivity properties according to a three-element equivalent circuit model. This method involves fitting the measured impedance data to an LCR circuit model that represents the electrical behaviour of the sample across the frequency of analysis. It was found that using an equivalent LCR circuit model in series, as seen in Figure 9 provides good accuracy to the impedance measurement and corresponding permittivity of polymeric aggregate materials.

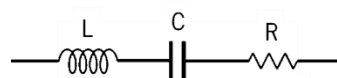


Figure 9. Equivalent LCR circuit diagram.

where, L represents the circuit inductance, R represents the resistance, and C represents the capacitance.

The equivalent impedance of the circuit, and representative of the sample material impedance, is given by the sum of the three individual elements in the equivalent circuit and expressed by the Equation 43.

$$Z = R + \frac{1}{i\omega C} + i\omega L = R - \frac{i}{\omega C} + i\omega L \quad (43)$$

$$|Z_{eq}| = \sqrt{R^2 + \left(\frac{1}{\omega C} - \omega L\right)^2} \quad (44)$$

Developing the mathematical calculation of the equivalent impedance it's possible to describe the electrical permittivity as a function of the angular frequency ( $\omega$ ). The real and imaginary components of permittivity can be calculated with Equations 45 and 46, respectively.

$$\varepsilon' = \frac{t}{\varepsilon_0 S} \left( \frac{C}{1 + \omega^2 C^2 R^2} \right) \quad (45)$$

$$\varepsilon'' = \frac{t}{\varepsilon_0 S} \left( \frac{\omega C^2 R}{1 + \omega^2 C^2 R^2} \right) = \frac{\sigma'}{\omega \varepsilon_0} \quad (46)$$

where, t is the material thickness, S the electrode surface area,  $\varepsilon_0$  is the permittivity of vacuum, C and R correspond to the measured capacitance and resistance of the equivalent impedance circuit.

The corresponding electrical conductivity measured along the material thickness ( $\sigma'Z$ ) can be calculated by Equation 47.

$$\sigma'Z = \frac{t}{SR} \frac{\omega^2 \tau_{RC}^2}{1 + \omega^2 \tau_{RC}^2} \quad (47)$$

### 3.3.5. Theoretical models

The typical configuration examined in experimental investigations for assessing the EM characteristics of a given substance or structure is the "slab geometry." This setup can be closely approximated when conducting measurements of transmission and reflection through a finite material slab.

Within the context of electromagnetic wave propagation in a vacuum, considering an angular frequency represented as  $\omega$ , the wave encounters the designated slab perpendicularly, composed of lossy material. The material possesses distinct properties, notably a complex electric permittivity denoted as  $\epsilon_2$  and a complex magnetic permeability referred to as  $\mu_2$ , both intricately dependent on the angular frequency  $\omega$ . These characteristics indicate the dispersive nature of the material. Additionally, it is postulated that the slab extends infinitely in directions perpendicular to the path of wave propagation.

The magnitude of the wave-vector in a vacuum is referred to as  $k_1 = \omega\sqrt{\mu_0\epsilon_0}$ , while in the material, it is designated as  $k_2 = \omega\sqrt{\mu_2\epsilon_2}$ . Typically,  $k_2$  is a complex quantity, indicating absorption within the material. The vacuum's impedance is represented as  $Z_0 = \sqrt{\frac{\mu_0}{\epsilon_0}}$ , and the material's impedance is denoted as  $Z_2 = \sqrt{\frac{\mu_2}{\epsilon_2}}$ , both of which are generally complex values.

The material slab is considered isotropic and homogeneous. However, the approach discussed can also be applied to stratified media, which consist of multiple layers composed of different materials. This extension is feasible only when the individual layers are themselves isotropic and homogeneous. This scenario holds particular importance in discussions regarding dielectric materials covered by conducting inks. For isotropic materials and normal incidence, both in-plane orthogonal polarizations are equivalent, allowing a study of just one of them.

The fields on the left side of the slab, within the slab, and on the right side of the slab are all solutions to the homogeneous Maxwell equations. Each region is defined by its own electric permittivity and magnetic permeability. Consequently, on the left side of the slab, the electric field component, for example, along the  $x$ -axis, is represented as  $E_L = E_L^i e^{ik_1 z} + E_L^r e^{-ik_1 z}$ . A similar expression holds for the right side of the slab and within the slab, with adjustments made for the specific components. The magnetic field is determined by utilizing the expression for the electric field within each region, relying on the Maxwell equations in the frequency domain.

In the absence of surface current and charge densities at the interfaces between the slab and the vacuum, continuity of the electric and magnetic fields in the three distinct regions is ensured by the requirement that the tangential components of  $E$  and  $H$  are preserved at these interfaces. This condition also applies to the normal components of  $D$  and  $B$ , although it's worth noting that these two conditions are interrelated with the former two.

It's important to highlight that if any face of the slab were to be covered with a few-layer pristine graphene or another conducting two dimensional (2D) material, this continuity condition would no longer hold. This discrepancy arises due to the presence of surface current and charge densities in such 2D materials. However, such configurations are typically not employed in the context of EMI applications due to the high cost associated with these pristine forms.

The scattering problem can be framed as follows: given the field components on the left side of the slab, the goal is to determine the field components on the right side. This relationship between the components is described by introducing the concept of the T matrix:

$$\begin{pmatrix} E_R^i \\ E_R^r \end{pmatrix} = \begin{pmatrix} T_{11} & T_{12} \\ T_{21} & T_{22} \end{pmatrix} \cdot \begin{pmatrix} E_L^i \\ E_L^r \end{pmatrix} \quad (48)$$

The elements of this matrix can be straightforwardly derived by connecting the field components on both sides of the slab. This is achieved by expressing the amplitudes through a system of two equations that establish the continuity of the tangential components of the fields at the left interface. A related concept is that of the S matrix, in which one expresses the outgoing fields from the slab in terms of the incoming fields.

These concepts align with principles introduced in Quantum Mechanics and Quantum Field Theory [8] and can be readily determined using a Vector Network Analyzer (VNA) that measures the scattering of electromagnetic waves in a transmission line configuration. This setup closely approximates the scenario of an infinite slab.

Another important parameter that can be introduced is the shielding effectiveness of the medium,  $SE_T = -10\log_{10}(T)$ , measured in decibels (dB). This parameter serves as a logarithmic measure of the medium's ability to efficiently absorb and reflect incoming electromagnetic waves. In the scenario of a perfectly absorbing medium, where T (transmission) equals 0,  $SE_T$  would be an infinite value. Conversely, in the case of a perfectly transparent medium, where T equals 1,  $SE_T$  would be 0, indicating that all energy passes through the medium without any loss.

Furthermore, to assess the extent to which the medium reflects radiation, one can introduce a quantity known as  $SE_R = -10\log_{10}(1 - R)$ . Utilizing these two parameters, one can define  $SE_A = SE_T - SE_R$ , which quantifies the efficiency of absorption. In an ideal scenario, the objective is to maximize  $SE_A$  and minimize  $SE_R$  to prevent interference from the device's own radiation. However, it's

important to note that these two parameters are generally interdependent and cannot be controlled independently.

In terms of the elements of the S matrix, these expressions serve as valuable formulas when directly measuring the elements using a VNA.

$$SE_T = -10\log_{10}(|S_{21}|^2) \quad (49)$$

$$SE_R = -10\log_{10}(1 - |S_{11}|^2) \quad (50)$$

$$SE_A = -10\log_{10}\left(\frac{|S_{21}|^2}{1 - |S_{11}|^2}\right) \quad (51)$$

The reflection and transmission factors for incoming waves from the left and right are, as expected, identical. Here,  $n_1(\omega) = \sqrt{\varepsilon_{1r}(\omega)}$  represents the refractive index of the medium to the left and right of the slab (with  $n_1 = 1$  for a vacuum), while  $n_2$  is the refractive index of the slab. It's important to note that these refractive indices are typically complex quantities. As mentioned earlier, it is assumed that the slab is isotropic, but the formula remains applicable for uniaxial materials with a symmetry axis along the direction of incidence.

When dealing with a thick slab in a vacuum, it's possible to disregard multiple internal reflections and instead treat the slab as a semi-infinite medium. This simplification allows for the derivation of a shielding efficiency estimate that is generally applicable. In this scenario, the transmission factor is represented by  $T \approx |t|^2 e^{-2d/\delta}$ , where  $t = \frac{2Z_{2r}}{Z_{2r}+1}$  is the relative amplitude of the transmitted field,  $\delta = \sqrt{\frac{2}{\omega\sigma_2\mu_0}}$  signifies the penetration depth of the material within the slab, while  $\sigma_2$  represents the material's conductivity. It is assumed to be constant within the range of frequencies under consideration.  $Z_{2r} = 1/n_2$  denotes the relative impedance of the material within the slab. In the context of a thick slab, the condition is that  $d \gg \delta$ .

Assuming that the material is highly conductive in the region of frequencies of interest, the result of shielding efficiency is:

$$SE_T \approx 10\log_{10}\left(\frac{\sigma_2}{4\varepsilon_0\omega}\right) + 10d\sqrt{2\omega\sigma_2\mu_0} \quad (52)$$

As evident from the preceding equation, the shielding efficiency exhibits a linear increase with the thickness of the slab, but it only increases proportionally to the square root of the material's conductivity. Therefore, from an economic perspective, it is more favourable to utilize a less expensive material with lower conductivity in larger quantities, rather than opting for a highly conductive (and costly) medium for EMI applications.

The reflection factor  $R \approx \left| \frac{Z_{2r}-1}{Z_{2r}+1} \right|^2$  signifies the relative amplitude of the reflected wave in the context of a semi-infinite slab. When considering a highly conductive material, the result is:

$$SE_R \approx 5 \log_{10} \left( \frac{\sigma_2}{8\epsilon_0\omega} \right) \quad (53)$$

For a structure composed of  $n$  layers of different materials, the analysis of the problem is similar. Nevertheless, it is essential to impose the continuity conditions for the tangential components of the electric and magnetic fields at  $n+1$  interfaces, in contrast to the two interfaces mentioned previously.

The scenario involving a thin layer of conducting material with a thickness  $d$  that covers a dielectric medium with a thickness  $D$  is of significant importance. The dielectric medium has refractive indices denoted as  $n_2$  and  $n_3$ , while the external medium possesses a refractive index equal to  $n_1$ . This scenario is essential, and it warrants explicit citation of the results for the components of the S matrix, presented in Appendix B. Supplementary information for the theoretical model

Once more, it is important to note that the assumption is made that the media are non-magnetic. In the case of vacuum,  $n_1$  is considered to be equal to 1.

The polymer composites tested as potential shielding materials exhibit significant experimental anisotropy between the in-plane components of the conductivity or permittivity tensors and the through-thickness components of these properties. This anisotropy can be attributed to the flow induced orientation from the injection moulding used in the production of these composites.

Given that the impedance bridge method allows for the measurement of only the through-thickness component of the permittivity tensor, it becomes necessary to establish a relationship between this component and the in-plane components. One straightforward approach is to assume that all microscopic relaxation time scales are isotropic, and thus, the anisotropy primarily arises from the macroscopic alignment of conductive fillers induced by the aforementioned injection moulding method.

Hence, it is possible to express the frequency-dependent conductivity tensor as

$$\sigma(\omega) = \sigma^0 \cdot f(\omega, \tau_1, \tau_2, \dots) \quad (54)$$

In this expression,  $\sigma^0$  represents the DC conductivity tensor, while  $f(\omega, \tau_1, \tau_2, \dots)$  is a dimensionless function that varies with frequency and is dependent on the microscopic relaxation time scales, such as  $\tau_1$ ,  $\tau_2$ , and so on.

A simple example of such behaviour is that of a Drude metal with a carrier's anisotropic effective mass. In such a case, the  $\sigma^0$  and  $F(T)$ , where  $n$  is the carrier density in the metal,  $E$  is the carrier's charge,  $T$  the single momentum relaxation rate due to inelastic collisions of the carriers with static impurities, and  $m^{-1}$  is the inverse effective mass tensor of the metal.

An illustrative example of this behaviour is found in a Drude metal with anisotropic effective carrier mass. In this instance, we have  $\sigma^0 = ne^2rm^{-1}$  and  $f(\omega, \tau) = \frac{1}{1-i\omega\tau}$ , where  $n$  stands for the carrier density in the metal,  $e$  represents the carrier's charge,  $\tau$  denotes the single momentum relaxation rate, attributed to inelastic collisions of the carriers with static impurities, and  $m^{-1}$  signifies the inverse effective mass tensor of the metal.

However, in this case, the assumption is that the inverse mass tensor reflects the anisotropy stemming from the band structure of the Drude metal. This band structure is determined by the microscopic crystalline structure of the conducting material in question.

On the other hand, when examining the polymer composites in question, their anisotropic conducting properties are determined at significantly larger scales, and the sources of this anisotropy differ from those affecting the band structure of the Drude metal.

If such a hypothesis is valid, it implies that  $\sigma_z(\omega) = \frac{\sigma_{xy}^0}{\sigma_z^0} \sigma_z(\omega)$ . This equivalence can be ascertained through a simple measurement of both the superficial DC conductivity and the through-thickness DC conductivity.

The dielectric tensor is connected to the optical conductivity tensor via the formula:

$$\varepsilon(\omega) = \varepsilon^\infty + \frac{i\sigma(\omega)}{\omega\varepsilon_0} \quad (55)$$



where  $\varepsilon^\infty$  represents the limiting value of the dielectric tensor at high frequencies [29]. Relaxation time-scales can be considered isotropic.

In the case of a rectangular sample, featuring dimensions of length  $L$ , width  $W$  and thickness  $d$ , its through-thickness resistance is denoted as  $R_z = \frac{1}{\sigma_z^\infty} \cdot \frac{d}{LW}$ . Similarly, the through-thickness capacitance of the sample is represented by  $C_z = \varepsilon_z^\infty \cdot \frac{LW}{d}$ . Consequently, the relaxation time linked to the equivalent RC circuit is defined as  $\tau_z = R_z C_z$ , which remains unaffected by any geometric aspects of the sample. The conclusions are similar to the resistance in the plane of the interface of the material.

Hence, it can be deduced that when assuming isotropic time-scales, measuring the through-thickness dielectric function and the associated ratio allows for the determination of the planar components of the dielectric function. These planar components are the ones relevant to the dispersion relation in the case of normal incidence of electromagnetic waves.

These equations were inputted in the Mathematica 10.2 software where the transcribed codes can be seen in Appendix C.

### 3.4 First approach onto SE of thermoplastic compounds<sup>2</sup>

An initial analysis on the topic of EM shielding of fibre-reinforced thermoplastic compounds was taken with the goal to answer the first research question:

- “What is the effectiveness of thermoplastics in blocking electromagnetic waves?”

This study fell within the scope of a research and development project together with Bosch Car Multimedia Portugal, S.A. At this stage, a variety of commercially accessible thermoplastics have been utilized to fabricate disk-shaped specimens with a thickness of 2mm through the injection moulding process. These specimens have undergone experimental evaluation to determine their shielding effectiveness, and their properties have been characterized through the application of a general theoretical model to describe the EM wave refraction within a homogeneous and isotropic material by means of the transfer matrix formalism.

---

<sup>2</sup> This subchapter resulted on the following paper: Martins, L.C., & Pontes, A.J. (2022). Fiber reinforced thermoplastics compounds for electromagnetic interference shielding applications. *Journal of Reinforced Plastics and Composites*, 41(5–6), 206–214. <https://doi.org/10.1177/07316844211051732>

### 3.4.1. Materials

The selected fibre-reinforced thermoplastic compounds, all commercially available from different suppliers, and were tested during this project to characterize their shielding potential to be applied to an electronic enclosure which required a minimum shielding level of 40 – 60 dB.

The adopted selection process was essentially based on the material’s electrical resistivity since SE is correlated to it. However, aspects such as stiffness, thermal stability, processability (by injection moulding) and costs were also considered.

All the selected compounds with respective polymer matrix, conductive fillers and datasheet electrical properties are shown in Table 1.

Table 1. Thermoplastic compounds with respective electrical properties.

<b>ID</b>	<b>Matrix</b>	<b>Reinforces (wt%)<sup>(1)</sup></b>	<b>Resistivity (Ohm.cm)<sup>(2)</sup></b>	<b>Conductivity (S/m)</b>
<b>M1</b>	PBT	30% CF	$< 10^1$	$> 10^1$
<b>M2</b>	PC	15% SSF	$10^4 - 10^6$	$10^{-4} - 10^{-2}$
<b>M3</b>	PBT	20% GF + 10% SSF	$< 10^2$	$> 10^0$
<b>M4</b>	PA6	30% LCF	$10^2 - 10^1$	$10^3 - 10^4$
<b>M5</b>	PP	30% CF + 5% SSF	$< 10^1$	$> 10^1$
<b>M6</b>	PP	35% CF + 5% SSF	$< 10^1$	$> 10^1$
(1) From pellets burnout				
(2) From datasheet				

### 3.4.2. Experimental procedure

In a first approach all the selected material were processed by injection moulding to produce flat samples, and their EM shielding was characterized both experimentally and theoretically. The adopted workflow is displayed on Figure 10.

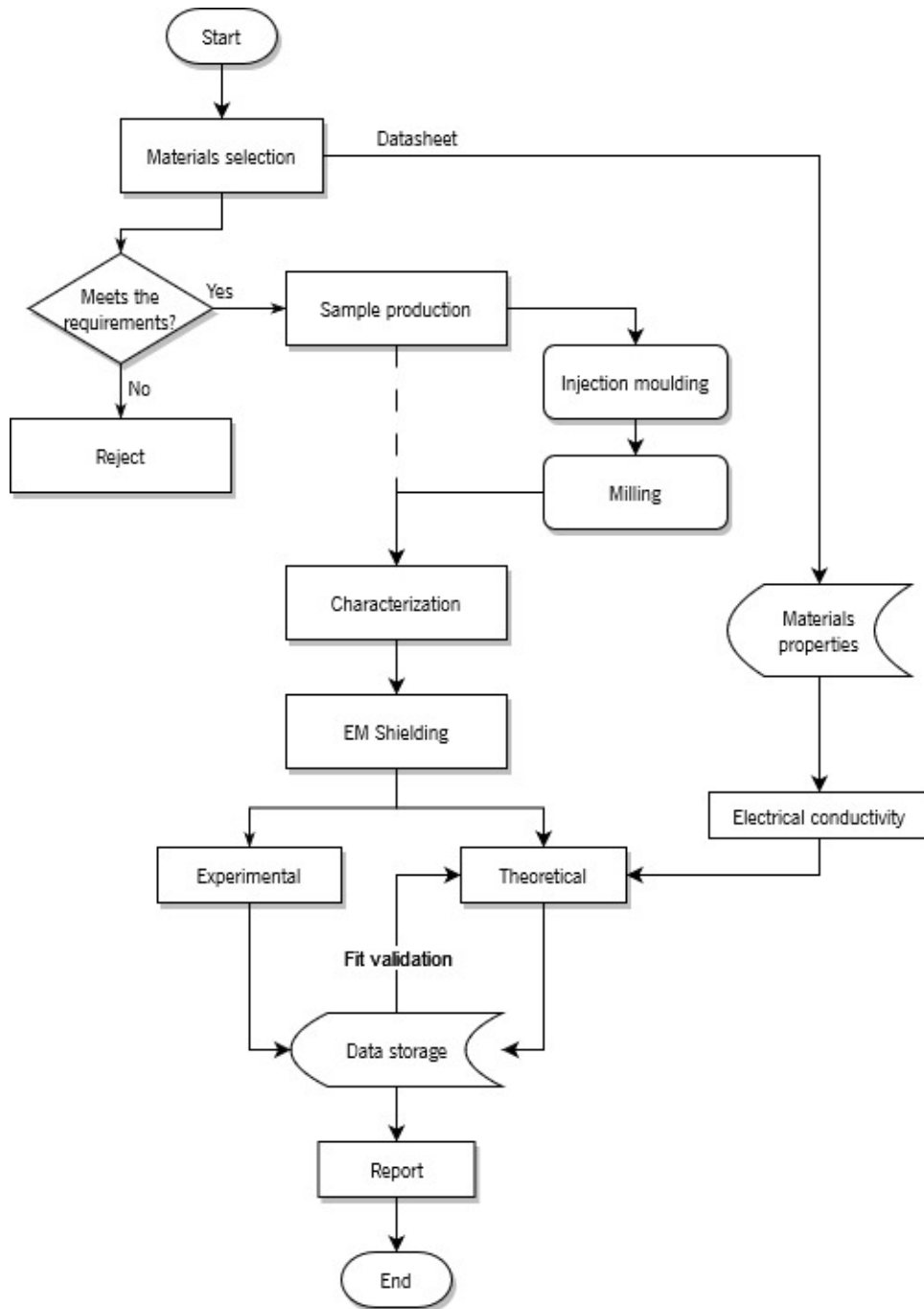


Figure 10. Workflow adopted in the first study.

Solid flat disk-shaped samples with nominal thickness of 2 mm and diameter of 60 mm were produced in an injection moulding press (*Ferromatik Elektra Evolution 110-300*). In this process, the thermoplastic compounds were injected into a two-cavity mould through a 1 mm thick fan gate, following the recommended guidelines from the respective material datasheet.

The generic dimensions of the mouldings as well as 3D modelled representation (including the feeding system) can be seen in Figure 11.

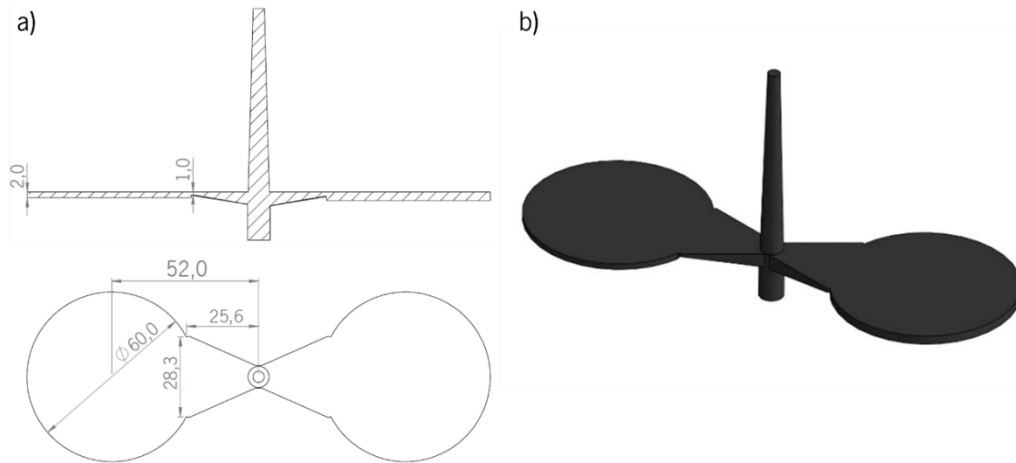


Figure 11. Injection moulding specimens: a) generic dimensions; b) 3D representation.

After the injection moulding cycle, a set of 5 “Load” samples and 1 “Reference” sample was produced for each material, as specified in Figure 12. The process to drill the sample’s holes and cut the toroid shape in “Reference” specimens were achieved in a milling machine.

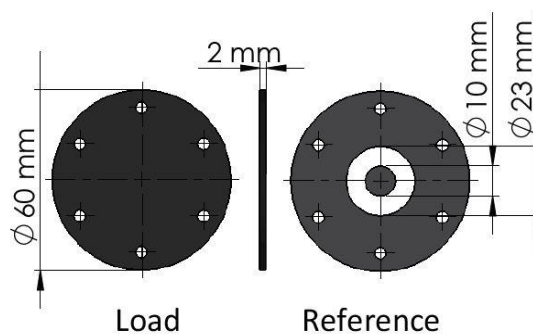


Figure 12. Disk shaped samples for EM shielding.

The shielding effectiveness was measured at the frequency range between 30 MHz and 3 GHz, following the procedure described in chapter 3.3.2., which follows the ASTM D4935. A VNA with an input power of 0 dBm was used to generate EM waves and record the transmission scattering parameters (S21) to determine the total EMSE according to Equation 32.

In conjunction with the experimental measurements, a theoretical assessment of the shielding performance for the chosen compounds was also conducted. This preliminary analysis employed the mathematical models described by the simplified transmission line of plane wave theory. As elaborated in the section 2.1, the adopted model, which results in the Equation 6, is particularly suited to describe the shielding for good electrical conductors with a uniform medium. Despite this, it serves as a reasonable foundation model for initially examining the shielding effectiveness of the injected compounds.

The employed theoretical model is rooted in the principle that the material, with given thickness, is treated as a homogeneous medium with constant electric and magnetic properties. This approach contrasts with the complex electrical properties ( $\sigma$ ,  $\epsilon$  and  $\mu$ ) and frequency-dependent properties necessary for a more accurate portrayal of the material's dispersion characteristics when a plane EM wave collides with its interface and propagates through its thickness.

Consequently, and due to the limited information from the supplier's datasheet, an assumption was made, considering the material as homogeneous and isotropic, endowed with permittivity and permeability equal to those of vacuum ( $\epsilon_r=1$  and  $\mu_r=1$ ), along with a constant electrical conductivity.

The conductivity values were approximated through iterative increments until the calculated shielding effectiveness matched the experimental results for the corresponding material. This fitting process for conductivity encompassed the entire frequency spectrum rather than being restricted to isolated frequency points, and it took numerous iterations to attain an adjusted value.

#### 3.4.3. Results and discussion

Figure 13 illustrates the average values recorded for samples of each compound. Addressing the research question that motivated this study, it is evident that a wide range in orders of magnitude exists for the shielding effectiveness level. This range spans from 20 dB to 100 dB, depending upon the frequency of interest and the content of conductive filler. Consequently, these thermoplastic compounds present themselves as highly promising materials capable of accommodating a diverse spectrum of shielding performance requirements.

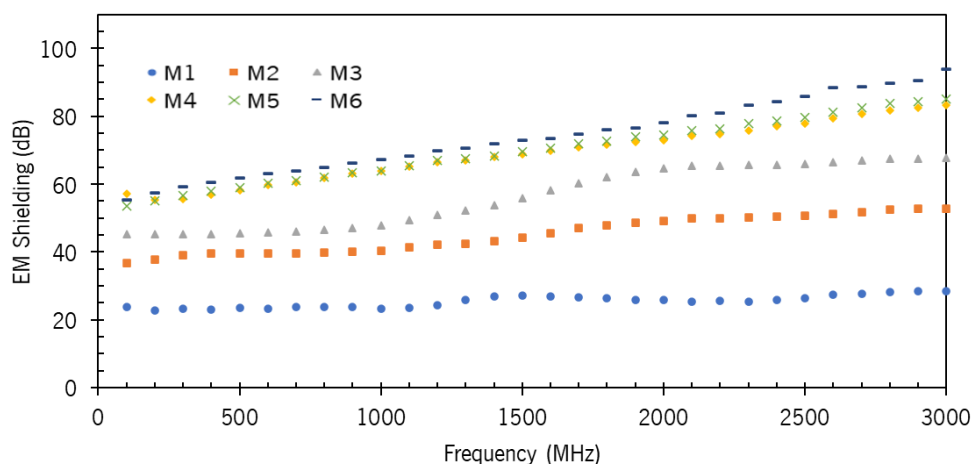


Figure 13. EM Shielding for the tested materials.

This study offers encouraging insights for engineers seeking to design an enclosure with a shielding requirement of at least 40 dB. By establishing this lower threshold, the range of scrutinized materials can be narrowed down to compounds M4, M5, and M6. Notably, M6 emerges as the most promising candidate, exhibiting shielding capabilities surpassing 60 dB across nearly the entire frequency spectrum and nearly reaching 100 dB at the highest measured frequency.

Moreover, by employing a linear regression model to the shielding outcomes, it is reasonable to anticipate that the shielding effectiveness of these materials, especially the M6 compound, could exceed 100 dB for frequency bands commonly associated with radar and/or other military applications, such as the X-band (8 – 12 GHz).

As it could be anticipated, the chosen compounds displayed distinct shielding characteristics, influenced by the conductive filler within the polymeric matrix. The electrical attributes of these fibres, along with their concentration, dimensions, and orientation within the polymeric matrix, shall impact the bulk properties of the specimens, leading to a broad range of shielding effectiveness. There is a clear escalation of shielding with the augmentation of fibre concentration. Nevertheless, a closer examination would reveal that not only the concentration holds significance, but also the inherent nature of the conductive filler itself.

The utilization of stainless-steel fibres (SSF) yielded superior outcomes in comparison to short carbon fibres (CF), even in cases where the SSF weight concentration was lower. This is evident when comparing M1 with M2 and M3. This discrepancy arises from the enhanced conductivity and ferromagnetic attributes of SSF, which contribute to greater EM absorption.

Long carbon fibres (LCF) exhibit superior shielding effectiveness when contrasted with short carbon fibres, as demonstrated by a comparison between M1 and M4 specimens. Compounds fortified with LCFs can even surpass the shielding capabilities of those containing SSF. The incorporation of LCFs holds considerable promise for the advancement of a plastic enclosure, as it not only enhances shielding efficiency but also provides a higher stiffness-to-weight ratio than SSF compounds.

The most optimal shielding outcomes were attained by utilizing compounds that employed a combination of CF and SSF, with the M6 compound standing out as the most effective. Consequently, a synergistic blend of these two fillers is highly recommended.

In relation to the theoretical evaluation, these calculations were performed by employing the discussed method that involved adjusting the electrical conductivity of an isotropic sample in systematic increments to approximate the experimental shielding effectiveness results. This approach was adopted due to the inadequacy of available material property data to serve as inputs.

It was determined that conductivity values of 50, 250, 500, 950, and 1100 S/m correspondingly yielded approximations to the experimental SE for M1, M2, M3, M4, M5, and M6. The experimental SE values, along with their corresponding simulated representations, are presented in Figure 14.

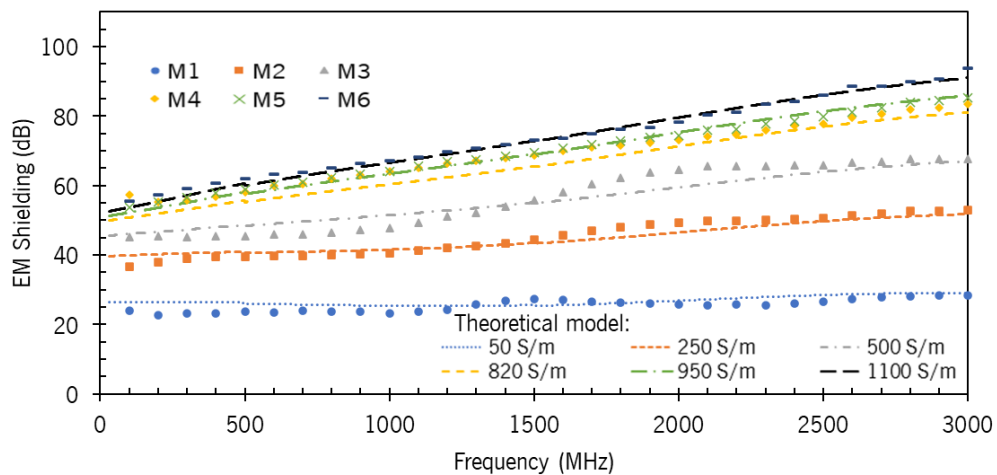


Figure 14. Experimental SE and fitted theoretical modelling.

It is evident that the electrical conductivity employed for the theoretical evaluation diverges from the imprecise DC resistivity data provided by materials suppliers. The shielding effectiveness is directly linked to the material's frequency-dependent and complex electrical properties. Hence, it becomes imperative to comprehensively characterize these properties to facilitate a reliable theoretical characterisation.

#### 3.4.4. Concluding remarks

Through this experimental approach, the EM shielding attributes of numerous thermoplastic composites were assessed. The findings emphasize a wide range in magnitudes, spanning from 20 dB to 100 dB, depending on factors such as the conductive reinforcement type, concentration, length, and orientation within the material samples. Particularly noteworthy is the combined utilization of carbon fibres and stainless-steel fibres, which exhibited superior shielding performance, registering shielding effectiveness values surpassing 60 dB across the majority of the tested frequency spectrum.

This study provided significant insights into the shielding effectiveness performance of thermoplastic compounds and a methodology to characterize their behaviour through a theoretical model. Nevertheless, several aspects still require clarification:

- Impact of injection moulding conditions: The influence of injection moulding conditions on the shielding performance of the compounds and their associated electrical properties needs further exploration. Investigating how variables such as temperature and injection speed affect the final material's electromagnetic behaviour could provide valuable insights.
- Measurement of electrical conductivity and permittivity: Establishing a robust method for accurately measuring the electrical conductivity and permittivity of thermoplastic compounds is crucial. This process could involve carefully designed experiments and possibly the development of new testing techniques to ensure reliable and consistent results.
- Anisotropic characteristics: Addressing the potential anisotropic characteristics of these materials and their implications for shielding effectiveness is an area that requires further examination.
- Refining theoretical models: Developing a more accurate theoretical model that comprehensively describes the electrical and electromagnetic properties of these thermoplastic composites is an ongoing challenge. This could involve incorporating complex electrical properties and frequency-dependent behaviour into the model, thus enabling a closer match between theoretical predictions and experimental results.

### **3.5 Effect of injection moulding conditions on the materials electromagnetic shielding and electrical conductivity<sup>3</sup>**

On a second phase, three injection moulded fibre reinforced thermoplastics were selected to further develop the shielding studies. The reason of this study is to provide an answer to the following three research questions:

- What's the impact of injection moulding parameters?
- How can the anisotropic conductivity of these composites be measured?

---

<sup>3</sup> This subchapter resulted on the following paper: Martins, L.C., Barbosa, C.N., Silva, S., Bernardo, P., Dias, G.R., Pontes, A.J. (2021). Polym. Eng. Sci., 61 (10), 2576. <https://doi.org/10.1002/pen.25784>



- What's the relationship between the anisotropic electrical conductivity and EM shielding properties of polymer compounds?

This study was also part of a research and development project together with Bosch Car Multimedia Portugal, S.A. During this phase of the research, an exploration was undertaken to analyse the anisotropic electrical conductivity (EC) and its interplay with EM shielding effectiveness in the context of injection moulded carbon-fibre reinforced polybutylene terephthalate (PBT) compounds. The investigation encompassed the characterization of 2mm thick injection mouldings, and variations in melt temperature, injection speed, and flow distance were considered to comprehend their impact.

An innovative experimental setup was deployed to quantify anisotropic EC along three distinct directions: parallel, perpendicular, and transversal to the flow. Notably, the injection moulding process induced significant anisotropy in the specimens of both compounds. Depending on the specific processing conditions, similar longitudinal conductivity values were observed, but higher transversal conductivity.

Concluding this phase of the study, a comparison between the electrical conductivity properties and electromagnetic shielding effectiveness (EMSE) revealed a direct relationship, consistent with the anticipated outcome.

### 3.5.1. Materials

This investigation employed two commercially available PBT thermoplastic compounds, loaded with carbon-based fillers like carbon fibres (CF) and/or carbon black (CB), and one PP-based thermoplastic compound, loaded with a mixture of CF, CB, and stainless-steel fibres (SSF). These materials are well-suited for injection moulding process, and some of their general properties are outlined in Table 2.

Table 2. Datasheet properties of the injection moulding compounds.

<b>Material</b>	<b>M7</b>	<b>M8</b>	<b>M9</b>
<b>Polymer matrix</b>	PBT	PBT	PP
<b>Filler Composition (wt%)</b>	20% CF + 10% CB	20% CF	15% CF + 15% CB + 10% SSF
<b>Density (g/cm<sup>3</sup>)</b>	1.36	1.38	1.21
<b>Tensile Modulus (GPa)</b>	12	12	9.45
<b>Surface Resistance (<math>\Omega</math>)</b>	$< 10^1$	$< 10^3$	$< 10^2$

### 3.5.2. Experimental procedure

In the subsequent phase of the study, both compounds underwent processing through the injection moulding technique to create flat samples. These samples were then subjected to characterization of their EM shielding capabilities and electrical conductivity, with a focus on establishing correlations between the two.

To gain a deeper understanding of the influence of injection moulding conditions, variations in melt temperature, injection speed, and flow distance were deliberately introduced. This approach allowed for a comprehensive assessment of how these injection moulding parameters impact both shielding effectiveness and electrical conductivity. The procedural workflow employed is depicted in Figure 15.

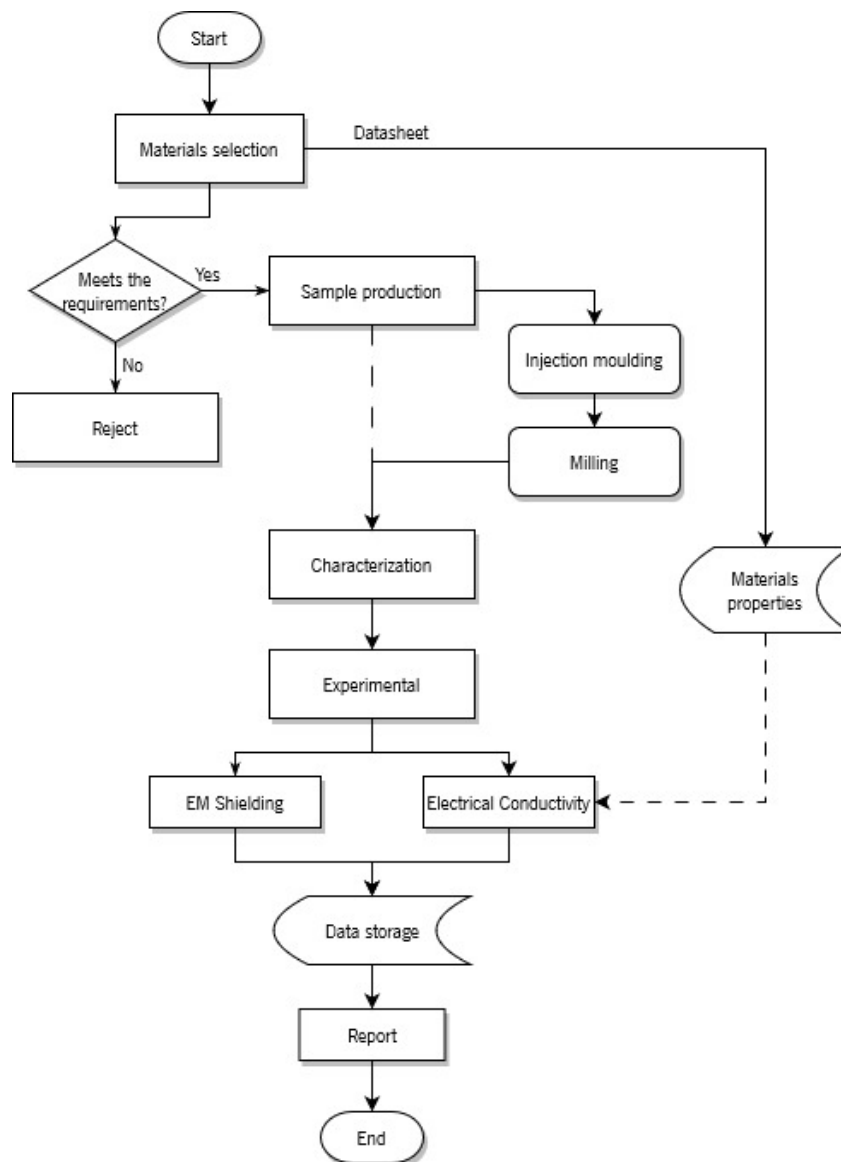


Figure 15. Workflow adopted in the second study.

Rectangular test samples, measuring 150x80x2 mm<sup>3</sup> (rectangular plates) were manufactured using an injection moulding press (*Ferromatik Milacron K85-S/2F*). During this procedure, both thermoplastic compounds were injected into a single-cavity mould via a 1.5mm thick flash gate.

The general dimensions of the mouldings, including a picture of an actual moulded part encompassing the feed system, can be found in Figure 16.

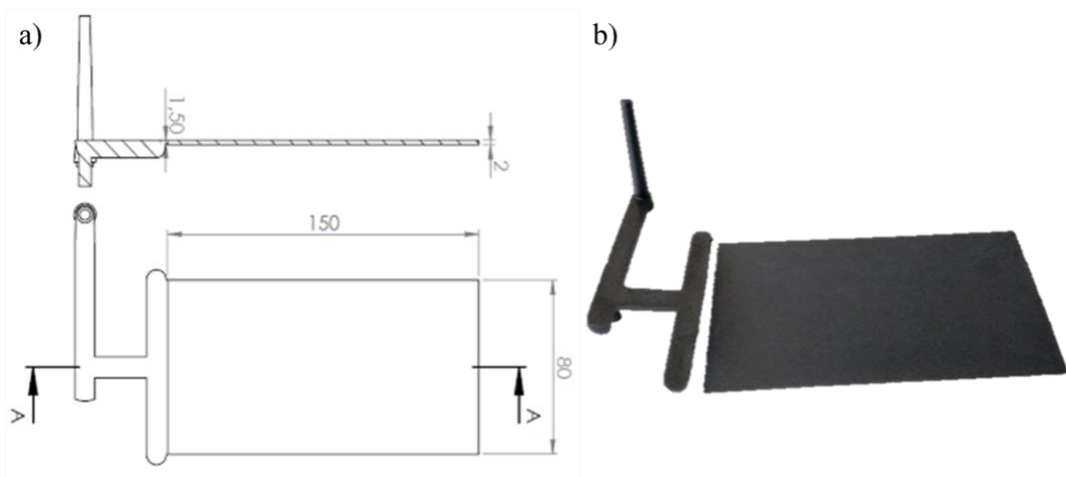


Figure 16. Injection moulding samples: a) Generic dimensions; b) sample picture

To assess the impact of injection moulding conditions, the moulded specimens of each compound were produced with two distinct levels for the melt temperature and injection speed, resulting in a set of four experimental conditions. Specifically, one set of experimental conditions (E01) encompassed lower values for both melt temperature and injection speed, a second condition (E02) consisted of a lower value for the melt temperature and a higher value for the injection speed, a third experimental condition (E03) was set with a high level for the melt temperature with a low value for the injection speed, while the last experimental conditions (E04) featured higher values for both variables. The design of these conditions is detailed in Table 3.

Table 3. Injection moulding experiment plan.

<b>Condition</b>	<b>Melt temperature (°C)</b>	<b>Injection speed (mm/s)</b>
<b>E01</b>	-	-
<b>E02</b>	-	+
<b>E03</b>	+	-
<b>E04</b>	+	+

The injection moulding process involved an initial step of filling the mouldings, wherein the required feeding stroke was determined to achieve cavity filling of approximately 98% - 99% of its total volume. Subsequently, parameters for the packing phase were established. The packing pressure was set at 80% of the pressure necessary for complete cavity filling. Meanwhile, the holding time was determined by incrementally increasing the duration of holding pressure until the sealing point was reached where the weight of the part stabilized, indicating the solidification of the gate.

The specific injection moulding conditions utilised for the experimental condition E01 and E04 were defined based on the datasheet guidelines and are outlined in Table 4. The remaining two intermediate production series were set with the same general conditions, differing in their respective melt temperature or injection speed following the conditions established in Table 3. Upon achieving a state of steady equilibrium, at least five specimens were produced for each material and experimental condition, forming the basis for subsequent investigations.

Table 4. Injection moulding conditions.

<b>Material</b>	<b>M7</b>		<b>M8</b>		<b>M9</b>	
<b>Experimental Plan</b>	<b>E01</b>	<b>E04</b>	<b>E01</b>	<b>E04</b>	<b>E01</b>	<b>E04</b>
<b>Melt Temperature (°C)</b>	250	265	240	260	240	260
<b>Injection speed (mm/s)</b>	50	200	60	110	60	110
<b>Injection Pressure (bar)</b>	1290	1300	1030	850	775	680
<b>Holding Pressure (bar)</b>	632	632	500	500	500	500
<b>Holding Time (s)</b>	5	5	5	5	6	6
<b>Mould Temperature (°C)</b>	80	80	80	80	70	70
<b>Cooling Time (s)</b>	15	15	15	15	20	20

After the injection moulding cycle, the shielding effectiveness was measured at the frequency range between 30 MHz and 3 GHz, following the procedure described in chapter 3.3.2. A VNA with an input power of 0 dBm was used to generate EM waves and record the transmission scattering parameters (S21) to determine the total EMSE according to Equation 32.

For every material and processing condition, a group of 5 "Load" samples and 1 "Reference" sample were meticulously produced, following the specifications outlined in Figure 17. The process involved drilling holes and shaping the specimens into a toroid configuration for the "Reference" samples, with these tasks being accomplished by a milling machine.

Furthermore, tests were conducted with consideration for the relative positioning of the moulding samples. This entailed conducting observations at two distinct areas: one situated near the gate and the other located at the opposite gate position. This strategic approach was adopted to analyse how material properties evolve as the flow distance within the moulding increases.

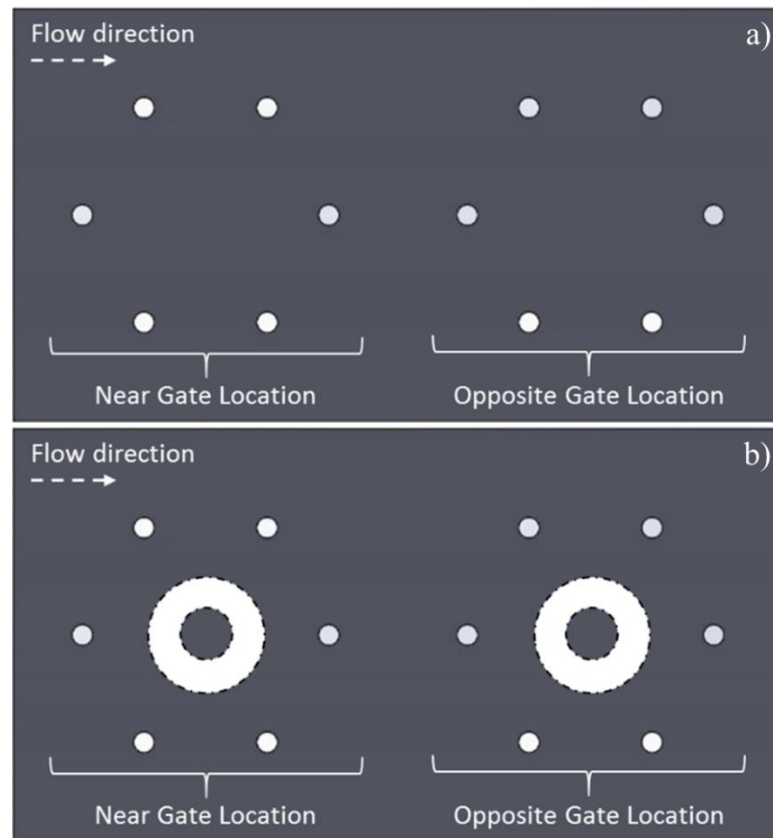


Figure 17. EMSE samples layout: a) load sample; b) reference sample

In conjunction with the shielding measurements, a complementary evaluation of electrical conductivity was conducted. This assessment involved measuring the electrical resistance across both the longitudinal and transversal directions of the specimens. This approach allowed for a comprehensive characterization of the anisotropic attributes exhibited by the injected compounds, as elaborated in section 3.3.3.

The electrical resistance measurements were carried out under ambient temperature conditions, employing a pair of customized 4-point copper electrodes (illustrated in Figure 18). A power source was utilized to supply a direct current (1mA) to the outer electrodes on the sample, while the DC voltage was measured across the two inner electrodes using a standard multimeter. The electrical resistance of each sample was then calculated utilizing Equation 37.



Evaluation of the longitudinal (in-plane) electrical conductivity was carried out along two orientations: perpendicular and parallel to the flow direction, and identified as samples A and B, respectively. Meanwhile, samples designated as C were employed to determine the transversal (through-plane) conductivity of the moulded parts.

The testing procedure was synchronized using a motorized test stand fitted with a digital force gauge, capable of handling loads up to a maximum of 250N. This setup was employed to assess the electrical conductivity of the moulded specimens in relation to the compression force exerted on the samples. The specimens were positioned between specially designed electrodes that were identical in nature.

### 3.5.3. Results and discussion

Before delving into the analysis of electromagnetic shielding and electrical conductivity properties of the moulded compounds, it is crucial to establish the stability of density values across the measured samples under various injection moulding conditions. Furthermore, it's worth noting that the thickness of the samples exhibited a slight increase as the melt temperature and injection speed were raised.

Table 5. Specimens' physical properties.

<b>Property</b>	<b>Part Thickness (mm)</b>			<b>Part Density (g/cm<sup>3</sup>)</b>		
	<b>M7</b>	<b>M8</b>	<b>M9</b>	<b>M7</b>	<b>M8</b>	<b>M9</b>
<b>E01. Near</b>	1.93	1.97	1.90	1.31	1.33	1.23
<b>E01. Opp.</b>	1.90	1.93	1.87	1.33	1.36	1.25
<b>E02. Near</b>	2.02	2.09	1.90	1.31	1.33	1.22
<b>E02. Opp.</b>	1.95	2.04	1.86	1.36	1.36	1.24
<b>E03. Near</b>	2.02	1.97	1.88	1.31	1.34	1.23
<b>E03. Opp.</b>	1.94	1.93	1.84	1.36	1.36	1.25
<b>E04. Near</b>	2.12	2.01	1.89	1.31	1.34	1.21
<b>E04. Opp.</b>	2.09	1.97	1.85	1.33	1.37	1.24

The subsequent sections discuss the impact of melt temperature, injection speed, and flow distance on both electromagnetic shielding effectiveness (EMSE) and electrical conductivity (EC). Additionally, the anisotropic conductivity of the moulded components is outlined, along with its relationship to the measured shielding properties.

The obtained results are visually depicted through various graphical figures and are elaborated upon in written form. For more comprehensive details, the reader is encouraged to refer to supplementary tables provided in Appendix D. Supplementary results to chapter 3.5.

### EM shielding results

The evaluation of electromagnetic shielding effectiveness (EMSE) within the automotive frequency band of 30 MHz to 3 GHz encompassed an analysis of the impact of injection moulding conditions (with variations in  $T_i$  and  $V_i$  at two levels) and the relative location of samples (near the gate and opposite the gate).

Figure 20, Figure 21, and Figure 22 present the average results at specific frequencies to all the experimental conditions for the M7, M8, and M9 compounds, respectively. To enhance the clarity of observation, the coordinate axes of these plots have been appropriately scaled.

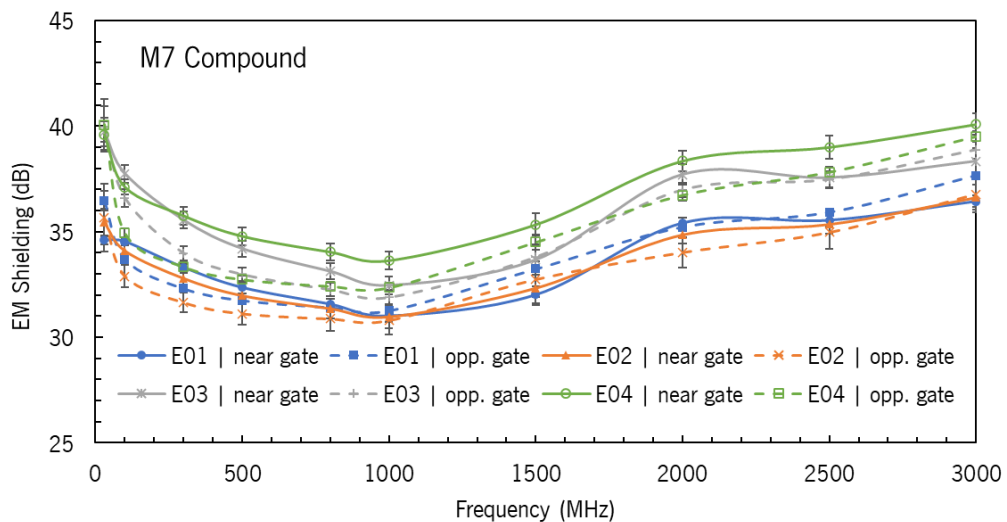


Figure 20. EM Shielding measured for the M7 Compound.



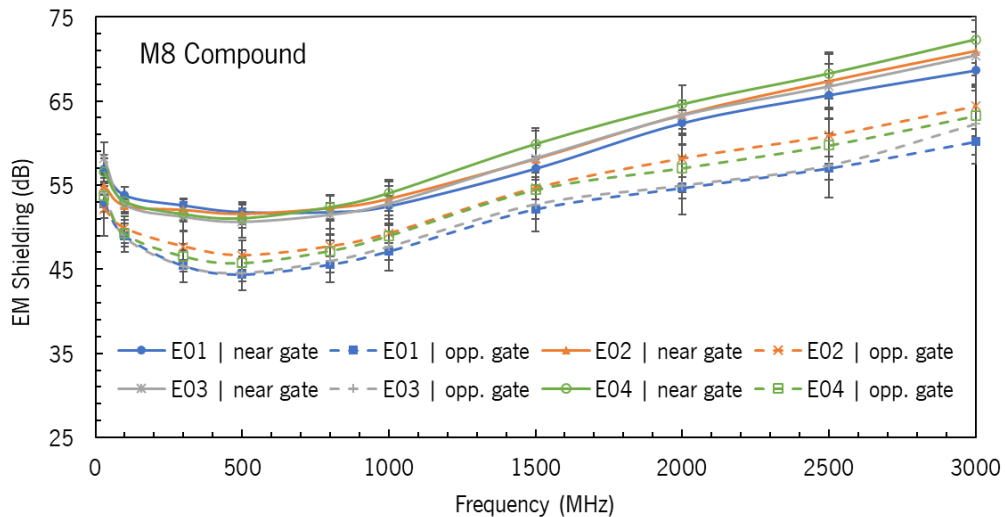


Figure 21. EM Shielding measured for the M8 Compound.

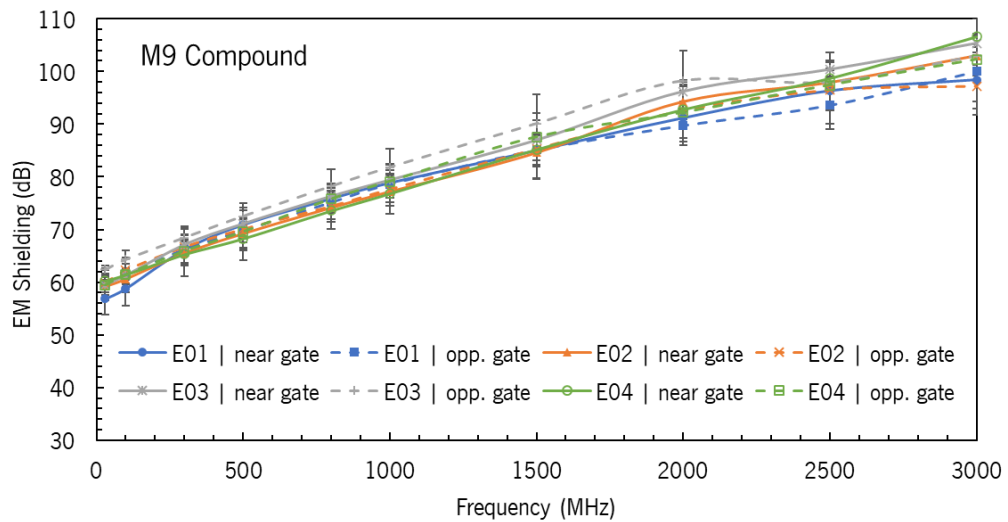


Figure 22. EM Shielding measured for the M9 Compound.

Within the observed frequency range, the SE of the M7 compound ranged from 30 – 40 dB, while the SE of M8 was situated in the 45 – 75 dB range. Notably, despite having a lower content of conductive filler (10% less), M8 displayed an improved performance of approximately 13 - 30 dB when compared to M8. This improvement was contingent on the frequency band and specific injection moulding conditions. Impressively, the M9 compound showcased a significant outperformance relative to the other two materials, being that its shielding fluctuated between 55 to 100 dB, depending on the frequency and processing condition. The incorporation of SSF in similar concentrations of CF and/or CB is believed to be the driving factor behind this notable enhancement in shielding performance. Once again, this investigation underscores the beneficial impact of the synergistic combination between CF and SSF on electromagnetic attenuation.

Consistent with theoretical projections, it was observed in the first study (chapter 3.4), the EM shielding demonstrated an upward trend with the escalation of frequency. This phenomenon is attributed to the diminishing wavelength in relation to the thickness of the specimen and the dimensions of conductive fillers. As the wavelength decreases, the attenuation of EM waves through the material is amplified due to absorption effects. However, for compounds M7 and M8, below 1 GHz, an apparent increase in shielding at lower frequencies is observed. It is important to note that this is not an intrinsic material effect, but rather a consequence of impedance mismatch within the experimental setup.

The impact of the selected frequency on the shielding performance of each compound specimen is evident. As the frequency increases (up to 3 GHz), there is a corresponding increase in shielding, with up to 8 dB improvement for M7, up to 19 dB for M8, and up to 45 dB for M9. Consequently, it's apparent that the effect of wave frequency on its scattering along a specimen's body is not uniform across all materials. Wave diffraction is also influenced by the electrical properties of the material, which, in turn, affect the shielding characteristics of the specimens. Thus, it can be observed that materials with superior shielding, primarily driven by higher conductivities, experience more significant improvements in shielding with increasing frequency.

Upon closer examination of the average results, distinct variations in EMSE are evident with regards to different injection moulding conditions ( $T_i$  and  $V_i$  varied in two levels) and sample relative location (near and opposite the gate). Depending on the observed frequency, the increase of injection moulding conditions can promote a variation in the material shielding effectiveness up to 5 dB (15%) for M7, up to 9 dB (14%) for M8, and 8 dB (9%) for M9. As such, the contribution of injection moulding conditions and the flow distance inside the mould cavity can be relevant to the shielding behaviour, especially to M7 as its lower overall shielding is at the lower limit of common established requirements for an electronic enclosure.

The impacts of injection moulding conditions and flow distance are more clearly elucidated in Figure 23, Figure 24, and Figure 25 (and complemented by the Table S4 to Table S7, available in Appendix D.) for M7, M8 and M9 compounds, respectively. This visual representation showcases the electromagnetic shielding effectiveness at different frequencies, encompassing the four experimental conditions and the two measurement areas (near and opposite the gate).

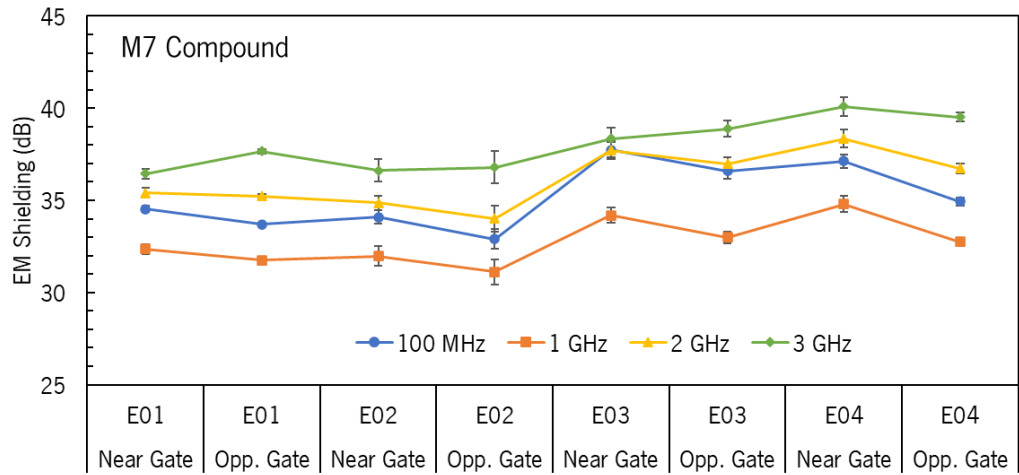


Figure 23. Effect of processing conditions on the EM shielding for the M7 compound.

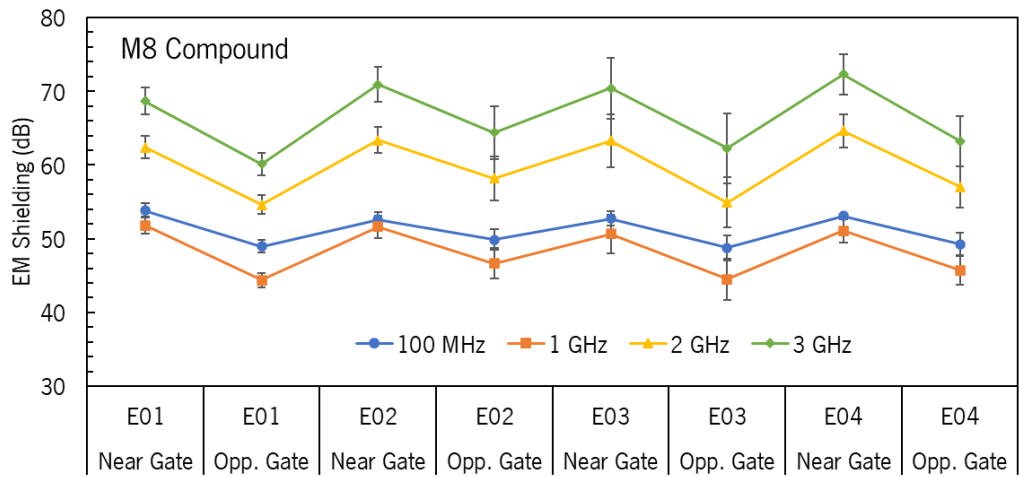


Figure 24. Effect of processing conditions on the EM shielding for the M7 compound.

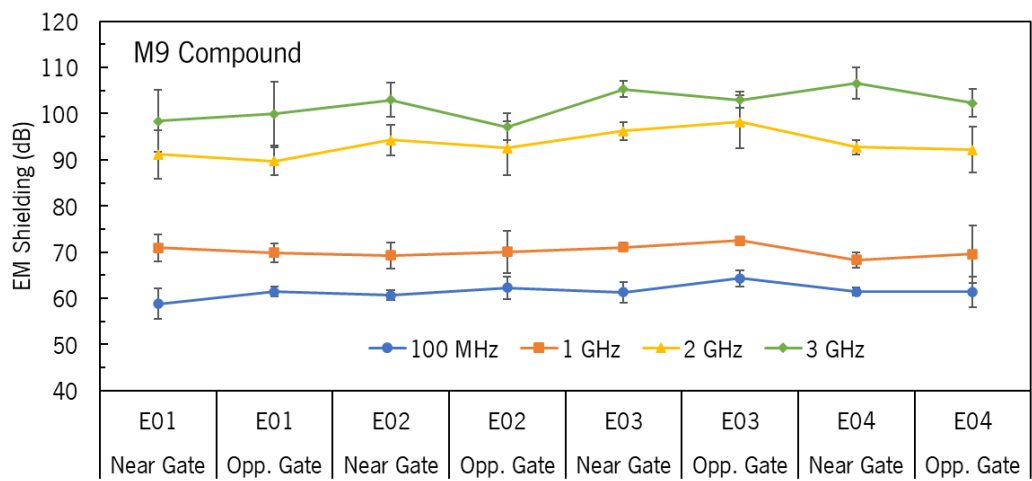


Figure 25. Effect of processing conditions on the EM shielding for the M7 compound.

As observed, and as briefly discussed at the beginning of this analysis, there are distinct variations in EMSE concerning different injection moulding conditions and sample relative locations. These variations are specific to each compound, but some similarities or trends can be identified and will be further explored. One common aspect among all three compounds is that the frequency effect appears to have a more significant impact on shielding properties than the changes induced by experimental conditions. Increasing the frequency range can lead to an increase in shielding of up to 8 dB for the M7 compound, up to 21 dB for the M8 compound, and up to 46 dB for the M9 compound. In contrast, the maximum variation induced by changes in experimental conditions was approximately 5 dB for the M7 compound, around 4 dB for the M8 compound, and up to 8 dB for the M9 compound.

Nonetheless, optimizing the materials' performance with respect to their processing conditions can be relevant for meeting the specific requirements of a particular product, especially when performance is near the lower end of the specified requirements, as seen with the M7 compound.

The analysis of the effect of injection moulding conditions (melt temperature and injection speed) on the EM shielding is discussed by comparing the increase (or decrease) in the average measured shielding with the increase in injection speed, established by the change in experimental conditions (E01 to E02 and/or E03 to E04), with the increase in temperature, established by the change in experimental conditions (E01 and/or E02 to E03 and/or E04), and with the increase of both combined parameters (E01 to E04).

It's evident that the effect of injection speed is not particularly significant for all three materials, but it generally appears to have a slight negative effect on the M7 and M9 compounds and a slight positive effect on the M8 compound.

For the M7 compound, the observed variations in the area near the gate ranged from -0.53 dB to +0.97 dB, while in the opposite region, the variations showed a negative impact of up to -1.23 dB. In the case of the M8 compound, the variations in the near gate area ranged from -0.46 dB (negative impact) to +2.08 dB (positive impact), while in the far region, the shielding varied from +0.69 dB to +2.81 dB. As for the M9 compound, the change in speed induced variations between -2.21 dB and +2.91 dB in the near region and a negative impact ranging from -1.06 dB to -1.85 dB in the region opposite the gate. However, all the observed variations are similar or lower than the standard deviation of the average shielding observed between different specimens, so it's challenging to draw conclusive insights from these variations, besides their apparent insignificance to the optimization process.

Regarding the influence of melt temperature, it's evident that an increase in melt temperature positively impacts the shielding for all three compounds, irrespective of their position, near or far from the gate. For the M7 compound, the average variations with an increase in melt temperature ranged from +1.45 dB to +3.21 dB (up to a 9.3% increase) in the near-gate position, while in the opposite region, the increase in shielding ranged from 0.63 dB to 2.91 dB (up to an 8.6% increase). In the case of the M8 compound, the shielding also improved with an increase in temperature, with an increase of up to 2.13 dB (a 3.5% increase) in the near region and up to 3.10 dB (a 5.2% increase) in the region opposite to the gate. As for the M9 compound, an increase in melt temperature led to an increase in shielding of up to 6.94 dB (a 7.1% increase) in the near region and an increase ranging from 2.69 dB to 8.46 dB (a 9.4% increase) in the region opposite to the gate. Therefore, on average, the increase in melt temperature significantly benefited the shielding of all three compounds, resulting in an improvement that can be up to almost 10%. Furthermore, the positive impact of the temperature increase was more pronounced in the region far from the gate for compounds M8 and M9, and less significant for M7 specimens.

Looking at the combined effect of an increase in melt temperature and injection speed by changing the experimental conditions from E01 to E04, it was also beneficial to the shielding of all the materials. However, since in some cases these two variables induced opposing effects on the measured shielding, their combined effect did not result in as significant an increase as that obtained with the isolated increase in melt temperature.

For the M7 compound, in the near gate region, the combined increase in melt temperature and speed had a positive effect, resulting in a slight improvement in shielding of up to 3.65 dB (a 10% increase). In the region opposite to the gate, however, the speed had a negative impact and partially offset the improvements induced by the melt temperature increase, resulting in a shielding increase of just 1.85 dB (a 4.9% increase).

In the case of the M8 compound, the combined increase in melt temperature and injection speed showed a synergistic effect, leading to further improvements in shielding of up to 3.66 dB (a 5.3% increase) in the near gate and up to 3.10 dB (a 5.2% increase) in the opposite gate regions.

As for the M9 compound, the increase in speed had a more significant negative impact than in the other two materials. On average, the increase in speed opposed the effect of the melt temperature increase, resulting in less improvement in the average shielding performance, with just a 1.5 dB increase

in the near gate and a 1 dB increase in the opposite gate. In contrast, the isolated effect of melt temperature induced an average shielding increase of 3 dB in the near region and 4 dB in the far region.

Regarding the relative sample position, which serves as an analysis of the effect of flow distance on material shielding, there is a clear reduction in shielding for both the M7 and M8 compounds. This effect varies with each experimental condition, but overall, the shielding performance is lower in the region far from the injection gate. The shielding of the M8 compound was the most affected, with a decrease of up to -9 dB (a 12% decrease), while the M7 shielding deteriorated by up to -2.2 dB (a 6% decrease).

In the case of the M9 compound, a consistent behaviour is not observed for the specimens produced with different experimental conditions. On average, a slight shielding decay is noticeable with an increase in distance in experiments E02 and E04, and a slight shielding improvement for experimental conditions E01 and E03. Depending on the tested frequency, a higher speed (E02 and E04), previously seen as having a negative impact, can result in a shielding variation from -5 dB (a 5% decrease) to +2 dB (a 3% increase). However, with a lower speed (E01 and E03), the shielding variation between the near and opposite gate locations ranges from approximately -2.4 dB (a 2% decrease) to +3 dB (a 5% increase), suggesting a positive effect on average.

In conclusion, this study demonstrates that an increase in flow length can lead to a decline in material shielding. However, the results suggest that M7 or M9 might be better suited for long flow parts, as they exhibit more stable properties along the flow path of the injection-moulded specimen. Furthermore, a lower speed is recommended to achieve better shielding performance along the entire specimen length.

To conclude this analysis, let's revisit the overall shielding performance of each compound and compare them. This comparison will consider their average shielding measured across the complete frequency band at each of the experimental conditions, with results displayed in Figure 26. Additionally, we will focus on the material attenuation and specific shielding, as indicated by the average values in in Figure 27 and Figure 28, respectively. Material attenuation represents the loss per millimeter of thickness in each material and is calculated by dividing the shielding by the specimen's thickness values (as shown in Table 5), with the unit of measurement in dB/mm. Specific shielding quantifies the measured shielding per volumetric weight of the material, calculated by dividing the measured shielding by the specimen's density from Table 5, and it is expressed in dB.cm<sup>3</sup>/g.

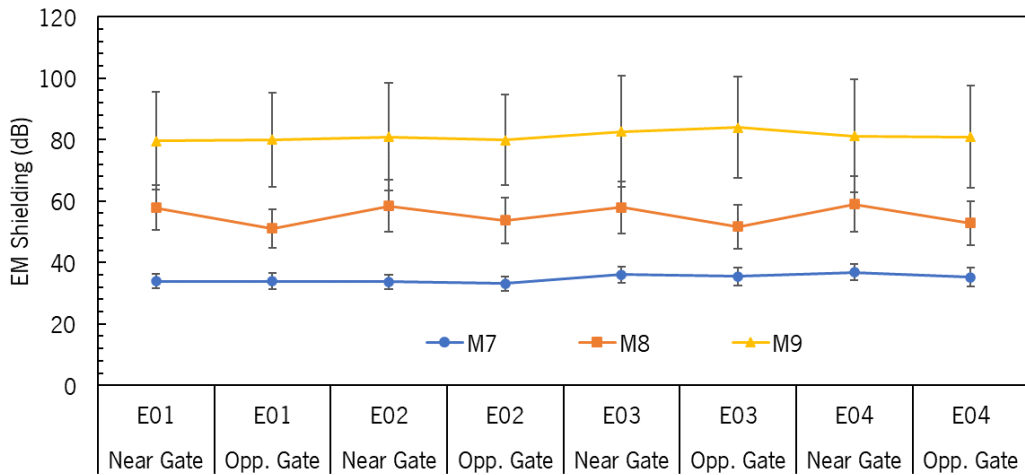


Figure 26. Average shielding measured for the three injected compounds at each experimental condition.

As discussed earlier, M9 compound stands out as the most effective material for shielding electromagnetic waves generated by the experimental apparatus, with an average shielding of around 80 dB and a broad, linear increase with frequency. M8 follows with an average shielding of 60 dB, which also rises with frequency but at a slower rate. M8 shielding was notably affected by the increase in flow distance, resulting in a decrease of up to -10 dB. On the other hand, M7 exhibited relatively poor performance, and was the only material with an average shielding below 40 dB.

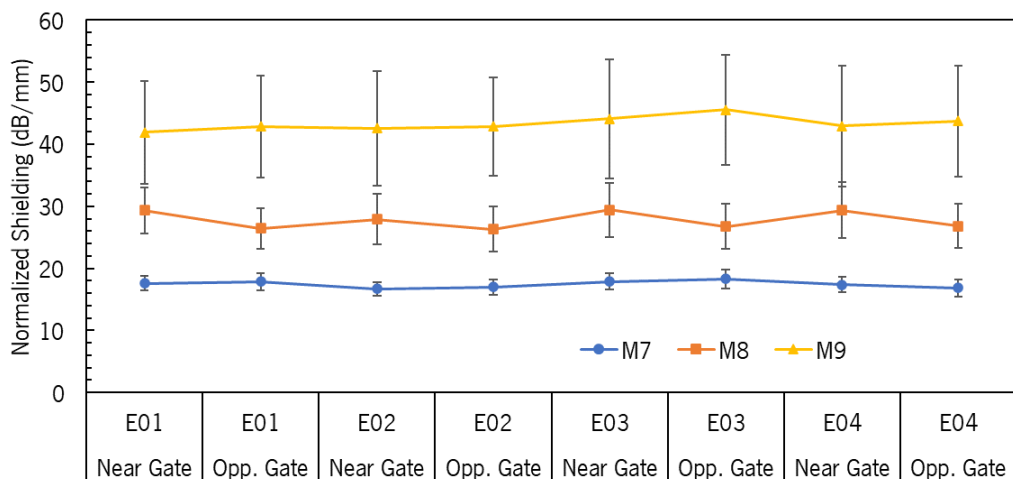


Figure 27. Normalized shielding for the three injected compounds at each experimental condition.

Concerning the compounds' normalized shielding, a property adjusted to account for thickness variations, a similar relative performance is observed across the three analysed compounds. Looking at the values in Figure 27, it's clear that M9 has the highest attenuation effect, at approximately 40 dB/mm,

followed by M8 with an average attenuation of almost 30 dB/mm. M7 has the lowest average attenuation at 17 dB/mm.

Evaluating the material's normalized shielding is crucial for determining the optimal part thickness required to achieve the desired shielding performance. Thus, assuming a linear model with constant properties, we can estimate that the M7 compound with a thickness of approximately 2.4 mm will achieve the required 40 dB shielding. However, it's important to note that these assumptions should be made cautiously since variations in thickness may result in different electrical properties after the injection moulding process.

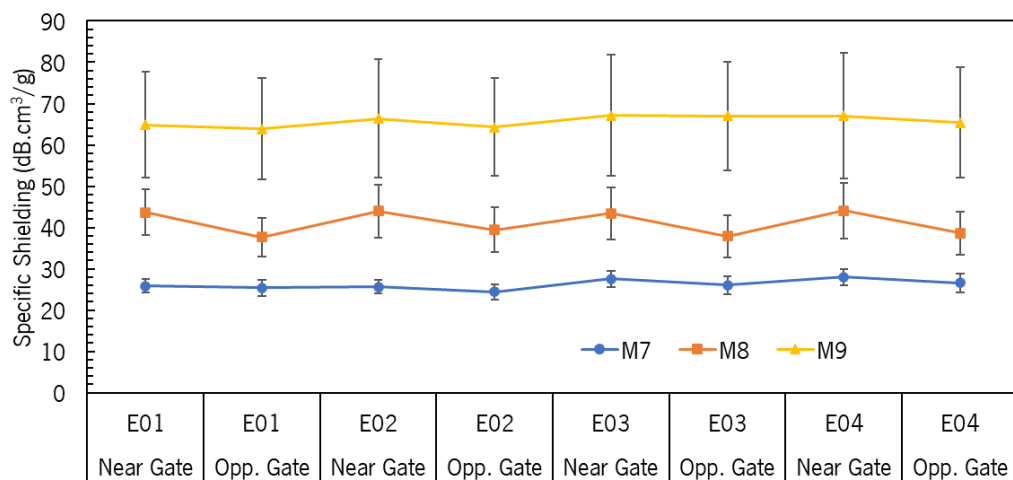


Figure 28. Specific shielding calculated for the three compounds at each experimental condition.

Regarding the specimens' specific shielding, a property that reflects the shielding effectiveness per added volumetric weight of the material, the same relative behaviour is observed. M9 compound, which is based on PP and has lower density than the other two PBT-based compounds, achieves a specific shielding of approximately 65 dB.cm<sup>3</sup>/g, which is much higher than the two other equivalent materials. M8 and M7 compounds have average specific shielding of approximately 41 dB.cm<sup>3</sup>/g and 26 dB.cm<sup>3</sup>/g, respectively.

Evaluating the specific shielding effectiveness of a material is crucial in the development of lightweight products. The M9 compound, with its lower density and higher shielding effectiveness, clearly offers a significant advantage when compared to other two materials.



### Electrical conductivity

The direct current Electrical conductivity (EC) was evaluated, considering the influence of injection moulding conditions (varying  $T_i$  and  $V_i$  in two levels), sample location (near and opposite the gate), and applied compression force, ranging from 20 to 200N. Furthermore, as described in the experimental protocol, EC measurements include an analysis in three specimen directions: in-plane/longitudinal (parallel and perpendicular to the flow) and through-plane (transversal to the flow).

The mean EC results for the three compounds are presented in Figure 29, Figure 30 and Figure 31 for M7, M8, and M9, respectively. These results are displayed as a function of the compression force for the two extremes of the experimental conditions (E01 and E04) and the two selected sample locations, near the gate and opposite the gate. A logarithmic scale was applied to the y-coordinate axes of the charts.

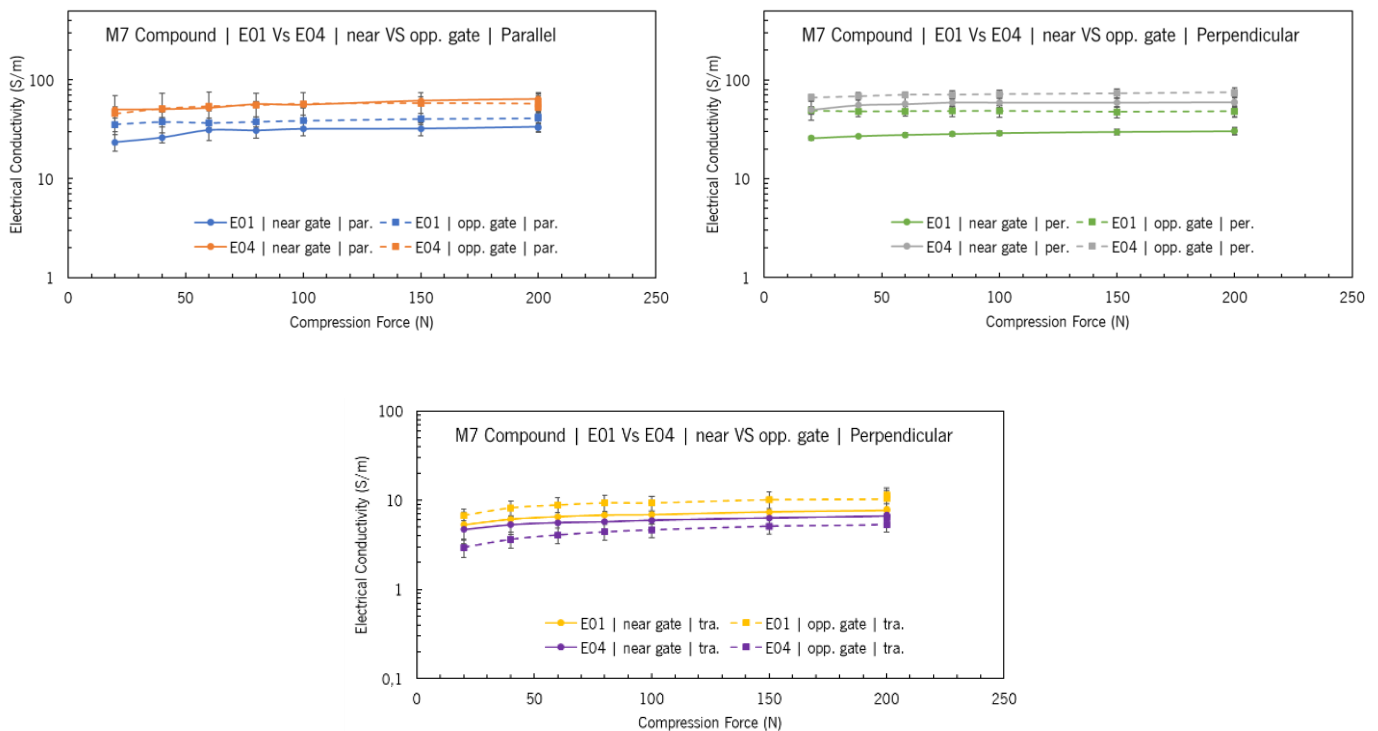


Figure 29. Measured conductivity in the parallel (top left), perpendicular (top right) and transversal (bottom) directions. Results belong to compound M7 and are shown in function of the applied compression force for different processing conditions and sample locations.

### Chapter 3. Thermoplastic compounds processed by injection moulding

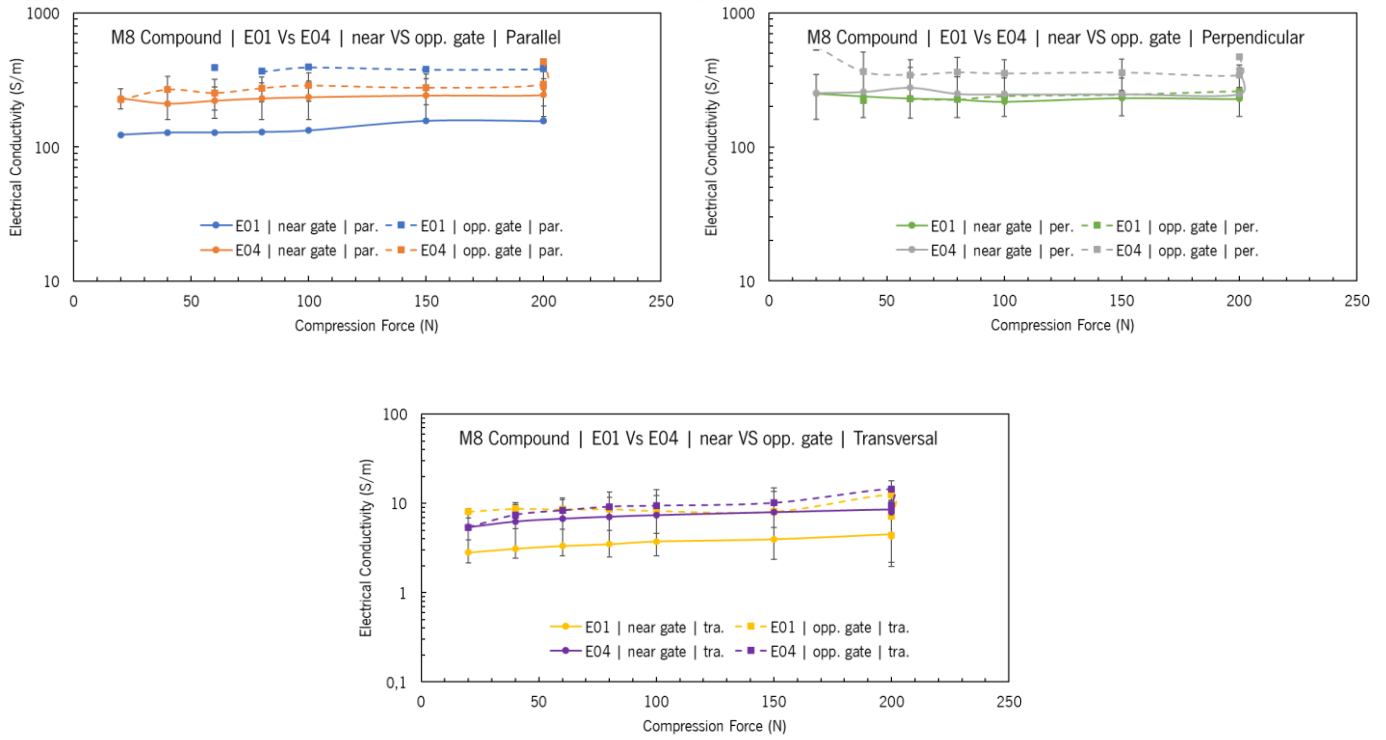


Figure 30. Measured conductivity in the parallel (top left), perpendicular (top right) and transversal (bottom) directions. Results belong to compound M8 and are shown in function of the applied compression force for different processing conditions and sample locations.

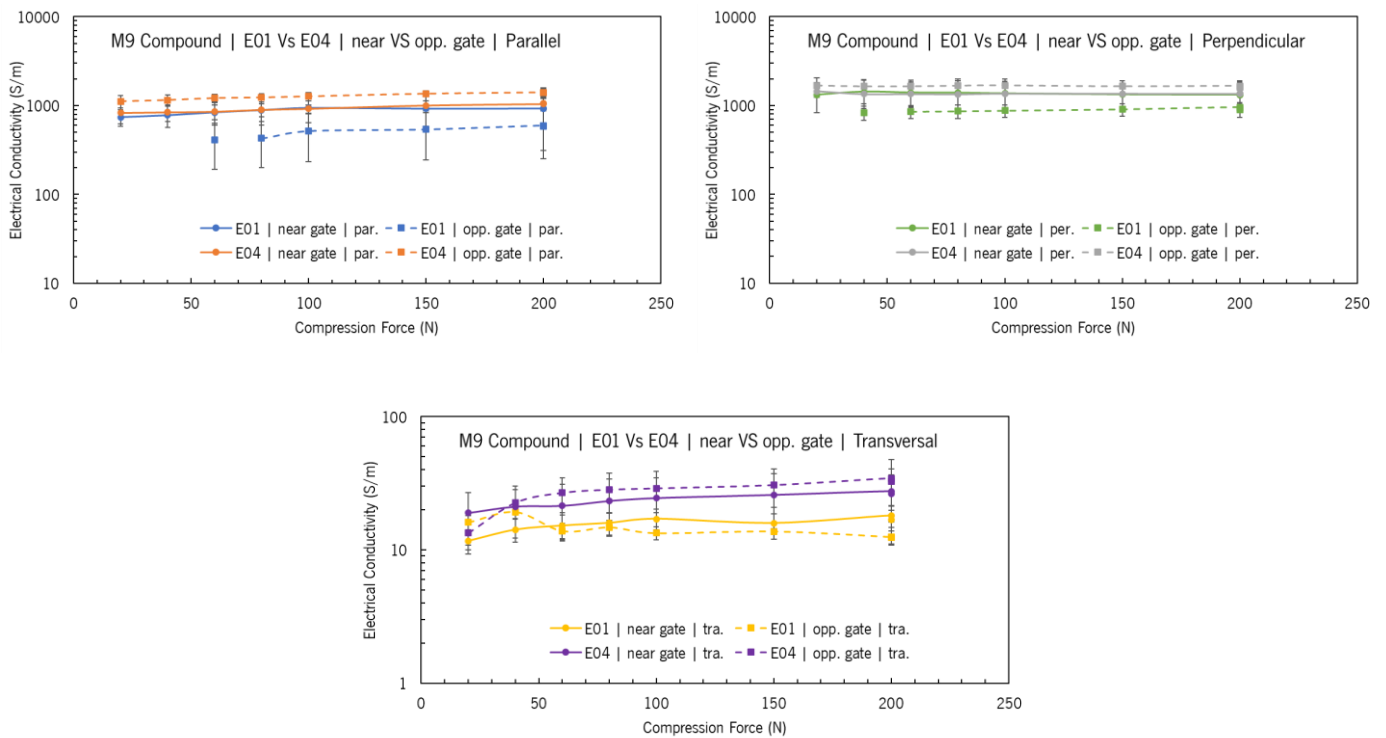


Figure 31. Measured conductivity in the parallel (top left), perpendicular (top right) and transversal (bottom) directions. Results belong to compound M9 and are shown in function of the applied compression force for different processing conditions and sample locations.

The average electrical conductivity of M7 specimens varied within the range of 23 – 64 S/m for the direction parallel to the flow, 25 – 75 S/m for the direction perpendicular to the flow, and 3 – 11 S/m for the direction transversal to the flow. In the case of M8 compound, the measured EC fell within the range of 123 – 432 S/m for the direction parallel to the flow, 218 – 564 S/m for the direction perpendicular to the flow, and 3 – 14 S/m for the direction transversal to the flow. For the EC measured in M9 samples, the values ranged from 411 – 1407 S/m for the direction parallel to the flow, 833 – 1682 S/m for the direction perpendicular to the flow, and 11 – 34 S/m for the direction transversal to the flow.

Thus, the measured electrical conductivity for the injected compounds aligns with the overall behaviour discussed in the EMSE analysis, where M9 exhibits the highest conductivity, reaching almost 1700 S/m, followed by M8 with a maximum measured EC of 564 S/m, and M7 with a much lower measured conductivity of up to 75 S/m. This behaviour was expected since EM shielding is directly proportional to the material's electrical conductivity.

Additionally, it's worth noting that despite having lower conductive filler content (less than 10%), M8 has longitudinal conductivity (parallel and perpendicular to flow) up to 7 times higher than the values measured for M7. However, transversal conductivity does not exhibit the same ratio, as it is quite similar for both materials, both within the range of around 10 S/m.

An important aspect observed in this study is the anisotropic behaviour of these compounds in the transversal direction. For both compounds, the measured EC is similar for the directions parallel and perpendicular to the flow (homogeneous in-plane), but it's approximately 7 times, 30 times, and 50 times higher in the transversal direction (heterogeneous through-plane) for M7, M8, and M9, respectively.

As reported, the electrical conductivities were obtained under different compression forces applied to the top electrode. Examining the EC charts from Figure 29 to Figure 31 and the Table S13 available in Appendix D, the results indicate that an increase in compression force from 20 N to 200 N led to a substantial increase in EC, particularly in the transversal measurements. This effect could be explained by the increased contact area between the copper electrodes and the specimen's surface and the specimen being squeezed more with higher force, which creates new conductive networks [107]. The

fact that the compression force induces more significant variations in the transversal measurements (above 40 percent points) supports this hypothesis.

The effects of the injection moulding conditions and sample relative location can be better observed in Figure 32 (with corresponding values in Table S12 available in Appendix D) which shows the electrical conductivities at 200N applied compression force for the three compounds and for the two experimental conditions and two specimen areas (near and opposite to gate).

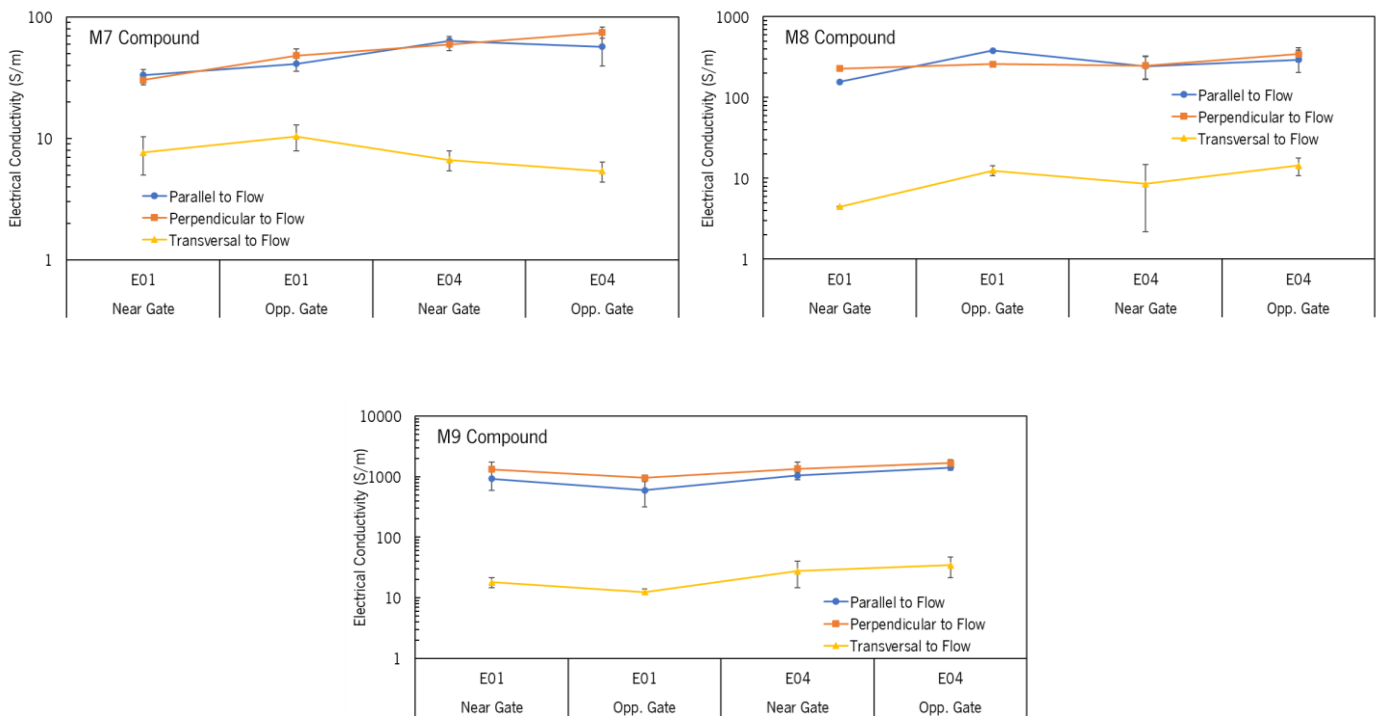


Figure 32. Electrical conductivity at 200 N compression force. Results for M7 (top left), M8 (top right) and M9 (bottom) at different processing conditions, sample locations and measurement direction.

When examining the EC measurements conducted with a compression force of 200 N, several noteworthy observations emerge. However, it's crucial to approach these interpretations with caution due to potential experimental errors that can result in measurements with high deviation values, particularly in the case of transversal specimens.

Firstly, there's a clear anisotropic characteristic across all the materials. The measured values for electrical conductivity in the parallel and perpendicular to flow directions are similar and significantly higher than the through-thickness conductivity. For M7, the longitudinal (parallel or perpendicular) conductivity falls within the range of 30 to 75 S/m, which is approximately 4x or 9x higher than the transversal EC measured in specimens produced under experimental conditions E01 and E04,

respectively. In the case of M8 specimens, the longitudinal conductivity ranges from 156 to 382 S/m, which is up to 50x and 30x higher than the measured transversal conductivity in specimens from E01 and E04, respectively. For M9 compound, the longitudinal conductivity surpasses 1000 S/m, reaching values significantly higher than the transversal conductivity, which can be up to 70x higher. Hence, there is a pronounced anisotropic behaviour in these materials' specimens that can be quantified using this measurement method.

Secondly, as mentioned earlier, the average measured conductivity for M9 compound exceeds 1000 S/m in the longitudinal direction, which is much higher than the other two grades with average conductivities of 270 S/m and 50 S/m for M8 and M7, respectively. Similarly, in the transversal direction, the average value of over 20 S/m measured in the M9 specimens is also higher than the measured values of 10 S/m and 7.5 S/m for M8 and M7, respectively. These results align with the shielding outcomes, indicating a direct correlation between shielding effectiveness and conductivity.

Third and final note, the experimental conditions and specimen location induced some variations to the conductivity of the injected specimens. There's an apparent positive effect with the increase of melt temperature and injection speed (from E01 to E04), especially for the longitudinal conductivity both in the parallel and perpendicular to the flow and in both measured regions near and opposite to the gate. Given that the measured electromagnetic shielding was positively impacted in all compounds with the variation from E01 to E04, an increase in conductivity was expected.

In the case of M7, the increase in injection moulding parameters led to increased specimen conductivity in the parallel and perpendicular directions but a decrease in the transversal direction. The increase in conductivity in the parallel direction was around 30 S/m near the gate location and 16 S/m at the opposite gate location. Similarly, the electrical conductivity increased in the perpendicular direction by approximately 29 S/m near the gate and 26 S/m at the opposite gate location. In contrast, the electrical conductivity decreased in the transversal direction by around 1 S/m near the gate location and 5 S/m (48%) at the opposite gate location.

For M8 specimens, the effect of increasing the injection moulding parameters was mainly positive for electrical conductivity in all directions, with one exception in the parallel conductivity measured at the opposite gate location where a decrease was observed. However, this variation could potentially be due to measurement errors. In all other cases, a positive effect was noted, with an increase of approximately 80 S/m in the longitudinal direction and 4 S/m in the transversal direction.

In the case of M9 specimens, a clear positive effect from the increase in melt temperature and speed was observed in all measured directions and locations. This positive variation was most noticeable in the opposite gate region, where there was an increase in electrical conductivity of over 700 S/m in the longitudinal direction and an increase of about 22 S/m in the transversal direction. However, it's worth noting that the previously measured shielding was nearly unchanged with the increase in experimental conditions, and the same behaviour was to be expected in the EC measurements.

Concerning the effect of flow distance, it's apparent that increasing the distance from the region near the gate to the region opposite the gate results in a non-uniform variation in the two different experimental conditions. Furthermore, these results differ among the three studied materials, with some cases demonstrating a significant increase in conductivity, while in others, there's an opposite effect with a decrease in conductivity.

Given that the measured electromagnetic shielding was negatively impacted by the increase in distance, particularly for M8 specimens, one might anticipate a decrease in conductivity. However, the data doesn't provide a clear and consistent effect to draw a conclusive analysis.

### **EC and EMSE relation**

The scattering of electromagnetic waves within a homogeneous and isotropic medium, or material, is intricately linked to the medium's intrinsic impedance. This wave impedance is governed by the material's electrical permittivity, magnetic permeability, and electrical conductivity.

In this section, a comparative analysis, examining the measured Electromagnetic Shielding Effectiveness (EMSE) in relation to the corresponding electrical conductivity (EC) values is undertaken. This analysis accounts for the direction of measurement, whether it's parallel, perpendicular, or transversal to the flow during the injection moulding process. Figure 33 presents a visual representation of the measured EMSE values for all the compounds, alongside their respective EC values. Additionally, a theoretical curve is provided to illustrate the expected EMSE for a homogeneous and an isotropic material with a specific constant EC. This theoretical curve is used for comparison with the experimental results.

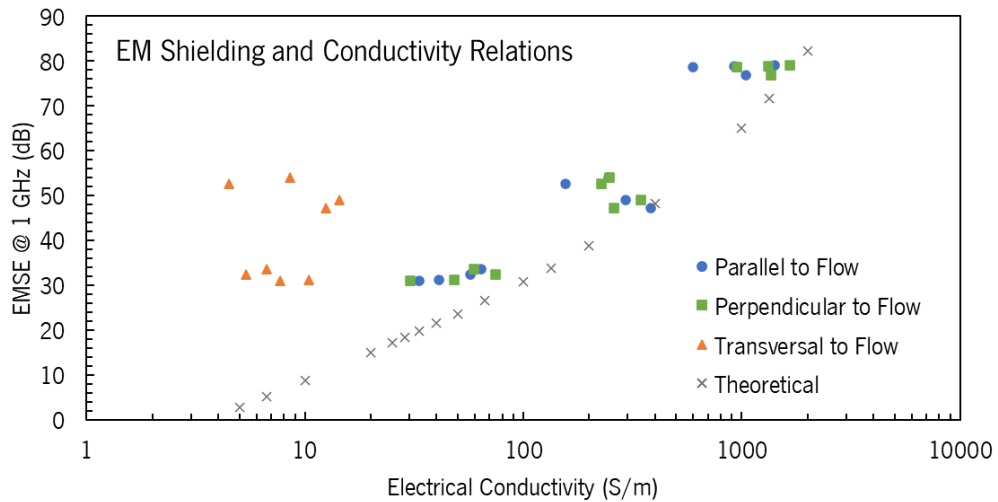


Figure 33. EMSE relation with both experimental (parallel, perpendicular, and transversal to flow) and theoretical EC. EC axis is plotted with a logarithmic scale.

As anticipated, both the experimental and theoretical data demonstrate that EMSE increases with an increase in EC, and this relationship follows an exponential trend due to the absorption mechanism of shielding.

Moreover, it's evident that the parallel and perpendicular conductivities fall within a similar range and align more closely with the theoretical data points. Hence, it can be concluded that the primary contributor to the EMSE of the mouldings is longitudinal (in-plane) conductivity, as it aligns more closely with theoretical predictions.

Another important observation from this analysis is that the experimental values for conductivity are likely to have been underestimated. This inference is drawn from the fact that most of the measured EC values are above the theoretical values or positioned to the left of the theoretical line. Therefore, a different or improved characterization process will need to be executed in future studies.

### 3.5.4. Concluding remarks

In the second experimental approach, the injection moulding of 2 mm thick rectangular plates was conducted using three different fibre-reinforced thermoplastics to enhance the shielding studies. This study delved into the impact of various injection moulding process conditions, specifically melt temperature, injection speed, and flow distance. Additionally, it focused on characterizing anisotropic electrical conductivity and its correlation with the shielding effectiveness.

The primary objective of this study was to gain a comprehensive understanding of how injection moulding parameters influence the EM shielding properties of polymeric compounds and how anisotropic EC relates to EM shielding.

Like the findings in the first study, it was evident that the EMSE is not solely determined by the concentration of conductive fibres within the polymer compound. Different types and/or aspect ratios of the carbon fibres resulted in varying shielding effectiveness. The M7 compound exhibited an EMSE ranging from 30 to 40 dB, while the M8 compound demonstrated an EMSE ranging from 45 to 75 dB, despite having 10% less carbon fibre content. Notably, the inclusion of short SSF in similar concentrations to CF significantly outperformed the other two materials. The M9 compound exhibited EMSE values between 50 and 100 dB, depending on the frequency and experimental conditions.

The study also included a brief analysis of normalized and specific shielding. These adjusted properties consider the effect of specimen thickness and density, which are crucial for engineers when designing or selecting more efficient materials for a specific enclosure. M9 displayed the highest attenuation at approximately 40 dB/mm, followed by M8 with an average attenuation of almost 30 dB/mm and M7 with an average attenuation of 17 dB/mm. In terms of specific shielding, M9 had an average value of around 65 dB.cm<sup>3</sup>/g, while M8 and M7 compounds exhibited average specific shielding values of approximately 41 dB.cm<sup>3</sup>/g and 26 dB.cm<sup>3</sup>/g, respectively.

A novel experimental apparatus was employed to measure the direct current EC in three directions: parallel, perpendicular, and transversal to the flow. This experimental procedure allowed for the assessment of anisotropic conductivity along the specimens. It was observed that the EC measurements in the longitudinal plane of the specimens, in both the parallel and perpendicular to flow directions, exhibited similar values and were significantly higher than the transversal (thru-thickness) conductivity. For M7, depending on the processing conditions and specimen location, the measured conductivities ranged from 25 to 75 S/m in the longitudinal direction and from 3 to 11 S/m in the transversal direction. In the case of M8, the conductivities were higher than those of M7, ranging from 123 to 564 S/m in the longitudinal direction and from 3 to 14 S/m in the transversal direction. M9's conductivity characteristics were outstanding compared to the other materials, with values exceeding 1000 S/m in the longitudinal direction and reaching up to 34 S/m in the transversal direction.

Furthermore, a correlation between anisotropic electrical conductivity and electromagnetic shielding was established. It was determined that longitudinal conductivity is the primary property contributing to



the shielding effect in these types of polymeric compounds with heterogeneous properties. Longitudinal conductivities closely aligned with the theoretical values projected for an isotropic material with constant conductivity. However, it's worth noting that the experimental apparatus needs improvement, as the results displayed high deviations, and the average measured values were likely underestimated.

The shielding effectiveness, as well as the electrical conductivity results, were influenced by variations in the experimental conditions during the injection moulding process and the flow distance along the mould cavity (near and opposite to the gate). After a thorough analysis of the results, it was evident that, on average, increasing the melt temperature had a beneficial effect on both the shielding and electrical conductivity of the three compounds.

The increase in melt temperature was found to have a positive impact, promoting an increase in shielding of up to 10% for M7 and M9 specimens and up to 4% for M8 specimens. Similarly, the electrical conductivity of the specimens increased with rising temperature. These findings agree with peer studies [84], [86].

Injection speed's effect was not particularly significant, with an average slight decrease of 1% in shielding for M7 and M9 compounds and a slight increase of up to 3% for M8 specimens, which is consistent with previous research [47], [84].

In terms of the relative sample position, whether near or opposite to the gate of the rectangular plate specimens, a noticeable reduction in shielding was observed for all the compounds, with M8 showing a more pronounced shielding decay of up to 12%.

To summarize, the study successfully addressed the research questions posed at the beginning: "What's the impact of injection moulding conditions?"; "How can the anisotropic conductivity of these composites be measured?"; "What's the relationship between the anisotropic electrical conductivity and EM shielding properties of polymer compounds?" The anisotropic electrical conductivity was measured and correlated with the electromagnetic shielding of three fibre-reinforced compounds. Additionally, the impact of two injection moulding variables, melt temperature and injection speed, was investigated for both electromagnetic shielding and electrical conductivity properties.

This investigation can indeed be further explored to advance our knowledge in the following fields:

- Influence of fibre concentrations: A more detailed study on how the type of fibre and its concentration within the polymeric compound impact electrical and shielding properties is

essential. Exploring a range of fibre loadings and types can provide a deeper understanding of these effects.

- Impact of injection moulding conditions: Investigating additional injection moulding parameters like gate type and specimen thickness is crucial. These factors can significantly affect the performance of parts, and assessing their influence on shielding and electrical properties would offer valuable insights.
- Measurement of electrical conductivity and permittivity: Developing new testing procedures or enhancing existing ones for more reliable and consistent results is vital. This includes measuring the DC anisotropic conductivity and characterizing the complex and frequency-dependent properties,  $\epsilon(\omega)$  and  $\sigma(\omega)$ , of thermoplastic compounds. Improved testing methods will aid in better understanding the electrical properties and shielding mechanisms of these materials.
- Refining theoretical models: Developing a comprehensive theoretical model that accurately describes the complex and frequency-dependent electrical and electromagnetic properties of these polymeric compounds is an important next step. Achieving a closer alignment between theoretical predictions and experimental results will enhance our understanding of these materials.

By addressing these areas, further progress can be made in the study of electromagnetic shielding properties in polymeric compounds, paving the way for more efficient and effective shielding materials.

### **3.6 An improved assessment on the relationship between the injection process, the EMSE and the frequency dependent properties**

The third and final study represents an enhanced analysis of the EM shielding behaviour and the corresponding electrical conductivity of heterogeneous polymeric composites produced through the injection moulding process. This study involved an expanded analysis of the anisotropic properties, along with an improved experimental procedure capable of measuring both DC and frequency-dependent electrical conductivity in both the longitudinal and through-thickness directions. The latter was achieved

by measuring the complex dielectric function of the material through an equivalent LCR model and extracting the conductivity using the theoretical relationship between them.

This analysis was conducted on five thermoplastic compounds, each containing a single type of conductive fibre in its composition. The goal was to compare how the nature and volume fraction of these fibres influenced the EM shielding and conductivity properties. To achieve this, three weight percentages of carbon fibre (CF) and two weight percentages of stainless-steel fibres (SSF) were added to a polycarbonate (PC) thermoplastic grade. The injection moulding process was used to produce specimens with two different thicknesses and two feeding system designs, resulting in a total of four samples for each material. This approach also allowed for the examination of how the type of injection moulding gate and material thickness affected EM shielding and electrical conductivity.

Additionally, a new theoretical characterization approach was introduced. The new model is based on frequency-dependent properties rather than the previous constant DC conductivity approach. The frequency-dependent and anisotropic properties used in the model were obtained by measuring the equivalent LCR impedance through the thickness of the specimens, while longitudinal properties were calculated by introducing an anisotropic ratio into the equation.

In summary, this study aimed to further develop the characterization of EM shielding and electrical conductivity in fibre-filled thermoplastic composites and provide answers to several research questions:

- What is the impact of injection moulding parameters on these composites?
- How can the anisotropic and frequency dependent electrical conductivity of these composites be precisely measured?
- How are electrical conductivity and dielectric function interconnected with the electromagnetic shielding properties of these polymer aggregates?
- How can the anisotropic characteristics of this compounds can be theoretically model to estimate the electromagnetic shielding?

#### 3.6.1. Materials

This investigation employed five commercially available PC thermoplastic compounds, filled with different weight percentages of carbon fibres (CF) or stainless-steel fibres (SSF). The objective is to compare the effects of the nature and volume fraction of these fibres on the measured properties of electromagnetic shielding and conductivity. Accordingly, three grades composed by PC filled with 10%,

15% and 30% of CF and two grades of PC filled with 10% and 15% of SSF acquired from *SABIC*, with commercial names and characteristics shown in Table 6.

Table 6. Datasheet properties of the injection moulding compounds.

<b>Material</b>	<b>LNP™ Stat-Kon™ DE0026</b>	<b>LNP™ Stat-Kon™ DE003</b>	<b>LNP™ Stat-Kon™ DE006</b>	<b>LNP™ Faradex™ DS0026I</b>	<b>LNP™ Faradex™ DS0036I</b>
<b>Polymer matrix</b>	PC	PC	PC	PC	PC
<b>Filler Composition (wt%)</b>	10% CF	15% CF	30% CF	10% SSF	15% SSF
<b>Density (g/cm<sup>3</sup>)</b>	1.23	1.26	1.32	1.26	1.29
<b>Tensile Modulus (GPa)</b>	8	12.2	19.6	2.49	2.5
<b>Surface Resistance (Ω)</b>	10 <sup>2</sup> - 10 <sup>6</sup>	10 <sup>2</sup> - 10 <sup>4</sup>	10 <sup>1</sup> - 10 <sup>3</sup>	2.3 x 10 <sup>1</sup>	10 <sup>2</sup> - 10 <sup>4</sup>

An assessment regarding the fibre characteristics was achieved by optical microscopy (*Olympus Transmission Microscope BH-2 + Leica DMC2900*) and by a magnifier (*Leica DMS1000*). A statistical analysis for the more than 1000 observed fibres regarding their length and diameter is presented in Table 7 and Figure 34.

Table 7. Average fibre length and diameter.

<b>Material</b>	<b>LNP™ Stat-Kon™ DE0026E</b>	<b>LNP™ Stat-Kon™ DE003</b>	<b>LNP™ Stat-Kon™ DE006</b>	<b>LNP™ Faradex™ DS0026I</b>	<b>LNP™ Faradex™ DS0036I</b>
<b>Average Length (μm)</b>	261.59	233.40	252.45	2806.97	3680.31
<b>Deviation (μm)</b>	134.10	106.72	82.44	818.23	885.49
<b>Average Diameter (μm)</b>	8.63	8.25	9.24	9.79	10.32
<b>Deviation (μm)</b>	0.80	1.13	1.09	1.09	0.66

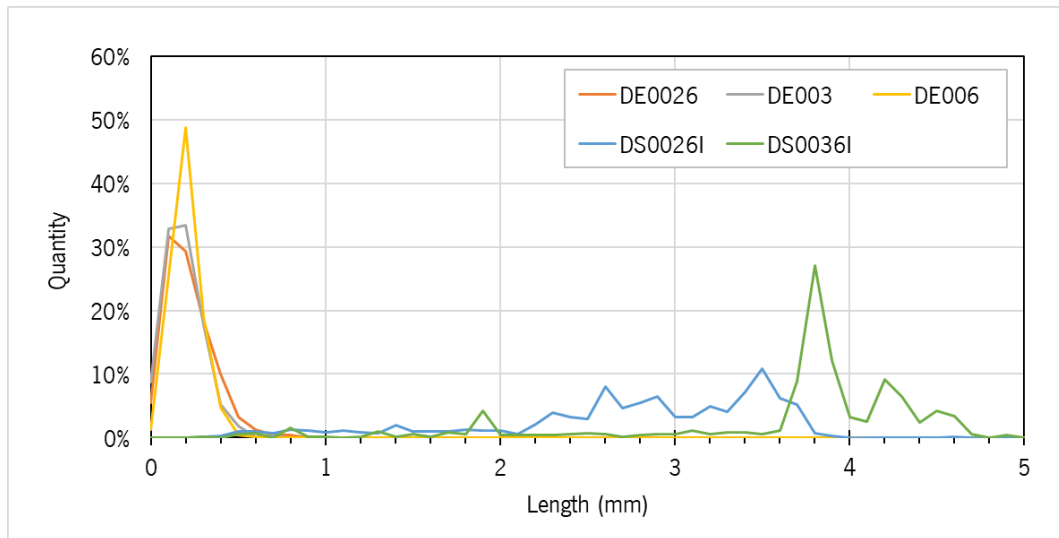


Figure 34. Fibres length histogram.

### 3.6.2. Experimental procedure

The study involved five different thermoplastic compounds that underwent the injection moulding process to create flat samples. These samples were then subjected to characterization to assess their EM shielding properties. Subsequently, smaller sections were cut from these samples, and their anisotropic DC and frequency-dependent electrical conductivity were measured in both the through-thickness and longitudinal directions.

To gain additional insights into how various processing parameters affect the material properties, the injection moulding process for the selected materials was conducted using four different mould cavities. This resulted in the production of samples with two different thicknesses and two different injection gates. This approach allowed for an analysis of how these injection moulding parameters influenced both shielding effectiveness and electrical conductivity.

Furthermore, a theoretical characterization process was developed, which considered anisotropic and frequency-dependent properties. This process comprised three key steps. Firstly, the DC electrical conductivity was measured in both the longitudinal (in-plane) and transverse (through-thickness) directions to determine the longitudinal-to-transverse (L/T) conductivity ratio. Secondly, the frequency-dependent dielectric properties were measured in the transverse direction of the specimens, and the corresponding electrical conductivity was calculated using an equivalent RLC impedance model. In the third and final step, the DC conductivity L/T ratio was used to adjust the longitudinal frequency-dependent conductivity.



during this procedure, the fibre-filled thermoplastic compounds were injected into a single-cavity mould via a direct sprue gate or via a side edge gate, as shown in Figure 36. Additionally, cavities with different depths were used to produce specimens with thicknesses of approximately 1.6 and 3 mm.

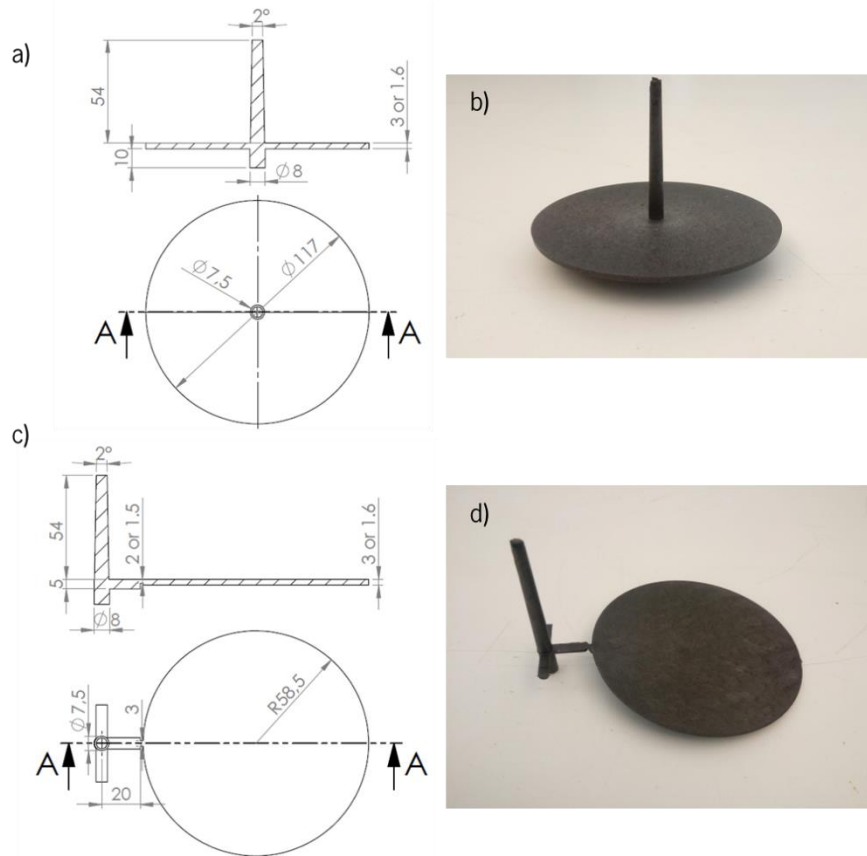


Figure 36. Injection moulding samples: a) and b) sprue gate; c) and d) side edge gate.

Summarizing, a set of four experiments were carried out for each fibre-filled material. One experiment condition (A) encompassed the injection of 3 mm thick parts via the direct sprue gate ( $\phi 7.5$  mm), the second condition (B) consisted of the production of 3 mm thick samples via the lateral edge gate (3 x 2 mm cross section), the third experimental condition (C) was set for the injection of 1.6 mm thick samples via the sprue gate ( $\phi 7.5$  mm), while the last experimental conditions (D) featured the injection of 1.6 mm thick samples via the lateral edge gate (3 x 1.5 mm cross section). The design of these conditions is detailed in Table 8, and was completed for each material, giving a total of 20 experiments.

Table 8. Experimental plan for the injection of disk-shaped samples.

Experimental Plan	A	B	C	D
Gate system	Direct Sprue	Lateral Edge	Direct Sprue	Lateral Edge
Part thickness (mm)	3	3	1.6	1.6

The corresponding injection moulding conditions input to the injection moulding machine are listed in the supplementary information (Appendix E. Supplementary results to chapter 3.6.) Table S15, and Table S16 for the CF and SSF filled materials, respectively. Upon achieving a state of steady equilibrium, at least six specimens were produced for each material and experimental condition, forming the basis for subsequent investigations.

After the injection moulding cycle, the shielding effectiveness was measured at the frequency range between 30 MHz and 3 GHz, following the procedure described in chapter 3.3.2. A VNA with an input power of 0 dBm was used to generate EM waves and record the transmission scattering parameters (S21) to determine the total EMSE according to Equation 32.

For every material and processing condition, a group of 5 "Load" samples and 1 "Reference" sample were meticulously produced, following the specifications outlined in Figure 37. The process involved the cutting of the sprue and feeding system, and drilling some holes as specified in the specimens' drawings.

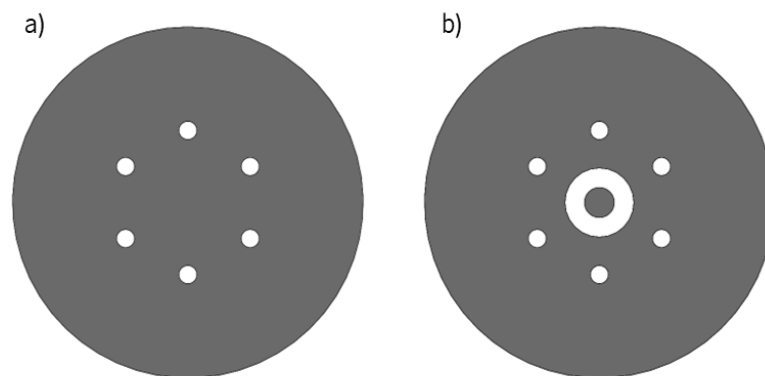


Figure 37. Samples drawing for EMSE test: a) load sample; b) reference sample.

In conjunction with the shielding measurements, a complementary evaluation of electrical conductivity was conducted. This assessment involved measuring the electrical resistance across both the longitudinal (in-plane) and transversal (through-thickness) directions of the specimens.

The electrical resistance measurements were conducted at ambient temperature using an improved test cell, different from the one used in in chapter 3.5. In this setup, electrical resistance was determined by recording voltage and current measurements through custom 4-point copper electrodes built on an FR-4 substrate. The new arrangement featured the use of a *Keithley 2635B SourceMeter* to supply a 1 mA direct current to the outer electrodes on the sample while reading the DC voltage across the two inner electrodes. The electrical resistance of each sample was then calculated using Equation 36.



Additionally, enhancements were made to the electrode cells. The updated version incorporated 75 Ohm BNC connectors soldered to the copper terminals, improving structural stability in the solder region. This modification also allowed for connecting the apparatus to an impedance bridge to perform electrical characterization in the frequency-dependent domain. The electrodes were mounted on a structure that housed both electrodes while permitting free vertical movement of the top electrode. By utilizing a handle screw and a digital force gauge (*IMADA ZTA-LM-110*) placed between the handle and the sample, the compression force applied to the samples could be controlled to be approximately 200 N.

The specimens were positioned between the two identical pairs of custom-made electrodes to measure the longitudinal conductivity (test cell shown in Figure 38) and the transversal conductivity (test cell shown in Figure 39).

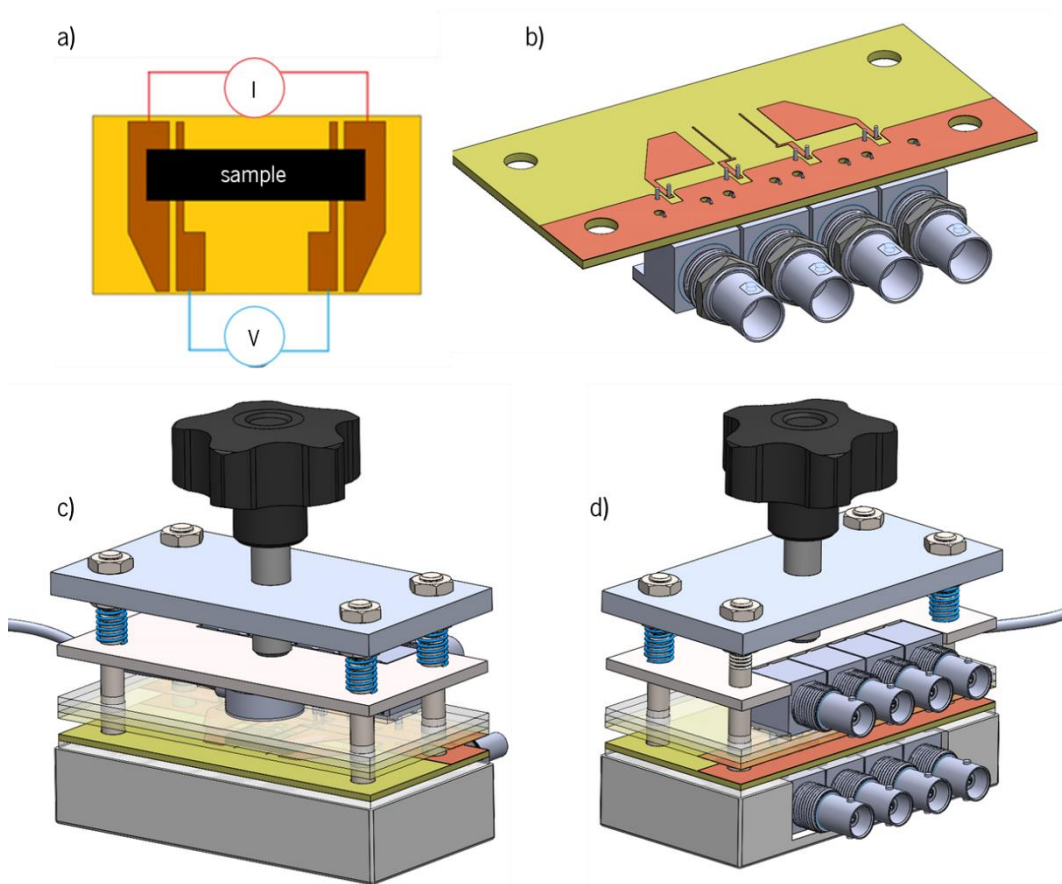


Figure 38. Virtual model for the longitudinal conductivity test cell: a) electrical schematic; c) bottom electrode conceptual model, b) and d) shows the assembly of the complete test cell, with accessories.

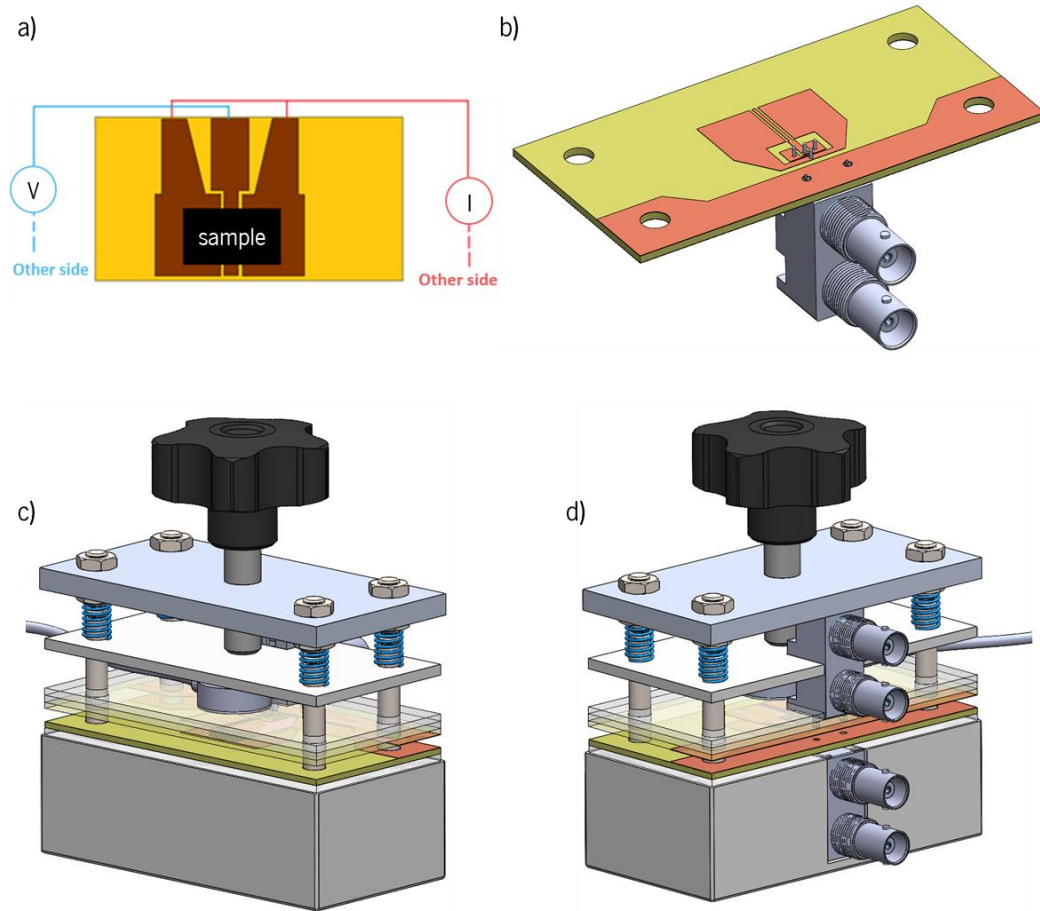


Figure 39. Virtual model for the transversal conductivity test cell: a) electrical schematic; c) bottom electrode conceptual model, b) and d) shows the assembly of the complete test cell, with accessories.

Testing was carried out on cut samples, which were obtained from the mouldings to evaluate the anisotropic conductivity properties. After conducting the EM shielding characterization, four samples were extracted from each of the moulded plates and labelled as samples A, B, C, and D. The specific dimensions and locations of these samples are illustrated in Figure 40.

Samples A and B were prepared to assess the longitudinal electrical conductivity in directions perpendicular and parallel to the flow, respectively. Sample C was designated for determining the transversal (through-thickness) conductivity of the moulded components.

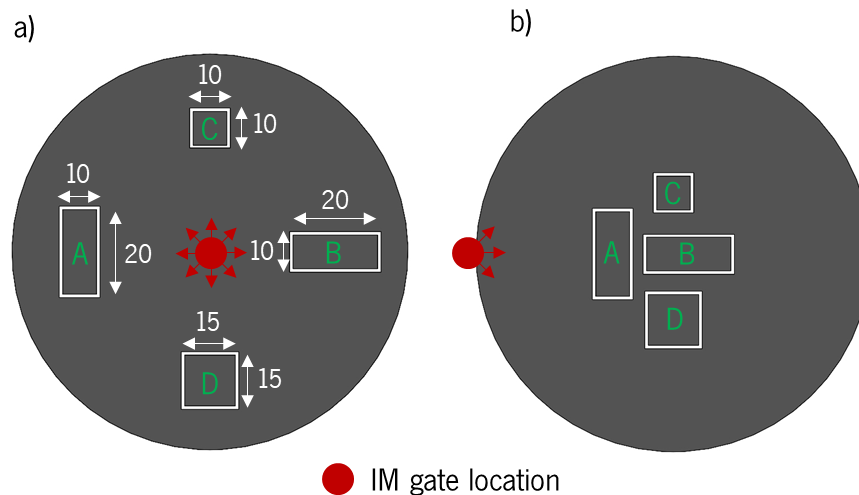


Figure 40. Samples general dimensions in millimetres and cutting operation scheme: A – sample for perpendicular measurements; B – sample for parallel measurements; C – sample for transversal measurements; D – sample for impedance measurements.

For samples labelled as D, they were extracted from the moulded parts and utilized to characterize the frequency-dependent conductivity through impedance analysis. In this procedure, a parallel plate method was employed, consisting of the *16453A Dielectric Material Fixture* connected to the *E4991A Impedance Analyzer*. This setup enabled the measurement of through-thickness electrical impedance and phase of the EM wave up to 1 GHz. This is a standard method used to determine the frequency-dependent and dielectric properties of a material specimen. It was employed to further investigate the complex permittivity ( $\epsilon'(\omega)$  and  $\epsilon''(\omega)$ ) and related frequency-dependent conductivity ( $\sigma(\omega)$ ) of the injection-moulded parts.

In this procedure, it was assumed that the tested material follows an equivalent LCR circuit diagram in series (L+C+R), as previously described in chapter 3.3.4. Electrical permittivity and frequency dependent conductivity This equivalent impedance was used to characterize the material's complex dielectric behaviour, and with appropriate mathematical conversions, it allowed for the characterization of the frequency-dependent conductivity in the transverse direction of the sample. Following this analysis, the frequency-dependent longitudinal conductivity was calculated by multiplying the longitudinal-to-transversal (L/T) ratio of proportionality obtained from the DC measurements.

In addition to the experimental characterization, an adjusted theoretical model was used to estimate the EM scattering phenomena occurring in these CF-filled or SSF-filled polymeric aggregates. The constitutive equation from the new model assumes a dissipative and homogeneous material with

anisotropic and frequency-dependent conductivity rather than the previous isotropic and constant DC conductivity approach. Here, the refraction of the EM waves is also described by transmission, reflection and absorption factors obtained from the transfer matrix formalism described in chapter 3.3.6. However, the new code written in the *Mathematica* software (see code for homogeneous material with anisotropic and frequency-dependent conductivity in Appendix C) was adjusted to define lossy properties of the medium according to the equivalent LCR inputs and the conductivity L/T ratio.

In addition to the properties presented above, the injection moulded parts were also measured in term of its thickness and density. A *Mitutoyo Digimatic Caliper* was used for measurement of the specimens' thickness. The parts density was measured with an analytical balance *AS 202.R2* from *Radwag* with *SDK 01 density kit* from *Scaltec Lda*, following to Archimedes principle. According to this principle, the volume of an immersed body is equal to the volume of the displaced volume. Therefore, a body immersed in a liquid is subjected to a buoyancy force equal to the weight of the liquid displaced by the volume of the body. The specific density is calculated using the equation:

$$\rho = \frac{W_{body,air} \times \rho_{liquid}}{W_{body,air} - W_{body,liquid}} \quad (56)$$

where  $W_{body,air}$  is the weight of the body in air,  $W_{body,liquid}$  is the weight of the body in the liquid and,  $\rho_{liquid}$  is the specific density of the liquid.

### 3.6.3. Results and discussion

This section addresses five primary points. The first point involves an analysis of the thickness and density of the parts. Generally, thickness and density can influence EM shielding and specific EM shielding, respectively. Therefore, evaluating these parameters is important for comparing the EM shielding performance with other materials and for quality and performance control of the injection moulding process [11], [108], [109].

The second section presents the characterization of EM shielding at 1 GHz for each material and under various experimental conditions. Additionally, an examination of the impact of thickness and density on the shielding effectiveness and completed this investigation by analysing the specific mechanisms of absorption and reflection.

The third section presents an analysis of direct current (DC) electrical conductivity in the injection-moulded compounds, emphasizing both longitudinal and transversal characteristics and the corresponding anisotropic longitudinal-to-transversal (L/T) ratio. Additionally, a brief theoretical estimation of the relationship between conductivity and shielding using the initial transfer matrix formalism, which describes the refraction of a homogeneous material with isotropic and constant conductivity.

The fourth section discusses the results obtained from the workflow used to characterize frequency-dependent conductivity via impedance measurements of an equivalent LCR circuit. Here, an analysis of the complex permittivity values and corresponding anisotropic conductivity is taken from equivalent impedance constitutive equations, incorporating the introduced anisotropic proportionality factor (L/T ratio from DC measurements).

The final topic of discussion introduces a new theoretical estimation for EM shielding of the fibre-filled compounds. This enhanced theoretical characterization utilizes frequency-dependent properties to describe the wave refraction induced by the anisotropic medium that characterizes these polymeric aggregates.

The results obtained are presented through various graphical figures. To simplify the analysis, the frequency-dependent properties discussed in this section are focused on the 1 GHz frequency. For more comprehensive details and additional data, the reader is encouraged to refer to supplementary tables provided in Appendix E. Supplementary results to chapter 3.6.

The thickness and density of the tested materials were measured for all specimens to verify the physical differences resulting from the injection moulding process. The measured values are presented in Figure 41 for thickness and Figure 42 for density.

In terms of specimen thickness, the obtained thicknesses were approximately the expected nominal value of 3 mm for conditions A and B, and 1.6 mm for conditions C and D. However, some thickness instabilities were observed in condition D, where the process was challenging to control.

It is expected that variations in specimen thickness will influence the fibre content and orientation in the internal structure of the specimens, resulting in different conductivity properties and corresponding electromagnetic shielding. Therefore, later in this analysis, the normalization of the EM shielding data to account for thickness effects will be addressed.

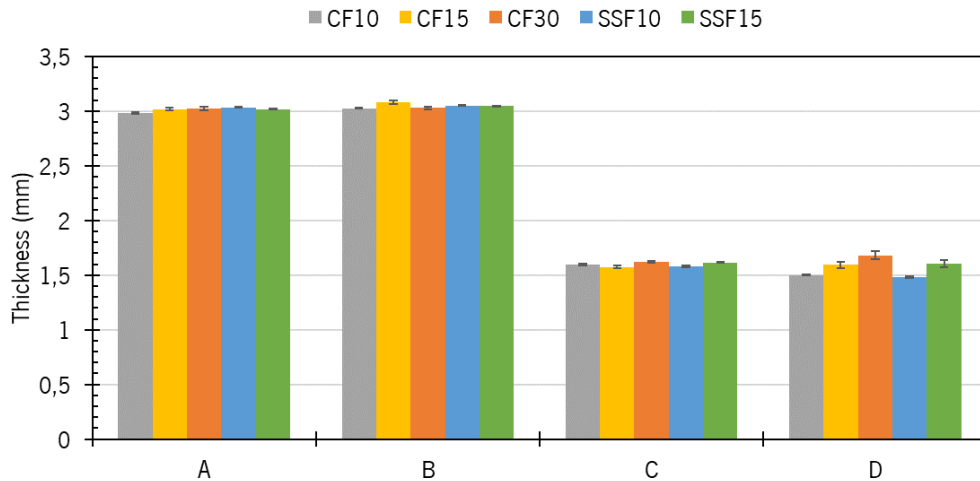


Figure 41. Average thickness measured in the material samples injected under each experimental condition (A, B, C and D). A and C used the sprue gate while B and D used the lateral edge gate.

The density of the developed materials (or produced parts) can be an important property to consider, especially if the lightweight nature of the part is a critical characteristic. As expected, the density of the produced specimens depends on the material and its fibre content, being directly proportional to the fibre's concentration in the specimen's structure. While there are slight variations in the measured densities, the average measured density values for each material were generally close to the values indicated in the material datasheets, as shown in Table 6. Later in this analysis, the normalization of the EM shielding data to account for density effects will be discussed.

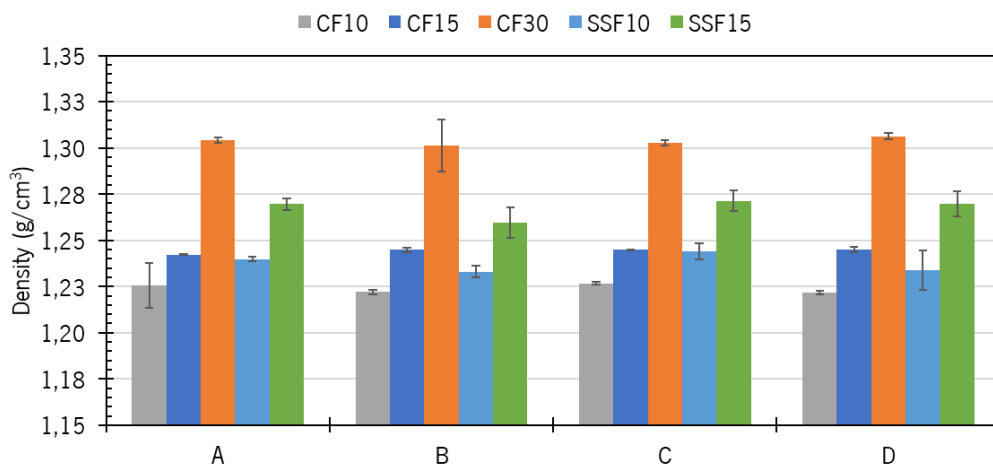


Figure 42. Density measured in the materials injected under each experimental condition (A, B, C and D). A and C used the sprue gate while B and D used the lateral edge gate.

### EM shielding: experimental analysis

The evaluation of EMSE shielding was taken in the frequency band of 30 MHz to 3 GHz encompassing an analysis of the impact of the specimen thickness and the injection moulding gate design (sprue gate at the centre and a lateral edge gate). To simplify the analysis, this discussion is focused on the 1 GHz results. The average EM shielding results for the five studied material is shown in Figure 43 for all the injection moulding conditions (A, B, C and D).

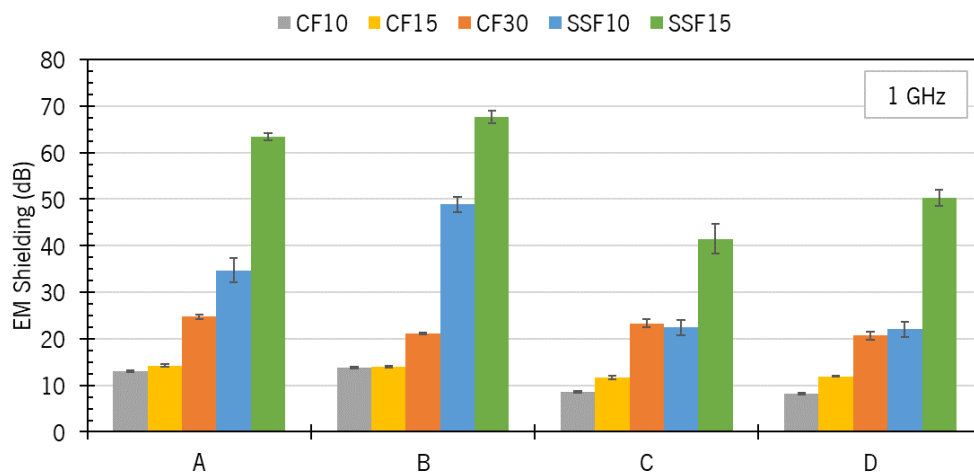


Figure 43. Average EMSE at 1 GHz for each fibre-filled compound (CF or SSF) injected under each experimental condition (A, B, C and D). A and C used the sprue gate while B and D used the lateral edge gate.

Analysing the results, it's evident that the electromagnetic shielding properties were influenced by the fibre content within the polymers and the experimental conditions. Depending on the processing conditions, the carbon-filled grades achieved electromagnetic shielding values in the range of 8 dB up to almost 25 dB, while the stainless-steel fibres (SSF) compounds achieved an improved electromagnetic shielding characteristic ranging from 22 dB in thinner samples to 67 dB in thicker samples.

Hence, it's evident that for the same fibre loading concentration (weight %), the isolated stainless-steel fibres induce much higher shielding compared to the isolated carbon fibres. The enhanced behaviour of the SSF varies depending on the injection moulding conditions, but on average, with a 10wt%, the SSF induces shielding almost three times higher than the CF, while with a 15wt%, this improvement is approximately 4.2 times higher. The increased fibre length, as shown in Figure 34, and a high magnetic permeability characteristic of SSF are the likely the reasons behind the improved shielding performance.

Regarding the thickness effect, as expected, there's a positive relationship with electromagnetic shielding. However, it was found that this positive effect is dependent on the percentage of fibre within the material and the gate design. The results suggest that fibre content is the predominant factor of the two variables. Generally, the electromagnetic shielding improvement with increased thickness is lower in materials with higher fibre content. In the case of SSF-filled materials, the average shielding in 3 mm thick samples is higher than 1.6 mm thick samples by nearly 80% and 40% for 10wt% and 15wt%, respectively. Similarly, in CF-filled materials, the average shielding in 3 mm thick samples is higher than 1.6 mm thick samples by nearly 60%, 20%, and only 4% for the loadings of 10wt%, 15wt%, and 30wt%, respectively. The increased fibre concentration in thinner samples likely leads to more electrical contacts within the anisotropic polymer aggregate, especially in thinner samples, resulting in an improved electrical network and higher conductivity, which mitigates the negative effect typically induced by a decrease in thickness.

The injection gate design also played a significant role in EM shielding with opposed results. On average, the shielding in the carbon-filled materials was up to 15% better in the samples produced by the sprue gate at the centre of the sample. In contrast, the specimens injected with SSF-filled materials using the sprue gate system showed lower shielding, almost 15% lower than the samples produced with the lateral gate. The choice of gate design can have a clear impact on the shielding properties and should be explored in the development phase of a product.

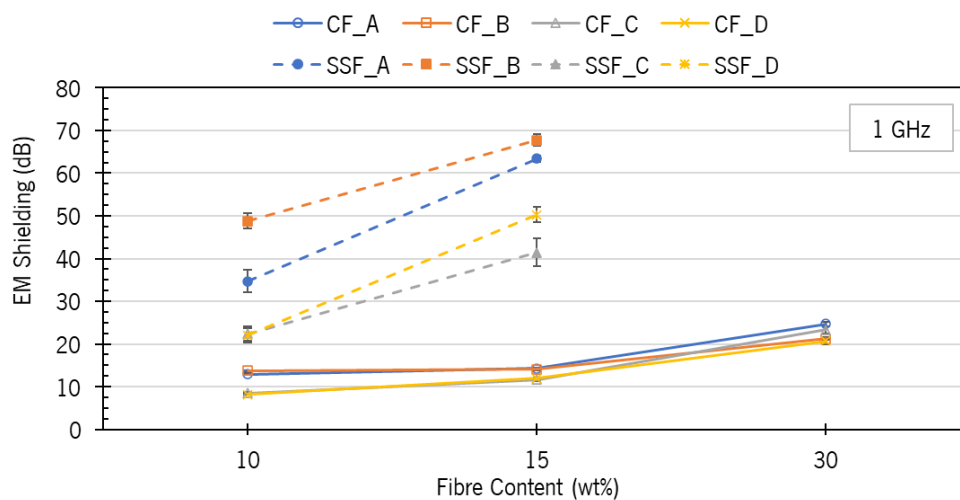


Figure 44. Effect of the CF or SSF fibre weight (wt) concentration on the EM shielding

Regarding the effect of the fibres content on the measured shielding, Figure 44, a positive effect with the increase of fibre percentage is evident. The observed variations differ in each experimental



condition, but the average results from all the specimens is considered, it's possible to see that the increase from 10% to 15% of SSF fibre loadings lead to an improvement of shielding of approx. 23 dB (80%). While for the CF-filled grades, the increase from 10% to 15% only improved the shielding in about 2 dB (23%) and the increase from 15% to 30% increased the EM shielding by approximately 9.5 dB (75%).

By assuming a linear projection model from the observed results from the carbon fibre compounds, with an  $R^2$  above 0.96, the observed results suggest that to achieve a 30 dB level of shielding with CF compounds, the CF weight percentage should be approximately above 40%. If the desired shielding level is set at 40 dB, then the CF percentage should be well above 50wt%. However, these estimates should be taken cautiously, as they are based on a linear projection from observed results and assume constant properties. As discussed, the electrical and EM shielding properties are not static and vary with the fibre concentration, thickness, and injection moulding conditions

The specific shielding, which reflects the shielding effectiveness per added volumetric weight of the material, is crucial for developing lightweight products. In this regard, the SSF-filled compounds outperform the CF-filled ones. Specimens filled with 15wt% of SSF achieve a specific shielding of approximately above 30 dB.cm<sup>3</sup>/g in thinner samples and above 50 dB.cm<sup>3</sup>/g in 3 mm thick samples. In contrast, the compounds with lower SSF content and the CF-filled compounds have a lower specific shielding, with the CF-filled compounds achieving less than 20 dB.cm<sup>3</sup>/g. This highlights the advantages of SSF-filled compounds for lightweight shielding applications.

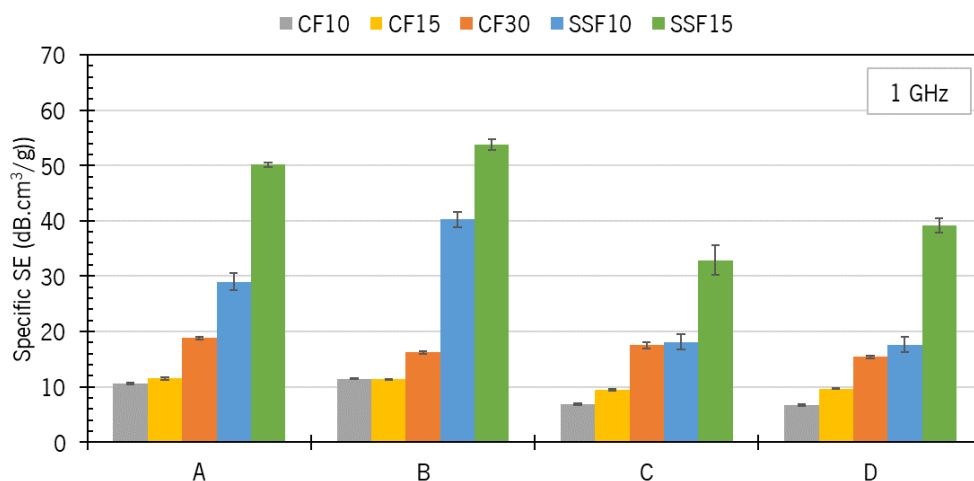


Figure 45. Average specific SE at 1 GHz for each fibre-filled compound (CF or SSF). Experimental conditions A and C used the sprue gate while B and D used the lateral edge gate.

The analysis for the absorption and reflection mechanisms of shielding was taken, with results shown in Figure 46 and Figure 47, respectively.

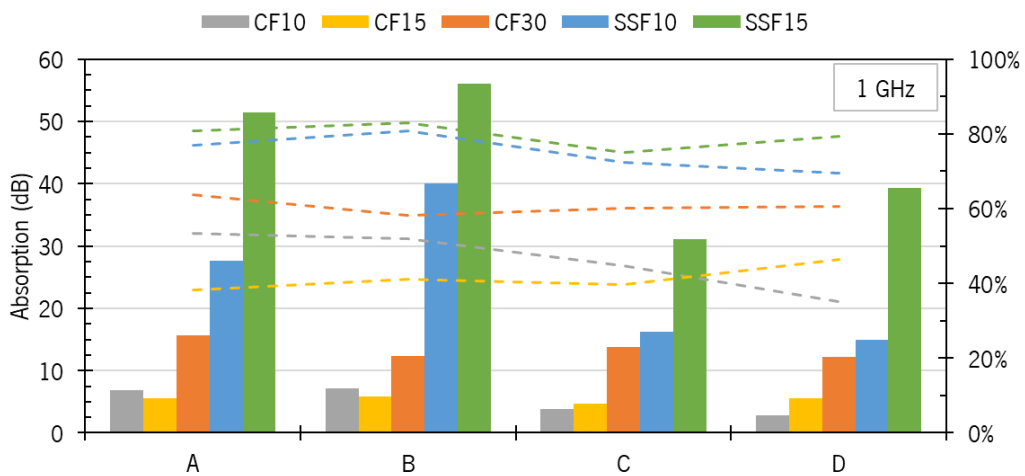


Figure 46. EM Shielding by absorption for the produced specimens. Values measured at 1 GHz.

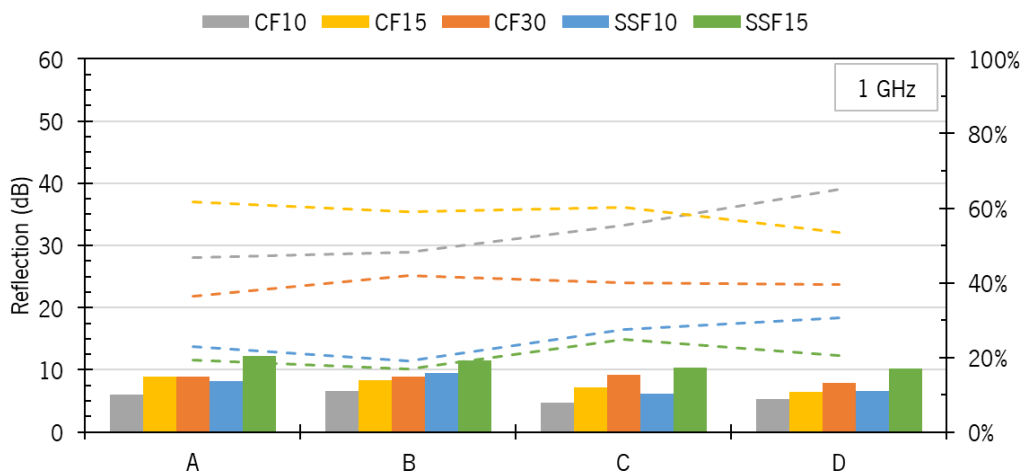


Figure 47. EM Shielding by reflection for the produced specimens. Values measured at 1 GHz.

An analysis of the results indicates that the absorption mechanism is the primary contributor to the EM shielding of SSF-filled materials. These materials consistently exhibited an absorption ratio of above 70% for all experimental conditions. In contrast, for CF-filled compounds, it is observed that the reflection mechanism is more predominant in the 10wt% and 15wt% grades, which have lower overall EM shielding. This is in contrast to the specimens produced with 30wt% CF, where the reflection mechanism plays a minor role, accounting for around 40% of the shielding.

Before jumping into an experimental characterization for the SSF and CF filled compounds anisotropic electrical conductivity, a theoretical assessment was taken to estimate the electrical to achieve the observed EM shielding properties discussed above.

In this section, theoretical values for the scattering of electromagnetic waves were calculated using the transfer matrix solution described earlier (chapter 3.3.5. Theoretical models). The model assumes that the material is nonmagnetic ( $\mu_r = 1$ ), homogeneous, with isotropic and constant electrical conductivity. To achieve the best fit to the experimental EM shielding measurements at 1 GHz, the characteristic impedance of the material slab, with the same thickness as the injection-moulded specimens, was and defined in the *Mathematica 10* solver by relative electrical permittivity ( $\epsilon_r$ ) of 2.9 and by iteratively adjust the electrical conductivity that provide the best fitting to the experimental shielding data.

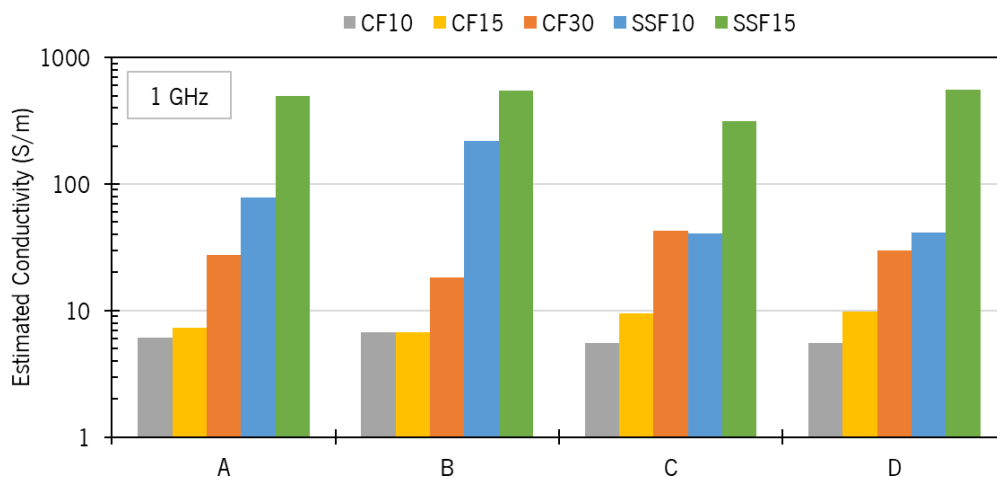


Figure 48. Electrical conductivity estimation to achieve the measured EM shielding. Transfer matrix theoretical model is based on a constant and isotropic conductivity.

Theoretical values for electrical conductivity are depicted in Figure 48. It can be observed that the expected conductivity falls within the range of 5.5 to 6.7 S/m for the 10wt% CF-filled compound, 6.7 to 9.8 S/m for the 15wt% CF-filled compound, and 18.1 to 42.7 S/m for the 30% CF-filled material. For the SSF-filled compounds, the theoretical conductivity is estimated to be between 40 and 220 S/m for the 10wt% specimens and between 315 and 560 S/m for the 15wt% specimens. However, estimations for the SSF-filled compounds should be approached cautiously due to the ferromagnetic characteristics not considered in the model.

Further examination of the estimations for the CF-filled materials indicates that the conductivity is expected to increase with an increase in CF wt%, according to a non-linear growth. Additionally, the results shown in Figure 49 reveal that theoretically higher conductivities are anticipated for thinner specimens, especially for compounds with a higher CF content. Increased fibre concentration is likely to lead to a more extensive electrical network within thinner specimens.

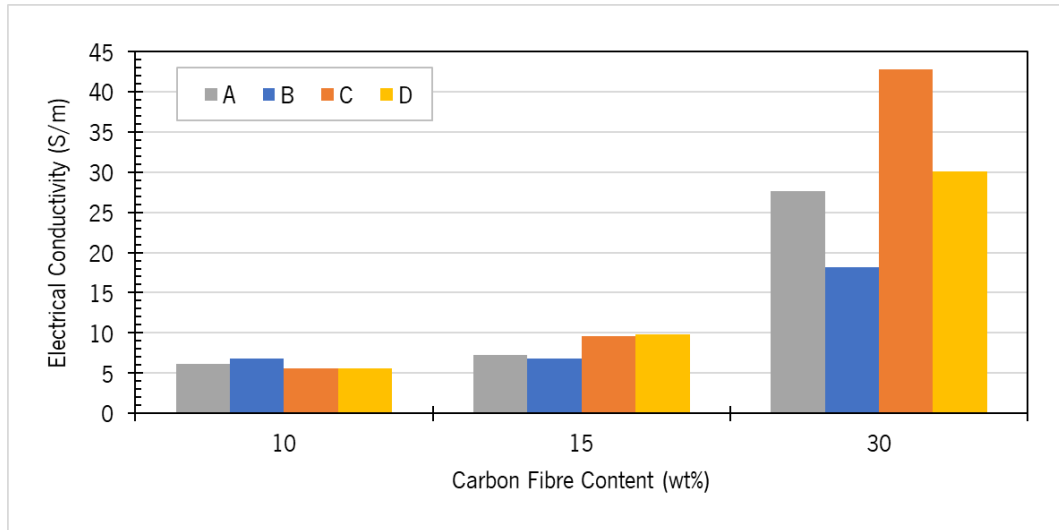


Figure 49. Theoretical estimation for effect of the CF concentration on the compound's electrical conductivity.

### Static electrical conductivity

In conjunction with the shielding measurements, a complementary evaluation of electrical conductivity (EC) was conducted. This assessment involved measuring the DC electrical resistance across both the longitudinal (in-plane) and transversal (through-thickness) directions of the specimens. The longitudinal conductivity was measured for both the parallel and perpendicular to the flow of the material inside the mould cavity. The average EC results for the five compounds are presented in Figure 50. These results are displayed for each injection moulding experimental condition.

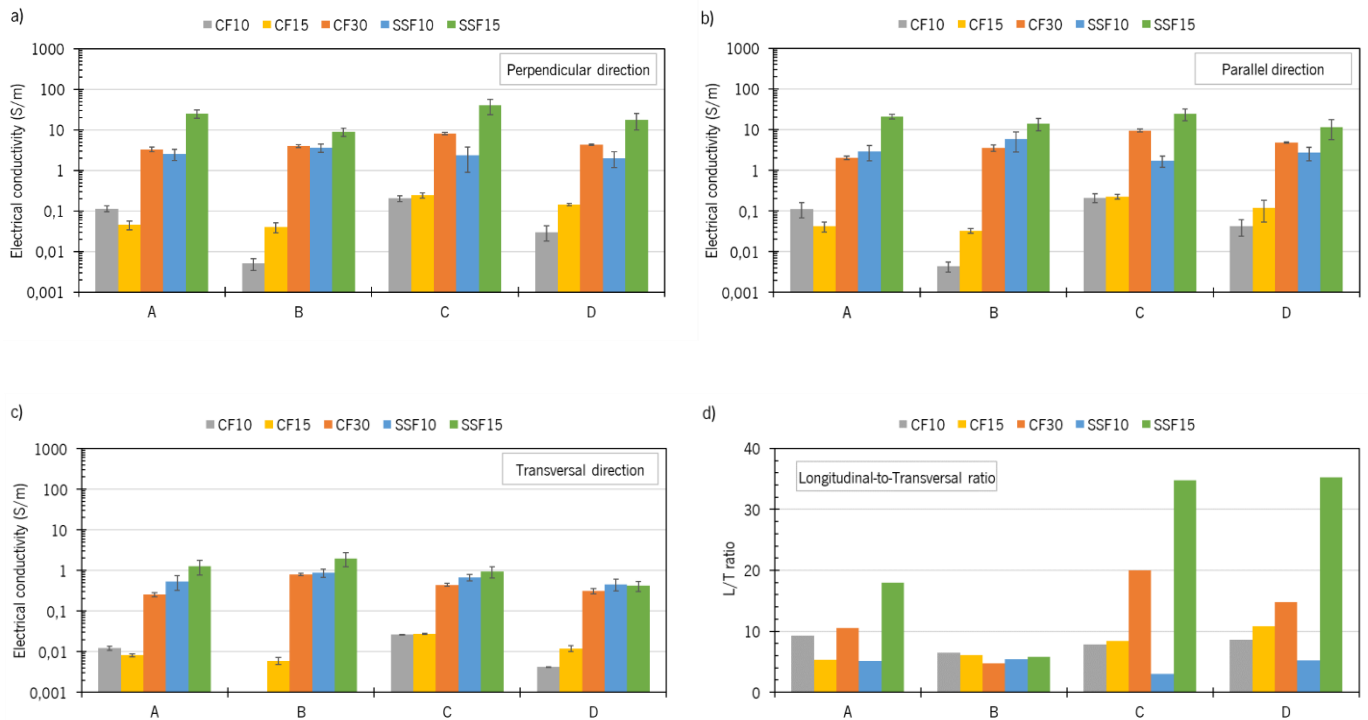


Figure 50. Measured conductivity in the perpendicular (a), parallel (b) and transversal (c) directions. Properties are shown for each material and experimental condition (A, B, C and D). d) shows relative the ratio between the longitudinal and transversal properties.

The observed results indicate the anisotropic behaviour of the CF and SSF-filled composites processed through injection moulding. This anisotropy is evident between the longitudinal and transversal directions, while the in-plane directions perpendicular and parallel to the flow exhibit similar conductivity. The anisotropic characteristic of these polymers can be defined by the proportionality ratio between the measured properties, as shown in Figure 50 d), This ratio will be important for future studies and understanding of the material's behaviour.

For longitudinal conductivities, considering the values shown in Appendix E, the general effects induced by the experimental conditions are as follows:

- Higher conductivities in specimens produced by the sprue gate at the centre (A and C) compared to specimens injected by the lateral edge gate. This effect can be attributed to the higher shear rates experienced by the material when passing through the edge gate. This increased shear rate likely causes more significant fibre breakage, resulting in shorter CF and SSF. Consequently, the reduced fibre length can have a direct impact on the overall electrical conductivity of the material.

- Higher conductivities in thinner specimens, especially for specimens with higher fibre content where a more packed electrical network is established.

Observing Figure 51, which displays the conductivity for CF-filled specimens, it's clear that conductivity increases with higher CF wt%, and this increase is better described by an exponential growth model.

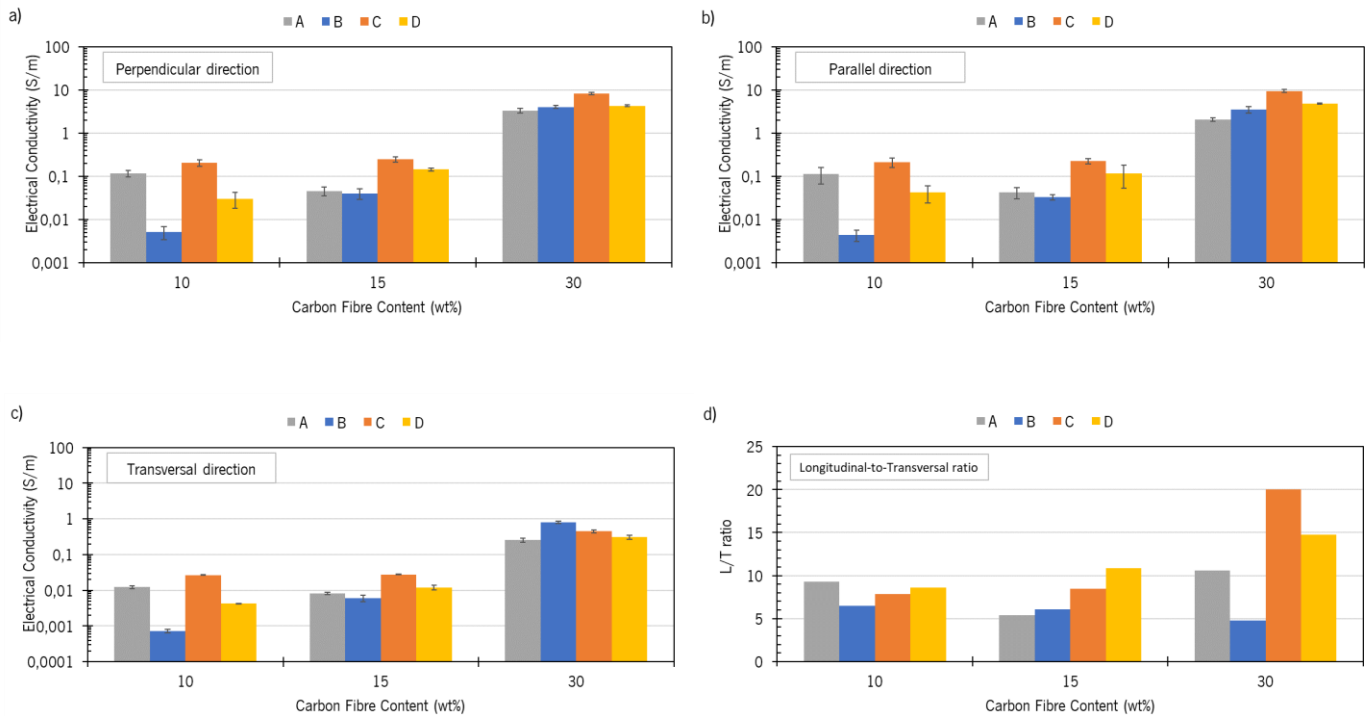


Figure 51. Effect of the CF percentages of the measured conductivity in the perpendicular (a), parallel (b) and transversal (c) directions. d) shows the longitudinal to transversal ratio.

The conductivity characterization provided valuable insights into the effect of injection moulding conditions. However, the measured values for the conductivity of these heterogeneous specimens may have been somewhat underestimated. According to the theoretical estimation, shown in Figure 48, the expected conductivity falls within specific ranges for the different materials, but in all cases the measured conductivity (longitudinal direction) is far inferior to the theoretical estimations and may not be a good representative for the EM scattering that occurs through the material. Therefore, further characterization of the complex dielectric function was undertaken to understand the frequency-dependent electrical conductivity, and this is discussed below.

### Frequency-dependent electrical conductivity

The EM shielding phenomenon is a frequency-dependent issue and, therefore, should be assessed using frequency-dependent properties rather than the static direct current (DC) measurements discussed earlier in this section and in previous studies. To gain a more comprehensive understanding of how these polymeric aggregates perform across different frequency ranges, this section delves into the matter.

For this purpose, samples from the carbon fibre (CF)-filled materials were extracted from the injection-moulded components and employed to characterise frequency-dependent conductivity using impedance analysis, extending up to 1 GHz. This method enables the investigation of complex permittivity ( $\epsilon'(\omega)$  and  $\epsilon''(\omega)$ ) and the associated frequency-dependent conductivity ( $\sigma(\omega)$ ). It employs an equivalent circuit diagram consisting of inductive (L), capacitive (C), and resistive (R) elements in series (L+C+R) to characterise the material when subjected to an electric field that passes through its thickness.

The procedure initiates with the measurement of electrical impedance and the corresponding phase of the signal for all specimens positioned between the dielectric material fixture. To simplify, this discussion will illustrate the adopted procedure for the 15wt% CF-filled specimens, but it applies to all specimens from the various materials analysed.

Figure 52 presents the electrical impedances measured for the 15wt% CF-filled material. This characterisation was employed to extract the LCR coefficients based on a series circuit diagram.

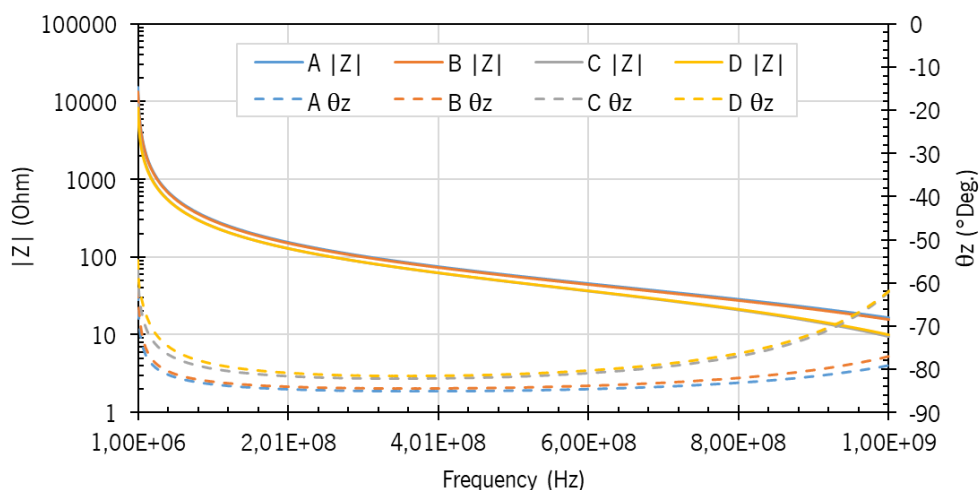


Figure 52. Linear impedance and respective phase angle for the 15wt% CF-filled specimens.

Afterwards, the equivalent impedance model can be calculated based on the obtained LCR parameters and the equations, obtaining an impedance of similar value to the measured by the equipment, as shown in Figure 53.

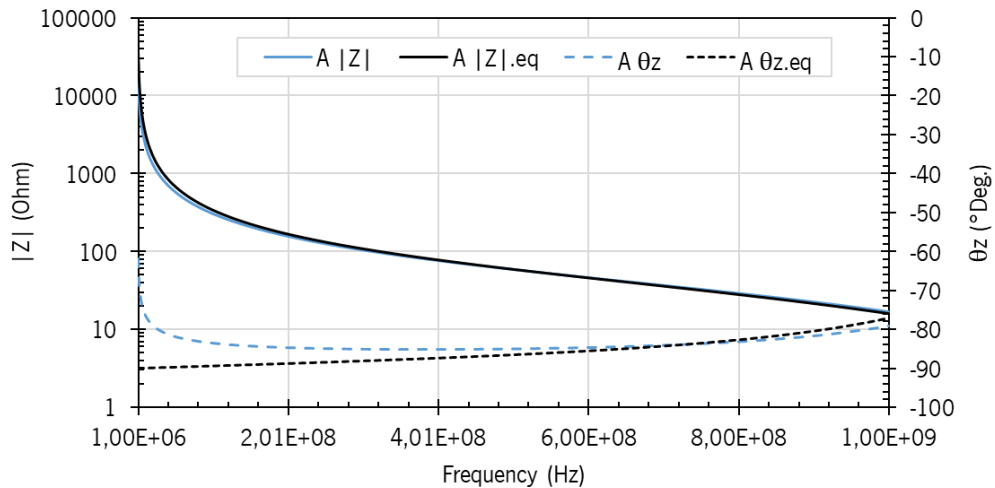


Figure 53. Equivalent impedance fitted to the initial linear impedance provided by the apparatus.

With an appropriate mathematical conversion, the equivalent impedance was used to analyse the electrical properties of the dielectric material which are characterized by its complex permittivity. The real part of permittivity ( $\epsilon'$ ), also called dielectric constant, represents the material's ability to store energy when an external electric field is applied. The imaginary part of permittivity ( $\epsilon''$ ) represents the loss dissipated in the material. An example of the obtained values for the complex permittivity can be seen in Figure 54.

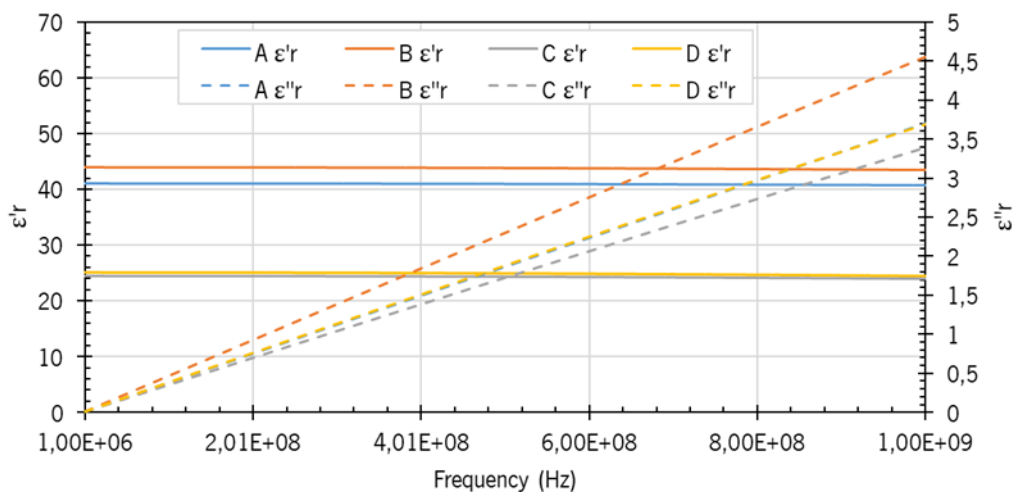


Figure 54. Complex permittivity for the 15% CF-filled material produced by each experimental condition.



The characterization of complex permittivity represents the frequency-dependent lossy properties in the transverse direction of the sample, which corresponds to through thickness. In other words, the frequency-dependent electrical conductivity obtained from the permittivity values also represents the conductivity along the through-thickness direction. This transversal conductivity ( $\sigma'Z$ ) can be calculated using the Equation 46. After the transversal conductivity characterization, the frequency-dependent longitudinal conductivity ( $\sigma'XY$ ) is determined by multiplying it with a longitudinal-to-transversal (L/T) ratio of proportionality like those obtained from the DC measurements.

Figure 55 displays both the transversal and longitudinal electrical conductivities characterized for the 15wt% CF-filled materials using the described equivalent impedance method. In contrast to static conductivity, this analysis revealed an increase in conductivity with frequency. This phenomenon may explain why the measured EM shielding is higher than the expected shielding based on the measured DC electrical conductivities.

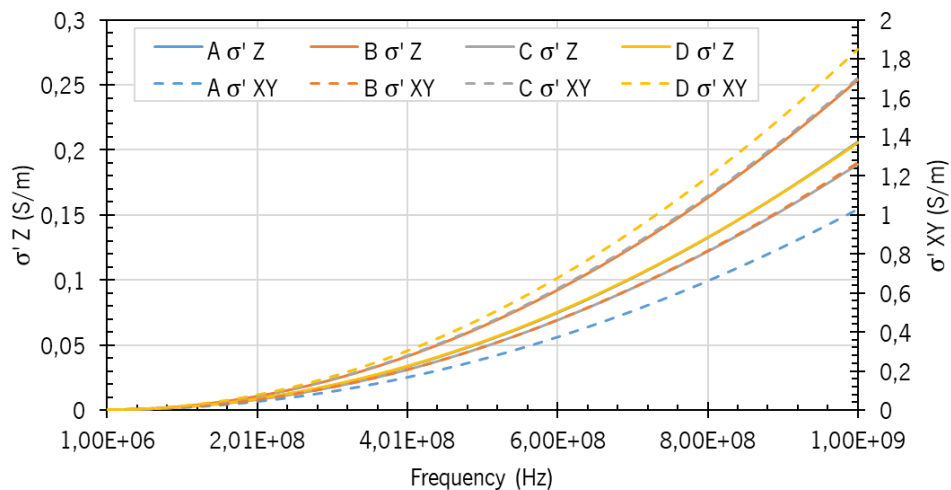


Figure 55. Real values for the frequency-dependent conductivity characterized for the 15wt% CF-filled material in both transversal ( $\sigma'Z$ ) and longitudinal ( $\sigma'XY$ ) directions.

**EM shielding: theoretical analysis**

Now that the frequency-dependent and anisotropic electrical conductivity has been characterized, a new theoretical model was applied to estimate the EM shielding of the fibre-filled materials. This theoretical model describes the refraction of EM waves using transmission, reflection, and absorption factors, which were derived from an adaptation of the transfer matrix formalism discussed in chapter 3.3.6.

The constitutive equations describing the material's refractive indices were written in *Mathematica 10.2* software, as shown in Appendix C. These equations define a dissipative, nonmagnetic material ( $\mu_r = 1$ ) with a relative permittivity ( $\epsilon_r$ ) of 2.9 and with anisotropic and frequency-dependent conductivity. The conductivity equation was adjusted to define the dissipative properties of the medium according to the equivalent LCR inputs and the conductivity L/T ratio.

The theoretical estimations for EM shielding of the CF-filled materials are depicted in Figure 56.

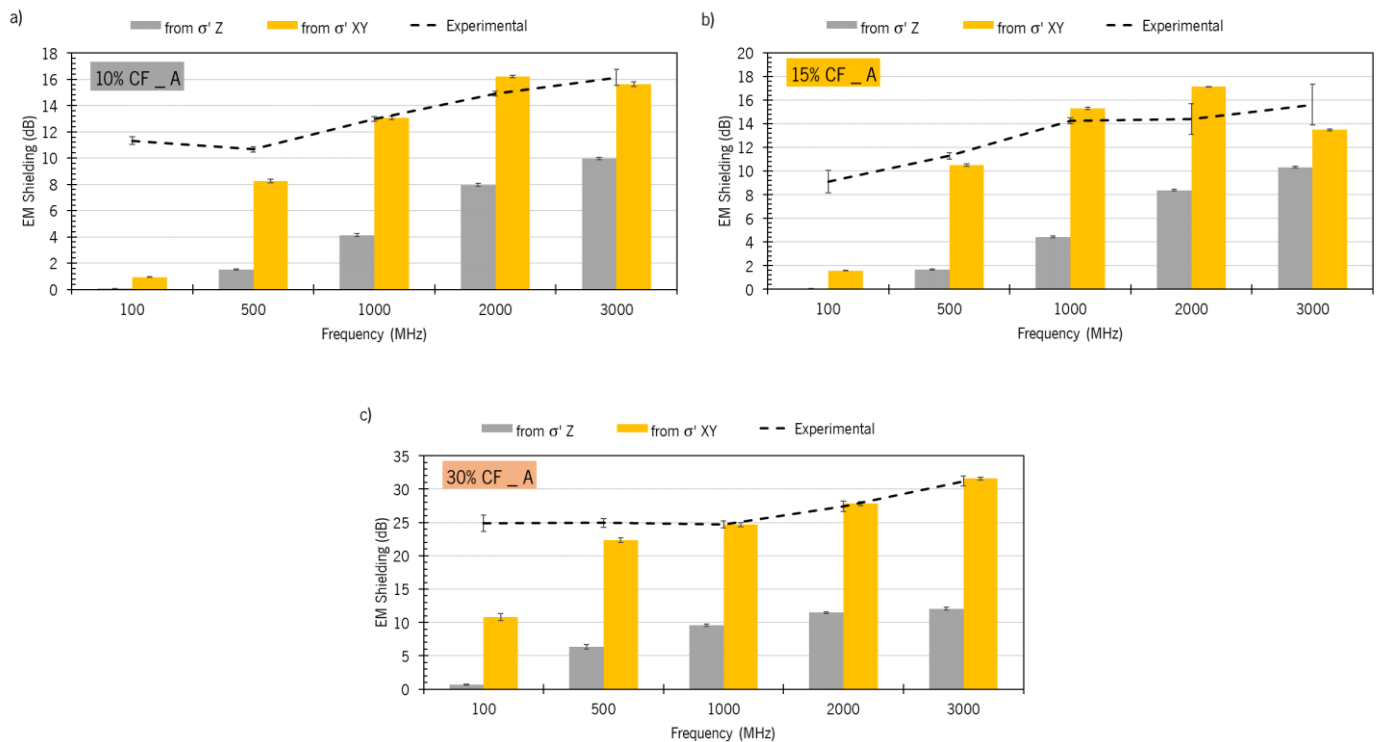


Figure 56. EM shielding theoretical estimations according to the LCR model. Results correspond to the experimental condition A, for 10% CF (a), 15% CF (b) and 30% CF (c).

Observing the theoretical estimations for EM shielding effectiveness in CF-filled materials, a good fit is achieved when the L/T conversion ratio from the DC measurements is applied to transform the through-thickness frequency-dependent conductivity into longitudinal conductivity. Therefore, the proposed experimental method, using impedance analysis in conjunction with static conductivity measurements, appears to be a suitable procedure for characterizing these fibre-filled polymers. It provides sufficient data that can be incorporated into improved numerical tools capable of estimating EM wave refraction for materials or products requiring EM shielding properties.

### **3.6.4. Concluding remarks**

This third study complete the proposed activity plan for the analysis of the EM shielding behaviour and the corresponding electrical conductivity of fibre-filled polymeric composites processed through the injection moulding method. This research had three main objectives: study the EM shielding and electrical conductivity variations induced by the polymeric composites and the injection moulding process; establish a correlation between the EM shielding and the electrical conductivity with anisotropic characteristics; and to develop a theoretical model suitable to characterize the shielding effectiveness of this heterogeneous and anisotropic materials.

Here, three CF-filled polycarbonates with different amounts of CF loadings (10%, 15% and 30%) and two additional grades composed of 10% and 15% of SSF were processed by injection moulding comprising two type of gate systems (direct sprue gate at the centre and lateral edge gate) to produce flat disk samples with distinct thickness of 3 and 1.6mm. Afterwards, an extended characterization for the EM shielding and electrical conductivity was achieved to assess these properties variations induced by material composition and by the injection process conditions.

In general, the observed results for EM shielding and electrical conductivity had similar behaviour induced by the materials nature and by the injection moulding conditions. This is true since shieling is directly proportional to conductivity, being the longitudinal conductivity the most relevant and with better correlation. Summarizing, the following results were observed:

- Effect of fibre nature: Specimens filled with SSF consistently outperformed CF-filled compounds, achieving substantially higher shielding characteristics. With a 10wt% loading, SSF induced shielding almost three times higher than CF, and this improvement increased to approximately 4.2 times with a 15wt% loading. This superior performance can be attributed to the increased fibre length and the high magnetic permeability of SSF.
- Effect of fibre content: Increasing fibre percentage had a positive effect on shielding, with SSF showing a more substantial improvement (approximately 23 dB or 80%) when moving from 10% to 15% fibre loadings. In contrast, CF-filled grades showed a smaller improvement when transitioning from 10% to 15%, with an approximately 2 dB (23%) increase. The jump from 15% to 30% led to a more substantial 9.5 dB (75%) improvement in electromagnetic shielding. With regard to the electrical conductivity in CF-filled specimens, an evident

conductivity increases with the increase of CF wt%, being that described by an exponential growth model.

- Effect of thickness: There is a positive correlation between material thickness and electromagnetic shielding, but this effect is dependent on the fibre content and gate design. Higher fibre content contributed more to shielding improvement. For SSF-filled materials, 3 mm thick samples exhibited nearly 80% higher shielding than 1.6 mm thick samples for 10wt%, and 40% higher for 15wt%. For CF-filled materials, the improvement with thickness was less pronounced, particularly with higher fibre content. The latter effect may be justified by the higher conductivity which observed in thinner specimens, especially those with higher amount of fibre where a more packed electrical network is established.
- Gate Design Impact: The choice of injection gate design significantly influenced electromagnetic shielding. On average, carbon-filled materials performed up to 15% better when produced with a sprue gate at the centre. In contrast, SSF-filled materials showed lower shielding, approximately 15% less when using the sprue gate system. The gate design is a crucial factor to consider in the development of products with electromagnetic shielding requirements.

Additionally, this analysis identified that absorption was the primary mechanism contributing to the electromagnetic shielding of SSF-filled materials, with absorption ratios consistently above 70%. In CF-filled compounds, especially those with 10wt% and 15wt%, the reflection mechanism played a more predominant role, resulting in lower overall electromagnetic shielding. However, in specimens with 30wt% CF, the absorption mechanism has a major role of approximately 60% of the shielding.

The conductivity characterization provided valuable insights into the effect of injection moulding conditions. However, the measured values for the conductivity of these heterogeneous specimens may have been somewhat underestimated, far inferior to the theoretical estimations and may not be a good representative for the EM scattering that occurs through the material. Since the EM shielding phenomenon is a frequency-dependent issue the correlated electrical conductivity should be assessed using frequency-dependent properties rather than the static direct current (DC) measurements. Therefore, the materials filled with CF were used to characterise the frequency-dependent conductivity using impedance analysis by employing an equivalent circuit diagram LCR in series to characterise the material through-thickness dielectric properties. Afterwards, the obtained frequency-dependent properties were inputted into a new the theoretical model based on the transfer matrix formalism in order to estimate the

EM shielding of the studied CF-filled materials. Results showed a good theoretical fit to the experimental shielding values when a longitudinal-to-transversal (L/T) ratio from the DC measurements is applied to transform the through-thickness frequency-dependent conductivity into longitudinal conductivity. Therefore, the proposed method, using impedance analysis in conjunction with static conductivity measurements, appears to be a suitable procedure for characterizing these fibre-filled polymers.

## **4. NEW DEVELOPMENTS OF ADVANCED MATERIALS**

## **4.1 Introduction**

In recent times, there have been significant discoveries and advancements in processing technologies, particularly in the development of innovative and advanced materials, including thermoplastic composites. These materials offer numerous advantages, such as the ability to custom-tune or enhance their electrical properties, leading to improved shielding performance.

One noteworthy technology in this domain is Additive Manufacturing (AM), which has seen substantial improvements and is gaining increasing interest. AM is emerging as a competitive manufacturing process capable of fabricating more efficient, intricate, and functional geometries with reduced time and material consumption. The potential to combine this technology with new materials opens the door to developing efficient products for EM shielding, offering a compelling alternative to traditional materials and manufacturing methods.

Another recent technological breakthrough is in the field of nanomaterials and nanocomposites. Graphene and its derivatives have generated growing interest in both the scientific and business communities. Their exceptional mechanical, optical, thermal, and electrical properties make these materials highly versatile and applicable in various industrial sectors, including advanced composites, electronics, and energy storage.

Recognizing these technological advancements and the market's demands, this research aimed to provide an experimental context for the potential application of AM technology and graphene in the realm of EM shielding for electronic enclosures and electrical cables. This research comprised two distinct studies:

- An innovative additive manufacturing technology was employed to investigate the EM properties of thermoplastic composites printed under varying conditions. This study was conducted in collaboration with *DONE Lab*, an advanced additive manufacturing laboratory specializing in prototypes and tools. The goal was to explore the potential of new AM technologies for developing EM shielding solutions.
- The second study involved a research partnership with *Graphenest, S.A.*, an industrial firm dedicated to designing and developing innovative technology for producing graphene and graphene derivatives. In this context, the study aimed to demonstrate the applicability of graphene in polymers with electromagnetic shielding characteristics.

## **4.2 Additive manufacturing<sup>4</sup>**

The objective of this research in the field of additive manufacturing (AM) was to address the following research question:

- "Can the additive manufacturing of continuous carbon fibre be an effective fabrication technology for developing products capable of blocking electromagnetic waves?"

This study was conducted in collaboration with *DONE Lab*, an advanced additive manufacturing laboratory in the School of Engineering at the University of Minho, Guimarães. The goal was to explore the potential of AM technologies as an efficient method for producing lightweight EM shielding enclosures with a high degree of design flexibility, fewer components, and reduced time to market.

As a result, this research focused on utilizing material extrusion technology to 3D print 2 mm thick specimens with a layer-by-layer process. These specimens were composed of a multi-material, combining micro-carbon fibre (CF) filled Nylon with layers reinforced by continuous carbon fibres (CCF) stacked with a 90° rotation to each other. This innovative and customizable approach aimed to produce enclosures requiring electromagnetic shielding properties, which had not been previously explored in similar studies.

### **4.2.1. Literature review**

Thermoplastic composites have been explored more intensively by conventional fabrication techniques, such as, compression moulding or injection moulding [46], [66], [70], [82], [108], [110]–[112]. However, recently, additive manufacturing (AM) technologies improved and are becoming more adopted to manufacture final products. AM is a competitive digital manufacturing process that allows to fabricate complex and functional geometries, due to the inherent design freedom that the layer-by-layer process enables. In combination with design exploration methods, such as, generative design and topology optimization, AM can overcome the traditional manufacturing limits and achieve a more efficient product performance while improving manufacturability, by reducing lead time, cost and material consuming [113], [114]. AM processes are commonly divided according to seven categories, namely: (i) binder jetting; (ii) direct energy deposition; (iii) material extrusion; (iv) VAT polymerization; (v) material

---

<sup>4</sup> This subchapter resulted on the following paper: Martins, L.C.; Silva, C.S.; Fernandes, L.C.; Sampaio, Á.M.; Pontes, A.J. Evaluating the Electromagnetic Shielding of Continuous Carbon Fiber Parts Produced by Additive Manufacturing. *Polymers* 2023, 15, 4649. <https://doi.org/10.3390/polym15244649>



jetting; (vi) sheet lamination; and (vii) laminated object manufacturing (LOM) [115]. Focusing on the material extrusion (ME) technology, it consists of a bottom-up process based on the extrusion of material in the filament form onto a build platform in a layer-by-layer process, where the filament is deposited on top of the subsequent deposited layer until the part to be produced is complete. At the end of the deposition, the filament solidifies [116]. The main benefits of the ME process include the ease and relative speed to produce functional products at a competitive cost, and also the large range of materials commercially available and the possibility to develop a customizable material adjusted to the product requirements [116], [117]. Regarding the part quality and mechanical properties, these are dependent on process parameters, such as, build orientation, layer thickness, layer adhesion, type of infill, air gap, raster angle and raster width [116], [118].

AM, specifically the ME technology, has been used in the development of plastic composite parts with electrical conductivity properties and EM shielding characteristics. Most of the studies report the optimization of the printing process and the manipulation of filament properties by adding conductive fillers, in order to improve the required property, either mechanical, electrical, thermal or electromagnetic [105], [106], [108], [119]–[124]. For example, the addition of CNT as a conductive nano-filler to the polymer filament, or a hybrid combination with one additional filler, such as CB, was developed to improve the electrical conductivity and/or electromagnetic shielding properties of the products printed by ME. Dorigato et al. [120] developed a multi walled carbon nanotubes (MWCNT) filled acrylonitrile-butadiene-styrene (ABS) compound showing that the MWCNT improved the tensile, electrical and thermal properties. Furthermore, they also report that these properties are also dependent on the printing orientation. Chizari et al. [108] used the ME process to produce conductive microstructures for the functional optimization of lightweight and semi-transparent EMI shields. They formulated a highly conductive carbon nanotubes/poly(lactic acid) (CNT/PLA) printable ink to fabricate 3D scaffolds with significant improvement to the specific EMSE relatively to CNT/PLA hot-pressed in solid forms ( $\sim 70$  vs  $\sim 37$  dB.cm<sup>3</sup>/g). Schmitz et al. [105], [121] fabricated samples via ME with an ABS filled with CNT, CB or a hybrid combination (CNT/CB). They reported that the electrical conductivity, EMSE and mechanical properties of printed parts were considerably dependent on the printing orientation. The EM shielding and respective electrical conductivity were more efficiently improved with the increase of CNT rather than increasing the CB amount. Furthermore, the EMSE increased with the increase layer thickness and showed an anisotropic behaviour when printed in the perpendicular orientation. Wang et al. [125] produced 3D-printing scaffold structures with carbon nanotube/poly(lactic acid) composite. The highly conductive CNTs coated on the 3D-printed PLA scaffolds increased the interconnected networks after

compression moulding which translated to an enhanced EMI shielding performance as high as 67 dB, while also improving the mechanical robustness of 3D-CNT/PLA. The use of AM methods with graphene-based polymer composites has been indicated as very promising for the enhancement of material properties to enable novel applications in fields like biomedicine, energy, sensing, and electromagnetic interference shielding [123].

Additive manufacturing can also be used to develop advanced materials as described by Fan et al. [19] and by Lee et al. [106]. By designing complex structures and arranging the distribution of materials with different physical parameters AM technology provides a direct and efficient way to develop metamaterials with electromagnetic absorption properties [19]. Under the ME printing process of a Graphene-polyamide-6 composite filament it was demonstrated that the introduction internal geometric assemblies significantly improved EMSE [106]. Moreover, the ME technology was used by Duan et al. [126] to fabricate gradient composite metastructures to effectively absorb microwave signals demonstrating that the designed metastructure with the thickness of 10 mm can achieve the 10 dB absorbing bandwidth in the frequency range from 5 to 40 GHz.

Recent advances allowed the development of products by a multi-material AM fabrication process of continuous fibre reinforced polymer composites with increased performance relatively to conventional short fibre filled filaments. Parmiggiani et al. [127] studied the mechanical resistance of components made with continuous carbon fibre (CCF) thermoplastic materials fabricated by ME focusing on the influence of the fibre orientation ( $0^\circ$ ,  $45^\circ$ , and  $90^\circ$ ) on the tensile and flexural properties of the produced parts [127]. Blok et al. [128] also used the ME technology from Markforged, Inc to study the print capability of CCF for further understanding the advantages and limitations of this printing process, in comparison to the printing of chopped short-CF filled polyamide filament. The tensile strength and stiffness of the CCF printed parts were more than an order of magnitude higher than the short fibre reinforced polyamide printed parts.

Current technology advances in AM highlight the fabrication of low cost, and high-efficient complex structures with electromagnetic shielding characteristics. However, at the time of writing, the authors are not aware of the existence of peer studies that encompasses the use of ME technology to print CCF reinforced materials to develop a functional enclosure for EMI shield. Hence the relevance of sharing the findings of this study with the scientific and engineering community. This study reports an evaluation of

the electromagnetic shielding performance obtained by specimens manufactured by continuous fibre reinforcement considering process parameters variation and specimen thickness.

### 4.2.2. Materials and methods

#### Materials

The materials used to produce the specimens were supplied by *Markforged, Inc.* The polymeric filament consisted of a chopped micro-CF reinforced Nylon composite, with trade name *Onyx™*. Main properties, provided by the manufacturer, include a tensile modulus of 2.4 GPa, a tensile train and break of 25 %, a flexural strength of 71 MPa, a flexural modulus of 3 GPa, a heat deflection temperature of 145 °C and, a density of 1.2 g/cm<sup>3</sup>. Regarding the reinforcement material, a continuous CF filament was selected that presents a tensile modulus of 60 GPa, a tensile train and break of 1.5 %, a flexural strength of 540 MPa, a flexural modulus of 51 GPa, a heat deflection temperature of 105 °C and, a density of 1.4 g/cm<sup>3</sup> [129].

#### Production

The Material Extrusion (ME) technology was used to produce two types of specimens, as shown in Figure 1 (a). The load specimen consists of a flat solid disk with six peripheral holes for fixation on the apparatus and is used for EMSE evaluation while, the reference specimen has a toroid shape section removed near the centre of the specimen and is used to create a baseline for the EMSE analysis. Both flat disk specimens are built of the same material and have the same diameter of 60 mm and thick-ness of 2 mm, which is a common thickness for plastic parts. The specimens were produced resorting to the continuous fibre reinforcement (CFR) process from *Markforged* with the equipment *Mark Two™*. Both specimens were built with the positioning shown in Figure 57 (b).

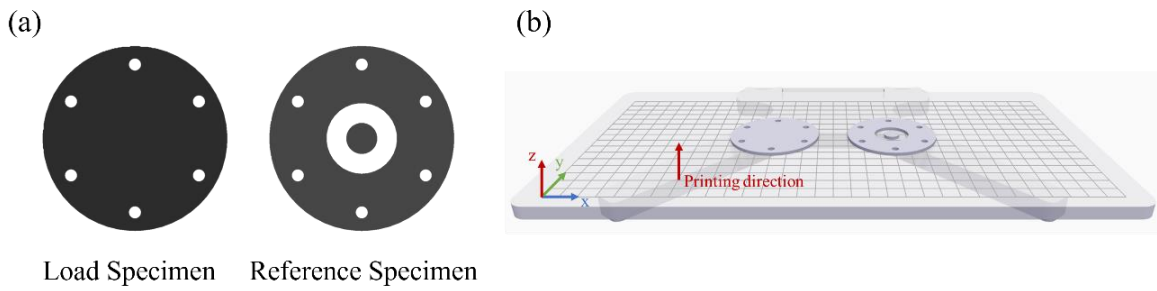


Figure 57. (a) CAD representation of the printed load and reference specimens; and (b) build platform depicting with specimens positioning for manufacturing, image from software Eiger™ 3D Printing Software from *Markforged*.

The printing process considered a layer height of 0.125 mm, a solid fill pattern (fill density of 100%) and two Onyx (0) peripheral wall layers (0.8 mm). The 2 mm thick specimens were printed in a unidirectional pattern at each individual layer with an alignment angle of  $-45^\circ$  or  $45^\circ$ , as shown in Figure 58, which were alternated between layers up to a total number of 16 layers. Such customization was carried according to the specifications permitted by the Markforged cloud software, *Eiger™*.

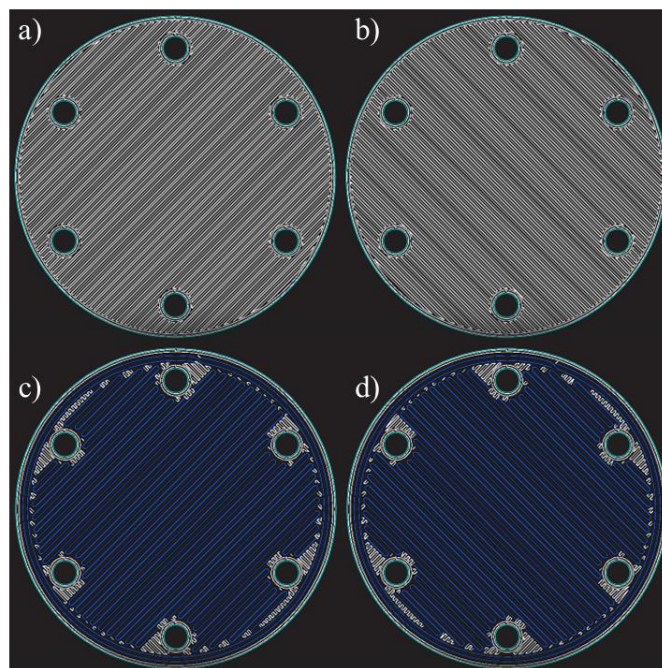


Figure 58. Printing patterns, established by the *Eiger™* 3D Printing Software, for *Onyx™* (white) and carbon fibre (blue): *Onyx™* with (a)  $-45^\circ$  pattern; (b)  $45^\circ$  pattern; and CF with (c)  $-45^\circ$  pattern; and (d)  $45^\circ$  pattern.


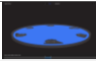
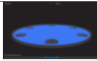
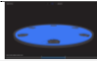
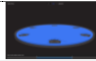
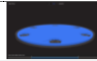
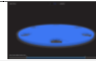
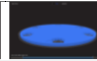
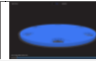
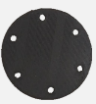








In this research, a total of 9 type of specimens were printed. One specimen was printed totally with *Onyx™*, while the remaining specimens were reinforced with continuous carbon fibres in some of the sliced layers of the sample. Since the *Eiger™* 3D Printing Software locks the first (layer 1) and last layer (layer 16) to be printed with *Onyx™*, the others 14 layers were used for CF insertion. As previously stated, the CF and *Onyx™* were printed in a unidirectional pattern with an alignment angle of  $-45^\circ$  or  $45^\circ$ , which was alternated in each layer. This process was used to produce composite samples with just 1 CF layer up to 14 layers, as shown in Table 9 and Table 10.

Table 9. Design layout for the produced specimens. O is *Onyx™* and CF is carbon fibre.

Layers	Designation of specimens (O - <i>Onyx™</i> ; CF is carbon fiber)									
	0 CF	1 CF	2 CF	4 CF	6 CF	8 CF	10 CF	12 CF	14CF	
<b>16</b>	O $45^\circ$	O $45^\circ$	O $45^\circ$	O $45^\circ$	O $45^\circ$	O $45^\circ$	O $45^\circ$	O $45^\circ$	O $45^\circ$	O $45^\circ$
<b>15</b>	O $-45^\circ$	O $-45^\circ$	O $-45^\circ$	O $-45^\circ$	O $-45^\circ$	O $-45^\circ$	O $-45^\circ$	O $-45^\circ$	O $-45^\circ$	CF $-45^\circ$
<b>14</b>	O $45^\circ$	O $45^\circ$	O $45^\circ$	O $45^\circ$	O $45^\circ$	O $45^\circ$	O $45^\circ$	O $45^\circ$	CF $45^\circ$	CF $45^\circ$
<b>13</b>	O $-45^\circ$	O $-45^\circ$	O $-45^\circ$	O $-45^\circ$	O $-45^\circ$	O $-45^\circ$	CF $-45^\circ$	CF $-45^\circ$	CF $-45^\circ$	CF $-45^\circ$
<b>12</b>	O $45^\circ$	O $45^\circ$	O $45^\circ$	O $45^\circ$	O $45^\circ$	CF $45^\circ$	CF $45^\circ$	CF $45^\circ$	CF $45^\circ$	CF $45^\circ$
<b>11</b>	O $-45^\circ$	O $-45^\circ$	O $-45^\circ$	O $-45^\circ$	CF $-45^\circ$	CF $-45^\circ$	CF $-45^\circ$	CF $-45^\circ$	CF $-45^\circ$	CF $-45^\circ$
<b>10</b>	O $45^\circ$	O $45^\circ$	O $45^\circ$	CF $45^\circ$	CF $45^\circ$	CF $45^\circ$	CF $45^\circ$	CF $45^\circ$	CF $45^\circ$	CF $45^\circ$
<b>9</b>	O $-45^\circ$	CF $-45^\circ$	CF $-45^\circ$	CF $-45^\circ$	CF $-45^\circ$	CF $-45^\circ$	CF $-45^\circ$	CF $-45^\circ$	CF $-45^\circ$	CF $-45^\circ$
<b>8</b>	O $45^\circ$	O $45^\circ$	CF $45^\circ$	CF $45^\circ$	CF $45^\circ$	CF $45^\circ$	CF $45^\circ$	CF $45^\circ$	CF $45^\circ$	CF $45^\circ$
<b>7</b>	O $-45^\circ$	O $-45^\circ$	O $-45^\circ$	CF $-45^\circ$	CF $-45^\circ$	CF $-45^\circ$	CF $-45^\circ$	CF $-45^\circ$	CF $-45^\circ$	CF $-45^\circ$
<b>6</b>	O $45^\circ$	O $45^\circ$	O $45^\circ$	O $45^\circ$	CF $45^\circ$	CF $45^\circ$	CF $45^\circ$	CF $45^\circ$	CF $45^\circ$	CF $45^\circ$
<b>5</b>	O $-45^\circ$	O $-45^\circ$	O $-45^\circ$	O $-45^\circ$	O $-45^\circ$	CF $-45^\circ$	CF $-45^\circ$	CF $-45^\circ$	CF $-45^\circ$	CF $-45^\circ$
<b>4</b>	O $45^\circ$	O $45^\circ$	O $45^\circ$	O $45^\circ$	O $45^\circ$	O $45^\circ$	CF $45^\circ$	CF $45^\circ$	CF $45^\circ$	CF $45^\circ$
<b>3</b>	O $-45^\circ$	O $-45^\circ$	O $-45^\circ$	O $-45^\circ$	O $-45^\circ$	O $-45^\circ$	O $-45^\circ$	CF $-45^\circ$	CF $-45^\circ$	CF $-45^\circ$
<b>2</b>	O $45^\circ$	O $45^\circ$	O $45^\circ$	O $45^\circ$	O $45^\circ$	O $45^\circ$	O $45^\circ$	O $45^\circ$	O $45^\circ$	CF $45^\circ$
<b>1</b>	O $-45^\circ$	O $-45^\circ$	O $-45^\circ$	O $-45^\circ$	O $-45^\circ$	O $-45^\circ$	O $-45^\circ$	O $-45^\circ$	O $-45^\circ$	O $-45^\circ$

Some theoretical characteristics for the load specimens printing design were provided by *Markforged Eiger™ 3D Printing Software* and are exhibited in Table 10. In this table it is possible to verify, in the first line, the CF volumes (in blue) inside the specimen's preview model. The *Onyx™* baseline specimen (first column, OCF) highlights the absence of CF as there are no blue outlines. The “print time”, “*Onyx™* volume”, “CF volume” and “part mass” characteristics are theoretical estimation provided by the software, while the “part density” is an arithmetic division between the “part mass” and the sum of the constituent's volumes. Additionally, Table 10 shows a photo of each produced specimen. Since the base and top layers are both printed in *Onyx™*, the appearance of the samples is identical.

Table 10. Load specimens' characteristics.

Layers	Designation of specimens ( <i>O</i> - <i>Onyx</i> <sup>TM</sup> ; <i>CF</i> is carbon fiber)								
	0 CF	1 CF	2 CF	4 CF	6 CF	8 CF	10 CF	12 CF	14CF
<b>Eiger<sup>TM</sup> model</b>									
<b>Print time (min)</b>	51	57	60	64	67	75	80	84	85
<b>CF <math>\Sigma</math> layer (mm)</b>	0	0.125	0.25	0.5	0.75	1	1.25	1.5	1.75
<b>Onyx<sup>TM</sup> (cm<sup>3</sup>)</b>	5.39	5.41	5.14	4.57	4.01	3.43	2.85	2.27	1.68
<b>CF volume (cm<sup>3</sup>)</b>	0	0.25	0.56	1.12	1.68	2.24	2.79	3.35	3.91
<b>Part mass (g)</b>	6.36	6.46	6.51	6.61	6.71	6.8	6.89	6.97	7.05
<b>Part density (g/cm<sup>3</sup>)</b>	1.18	1.14	1.14	1.16	1.18	1.20	1.22	1.24	1.26
<b>Part photo</b>									

### Characterization

This section presents the characterization procedure defined for the specimens produced, which includes an evaluation of the quality of the specimens and an electrical evaluation based on the electromagnetic shielding effectiveness and electrical conductivity.

#### Thickness, and density

Specimens' density was measured following to Archimedes principle. According to this principle, the volume of an immersed body is equal to the volume of the displaced volume. Therefore, a body immersed in a liquid is subjected to a buoyancy force equal to the weight of the liquid displaced by the volume of the body. The specific density is calculated using the equation:

$$\rho = \frac{W_{body,air} \times \rho_{liquid}}{W_{body,air} - W_{body,liquid}} \quad (57)$$

where  $W_{body,air}$  is the weight of the body in air,  $W_{body,liquid}$  is the weight of the body in the liquid and,  $\rho_{liquid}$  is the specific density of the liquid.

The procedure for the density measurement was performed with an analytical balance AS 202.R2 from Radwag with SDK 01 density kit from Scaltec Lda.

Regarding the measurement of the specimens' thickness, a Mitutoyo Digimatic Caliper was used.

#### Morphology

The morphology of the printed specimens was observed along the thickness cross-section with a Leica DMS1000 digital microscope using a magnification of 6 times.

#### Electromagnetic shielding effectiveness

Printed specimens' shielding effectiveness was measured at the frequency range between 30 MHz and 3 GHz, following the procedure described in chapter 3.3.2. EM Shielding procedure. A VNA with an input power of 0 dBm was used to generate EM waves and record the transmission S-parameters to determine the total EMSE according to Equation 32. The shielding mechanisms of reflection ( $SE_R$ ) and absorption ( $SE_A$ ) were calculated using Equation 28 and 29, respectively.

#### Electrical conductivity

The electric volume resistivity ( $\rho$ ) of the filaments was measured according to the Ohms law using a four-point probe method using the Keithley 2635B SourceMeter and Keithley 5809 clips according to the equation:

$$\rho (\Omega. cm) = \frac{V \times A}{I \times l} \quad (58)$$

where  $V$  is the applied voltage,  $A$  is the area of the filament cross-section,  $I$  is the reading current and  $l$  if the distance between the clip electrodes.

For printed specimens, the electrical volume resistivity was measured according to the ASTM D257 standard "Standard Methods of Test for Electrical Resistance of Insulation Materials" by using the Keithley 2635B SourceMeter and the Keithley 8009 resistivity. The volume resistivity, in accordance with the ASTM standard D257, was calculated with the following equation:

$$\rho = \frac{A}{t} R, \quad (59)$$

where  $\rho$  is the volume resistivity measured in  $\Omega \cdot \text{cm}$ ,  $A$  is the effective area ( $\text{cm}^2$ ) of the guarded electrode applied for the measurement,  $t$  is the average thickness of the specimen measured in  $\text{cm}$  and  $R$  is the volume resistance in  $\Omega$ .

Keithley Model 8009 resistivity test fixture uses circular electrodes with an effective diameter of the guarded electrode of 5.40  $\text{cm}$ . The effective area ( $A$ ) is calculated based on equation 59:

$$A = \frac{D_0^2}{4} \pi, \quad (60)$$

Where  $D_0$  is the effective diameter measured in  $\text{cm}$ .

By replacing the calculated effective area value ( $A$ ) and considering the ohms law previously mentioned that enables to replace  $R$  by  $V/I$ , the equation changes to:

$$\rho (\Omega \cdot \text{cm}) = \frac{22.9 \times V}{t \times I} \quad (61)$$

where  $V$  is the applied voltage,  $t$  is the average thickness of the specimen, and  $I$  is the reading current.

The electrical volume conductivity ( $\sigma$ ) is the reciprocal of electrical resistivity. Hence, for both filament and printed specimens, it can be calculated according to:

$$\sigma (\text{S/m}) = \frac{1}{\rho} \quad (62)$$

### 4.2.3. Results and discussion

This section presents the results and respective discussion, and it is divided in two main points. In the first point it is presented a discussion of some aspects related to the quality of the produced specimens, in particular, the measured thickness, weight, and density, in comparison to the estimations provided by the software *Eiger™*. A morphologic evaluation is also shown in relation to the weight and density of the composite specimens. In the second point, the results and discussion of the most important aspect of the research, the electromagnetic shielding of the printed composites, is presented as a function



of the of the number of continuous CF layers is presented. Lastly, a brief comparison regarding the performance of these material in comparison with materials in the same property category is presented.

### **Quality of the printed composite specimens**

The thickness, weight and density were measured on all specimens to verify the physical differences obtained from the respective printing process. Generally, thickness and density can influence the EM shielding and specific EM shielding, respectively [11], [108], [109]. Therefore, their evaluation is important to investigate the EM shielding relatively to other materials and is also important for quality and performance control of the printing process. The respective measured values are shown in Table 11, and a comparative analysis with the theoretical values from the software are shown in Figure 59.

Table 11. Specimen's average physical dimensions.

<b>ID</b>	<b>0 CF</b>	<b>1 CF</b>	<b>2 CF</b>	<b>4 CF</b>	<b>6 CF</b>	<b>8 CF</b>	<b>10 CF</b>	<b>12 CF</b>	<b>14 CF</b>
<b>Thickness (mm)</b>	1.99	2.00	2.01	2.01	2.00	2.02	2.03	2.03	2.03
<b>Weight (g)</b>	5.994	6.131	6.228	6.232	6.308	6.351	6.384	6.403	6.455
<b>Density (g/cm<sup>3</sup>)</b>	1.142	1.137	1.161	1.135	1.134	1.123	1.121	1.106	1.150

Regarding specimen thickness, it's noteworthy that measurements were consistent across all samples and closely aligned with the nominal thickness of 2 mm. This implies that any variation in shielding performance is primarily due to differences in composite content (such as *Onyx™* and CF layers) and the internal morphology throughout the specimen's thickness.

However, in terms of specimen weight, a variation from the expected values indicated by the software was observed. On average, the measured weights were approximately 6% lower than the software's estimates. This discrepancy in weight is a consequence of the specimens having a lower real density. The experimental data reveals that the real density values are roughly 4.6% lower, on average, than those estimated. This difference in density is attributed to the presence of voids within the specimens, particularly between layers. This is evident through microscopic analysis, as shown in Figure 60.

The density difference to nominal values is higher for the specimens with higher CF layers, especially for the specimens with 8, 10 and 12 layers of CF (8 CF, 10 CF and 12 CF) where the presence of voids is more evident. The existence of porosity leads to gaps between successive layers, impacting the connectivity of the layers and consequently affecting the electrical conductivity and electromagnetic shielding of the specimens. This effect was also observed in the research made by Blok (2018)[128].

Therefore, understanding and managing these variations is crucial to ensure consistent and reliable EM shielding properties in printed specimens.

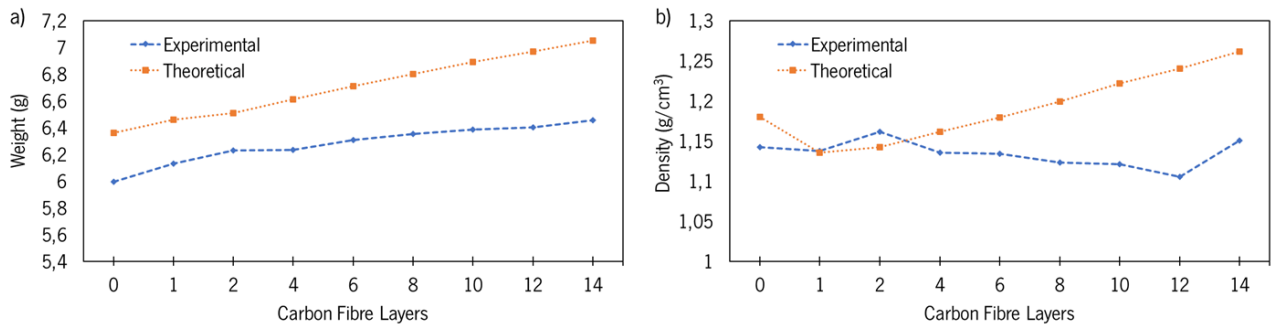


Figure 59. Experimental and theoretical values for: (a) part weight; and (b) part density.

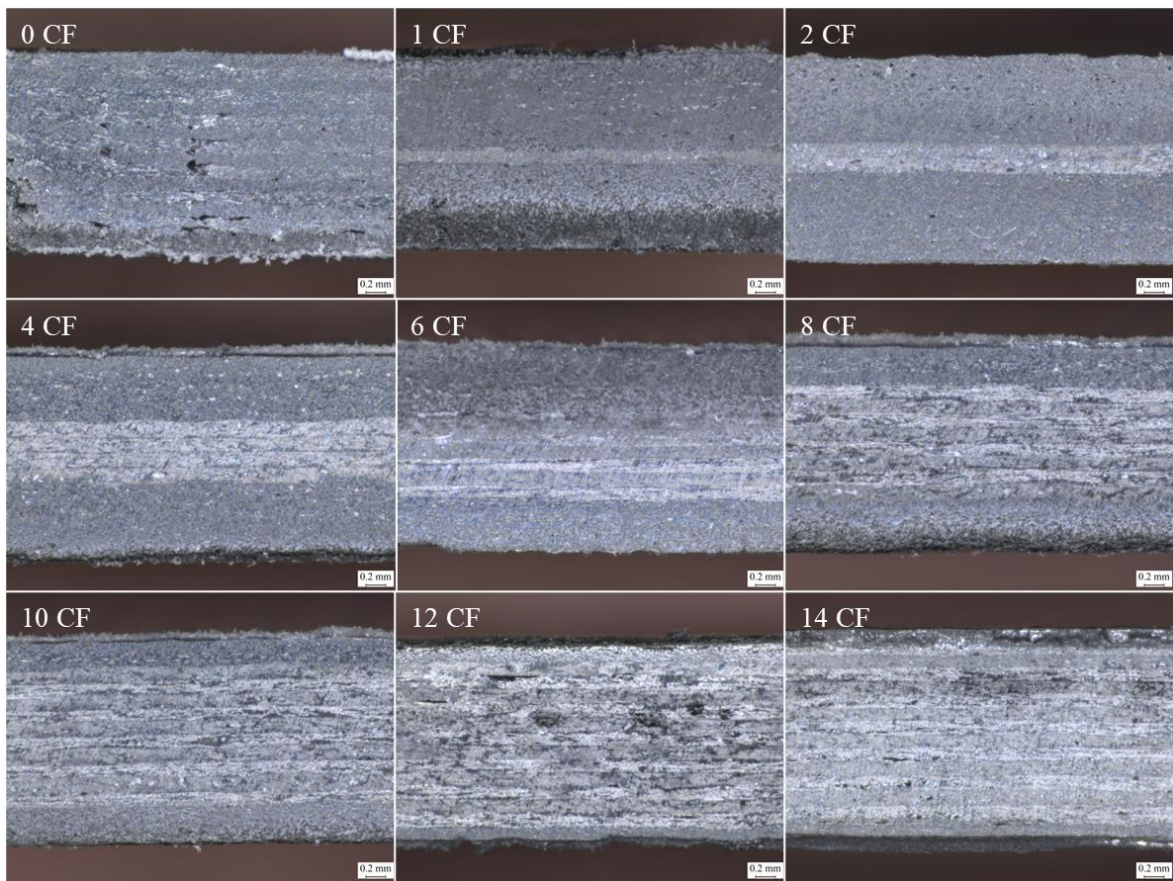


Figure 60. Microscopy of specimen's cross-section.

### Electromagnetic shielding

The analysis of EM shielding performance reveals a substantial improvement when continuous CF layers are integrated into the internal layers of the composite specimens. Shielding performance increases

from less than 10 dB (0 CF layers) to approximately 70 dB (14 CF layers), as illustrated by the average total shielding in Figure 61. This enhancement becomes more pronounced when at least 2 CF layers are combined, leading to a noticeable jump in shielding effectiveness (SE) from 1 CF layer to 2 CF layers. This phenomenon is attributed to the two CF layers overlapping and creating a thicker CF printed pattern, which reduces the presence of voids between CF deposited filaments within the same layer.

Furthermore, for specimens with more than two CF layers, a linear relationship is observed between EM shielding effectiveness (EMSE) and the inclusion of two additional CF layers. This behaviour is depicted in Figure 61 (b), and the linearity coefficient varies with frequency. On average, the EMSE increases by approximately 4 dB with the addition of two combined CF layers. This finding suggests that increasing the number of continuous CF layers can significantly enhance the EM shielding performance, making it a valuable design parameter for achieving higher shielding effectiveness.

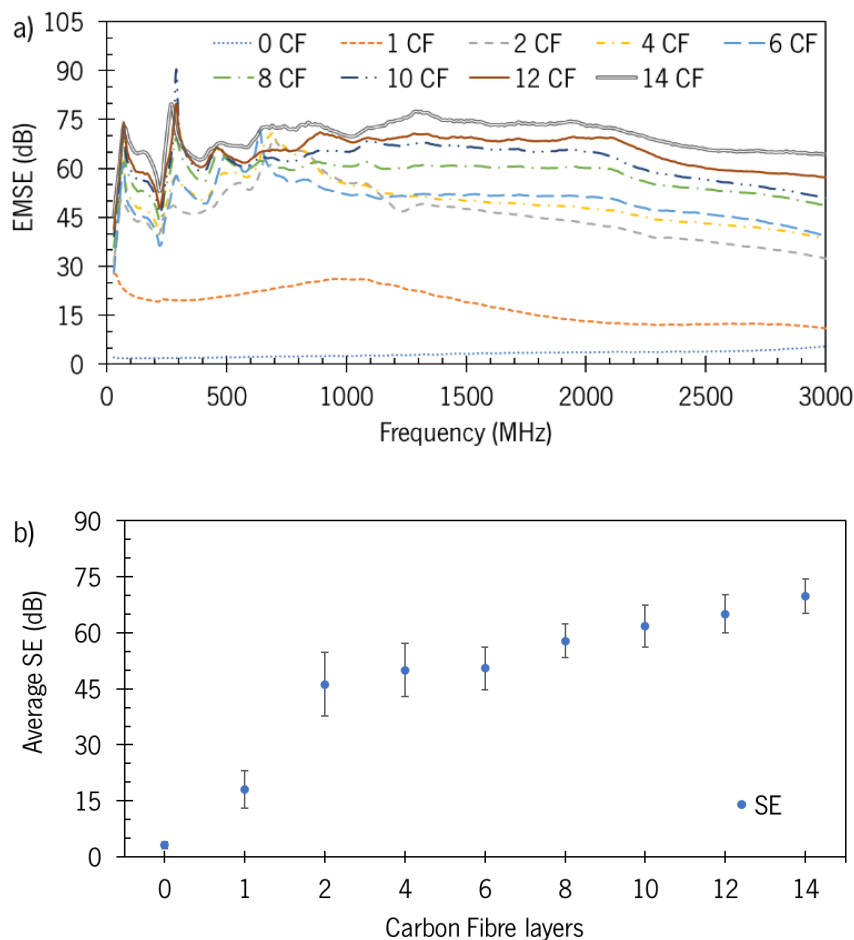


Figure 61. a) EMSE for all specimens as function of frequency; b) Average EMSE as function of CF layers.

The frequency dependent EMSE results shown in Figure 61 (a) reveals an interesting behaviour. The shielding performance for *Onyx™* without continuous CF (represented by the blue-dotted line) increases with wave frequency, though remaining below 10 dB across the entire frequency range. This modest shielding is attributed to the filament being filled with chopped CF, providing some shielding capability to the specimen.

However, the composite specimens with at least one continuous CF layer exhibit resonance-like characteristics below 800 MHz, in contrast to the stable and linear increase observed with *Onyx™* (0 CF). This resonance effect is not yet fully understood but may be related to an antenna effect induced by the length of the continuous CF.

Moreover, the interaction of EM waves with specimens containing continuous CF layers has a distinct impact. Above 1 GHz, the shielding provided by the CF layers decreases with increasing frequency, contrary to the behaviour observed in specimens made entirely of *Onyx™*. This drop in shielding can be reasonably explained by shorter waves traveling through gaps in the mesh screen created by the stacked CF layers. This phenomenon is analogous to the behaviour of shielding materials such as metallic wire meshes, ventilation panels, or scaffolds, where shielding performance is influenced by the cross-section and depth of the apertures [4], [22], [108]. However, this effect wasn't expected for the wavelengths examined in this study, as the dimensions of these gaps or voids are much smaller than half the wavelength. This behaviour may warrant further investigation to better understand the interaction of EM waves with continuous CF structures at different frequencies.

In the analysis of shielding properties for a given material, it is crucial to distinguish between the discrete mechanisms of absorption ( $SE_A$ ) and reflection ( $SE_R$ ). These mechanisms, along with the total shielding ( $SE_T$ ), which is the sum of both components, provide a comprehensive understanding of the material's electromagnetic shielding behaviour. These components are represented as shown in (Figure 62 (b) for absorption and Figure 62 (c) for reflection). This distinction helps in evaluating how a material interacts with electromagnetic waves, contributing to its overall shielding effectiveness.

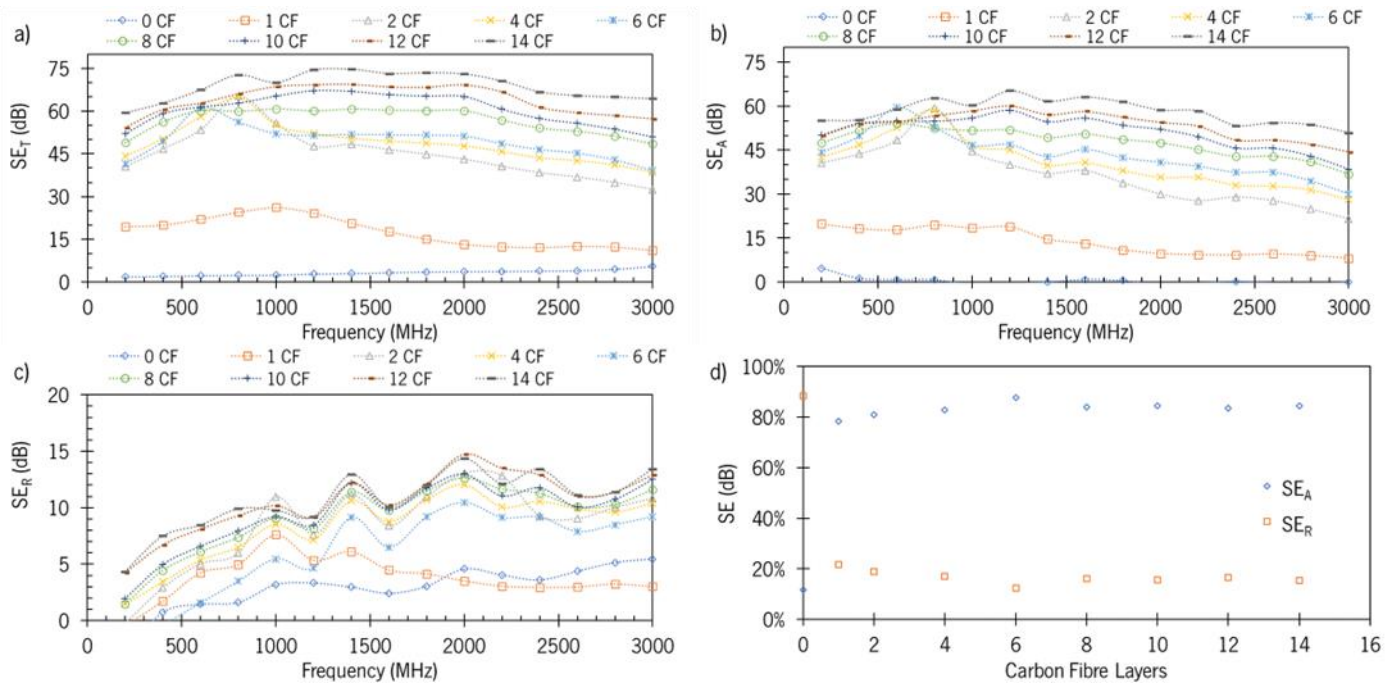


Figure 62. a) Total shielding ( $SE_T$ ) along the frequency range; b) Absorption shielding ( $SE_A$ ) along the frequency range; c) Reflection shielding ( $SE_R$ ) along the frequency range; d) Average ratio for each shielding mechanism.

This analysis shows that, except for the Onyx™ specimen (0 CF), absorption is the dominant shielding mechanism for the printed composite specimens. The specimen with 0 CF layers demonstrated negligible shielding by absorption and an increase in reflection shielding with frequency, up to 5.5 dB. As for the specimens composed of continuous CF, the absorption shielding increased with the number of CF layers, like the total EM shielding previously discussed. Furthermore, the absorption effect appears to decrease at higher frequencies. In the case of the composite made with 2 CF layers, the measured absorption shielding is above 40 dB at lower frequencies and decreases to approximately 20 dB at 3 GHz. For the specimens composed of 14 CF layers, the shielding by absorption is above 55 dB at its lowest, with a peak value of 65 dB at 1.2 GHz, and it decays to nearly 50 dB at the upper frequency of 3 GHz. In contrast, the shielding by reflection observed in the printed composites with more than one CF layer appears to increase with frequency but is less relevant to the overall shielding, with observed values lower than 15 dB. On average, the absorption of EM waves in the specimens printed with continuous CF is responsible for approximately 80% of the shielding behaviour. Hence, the printing of continuous CF layers can result in rather suitable radar absorber materials.

The main reason for the improvement in shielding with the addition of more CF layers is the increase in the relative thickness of the material, in this case, continuous CF, which has much higher electrical conductivity than the chopped CF inside the Onyx™ baseline material. This interpretation is supported by

the electrical conductivity measured for both Onyx™ and CF filaments before they underwent the printing process, as shown in Table 12. The electrical conductivity results demonstrate that continuous CF has a conductivity between 13 to 143 S/m (electrical resistivity between 1 to 23 Ω.cm), which is almost 10 orders of magnitude higher than the electrical conductivity of Onyx™. Therefore, since shielding is proportional to the material's electrical conductivity and thickness, it is expected that the existence of a larger layer of conductive continuous CF will lead to increased shielding effectiveness. However, since the printing of continuous CF is restricted to the inner layers of the specimen (Onyx™ is printed on the bottom and top layers), the improvement of electrical volume conductivity (reduction of electrical resistivity) with the increase of CF layers was not observed in the experimental measures. All composite specimens exhibited an electrical conductivity on the order of  $1 \times 10^{-10}$  S/m (electrical resistivity on the order of  $1 \times 10^{11}$  Ω.cm), which is similar to the values measured for the specimen without continuous CF.

Table 12. Measured electrical resistivity for filaments and printed specimens.

Filament	<i>Onyx™</i>		Carbon Fibre			
	Pre-processing	Pos-processing	Pre-processing		Pos-processing	
$\sigma$ (S/m)	$4.88 \times 10^9$	$1.38 \times 10^8$	142.89		13.13	
$\rho$ (Ω.cm)	$2.11 \times 10^{-10}$	$8.16 \times 10^{-9}$	1.18		23.32	

Specimen	0 CF	1 CF	2 CF	4 CF	6 CF	8 CF	10 CF	12 CF	14 CF
$\sigma$ (S/m) $\times 10^{-10}$	1.52	1.87	1.71	2.08	2.27	2.36	2.40	2.13	7.30
$\rho$ (Ω.cm) $\times 10^{-11}$	6.59	5.36	5.86	4.81	4.41	4.24	4.16	4.69	1.37

When attempting to estimate the EM shielding effectiveness based on the electrical conductivity measured in the as-built specimens, one will observe that, for this specific type of material, the shielding estimations are likely to be underestimated and fail to represent the actual measured values illustrated in the preceding graphs. As depicted in Figure 63, assuming an electrical conductivity in the order of  $10^{-10}$  S/m (electrical volume resistivity exceeding  $10^{11}$  Ω.cm), as measured, would suggest almost negligible shielding. However, the real shielding of the specimens ranges from 10 dB to 70 dB, depending on the number of carbon fibre (CF) layers. Achieving this level of shielding requires an electrical conductivity near or above 5 S/m (electrical resistivity near or below 20 Ω.cm), which aligns with the conductivity measured for the isolated carbon fibres. Therefore, to accurately calculate EM shielding using theoretical

models, one must consider the inherent electrical properties of the CF, as these are the primary contributors to the shielding performance.

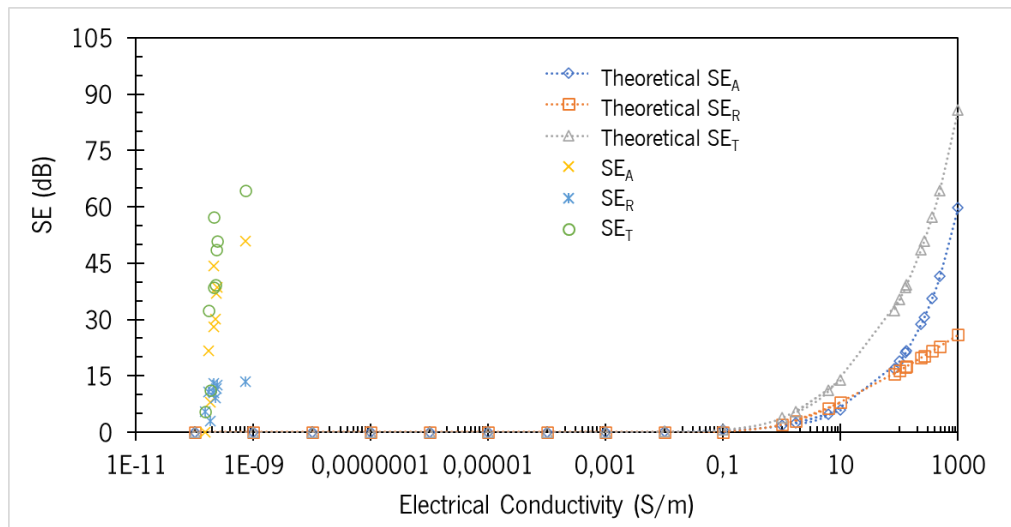


Figure 63. EM shielding and resistivity relation. EMSE is expected to decrease for higher resistivities by power law.

As previously mentioned, and reported in other studies [106], [108], [109], it's important to investigate the impact introduced by the composite thickness and density on the overall electromagnetic shielding in order to assess the shielding performance in relation to different materials. Hence, to account for these variations, the normalized shielding (SE divided by the specimen's thickness) and the specific shielding (SE divided by the specimen's density) were calculated and are presented in Figure 64 and Figure 65, respectively. These normalized and specific shielding values provide a more accurate assessment of the shielding performance, removing the impact of variations in thickness and density and enabling a direct comparison between different specimens and materials.

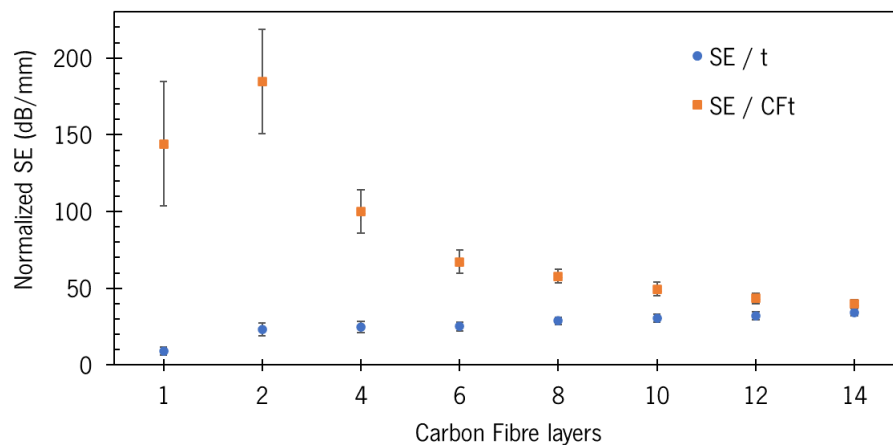


Figure 64. Normalized shielding effectiveness for the specimen's thickness (t) and per added CF layer (CFt).

The analysis of the normalized shielding ( $SE/t$ ) for composites with at least two CF layers revealed values ranging from 23 dB/mm to 34 dB/mm, depending on the number of CF layers. The normalized shielding showed a linear growth with the addition of two more CF layers, increasing by a factor of 1.2 with each additional pair of CF layers. If these composites were a homogeneous material, one could assume that it's possible to improve the shielding by almost 30 dB per each additional millimetre of thickness added to the part.

However, it's important to note that the shielding effect is primarily due to the inner CF layers of the composite, rather than the overall composite thickness. To account for this, the normalized shielding was adjusted by dividing the measured EMSE by the effective CF layer thickness ( $SE/CFt$ ). The adjusted values (orange squares) indicate that the isolated CF layer can achieve a shielding effectiveness of nearly 185 dB/mm when there are two CF layers. As the number of CF layers increases, the normalized SE decreases, following a power-law function with an average power of -0.7. This analysis demonstrates the critical role of continuous CF layers in providing effective shielding. It also emphasizes that while adding more CF layers improves shielding, the additional shielding gain diminishes with each combination of two CF layers, following power-law relationship.

Regarding the specific shielding ( $SE/\rho$ ), which is an important metric to consider when producing lightweight components, one can observe, in the Figure 65, that above two CF layers these composites have a specific shielding from near 40 dB.cm<sup>3</sup>/g up to 60 dB.cm<sup>3</sup>/g.

Regarding the specific shielding ( $SE/\rho$ ), which is an important metric to consider when producing lightweight components. As a higher specific shielding means that a better EM barrier can be achieved with a lightweight material, which an important aspect for energy savings. One can observe, in the Figure 65, that above two CF layers these composites have a specific shielding from near 40 dB.cm<sup>3</sup>/g up to 60 dB.cm<sup>3</sup>/g.



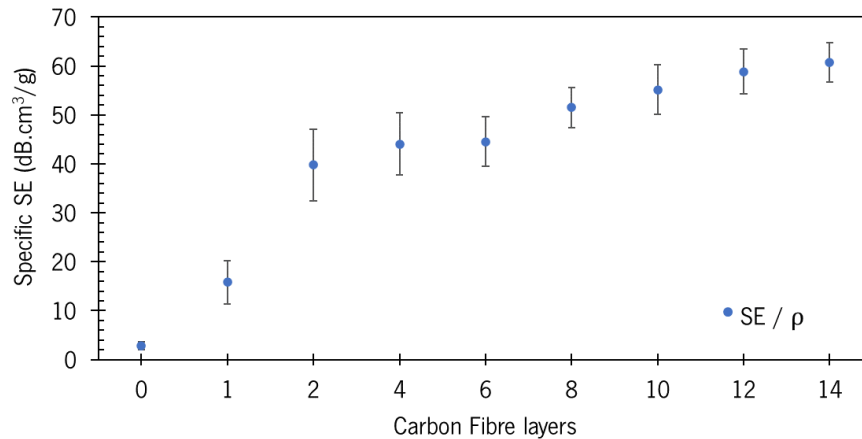


Figure 65. Specific EM Shielding for each composite formulation.

In comparison to other composites manufactured through additive manufacturing, particularly ME technology, it is evident that the printed composites utilizing continuous carbon fibre demonstrate superior performance in contrast to materials produced by other researchers. The printed composites from this work, particularly those with at least two CF layers achieve an average SE ranging from 45 to 70 dB, a normalized shielding ranging from 23 to 34 dB/mm, and specific shielding values between 40 to 60 dB.cm<sup>3</sup>/g. This performance notably surpasses the average shielding of 30 dB, normalized shielding of approximately 21 dB/mm, and specific shielding of about 42 dB.cm<sup>3</sup>/g achieved in related studies [105], [106], [108], [121], [125].

However, as previously mentioned, there are limited direct peer studies to compare these results due to the novelty of using AM with continuous CF for electromagnetic shielding. Hence, by comparing the developed composites to materials produced by conventional technologies, like injection moulding [22], [111] or compression moulding [102], [104], [130]–[132], it's possible obtain similar or better performance than the other materials.

#### 4.2.4. Concluding remarks

The printing of continuous carbon fibre by material extrusion technique was used to produce 2 mm thick composite parts with electromagnetic shielding that can reach 70 dB in the frequency band of 0.03 – 3 GHz. This is an improvement of more than 22 times, from the baseline printed composite polyamide material (Onyx™) without any continuous carbon fibre layer. From a commercial standpoint, a material capable of achieve an electromagnetic shielding above 30 dB, which blocks more than 99.9% of electromagnetic waves from being transmitted is considered adequate for practical applications.

Therefore, this research evidence an innovative and customizable approach to produce lightweight enclosures for electromagnetic shielding purposes.

One of the advantages of these composites is related to the possibility to fit the performance as required by easily modifying the internal structure of the composite, since, depending on the carbon fibre layers and the frequency of interest, these composites can reach an electromagnetic shielding efficiency in the range of 40 to 70 dB, or even higher for thicker specimens. The effect of the number of carbon fibre layers was evaluated and it was found that an increase of a combination of two carbon fibre layers lead to a linear increase of shielding at a rate of approx. 4 dB, which corresponds to an effectiveness increase of almost 2 dB/mm. However, above two carbon fibre layers the addition of carbon fibre tends to be less effective since the electromagnetic shielding efficiency improvement per added carbon fibre layer diminishes following a power-law function with a power of -0.7.

This study also found that the absorption shielding ( $SE_A$ ) for these additive manufacturing composite materials have ranges between 80% to 90%, which thus demonstrates the adsorption-dominated shielding mechanism. This aspect and a specific shielding up to 60 dB.cm<sup>3</sup>/g places these additive manufacturing composites as a possible and rather new lightweight solution for electromagnetic shielding, specifically for applications which require a high absorption rate.

Although this study shows promising results, there are several avenues to further explore the use of AM for producing complex structures with continuous fibre and to improve electromagnetic shielding:

- Effect of different orientations: Some preliminary results suggests that specimens printed in the vertical direction have lower shielding than the specimens produced in this study (horizontal printing). Hence, a more detailed study of how different printing orientations affect EM shielding would provide valuable insights.
- Additional materials: Experimenting with different materials is another direction to consider. Using enhanced polymeric filaments or different types of continuous fibres, such as stainless steel or nickel-coated carbon fibres, can potentially improve EM shielding properties. These materials could offer superior performance compared to the materials used in the current study.

- Performance of an enclosure: Develop a concept for a 3D enclosure that demonstrates the EM shielding capabilities in a real-case scenario. This practical application can showcase the effectiveness of AM-produced shielding structures in practical use cases.

### **4.3 Graphene based coatings**

This study was conducted in collaboration with Graphenest S.A., an industrial firm from Paradela do Vouga, dedicated to the design, development, and optimization of an innovative technology for producing graphene and graphene derivatives. Their mission is to become fundamental by providing innovative and leading graphene-based shielding solutions and technology to our everyday products.

Therefore, the purposed objective to this research was to implement the products from Graphenest innovative and proprietary state-of-the-art graphene production technology and answer to the following question:

- "How efficient is the EM shielding provided by the graphene-based solutions"

In a brief, this research focused on the EM shielding analysis to several graphene-based coatings painted on a polymeric substrate, specifically silicone. The findings from this study supported the development of a graphene-based solution to be release to the market and be implemented as a coating for electrical cables shielding barrier.

#### **4.3.1. Literature review**

Graphene is a carbon allotrope with two-dimensions, single-atom-thick carbon sheet with 0.142nm of carbon-carbon (C-C) bond length. Due to the unique spatial and bonding arrangement of atoms through sp<sup>2</sup> hybridization of all of the C-C bonds across the sheet, graphene has excellent mechanical, optical, thermal and electrical properties, which have contributed to the gradual increase in its visibility (and that of its derivative materials) among the scientific and business community, particularly as a result of its potential in the context of a diverse range of industrial application areas [133]–[136].

Currently, metal is the most commonly used material for electromagnetic shielding applications. However, the utilization of materials like graphene, which can absorb electromagnetic radiation in the microwave range, offers a versatile approach to create tailored shielding composites or structures with

specific electrical and electromagnetic shielding properties. This customization is particularly beneficial for applications like radar absorption, and allows the design of lightweight components.

For instance, Kumar and his team developed thin, extensive layers of reduced graphene oxide, forming a laminate with a thickness of 10  $\mu\text{m}$ , which exhibited an electromagnetic shielding effectiveness of 20 dB at 1 GHz [137].

Paliotta et al [96] developed a flexible and electrically conducting shielding material for radio frequency applications. They created this material using a graphene-based porous paper composed of multilayer graphene (MLG) micro-sheets. A liquid-phase exfoliation process was employed to produce MLG-suspensions through a nano-porous alumina membrane. The produced MLG papers demonstrated excellent electrical conductivity, measuring up to 1443.2 S/cm, with approximately 43% porosity. These papers were highly flexible and provided shielding effectiveness of up to 55 dB at 18 GHz, all with a thickness of 18  $\mu\text{m}$ . Additionally, they employed transmission line modelling to calculate the EMI shielding of an infinite isotropic slab exposed to a plane wave with normal incidence.

Hong et al [138] employed the chemical vapor deposition (CVD) method to create a single monolayer of graphene with a thickness of 0.3 nm. This monolayer achieved an electromagnetic interference (EMI) shielding effectiveness of 2.27 dB, provided by a conductivity of  $5.25 \times 10^6$  S/m, which falls below the theoretically estimated conductivity for an ideal graphene monolayer. Zhang and his team also utilized the CVD process to synthesize graphene, using nickel powder as a catalyst. The resulting graphene paper, with a thickness of 50  $\mu\text{m}$ , displayed high electrical conductivity, reaching up to 1136 S/cm, and exhibited excellent EMI shielding effectiveness of 60 dB, which corresponds to a specific shielding value of 68.38 dB.cm<sup>3</sup>/g [139].

Another notable example involves the development of lightweight and flexible graphene foam composites. Chen et al. created ultralow-density graphene/PDMS foam composites with an exceptional specific electromagnetic interference (EMI) shielding effectiveness ranging from 300 to 500 dB.cm<sup>3</sup>/g, depending on the frequency range. These values significantly surpass those of typical metals, such as solid copper (10 dB.cm<sup>3</sup>/g) and CNT/polymer foam nanocomposites (33.1 dB.cm<sup>3</sup>/g) [140].

The research related to the use of graphene combined with polymer composites is well established, stating electrical and shielding properties ranging from the most modest up to incredible improvements,

depending on the processing technology, graphene quality and volumetric concentration, sample thickness and frequency of observation [134][141][142][141][135][143]

In some studies, bulk blends of graphene composites have been shown to enhance the EM shielding effectiveness performance. For instance, an 8.8% (v/v) graphene/epoxy composite achieved approximately 21 dB shielding [142], a 5.6% (v/v) graphene/polystyrene composite achieved an EMSE of around 19 dB [141], and a 4.2% (v/v) graphene/polymethylmethacrylate composite reached about 30 dB of SE [144].

Cao et al. [135] conducted an extensive evaluation of SE in graphene-based composites and provided a detailed description of its mechanisms, emphasizing the significance of the composites' architectures, whether in the form of paper, films, or foams. They found that developing ultrathin materials with EMI shielding and special architectures remains a challenge.

Song et al. [145] developed flexible networks composed solely of carbon, specifically a carbon nanofiber–graphene–carbon nanofiber (CNF-G-CNF) system, with a thin thickness of 0.26 mm. In this case, the shielding properties were attributed to the electrically conductive interconnects, greatly enhanced by the formation of CNF-G-CNF heterojunctions. They reported an absorption efficiency of approximately 98%, indicating a significant contribution of the absorption phenomenon to EMI shielding.

Graphene composite foams are also being explored as future directions for EMI shielding materials, given their lightweight properties and high SE. For example, Chen et al. [140] and Yan et al. [143] produced graphene/polydimethylsiloxane (PDMS) and graphene/polystyrene (PS) composite foams, respectively. In both cases, the interconnected 3D networks achieved satisfactory and stable SE and EMI, even though they had low densities.

Li et al. [123] also conducted forward-looking research that explored the potential opportunities and challenges in utilizing the distinctive physical properties of graphene and its composites in conjunction with additive manufacturing capabilities, to manufacture intricate 3D objects layer by layer. This comprehensive overview sought to leverage the multifunctional properties and potential applications of graphene-based composites produced using a range of AM methods, to be applied in the field of EMI shielding.

Thermoplastic composites offer several advantages but also pose challenges. Their heterogeneous structure results in anisotropic properties that depend on process conditions. However, this anisotropic

character provides opportunities to create conductive interconnections and expand the effective reflection regions within the plane. Therefore, composites with aligned distributed graphene have garnered significant interest. For instance, Song et al. [146] manufactured graphene/wax composites and reported superior SE to EMI in comparison to composites with randomly distributed graphene. Shen et al. [147] described the production of aligned graphene films through the direct evaporation of a graphene oxide (GO) suspension under moderate heating conditions, followed by graphitization. This process improved absorption and reflection properties. Moreover, Yousefi et al. [148] reported an excellent SE of 38 dB for EMI with aligned nanomaterial in graphene/epoxy composites.

In a study by Batrakov et al. [149], the significance of composite thickness in EM shielding was discussed. They proposed a method of microwave shielding using nanometric pyrolytic carbon (PyC) films, which were composed of interlaced graphene ribbons. The research team reported that PyC films with a thickness of 30-75 nanometres could achieve a 60% attenuation of the incident power at 28 GHz, primarily through the absorption of the radiation. However, they also found that substituting PyC with few-layer graphene (FLG) could provide a microwave radiation attenuation of 40% with a much thinner thickness of just 5 nanometres. In different research, Batrakov et al. [150] conducted a study on the absorption of electromagnetic waves using graphene/polymethyl methacrylate (PMMA) multilayers. They reported that, at frequencies around 30 GHz, the absorption coefficient reaches its maximum when 6 layers of graphene are present. They noted that the most significant contribution to the EM shielding came from the graphene layers separated by the PMMA. However, it was observed that when the number of layers exceeded 6, the absorption effect diminished, and the dominant phenomenon shifted to reflection.

Agnihotri et al. [151] conducted a study in which they prepared composites consisting of graphite nanoplatelets and poly(3,4-ethylenedioxythiophene)-poly(styrenesulfonate) (PEDOT:PSS) with varying proportions of graphite. Using this conductive polymer instead of a conventional polymer allowed them to achieve high EMSE with lower additive loads. This approach also helped avoid common issues associated with spongy structures, such as crack formation. The research by this team demonstrated that these composites provided SE ranging from 30 dB (with 0.5% mass/mass of graphite) to an impressive 70 dB (with 25% mass/mass of graphite) for thicknesses as thin as 0.8 mm. Moreover, due to their low density, these composites achieved specific EMI shielding values of up to 67.3 dB.cm<sup>3</sup>/g, which remained high in comparison to spongy structures designed specifically for EMI shielding.

The field of graphene-related research has grown at a spectacular pace since single-layer flakes were first isolated in 2004. What began as an exciting material for fundamental physics has now become the focus of efforts by scientists in a wide range of fields. Chemists and materials scientist are busily working on developing new technologies or improving current methods to increase production yields and achieving better properties which allow the creation of novel devices to exploit graphene's extraordinary properties. This research capitalizes on this secular innovation trend trying to bring new insights and products to the realm of graphene-based solution for electromagnetic shielding.

### 4.3.2. Materials and methods

#### Materials

*Graphenest S.A.* has designed and developed an innovative technology based on a method of exfoliating graphite in a liquid medium (organo-aqueous) by means of ultrasonic cavitation aided by milling (mechanical exfoliation), as a way of ensuring a more efficient production of graphene and its derivative materials in an adjustable quality, quantity, and at a fair price to address the needs of industry.

It is in the context that the GNESIS project arose, with the general aim of scaling up Graphenest's technology and demonstrate the applicability of the graphene obtained from this technology in three different areas of application: anti-corrosive paints; polymers with electromagnetic shielding; and touchscreen electrodes.

*Graphenest S.A.* supplied several production batches of graphene nanoparticles, which included both FLG and MLG. A total of six graphene-based solutions were developed, and an additional two solutions were mixed with metallic particles. These graphene-based solutions were then combined with polymeric materials to create structures and materials suitable for EM shielding applications, particularly designed to mitigate electromagnetic interference.

One of the specific applications within this project involved applying the graphene-based coatings to a 2.2 mm thick silicone substrate, grade *Bluesil™* by *Elkem Silicones*. The goal was to develop a novel concept for EMI shielding of electric cables, with a specified requirement of achieving a shielding effectiveness of at least 30 dB. This technology aims to enhance the shielding capabilities of these cables and replace the standard metallic mesh.

## **Production**

Samples were prepared by applying the graphene-based solutions as a coating on a 100 x 100 mm, 2.2 mm thick silicone substrate. This coating process involved the manual application of the solution to the silicone slab using a conventional spray gun, as shown in Figure 66. These conventional spray guns are designed to atomize the paint using low volume and high pressure, with separate channels for air and material that mix inside the gun. A skilled operator can manually control the gun to ensure the application of a uniform coating with thickness adjusted according to the number of paint layers.

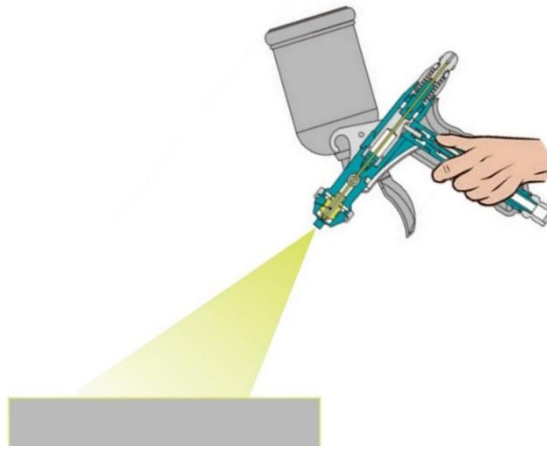


Figure 66. Schematic of a conventional manual spray gun.

## **Characterization**

This section presents the characterization procedure defined for the specimens. The characterization includes an experimental observation on the coating's electromagnetic shielding effectiveness and electrical conductivity. Additionally, a theoretical assessment for EM scattering through a multilayer material with predefined properties was achieved to predict the EMSE of the graphene-based coatings.

### Electromagnetic shielding effectiveness

Printed specimens' shielding effectiveness was measured at the frequency range between 30 MHz and 3 GHz, following the procedure described in chapter 3.3.2. EM Shielding procedure. A VNA with an input power of 0 dBm was used to generate EM waves and record the transmission S-parameters to determine the total EMSE according to Equation 32.



Electrical conductivity

The electric conductivity of the specimens was measured by Graphenest team, according to the Ohms law using a conventional multimeter and calculated with the equation:

$$\sigma (S/m) = \frac{I \times l}{V \times A}$$

where  $V$  is the applied voltage,  $A$  is the area of the specimen cross-section,  $I$  is the reading current and  $l$  if the distance between the multimeter probes.

Theoretical modelling

In addition to the experimental characterization, the use of numerical tools that can estimate the electromagnetic scattering phenomena when interacts with different materials. This study seeks to generalize the shielding of these heterostructures, theoretically, in order to determine the dielectric function of the graphene and is relevant to a better development process of these materials and structures to improve the performance and avoid failure.

The approach to be adopted for modelling the afore mentioned graphene coatings on silicone will consider that the specimens are composed of two layers, where, within each one, it is considered that the material that constitutes it is homogeneous, as well as isotropic and dissipative, each one of them with a specific refractive index.

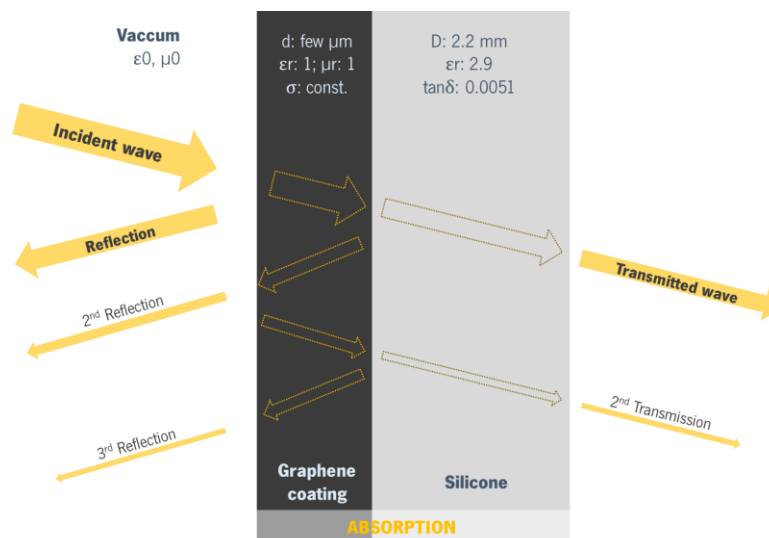


Figure 67. Normal plane wave incidence scattering along a heterogeneous specimen. Geometry of a thin layer of conducting material of thickness  $d$  covering a silicone dielectric of thickness  $D$ .

The refraction of plane waves by such heterostructures can be adequately described using the transfer matrix formalism described in chapter 3.3.6. The constitutive equations describing the material's refractive indices were written in *Mathematica 10.2* software, as shown in Appendix C, where the graphene coating (1<sup>st</sup> layer) was defined with dissipative characteristics with relative permeability ( $\mu_r$ ) of 1 relative permittivity ( $\epsilon_r$ ) of 2.9 and constant electrical conductivity. The 2.2 mm thick silicone substrate (2<sup>nd</sup> layer) was defined as dissipative dielectric with  $\epsilon_r$  of 2.9,  $\tan\delta$  of 0.0051 and  $\mu_r$  of 1.

### **4.3.3. Results and discussion**

Graphenest produced multiple formulations of graphene-based ink under various experimental conditions. This was done to refine the production process and assess the suitability of graphene in applications requiring electromagnetic shielding. These ink formulations consisted of graphene nanoparticles with varying dimensions and layer numbers, ranging from FLG to MLG. It's reasonable to expect that these diverse production conditions would yield graphene of varying quality, resulting in a wide range of electrical properties and corresponding EM shielding effectiveness.

The electromagnetic shielding of these materials deposited under a silicone rubber substrate was evaluated experimentally and from a theoretical point of view, aiming for an attenuation of at least 30 dB. The development of polymeric coatings with graphene was chosen due to the convenience of fine-tuning their properties for optimal shielding efficiency, particularly in terms of conductivity and thickness. Additionally, the ease of application using spray deposition methods played a crucial role in guiding the research. Starting with a silicone substrate allowed to expedite the studies and tests, helping to determine the necessary amount of graphene for achieving a specific level of shielding and enabling precise control over the coating thickness.

The initial findings from the graphene-based coatings applied to a silicone substrate indicated that layer thicknesses typically ranging from 100 to 300 micrometers and an average measured sheet resistance within the range of 50 to 100 Ohm/sq led to unsatisfactory shielding efficiencies, all falling below 15 dB across the entire frequency spectrum from 30 MHz to 3 GHz. Detailed results can be found in Table S43 and Figure S2 in the supplementary results in Appendix H. For the sake of simplicity, the analysis of the shielding results will focus exclusively on the values measured at 1 GHz, as illustrated in Figure 68.

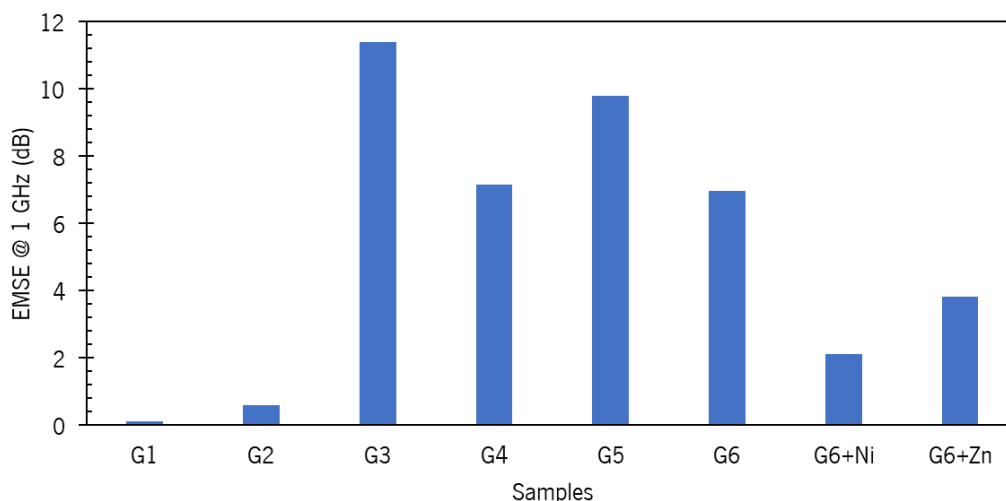


Figure 68. EM shielding measured at 1 GHz to the six graphene-based inks painted on silicone.

The results are presented in the chronological order of development from G1 to G6. As observed, there was a general improvement in shielding effectiveness, however, none of the graphene-based coatings met the minimum EM shielding requirement of 30 dB. Even the inclusion of a small percentage of metallic particles (Nickel or Zinc) in the G6 formulation proved to be ineffective in achieving the desired shielding improvement.

A theoretical assessment was conducted to describe the EM shielding of the developed graphene coatings as a function of their conductivity and thickness. This theoretical model assumes that the specimens consist of two dissipative layers: a thin graphene layer with variable thickness and a 2.2 mm thick silicone layer. Both layers are characterized by homogeneous, isotropic properties with constant electrical conductivity in the case of graphene and a constant tangent loss of 0.0051 in the case of silicone.

In this theoretical analysis, the exhibited results in Figure 69 show, as discussed in previous chapters, that the EM shielding of the coating is proportional to the graphene thickness and conductivity, with a defined logarithmic growth ratio of similar value.

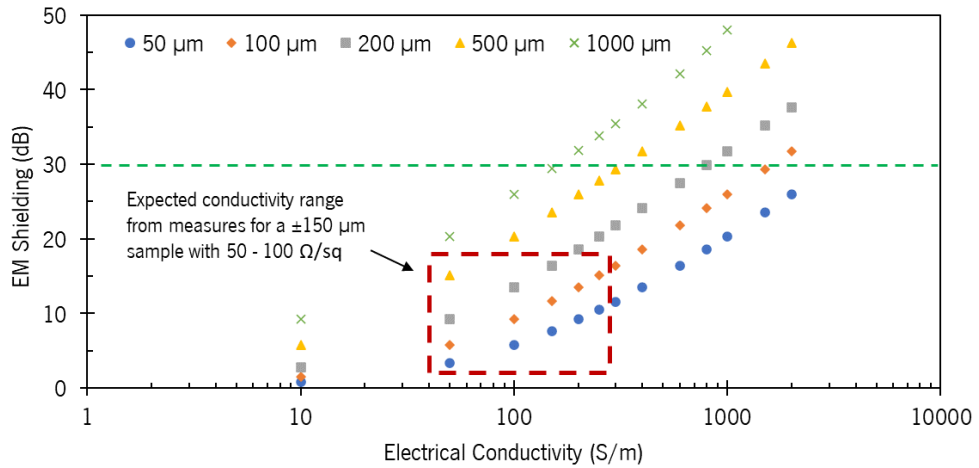


Figure 69. Theoretical estimate for the effect of electrical conductivity on EM shielding for graphene-based conductive coatings.

Since the EM shielding performance of the produced graphene coatings was unsatisfactory, the theoretical analysis provided insights into how to develop further coatings to achieve the 30 dB target. The answer to this question is clear: to improve the coating's shielding, one should increase the coating thickness and/or enhance the graphene's electrical conductivity. For instance, if the coating thickness remains between 100 to 200 micrometres, then the graphene solution must be improved to achieve a conductivity near 1000 S/m. On the other hand, if the graphene quality remains the same, with conductivities in the range of 150 S/m, then the thickness of the coating must be increased to over 1 mm. Therefore, considering the research time horizon and budget, it was decided to study the EM shielding of the developed graphene inks with an increased coating thickness, as shown in Figure 70.

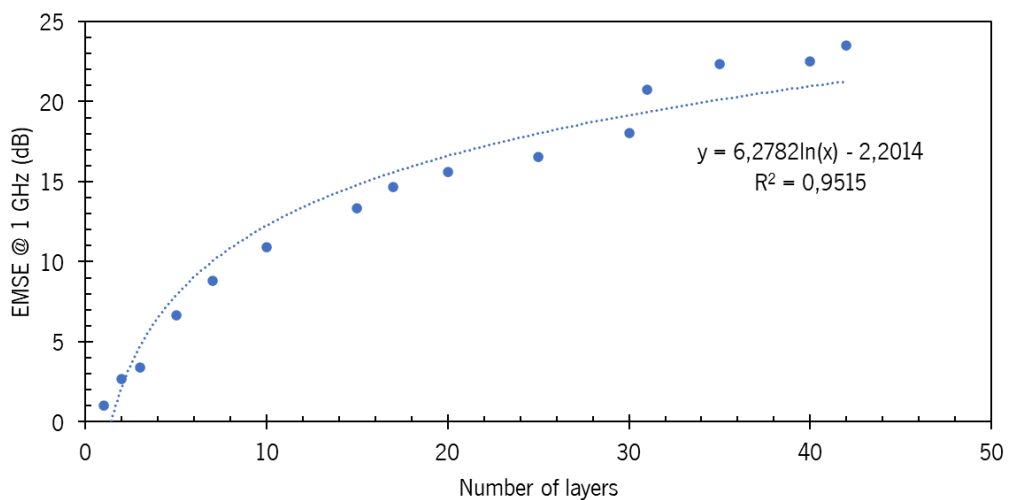


Figure 70. Effect of the number of graphene layers on the EM shielding.

By superimposing several layers of graphene paint, up to 42 layers, it is possible to observe that at 1 GHz, the EM shielding reached a level of almost 25 dB. This is an improvement of nearly 2 times the average values measured previously. Moreover, at higher frequencies, it was possible to achieve the desired 30 dB level of shielding effectiveness, as detailed in Table S44 from the Appendix H. Supplementary results to chapter 4.3..

Furthermore, it can be seen that the increase in the number of layers leads to an increase in shielding with a logarithmic growth. This implies that the benefit from adding new layers is lower than that from the previous ones.

By considering an average 20  $\mu\text{m}$  thick layer per spray gun passage, we can convert the number of deposited graphene layers into a nominal thickness value. The impact of this adjusted layer thickness on the measured EM shielding can be seen in Figure 71. With this reasonable assumption, it becomes apparent that the measured properties align with the theoretical projections for graphene with conductivity in the range of 50 to 100 S/m, which coincides with some of the values measured by Graphenest. Furthermore, it was found that the maximum measured shielding was achieved by applying a graphene coating with a thickness of almost 1 mm.

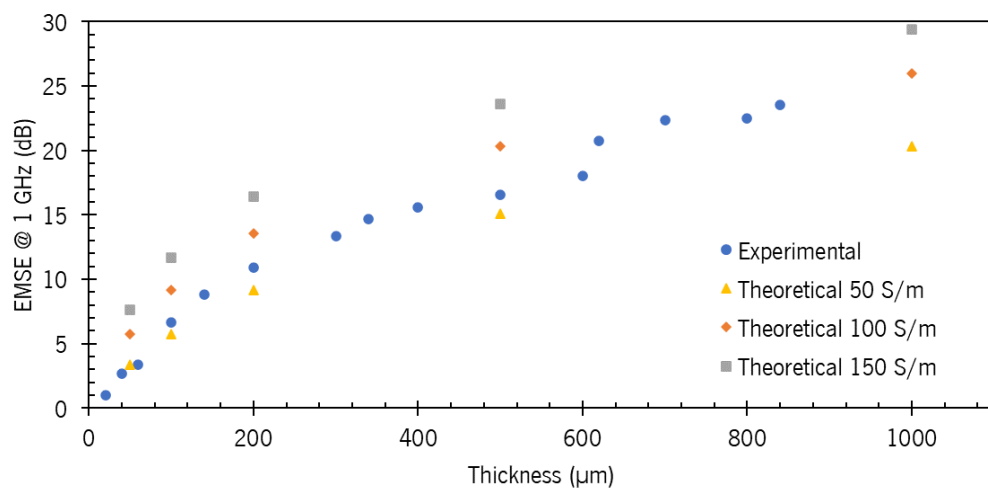


Figure 71. Effect of the graphene layer thickness on the EM shielding. Results show similar characteristics to the theoretical estimations.

#### **4.3.4. Concluding remarks**

The use of graphene-based solutions, combined with polymers, was investigated to develop products with EM shielding characteristics capable of mitigating electromagnetic interference. These graphene solutions, available in both FLG and MLG forms, and with different particle dimensions, were developed through an innovative process by *Graphenest S.A.*

This research has determined that the graphene-based coatings, when applied to a silicone substrate, with layer thicknesses typically ranging from 100 to 300 micrometres and an average measured sheet resistance within the range of 50 to 100 Ohm/sq, resulted in unsatisfactory shielding efficiencies of below 15 dB across the entire frequency spectrum from 30 MHz to 3 GHz

A theoretical model was utilized to estimate the EM shielding behaviour of these graphene-based coatings, aiming to guide the development of coatings capable of meeting the 30 dB requirement. The model demonstrated that to enhance the coating's shielding, it is necessary to increase the coating thickness and/or improve the graphene's electrical conductivity. For instance, if the coating thickness remains between 100 to 300 micrometres, then the graphene solution must be enhanced to achieve a conductivity near 1000 S/m. Conversely, if the graphene quality remains the same, with conductivities in the range of 150 S/m, then the thickness of the coating must be increased to over 1 mm.

By increasing the coating thickness through the application of several layers of graphene paint, up to 42 layers, the EM shielding was improved by a factor of two, reaching a level of almost 25 dB at 1 GHz, and even achieving 30 dB at higher frequencies.

This study yielded unsatisfactory results regarding the stated objective of achieving a 30 dB shielding. Nevertheless, it has provided valuable insights that *Graphenest S.A.* is applying to enhance future developments of graphene-based electromagnetic shielding solutions.

Moreover, there are additional studies can be explored in future research, leading to new possibilities for improving electromagnetic shielding in a variety of applications.

- Industrial case study: The application of these graphene-based coatings can and should be implemented in a real industrial product. The electromagnetic scattering within a silicone electrical cable differs from the normal incident wave described and tested in this research. Therefore, it is a scenario

that should be explored for the potential application of graphene in protecting electrical cables against unwanted EMI.

- Different polymeric composites: Experimenting with different materials is another avenue to consider. These graphene solutions can be employed to enhance the properties of polymeric filaments for additive manufacturing and other conventional manufacturing processes like injection or compression moulding.

## **5. CONCLUSIONS**



## 5.1 General conclusion

The main goal of this research was to perform an experimental and theoretical characterization of the electromagnetic shielding effectiveness of thermoplastic composites. For this purpose, five research questions were formulated which are now possible to be answered.

### **What is the effectiveness of thermoplastics in blocking electromagnetic waves?**

The findings of this research underscore a significant variation in electromagnetic shielding effectiveness, ranging from 20 dB to 100 dB. This variability is influenced by factors such as the type of conductive reinforcement, its concentration, length, and orientation within the material samples. Particularly remarkable is the use of both carbon fibres and stainless-steel fibres, which demonstrated an exceptional shielding performance exceeding 60 dB from 30 MHz up to 3 GHz.

### **How do injection moulding parameters influence fibre orientation, concentration, and subsequent properties of a specimen, ultimately leading to optimal EM shielding performance?**

In the three main studies conducted as part of this research, the effect of the injection moulding process was thoroughly investigated, considering various factors such as melt temperature, injection speed, flow distance, gate design, and part thickness. Summarizing, an increase in melt temperature was found to have a positive impact on shielding, leading to an improvement of up to 10%. This increase in temperature also had a similarly positive effect on static electrical conductivity. The injection speed, on the other hand, had a negative but not particularly significant effect on shielding. It induced an average decrease of 1% in the studied materials. The flow distance along the mould cavity, whether near or opposite to the gate, had a negative effect on shielding for all the compounds. This resulted in a reduction of shielding of up to 12% in some cases. The gate design was found to significantly influence electromagnetic shielding and electrical conductivity. A sprue gate at the centre of the part induced higher electromagnetic shielding compared to the lateral edge gate with a smaller cross-section. The thickness of the part generally had a direct positive effect on electromagnetic shielding. However, it was observed that in thinner samples, there's an increase in electrical conductivity that counters the decrease in shielding, thereby balancing the overall performance.

These findings highlight the complex interplay of various factors in the injection moulding process and their impact on electromagnetic shielding and electrical conductivity of the materials.

**How are the electrical conductivity and dielectric function interconnected with the electromagnetic shielding properties of polymer aggregates?**

The research has revealed a clear relationship between electromagnetic shielding effectiveness and electrical conductivity. As EC increases, the EMSE also increases, and this relationship follows an exponential trend primarily due to the absorption mechanism of shielding. Additionally, the study has shown that the longitudinal conductivity with frequency-dependent properties plays a crucial role in the shielding of the polymer compounds.

**How can the anisotropic conductivity and dielectric function of these heterogeneous composites be precisely measured?**

This research has introduced two experimental procedures for measuring anisotropic electrical conductivity. The first method involves static (DC) measurements, which have shown some underestimation of the materials' conductivities. Therefore, this approach should be further improved in future studies. The second experimental procedure was developed to characterize frequency-dependent conductivity using an equivalent electrical impedance model. This method has yielded promising results, particularly when a conversion ratio from the static measurements was applied to adapt the through-thickness conductivity for the longitudinal direction.

**How can the electromagnetic properties of these polymeric compounds be theoretically evaluated to forecast the performance of a given product?**

The studies conducted in this research have revealed that, despite the heterogeneous nature of polymer compounds resulting from the distribution of fibres during the injection process, it's possible to represent them theoretically using only their bulk properties, specifically transverse and longitudinal conductivity. In this context, a theoretical model based on the transfer matrix of refractive indices for a homogeneous dissipative medium with conductivity defined by the equivalent LCR impedance and adjusted longitudinal properties has proven to be the most accurate approach for estimating the electromagnetic shielding of these polymeric aggregates.

Furthermore, in addition to the studies involving the injection moulding of fibre-filled thermoplastic compounds, two additional investigations were carried out to explore recent advancements in electromagnetic shielding properties enabled by graphene-based solutions and complex materials

produced through additive manufacturing. The results of these studies have highlighted the promising potential of these innovative materials and technologies for various applications requiring electromagnetic shielding characteristics.

### **Can the additive manufacturing of continuous carbon fibre be an effective fabrication technology for developing products capable of blocking electromagnetic waves?**

The printing of continuous carbon fibre by material extrusion technique was used to produce 2 mm thick composite parts with electromagnetic shielding that can reach 70 dB. This is an improvement of more than 22 times, from the baseline printed composite polyamide material (Onyx™) without any continuous carbon fibre layer. The versatility of these composites offers a significant advantage, allowing for tailored performance through easy modification of the internal structure. Depending on the number of CF layers and frequency, these composites exhibit EMSE ranging from 40 to 70 dB, with potential for even higher efficiency in thicker specimens. Additionally, the investigation identified absorption shielding ranging from 80% to 90%, indicating an adsorption-dominated shielding mechanism, and combining with a specific shielding up to 60 dB.cm<sup>3</sup>/g, these additive manufacturing composites emerge as a promising lightweight solution for electromagnetic shielding, particularly in applications demanding high absorption rates.

### **How efficient is the EM shielding provided by the graphene-based solutions?**

The graphene in the form of FLG and MLG dispersed in a solution to coat a silicone substrate was investigated as a potential EM shielding solution. Produced coatings with typical layer thicknesses ranging from 100 to 300 micrometres and an average measured sheet resistance within the range of 50 to 100 Ohm/sq, resulted in unsatisfactory shielding efficiencies below 15 dB across the entire frequency spectrum from 30 MHz to 3 GHz. This level of shielding can still be used in some less demanding applications, but if the required EMSE is higher than 30 dB then to achieve it was found that is necessary to increase the coating thickness and/or improve the graphene's electrical conductivity. For instance, if the coating thickness remains between 100 to 300 micrometres, then the graphene solution must be enhanced to achieve a conductivity near 1000 S/m. Conversely, if the graphene quality remains the same, with conductivities in the range of 150 S/m, then the thickness of the coating must be increased to over 1 mm.

## 5.2 Future research opportunities

Based on the results and insights gained from this research, the following areas of study and improvements can be considered:

- Enhancement of the Conductivity Apparatus: Continue to develop the static (DC) conductivity experimental apparatus to improve accuracy. In addition to its improvement these electrodes should be tested in conjunction with an impedance analyser to perform electrical characterization in the frequency-dependent domain. The latter should be studied more carefully in polymeric compounds containing ferromagnetic fillers.
- Microstructure Analysis: Investigate filler concentration and dispersion through microstructure observation. Understanding the material's internal structure and how fillers are distributed can provide valuable insights into their shielding effectiveness and electrical conductivity properties of fibre-filled thermoplastic compounds.
- Additive Manufacturing Studies: Expand the research on additive manufacturing of continuous carbon fibre-reinforced thermoplastics by analysing the EM shielding effectiveness of structures manufactured in different printing directions.
- Graphene Applications: Explore the application of graphene onto various materials and processing technologies.
- Real-World Case Studies: Apply CF, SSF or graphene-filled polymers to real industrial case studies. Develop an experimental and theoretical characterization of electromagnetic shielding for complex 3D structures used in practical applications.
- Economic and environmental impact: Comprehending the economic and environmental benefits achievable with the utilization of polymeric compounds for electromagnetic shielding is pivotal for industrial adoption. Therefore, an investigation into this topic is imperative.

These future studies will contribute to a deeper understanding of electromagnetic shielding materials and their practical applications, as well as advance the development of more effective shielding solutions in various industries.

# REFERENCES

- [1] E. Hanada *et al.*, "Electromagnetic interference on medical equipment by low-power mobile telecommunication systems," *IEEE Trans. Electromagn. Compat.*, vol. 42, no. 4, pp. 470–476, 2000, doi: 10.1109/15.902316.
- [2] K. L. Kaiser, *Electromagnetic Shielding*. Boca Raton: CRC Press, 2005.
- [3] D. A. Weston, *Electromagnetic compatibility: principles and applications*, 2nd ed. New York: Marcel Dekker, 2001.
- [4] X. C. Tong, *Advanced Materials and Design for Electromagnetic Interference Shielding*. Boca Raton: CRC Press, 2009.
- [5] N. Bryant, "EMI Shielding Effects of Carbon Nanotubes on Traditional EMI Plastics," in *IEEE International Symposium on Electromagnetic Compatibility (EMC)*, 2010, pp. 194–197.
- [6] N. Bryant, "Using Long Fiber Nickel Coated Carbon Fiber (LFNCCF) to produce Light Weight EMI Shielding Plastic Composites," in *2013 IEEE International Symposium on Electromagnetic Compatibility*, 2013, pp. 371–375.
- [7] V. P. Kodali, *Engineering electromagnetic compatibility: principles, measurements, and technologies*. New York: IEEE Press, 1996.
- [8] D. Jiang *et al.*, "Electromagnetic Interference Shielding Polymers and Nanocomposites - A Review," *Polym. Rev.*, vol. 59, no. 2, pp. 280–337, 2019, doi: 10.1080/15583724.2018.1546737.
- [9] D. D. . Chung, "Electromagnetic interference shielding effectiveness of carbon materials," *Carbon N. Y.*, vol. 39, no. 2, pp. 279–285, 2001, doi: 10.1016/S0008-6223(00)00184-6.
- [10] S. Geetha, K. K. S. Kumar, C. R. K. Rao, M. Vijayan, and D. C. Trivedi, "EMI Shielding: Methods and Materials – A Review," *J. Appl. Polym. Sci.*, vol. 112, no. 1, pp. 2073–2086, 2009, doi: 10.1002/app.
- [11] M. H. Al-saleh and U. Sundararaj, "Electromagnetic interference shielding mechanisms of CNT / polymer composites," *Carbon N. Y.*, vol. 47, no. 7, pp. 1738–1746, 2009, doi: 10.1016/j.carbon.2009.02.030.
- [12] C. Morari, I. Balan, J. Pintea, E. Chitanu, and I. Iordache, "Electrical Conductivity and Electromagnetic Shielding Effectiveness of Silicone Rubber Filled With Ferrite and Graphite Powders," *Prog. Electromagn. Res. M*, vol. 21, no. September, pp. 93–104, 2011, doi: 10.2528/PIERM11080406.
- [13] D. D. L. Chung, "Materials for Electromagnetic Interference Shielding," *J. Mater. Eng. Perform.*, vol. 9, no. 3, pp. 350–354, 2000, doi: 10.1361/105994900770346042.
- [14] M. H. Al-Saleh and U. Sundararaj, "Electromagnetic interference shielding mechanisms of CNT/polymer composites," *Carbon N. Y.*, vol. 47, no. 7, pp. 1738–1746, 2009, doi: 10.1016/j.carbon.2009.02.030.
- [15] P. Saini and M. Arora, "Microwave Absorption and EMI Shielding Behavior of Nanocomposites Based on Intrinsically Conducting Polymers , Graphene and Carbon Nanotubes," in *New Polymers for special applications*, 2012, pp. 71–112.
- [16] S. Yang, K. Lozano, A. Lomeli, H. D. Foltz, and R. Jones, "Electromagnetic interference shielding effectiveness of carbon nanofiber/LCP composites," *Compos. Part A Appl. Sci. Manuf.*, vol. 36, no. 5, pp. 691–697, 2005, doi: 10.1016/j.compositesa.2004.07.009.
- [17] Y. Bhattacharjee, I. Arief, and S. Bose, "Recent trends in multi-layered architectures towards screening electromagnetic radiation: Challenges and perspectives," *J. Mater. Chem. C*, vol. 5, no. 30, pp. 7390–7403, 2017, doi: 10.1039/c7tc02172k.
- [18] D. Munalli, G. Dimitrakis, D. Chronopoulos, S. Greedy, and A. Long, "Electromagnetic shielding effectiveness of carbon fibre reinforced composites," *Compos. Part B Eng.*, vol. 173, no. December 2018, p. 106906, 2019, doi: 10.1016/j.compositesb.2019.106906.
- [19] J. Fan *et al.*, "A review of additive manufacturing of metamaterials and developing trends," *Mater. Today*, vol. xxx, no. xx, 2021, doi: 10.1016/j.mattod.2021.04.019.
- [20] S. Yuan, S. Li, J. Zhu, and Y. Tang, "Additive manufacturing of polymeric composites from material processing to structural design," *Compos. Part B Eng.*, vol. 219, no. November 2020, p. 108903, 2021, doi:

- 10.1016/j.compositesb.2021.108903.
- [21] T. K. Das and S. Prusty, "Review on Conducting Polymers and Their Applications," *Polym. - Plast. Technol. Eng.*, vol. 51, no. 14, pp. 1487–1500, 2012, doi: 10.1080/03602559.2012.710697.
- [22] L. C. Martins and A. J. Pontes, "Fiber reinforced thermoplastics compounds for electromagnetic interference shielding applications," *J. Reinf. Plast. Compos.*, 2021, doi: 10.1177/07316844211051732.
- [23] S. K. Chiu *et al.*, "Electromagnetic shielding of plastic material in laser diode modules," in *IEEE Electronic Components and Technology Conference*, 2001, pp. 645–647, doi: 10.1109/ECTC.2001.927797.
- [24] J. M. Thomassin, C. Jérôme, T. Pardoën, C. Bailly, I. Huynen, and C. Detrembleur, "Polymer/carbon based composites as electromagnetic interference (EMI) shielding materials," *Mater. Sci. Eng. R Reports*, vol. 74, no. 7, pp. 211–232, 2013, doi: 10.1016/j.mser.2013.06.001.
- [25] S. Sankaran, K. Deshmukh, M. B. Ahamed, and S. K. Khadheer Pasha, "Recent advances in electromagnetic interference shielding properties of metal and carbon filler reinforced flexible polymer composites: A review," *Compos. Part A Appl. Sci. Manuf.*, vol. 114, no. April, pp. 49–71, 2018, doi: 10.1016/j.compositesa.2018.08.006.
- [26] M. H. Al-Saleh and U. Sundararaj, "Electromagnetic interference (EMI) shielding effectiveness of PP/PS polymer blends containing high structure carbon black," *Macromol. Mater. Eng.*, vol. 293, no. 7, pp. 621–630, 2008, doi: 10.1002/mame.200800060.
- [27] D. D. L. Chung, "Materials for Electromagnetic Interference Shielding," *J. Mater. Eng. Perform.*, vol. 9, no. 3, pp. 350–354, 2000, doi: 10.1361/105994900770346042.
- [28] D. J. Griffiths, "Introduction-to-Electrodynamics\_griffith," *Prentice Hall*, vol. 3rd editio. 1999.
- [29] J. D. Jackson, *Classical Electrodynamics*. John Wiley & Sons, Inc., 1998.
- [30] M. Born and E. Wolf, *Principles of Optics: Electromagnetic Theory of Propagation, Interference and Diffraction of Light*. Pergamon Press, 1980.
- [31] M. A. Dupertuis and M. J. Proctor, "Generalization of complex Snell–Descartes and Fresnel laws," *J. Opt. Soc. Am.*, vol. 11, no. 3, pp. 1159–1166, 1994, doi: 10.1364/oam.1990.fz10.
- [32] F. Frezza and N. Tedeschi, "On the electromagnetic power transmission between two lossy media: discussion," *J. Opt. Soc. Am. A*, vol. 29, no. 11, p. 2281, 2012, doi: 10.1364/josaa.29.002281.
- [33] J. E. Vitela, "Electromagnetic waves in dissipative media revisited," *Am. J. Phys.*, vol. 72, no. 3, pp. 393–403, 2004, doi: 10.1119/1.1639010.
- [34] S. Y. Kim and K. Vedam, "Analytic solution of the pseudo-Brewster angle," *J. Opt. Soc. Am. A*, vol. 3, no. 11, p. 1772, 1986, doi: 10.1364/josaa.3.001772.
- [35] F. X. Canning, "Corrected Fresnel coefficients for lossy materials," *IEEE Antennas Propag. Soc. AP-S Int. Symp.*, no. 4, pp. 2123–2126, 2011, doi: 10.1109/APS.2011.5996930.
- [36] J. Shen, H. Yu, and J. Lu, "Light propagation and reflection-refraction event in absorbing media," *Chinese Opt. Lett.*, vol. 8, no. 1, pp. 111–114, 2010, doi: 10.3788/COL20100801.0111.
- [37] Y. Zang, J. Chen, and S. He, "Theoretical study of visible light refraction phenomena occurring at noble metal-air interfaces," *Opt. Mater. (Amst.)*, vol. 46, pp. 276–281, 2015, doi: 10.1016/j.optmat.2015.04.032.
- [38] K. E. Oughstun and C. L. Palombini, "Fresnel Reflection and Transmission Coefficients for Temporally Dispersive Attenuative Media," *Radio Sci.*, vol. 53, no. 11, pp. 1382–1397, 2018, doi: 10.1029/2018RS006646.
- [39] R. J. Churchill and T. G. Philbin, "Electromagnetic reflection, transmission, and energy density at boundaries of nonlocal media," *Phys. Rev. B*, vol. 235422, no. 23, pp. 1–11, 2016, doi: 10.1103/PhysRevB.94.235422.
- [40] H. Weber, "The Fresnel equations for lossy dielectrics and conservation of energy," *J. Mod. Opt.*, vol. 61, no. 15, pp. 1219–1224, 2014, doi: 10.1080/09500340.2014.928375.
- [41] W. H. Lin, C. J. Wu, and S. J. Chang, "ANGULAR DEPENDENCE OF WAVE REFLECTION IN A LOSSY SINGLE-NEGATIVE BILAYER," *Prog. Electromagn. Res.*, vol. 107, pp. 253–267, 2010.
- [42] X. Luo and D. D. L. Chung, "Electromagnetic interference shielding using continuous carbon-fiber carbon-matrix and polymer-matrix composites," *Compos. Part B Eng.*, vol. 30, no. 3, pp. 227–231, 1999, doi: 10.1016/S1359-

## References

---

- 8368(98)00065-1.
- [43] M. Rahaman, T. K. Chaki, and D. Khastgir, "Shielding with conductive polymer and carbon fiber composites," in *Society of Plastics Engineers Proceedings*, 2012, pp. 2–4, doi: 10.1002/spepro.003964.
- [44] S. Das Ramôa, G. M. Barra, R. V. Oliveira, M. G. De Oliveira, M. Cossa, and B. G. Soares, "Electrical, rheological and electromagnetic interference shielding properties of thermoplastic polyurethane/carbon nanotube composites," *Polym. Int.*, vol. 62, no. 10, pp. 1477–1484, 2013, doi: 10.1002/pi.4446.
- [45] a. Ameli, P. U. Jung, and C. B. Park, "Electrical properties and electromagnetic interference shielding effectiveness of polypropylene/carbon fiber composite foams," *Carbon N. Y.*, vol. 60, pp. 379–391, 2013, doi: 10.1016/j.carbon.2013.04.050.
- [46] M. Arjmand, M. Mahmoodi, G. A. Gelves, S. Park, and U. Sundararaj, "Electrical and electromagnetic interference shielding properties of flow-induced oriented carbon nanotubes in polycarbonate," *Carbon N. Y.*, vol. 49, no. 11, pp. 3430–3440, 2011, doi: 10.1016/j.carbon.2011.04.039.
- [47] W.-S. Cheng, C.-S. Chen, S.-C. Chen, and R.-D. Chien, "Investigation of the Effects of Injection Molding Processing Parameters on Conductive Polymeric Composites for Electromagnetic Interference Shielding Effectiveness," *Polym. Plast. Technol. Eng.*, vol. 48, no. 2, pp. 216–220, 2009, doi: 10.1080/03602550802634592.
- [48] S. Geetha, K. K. S. Kumar, C. R. K. Rao, M. Vijayan, and D. C. Trivedi1, "EMI Shielding: Methods and Materials—A Review," *J. Appl. Polym. Sci.*, vol. 112, no. 5, pp. 2073–2086, 2009, doi: 10.1002/app.
- [49] C. Huang and C. Wu, "The EMI shielding effectiveness of PC/ABS/nickel-coated- carbon-fibre composites," *Eur. Polym. J.*, vol. 36, pp. 2729–2737, 2000.
- [50] P. H. Lee, S. C. Chen, J. S. Huang, R. D. Chien, and S. C. Lee, "Effects of Molding Conditions on the Electromagnetic Interference Performance of Injection Molded ABS Parts with Conductive Fibers," in *ANTEC Proceedings*, 2005, pp. 635–639.
- [51] S. K. H. Gulrez *et al.*, "A Review on Electrically Conductive Polypropylene and Polyethylene," *Polym. Compos.*, vol. 35, pp. 900–914, 2014, doi: 0.1002/pc.22734.
- [52] M. Jouni, D. Djurado, V. Massardier, and G. Boiteux, "A representative and comprehensive review of the electrical and thermal properties of polymer composites with carbon nanotube and other nanoparticle fillers," *Polym. Int.*, vol. 66, no. 9, pp. 1237–1251, 2017, doi: 10.1002/pi.5378.
- [53] A. Kausar, S. Ahmad, and S. M. Salman, "Effectiveness of Polystyrene/Carbon Nanotube Composite in Electromagnetic Interference Shielding Materials: A Review," *Polym. - Plast. Technol. Eng.*, vol. 56, no. 10, pp. 1027–1042, 2017, doi: 10.1080/03602559.2016.1266367.
- [54] N. Bagogia, V. Choudhary, and D. K. Sharma, "A review on the mechanical, electrical and EMI shielding properties of carbon nanotubes and graphene reinforced polycarbonate nanocomposites," *Polym. Adv. Technol.*, vol. 29, no. 6, pp. 1547–1567, 2018, doi: 10.1002/pat.4277.
- [55] P. Banerjee, Y. Bhattacharjee, and S. Bose, "Lightweight Epoxy-Based Composites for EMI Shielding Applications," *J. Electron. Mater.*, vol. 49, no. 3, pp. 1702–1720, 2020, doi: 10.1007/s11664-019-07687-5.
- [56] J. Martinsson and J. L. White, "Characteristics of Thermoplastics Containing Electrically Conducting Asymmetric Particles: Anisotropic Electrical Conductivity of Injection Molded Parts and Extrusion Behavior," vol. 7, no. 5, pp. 302–314, 1986.
- [57] R. M. Simon, "Emi Shielding With Conductive Plastics.," in *IEEE International Symposium on Electromagnetic Compatibility*, 1983, pp. 281–285.
- [58] B. D. Mottahed and S. Manoochehri, "A review of research in materials, modeling and simulation, design factors, testing, and measurements related to electromagnetic interference shielding," *Polym. Plast. Technol. Eng.*, vol. 34, no. 2, pp. 271–346, 1995, doi: 10.1080/03602559508015827.
- [59] U. Lundgren, J. Ekman, and J. Delsing, "Shielding Effectiveness Data on Commercial Thermoplastic Materials," *IEEE Trans. Electromagn. Compat.*, vol. 48, no. 4, pp. 766–773, 2006.
- [60] A. Rahman, I. Ali, S. M. Al Zahrani, and R. H. Eleithy, "A review of the applications of nanocarbon polymer composites," *Nano*, vol. 6, no. 3, pp. 185–203, 2011, doi: 10.1142/S179329201100255X.
- [61] M. Weber and M. R. Kamal, "Microstructure and volume resistivity of composites of isotactic polypropylene reinforced

- with electrically conductive fibers," *Polym. Compos.*, vol. 18, no. 6, pp. 726–740, 1997, doi: 10.1002/pc.10325.
- [62] A. Ameli, M. Nofar, S. Wang, and C. B. Park, "Lightweight Polypropylene/Stainless-Steel Fiber Composite Foams with Low Percolation for Efficient Electromagnetic Interference Shielding," *ACS Appl. Mater. Interfaces*, no. 6, pp. 11091–11100, 2014.
- [63] S. Mondal *et al.*, "Electrical conductivity and electromagnetic interference shielding effectiveness of nano-structured carbon assisted poly(methyl methacrylate) nanocomposites," *Polym. Eng. Sci.*, vol. 60, no. 10, pp. 2414–2427, 2020, doi: 10.1002/pen.25480.
- [64] Y. Bhattacharjee, V. Bhingardive, S. Biswas, and S. Bose, "Construction of a carbon fiber based layer-by-layer (LbL) assembly—a smart approach towards effective EMI shielding," *RSC Adv.*, vol. 6, no. 113, pp. 112614–112619, 2016, doi: 10.1039/C6RA24238C.
- [65] Y. Jia, T. D. Ajayi, B. H. Wahls, K. R. Ramakrishnan, S. Ekkad, and C. Xu, "Multifunctional Ceramic Composite System for Simultaneous Thermal Protection and Electromagnetic Interference Shielding for Carbon Fiber-Reinforced Polymer Composites," *ACS Appl. Mater. Interfaces*, vol. 12, no. 52, pp. 58005–58017, 2020, doi: 10.1021/acscami.0c17361.
- [66] M. H. Al-saleh and U. Sundararaj, "Microstructure, Electrical, and Electromagnetic Interference Shielding Properties of Carbon Nanotube/Acrylonitrile – Butadiene – Styrene Nanocomposites," *J. Polym. Sci. - Part B Polym. Phys.*, vol. 50, no. 19, pp. 1356–1362, 2012, doi: 10.1002/polb.23129.
- [67] M. H. Al-Saleh, W. H. Saadeh, and U. Sundararaj, "EMI shielding effectiveness of carbon based nanostructured polymeric materials: A comparative study," *Carbon N. Y.*, vol. 60, pp. 146–156, 2013, doi: 10.1016/j.carbon.2013.04.008.
- [68] M. H. Al-Saleh, "Influence of conductive network structure on the EMI shielding and electrical percolation of carbon nanotube/polymer nanocomposites," *Synth. Met.*, 2015, doi: 10.1016/j.synthmet.2015.03.032.
- [69] M. H. Al-saleh, "Electrical, EMI shielding and tensile properties of PP/PE blends filled with GNP:CNT hybrid nanofiller," *Synth. Met.*, vol. 217, pp. 322–330, 2016.
- [70] M. Arjmand, T. Apperley, M. Okoniewski, and U. Sundararaj, "Comparative study of electromagnetic interference shielding properties of injection molded versus compression molded multi-walled carbon nanotube/polystyrene composites," *Carbon N. Y.*, vol. 50, no. 14, pp. 5126–5134, 2012, doi: 10.1016/j.carbon.2012.06.053.
- [71] M. H. Zhang and J. K. Chen, "Electrical and thermal properties of stainless steel fibers and carbon nanotubes reinforced polyamide-6," *Plast. Rubber Compos.*, vol. 42, no. 10, pp. 437–445, 2013, doi: 10.1179/1743289813Y.0000000063.
- [72] J. M. K. Julia A. King, Rodwick L. Barton, Rebecca A. Hauser, "Synergistic Effects of Carbon Fillers in Electrically and Thermally Conductive Liquid Crystal Polymer Based Resins," *Polym. Compos.*, vol. 29, no. 4, pp. 421–428, 2008, doi: 10.1002/pc.
- [73] Z. Fan, C. Zheng, T. Wei, Y. Zhang, and G. Luo, "Effect of carbon black on electrical property of graphite nanoplatelets/epoxy resin composites," *Polym. Eng. Sci.*, vol. 49, no. 10, pp. 2041–2045, 2009, doi: 10.1002/pen.21445.
- [74] P. E. A. Tokobaro, N. M. Larocca, E. H. Backes, and L. A. Pessan, "Effects of mineral fillers addition and preparation method on the morphology and electrical conductivity of epoxy/multiwalled carbon nanotube nanocomposites," *Polym. Eng. Sci.*, vol. 61, no. 2, pp. 538–550, 2021, doi: 10.1002/pen.25598.
- [75] A. Shayesteh Zeraati, A. Mende Anjaneyalu, S. P. Pawar, A. Abouelmagd, and U. Sundararaj, "Effect of secondary filler properties and geometry on the electrical, dielectric, and electromagnetic interference shielding properties of carbon nanotubes/polyvinylidene fluoride nanocomposites," *Polym. Eng. Sci.*, vol. 61, no. 4, pp. 959–970, 2021, doi: 10.1002/pen.25591.
- [76] S. Zhou, A. N. Hrymak, and M. R. Kamal, "Microinjection molding of polypropylene/multi-walled carbon nanotube nanocomposites: The influence of process parameters," *Polym. Eng. Sci.*, vol. 58, pp. E226–E234, 2018, doi: 10.1002/pen.24682.
- [77] S. I. S. Shaharuddin, M. S. Salit, and E. S. Zainudin, "A review of the effect of molding parameters on the performance of polymeric composite injection molding," *Turkish J. Eng. Environ. Sci.*, vol. 30, pp. 23–34, 2006, doi: 10.3906/sag-1207-74.



## References

---

- [78] C. Severance and D. Nobbs, "Effect of Processing Parameters on Electrical Properties of Electrically Conductive Composites," in *ANTEC Proceedings*, 2006, pp. 471–475.
- [79] S. Y. Yang, C. Y. Chen, and S. H. Parng, "Effects of conductive fibers and processing conditions on the electromagnetic shielding effectiveness of injection molded composites," *Polym. Compos.*, vol. 23, no. 6, pp. 1003–1013, 2002, doi: 10.1002/pc.10496.
- [80] S. C. Chen, R. Der Chien, P. H. Lee, and J. S. Huang, "Effects of molding conditions on the electromagnetic interference performance of conductive ABS parts," *J. Appl. Polym. Sci.*, vol. 98, no. 3, pp. 1072–1080, 2005, doi: 10.1002/app.22241.
- [81] C. S. Chen, W. R. Chen, S. C. Chen, and R. Der Chien, "Optimum injection molding processing condition on EMI shielding effectiveness of stainless steel fiber filled polycarbonate composite," *Int. Commun. Heat Mass Transf.*, vol. 35, no. 6, pp. 744–749, 2008, doi: 10.1016/j.icheatmasstransfer.2008.02.006.
- [82] M. Mahmoodi, M. Arjmand, U. Sundararaj, and S. Park, "The electrical conductivity and electromagnetic interference shielding of injection molded multi-walled carbon nanotube/polystyrene composites," *Carbon N. Y.*, vol. 50, no. 4, pp. 1455–1464, 2012, doi: 10.1016/j.carbon.2011.11.004.
- [83] A. Ameli, P. U. Jung, and C. B. Park, "Effects of process variables on through-plane electrical conductivity of injection-molded carbon fiber/polypropylene composite foams," 2012.
- [84] N. Bryant, "Property Optimization of EMI Compounds through the DOE Process," 2013. [Online]. Available: <https://www.rtpcompany.com/education/white-papers/property-optimization-of-emi-compounds-through-the-doe-process/>.
- [85] S. C. Chen, R. Der Chien, P. H. Lee, and J. S. Huang, "Effects of molding conditions on the electromagnetic interference performance of conductive ABS parts," *J. Appl. Polym. Sci.*, vol. 98, no. 3, pp. 1072–1080, 2005, doi: 10.1002/app.22241.
- [86] P. Lee, "Study on Effects of Molded Conditions on the Fiber Orientation and Electrical Conductivity of Injection Molded Bipolar Plate for Fuel Cell," 1996.
- [87] M. Mahmoodi, M. Arjmand, U. Sundararaj, and S. Park, "The electrical conductivity and electromagnetic interference shielding of injection molded multi-walled carbon nanotube / polystyrene composites," *Carbon N. Y.*, vol. 50, no. 4, pp. 1455–1464, 2011, doi: 10.1016/j.carbon.2011.11.004.
- [88] B. Archambeault, O. M. Ramahi, and C. Brench, *EMI/EMC Computational Modeling Handbook*, Second Edi. Kluwer Academic Publishers, 2001.
- [89] W. Al-shabib and S. W. Lachowicz, "Modelling of polyaniline for wi-fi electromagnetic interference shielding Modelling of Polyaniline for Wi-Fi Electromagnetic Interference Shielding," 2013.
- [90] W. Dagang *et al.*, "Numerical modeling of periodic composite media for electromagnetic shielding application," 2007.
- [91] N. B. Janda, J. M. Keith, J. A. King, W. F. Perger, and T. J. Oxby, "Shielding-Effectiveness Modeling of Carbon-Fiber/Nylon-6,6 Composites," *J. Appl. Polym. Sci.*, vol. 96, no. 1, pp. 62–69, 2005, doi: 10.1002/app.21426.
- [92] J. M. Keith, N. B. Janda, J. A. King, W. F. Perger, and T. J. Oxby, "Shielding Effectiveness Density Theory for Carbon Fiber / Nylon 6 , 6 Composites," *Polym. Compos.*, vol. 26, pp. 671–678, 2005, doi: 10.1002/pc.20139.
- [93] M. Y. Koledintseca, J. Drewniak, R. DuBroff, K. Rozanov, and B. Archambeault, "Modeling of shielding Composite Materials and Structures for Microwave Frequencies," *Prog. Electromagn. Res. B*, vol. 15, pp. 197–215, 2009.
- [94] Z. Liu and Z. Zhou, "Computation of shielding effectiveness for electromagnetic shielding blended fabric," *Prz. Elektrotechniczny*, vol. 89, no. 3, pp. 228–230, 2013.
- [95] D. Micheli, "Broadband electromagnetic characterization of carbon foam to metal contact," *Carbon N. Y.*, vol. 68, pp. 149–158, 2013, doi: 10.1016/j.carbon.2013.10.074.
- [96] L. Paliotta *et al.*, "Highly conductive multilayer-graphene paper as a flexible lightweight electromagnetic shield," *Carbon N. Y.*, vol. 89, pp. 260–271, 2015, doi: 10.1016/j.carbon.2015.03.043.
- [97] ASTM International, "ASTM D 4935-99: Standard Test Method for Measuring the Electromagnetic Shielding Effectiveness of Planar Materials," vol. 10.02, p. 10, 1999, doi: 10.1520/D4935-99.
- [98] Y. K. Hong, C. Y. Lee, C. K. Jeong, D. E. Lee, K. Kim, and J. Joo, "Method and apparatus to measure electromagnetic interference shielding efficiency and its shielding characteristics in broadband frequency ranges," *Rev. Sci. Instrum.*,

- vol. 74, no. 2, pp. 1098–1102, 2003, doi: 10.1063/1.1532540.
- [99] M. S. Sarto and A. Tamburrano, “Innovative test method for the shielding effectiveness measurement of conductive thin films in a wide frequency range,” *IEEE Trans. Electromagn. Compat.*, vol. 48, no. 2, pp. 331–341, 2006, doi: 10.1109/TEMC.2006.874664.
- [100] H. Vasquez, L. Espinoza, and K. Lozano, “Simple Device for Electromagnetic Interference Shielding Effectiveness Measurement,” *IEEE Trans. Electromagn. Compat.*, pp. 62–68, 2009.
- [101] P. Andersen, “International electrotechnical commission documents CISPR 12 and CISPR 25 - An overview,” *IEEE Int. Symp. Electromagn. Compat.*, pp. 10–13, 2007, doi: 10.1109/ISEMC.2007.36.
- [102] F. M. Oliveira, L. Martins, N. V. Dencheva, T. A. Ezquerro, and Z. Z. Denchev, “Tunable Electromagnetic Interference Shielding Properties of Binary Thermoplastic Composites Prepared by Reactive Microencapsulation,” *ACS Appl. Polym. Mater.*, vol. 4, no. 5, pp. 3482–3490, 2022, doi: 10.1021/acsapm.2c00084.
- [103] F. Ren *et al.*, “Large-scale preparation of segregated PLA/carbon nanotube composite with high efficient electromagnetic interference shielding and favourable mechanical properties,” *Compos. Part B Eng.*, vol. 155, no. August, pp. 405–413, 2018, doi: 10.1016/j.compositesb.2018.09.030.
- [104] W. Kong *et al.*, “Polyaniline-decorated carbon fibers for enhanced mechanical and electromagnetic interference shielding performances of epoxy composites,” *Mater. Des.*, vol. 217, p. 110658, 2022, doi: 10.1016/j.matdes.2022.110658.
- [105] D. P. Schmitz, S. Dul, S. D. A. S. Ramoa, B. G. Soares, G. M. O. Barra, and A. Pegoretti, “Effect of printing parameters on the electromagnetic shielding efficiency of ABS/carbonaceous-filler composites manufactured via filament fused fabrication,” *J. Manuf. Process.*, vol. 65, no. June 2020, pp. 12–19, 2021, doi: 10.1016/j.jmapro.2021.02.051.
- [106] K. P. M. Lee, T. Baum, R. Shanks, and F. Daver, “Electromagnetic interference shielding of 3D-printed graphene–polyamide-6 composites with 3D-printed morphology,” *Addit. Manuf.*, vol. 43, no. May, p. 102020, 2021, doi: 10.1016/j.addma.2021.102020.
- [107] N. C. Das, T. K. Chaki, and D. Khastgir, “Effect of processing parameters, applied pressure and temperature on the electrical resistivity of rubber-based conductive composites,” *Carbon N. Y.*, vol. 40, no. 6, pp. 807–816, 2002, doi: 10.1016/S0008-6223(01)00229-9.
- [108] K. Chizari, M. Arjmand, Z. Liu, U. Sundararaj, and D. Therriault, “Three-dimensional printing of highly conductive polymer nanocomposites for EMI shielding applications,” *Mater. Today Commun.*, vol. 11, pp. 112–118, 2017, doi: 10.1016/j.mtcomm.2017.02.006.
- [109] C. H. Cui *et al.*, “A high heat-resistance bioplastic foam with efficient electromagnetic interference shielding,” *Chem. Eng. J.*, vol. 323, no. 24, pp. 29–36, 2017, doi: 10.1016/j.cej.2017.04.050.
- [110] A. Ameli, P. U. Jung, and C. B. Park, “Low Percolation Threshold and Improved Electromagnetic Interference Shielding Effectiveness Polypropylene/Carbon Fiber Composites Through Fo,” in *ANTEC Proceedings*, 2013, pp. 6–11.
- [111] L. C. Martins, C. N. Barbosa, S. Silva, P. Bernardo, G. R. Dias, and A. J. Pontes, “Effect of processing conditions on electromagnetic shielding and electrical resistivity of injection-molded polybutylene terephthalate compounds,” *Polym. Eng. Sci.*, vol. 61, no. 10, pp. 2576–2588, 2021, doi: 10.1002/pen.25784.
- [112] G. Wang, G. Zhao, S. Wang, L. Zhang, and C. B. Park, “Injection-molded microcellular PLA/graphite nanocomposites with dramatically enhanced mechanical and electrical properties for ultra-efficient EMI shielding applications,” *J. Mater. Chem. C*, vol. 6, no. 25, pp. 6847–6859, 2018, doi: 10.1039/c8tc01326h.
- [113] Y. Zhang, Z. Wang, Y. Zhang, S. Gomes, and A. Bernard, “Bio-inspired generative design for support structure generation and optimization in Additive Manufacturing (AM),” *CIRP Ann.*, vol. 69, no. 1, pp. 117–120, 2020, doi: 10.1016/j.cirp.2020.04.091.
- [114] V. N. Hoang, N. L. Nguyen, P. Tran, M. Qian, and H. Nguyen-Xuan, “Adaptive Concurrent Topology Optimization of Cellular Composites for Additive Manufacturing,” *JOM*, vol. 72, no. 6, pp. 2378–2390, 2020, doi: 10.1007/s11837-020-04158-9.
- [115] S. D. Nath and S. Nilufar, “An overview of additive manufacturing of polymers and associated composites,” *Polymers (Basel)*, vol. 12, no. 11, pp. 1–33, 2020, doi: 10.3390/polym12112719.
- [116] B. Redwood, F. Schöffner, and B. Garret, *The 3D Printing Handbook: Technologies, design and applications*.

## References

---

- Amsterdam: 3D Hubs, 2017.
- [117] T. D. Ngo, A. Kashani, G. Imbalzano, K. T. Q. Nguyen, and D. Hui, "Additive manufacturing (3D printing): A review of materials, methods, applications and challenges," *Compos. Part B Eng.*, vol. 143, no. December 2017, pp. 172–196, 2018, doi: 10.1016/j.compositesb.2018.02.012.
- [118] K. P. Motaparti, M. C. Leu, K. Chandrashekhara, and L. R. Dharani, "Effect of Build Parameters on Mechanical Properties of Ultem 9085 Parts By Fused Deposition Modeling," Missouri University of Science and Technology, 2016.
- [119] R. T. L. Ferreira, I. C. Amatte, T. A. Dutra, and D. Bürger, "Experimental characterization and micrography of 3D printed PLA and PLA reinforced with short carbon fibers," *Compos. Part B Eng.*, vol. 124, pp. 88–100, 2017, doi: 10.1016/j.compositesb.2017.05.013.
- [120] A. Dorigato, V. Moretti, S. Dul, S. H. Unterberger, and A. Pegoretti, "Electrically conductive nanocomposites for fused deposition modelling," *Synth. Met.*, vol. 226, pp. 7–14, 2017, doi: 10.1016/j.synthmet.2017.01.009.
- [121] D. P. Schmitz *et al.*, "Electromagnetic interference shielding effectiveness of ABS carbon-based composites manufactured via fused deposition modelling," *Mater. Today Commun.*, vol. 15, pp. 70–80, Jun. 2018, doi: 10.1016/J.MTCOMM.2018.02.034.
- [122] V. B. Mohan, B. J. Krebs, and D. Bhattacharyya, "Development of novel highly conductive 3D printable hybrid polymer-graphene composites," *Mater. Today Commun.*, vol. 17, no. September, pp. 554–561, 2018, doi: 10.1016/j.mtcomm.2018.09.023.
- [123] Y. Li *et al.*, "Additive manufacturing high performance graphene-based composites: A review," *Compos. Part A Appl. Sci. Manuf.*, vol. 124, no. May, p. 105483, 2019, doi: 10.1016/j.compositesa.2019.105483.
- [124] C. J. Hohimer, G. Petrossian, A. Ameli, C. Mo, and P. Pötschke, "3D printed conductive thermoplastic polyurethane/carbon nanotube composites for capacitive and piezoresistive sensing in soft pneumatic actuators," *Addit. Manuf.*, vol. 34, no. April, p. 101281, 2020, doi: 10.1016/j.addma.2020.101281.
- [125] Y. Wang *et al.*, "3D-printing of segregated carbon nanotube/poly(lactic acid) composite with enhanced electromagnetic interference shielding and mechanical performance," *Mater. Des.*, vol. 197, p. 109222, 2021, doi: 10.1016/j.matdes.2020.109222.
- [126] Y. Duan *et al.*, "A wide-angle broadband electromagnetic absorbing metastructure using 3D printing technology," *Mater. Des.*, vol. 208, p. 109900, 2021, doi: 10.1016/j.matdes.2021.109900.
- [127] A. Parmiggiani, M. Prato, and M. Pizzorni, "Effect of the fiber orientation on the tensile and flexural behavior of continuous carbon fiber composites made via fused filament fabrication," *Int. J. Adv. Manuf. Technol.*, vol. 114, no. 7–8, pp. 2085–2101, 2021, doi: 10.1007/s00170-021-06997-5.
- [128] L. G. Blok, M. L. Longana, H. Yu, and B. K. S. Woods, "An investigation into 3D printing of fibre reinforced thermoplastic composites," *Addit. Manuf.*, vol. 22, no. July, pp. 176–186, 2018, doi: 10.1016/j.addma.2018.04.039.
- [129] Markforged, "Material Datasheet: Composites v5.2," 2022. [Online]. Available: <https://www-objects.markforged.com/craft/materials/CompositesV5.2.pdf>.
- [130] P. Song *et al.*, "Obviously improved electromagnetic interference shielding performances for epoxy composites via constructing honeycomb structural reduced graphene oxide," *Compos. Sci. Technol.*, vol. 181, no. May, p. 107698, 2019, doi: 10.1016/j.compscitech.2019.107698.
- [131] S. Kashi, R. K. Gupta, T. Baum, N. Kao, and S. N. Bhattacharya, "Morphology, electromagnetic properties and electromagnetic interference shielding performance of poly(lactide)/graphene nanoplatelet nanocomposites," *Mater. Des.*, vol. 95, pp. 119–126, 2016, doi: 10.1016/j.matdes.2016.01.086.
- [132] G. Gedler, M. Antunes, J. I. Velasco, and R. Ozisik, "Enhanced electromagnetic interference shielding effectiveness of polycarbonate/graphene nanocomposites foamed via 1-step supercritical carbon dioxide process," *Mater. Des.*, vol. 90, pp. 906–914, 2016, doi: 10.1016/j.matdes.2015.11.021.
- [133] M. J. Allen, V. C. Tung, and R. B. Kaner, "Honeycomb carbon: A review of graphene," *Chem. Rev.*, vol. 110, no. 1, pp. 132–145, 2010, doi: 10.1021/cr900070d.
- [134] X. Fu, C. Yao, and G. Yang, "Recent advances in graphene/polyamide 6 composites: A review," *RSC Adv.*, vol. 5, no. 76, pp. 61688–61702, 2015, doi: 10.1039/c5ra09312k.

- [135] M. S. Cao, X. X. Wang, W. Q. Cao, and J. Yuan, "Ultrathin graphene: electrical properties and highly efficient electromagnetic interference shielding," *J. Mater. Chem. C*, vol. 3, no. 26, pp. 6589–6599, 2015, doi: 10.1039/c5tc01354b.
- [136] H. Kim, A. A. Abdala, and C. W. MacOsco, "Graphene/polymer nanocomposites," *Macromolecules*, vol. 43, no. 16, pp. 6515–6530, 2010, doi: 10.1021/ma100572e.
- [137] P. Kumar, F. Shahzad, S. Yu, S. M. Hong, Y. H. Kim, and C. M. Koo, "Large-area reduced graphene oxide thin film with excellent thermal conductivity and electromagnetic interference shielding effectiveness," *Carbon N. Y.*, vol. 94, pp. 494–500, 2015, doi: 10.1016/j.carbon.2015.07.032.
- [138] S. K. Hong *et al.*, "Electromagnetic interference shielding effectiveness of monolayer graphene," *Nanotechnology*, vol. 23, no. 45, 2012, doi: 10.1088/0957-4484/23/45/455704.
- [139] L. Zhang *et al.*, "Preparation and characterization of graphene paper for electromagnetic interference shielding," *Carbon N. Y.*, vol. 82, no. C, pp. 353–359, 2015, doi: 10.1016/j.carbon.2014.10.080.
- [140] Z. Chen, C. Xu, C. Ma, W. Ren, and H. M. Cheng, "Lightweight and flexible graphene foam composites for high-performance electromagnetic interference shielding," *Adv. Mater.*, vol. 25, no. 9, pp. 1296–1300, 2013, doi: 10.1002/adma.201204196.
- [141] D. X. Yan, P. G. Ren, H. Pang, Q. Fu, M. B. Yang, and Z. M. Li, "Efficient electromagnetic interference shielding of lightweight graphene/polystyrene composite," *J. Mater. Chem.*, vol. 22, no. 36, pp. 18772–18774, 2012, doi: 10.1039/c2jm32692b.
- [142] J. Liang *et al.*, "Electromagnetic interference shielding of graphene/epoxy composites," *Carbon N. Y.*, vol. 47, no. 3, pp. 922–925, 2009, doi: 10.1016/j.carbon.2008.12.038.
- [143] D. X. Yan *et al.*, "Structured reduced graphene oxide/polymer composites for ultra-efficient electromagnetic interference shielding," *Adv. Funct. Mater.*, vol. 25, no. 4, pp. 559–566, 2015, doi: 10.1002/adfm.201403809.
- [144] H. Bin Zhang, W. G. Zheng, Q. Yan, Z. G. Jiang, and Z. Z. Yu, "The effect of surface chemistry of graphene on rheological and electrical properties of polymethylmethacrylate composites," *Carbon N. Y.*, vol. 50, no. 14, pp. 5117–5125, 2012, doi: 10.1016/j.carbon.2012.06.052.
- [145] W. L. Song, J. Wang, L. Z. Fan, Y. Li, C. Y. Wang, and M. S. Cao, "Interfacial engineering of carbon nanofiber-graphene-carbon nanofiber heterojunctions in flexible lightweight electromagnetic shielding networks," *ACS Appl. Mater. Interfaces*, vol. 6, no. 13, pp. 10516–10523, 2014, doi: 10.1021/am502103u.
- [146] W. L. Song *et al.*, "Alignment of graphene sheets in wax composites for electromagnetic interference shielding improvement," *Nanotechnology*, vol. 24, no. 11, 2013, doi: 10.1088/0957-4484/24/11/115708.
- [147] B. Shen, W. Zhai, and W. Zheng, "Ultrathin flexible graphene film: An excellent thermal conducting material with efficient EMI shielding," *Adv. Funct. Mater.*, vol. 24, no. 28, pp. 4542–4548, 2014, doi: 10.1002/adfm.201400079.
- [148] N. Yousefi *et al.*, "Highly aligned graphene/polymer nanocomposites with excellent dielectric properties for high-performance electromagnetic interference shielding," *Adv. Mater.*, vol. 26, no. 31, pp. 5480–5487, 2014, doi: 10.1002/adma.201305293.
- [149] K. Batrakov *et al.*, "Enhanced microwave shielding effectiveness of ultrathin pyrolytic carbon films," *Appl. Phys. Lett.*, vol. 103, no. 7, 2013, doi: 10.1063/1.4818680.
- [150] K. Batrakov *et al.*, "Flexible transparent graphene/polymer multilayers for efficient electromagnetic field absorption," *Sci. Rep.*, vol. 4, pp. 1–5, 2014, doi: 10.1038/srep07191.
- [151] N. Agnihotri, K. Chakrabarti, and A. De, "Highly efficient electromagnetic interference shielding using graphite nanoplatelet/poly(3,4-ethylenedioxythiophene)-poly(styrenesulfonate) composites with enhanced thermal conductivity," *RSC Adv.*, vol. 5, no. 54, pp. 43765–43771, 2015, doi: 10.1039/c4ra15674a.

# **APPENDICES**

In the following sections, additional details related to the main document are provided in the form of  
appendices.

**Appendix A.** Supplementary information regarding the EM shielding apparatus.

The EM shielding apparatus, as illustrated in Figure S1, consists of a metallic structure housing various equipment and accessories for performing EM shielding characterization. The core of the apparatus comprises a Vector Network Analyzer (VNA) connected to three distinct waveguides. These waveguides include a coaxial waveguide complying with the ASTM D4935 standard, enabling shielding measurements up to 1.5 GHz. A smaller version of the standard coaxial waveguide (Flange Ø60mm) extends the frequency range up to 5 GHz, while a rectangular waveguide WR430 facilitates measurements in the TE mode within the 1.72 – 2.6 GHz range.

The station serves the purpose of offering multiple testing methods to assess the EM shielding of materials or structures under examination. The coaxial waveguides are employed for standardized EM shielding analyses, while the rectangular waveguide permits the examination of materials with or without apertures (useful for studying EM wave propagation through venting grids). These waveguides are housed within an aluminium structure that serves as a fixture. Additionally, a pneumatic actuator is utilized to provide vertical movement, allowing for the easy opening, and closing of the waveguides to facilitate the swapping of samples.

Furthermore, this station is designed to function as a compact and portable anechoic chamber, facilitating a rapid and simplified evaluation of the EM radiated shielding characteristics of the device under investigation. This feature allows for a quick assessment of the Electromagnetic Shielding Effectiveness (EMSE) concerning design concepts for the structure and its constituent materials.

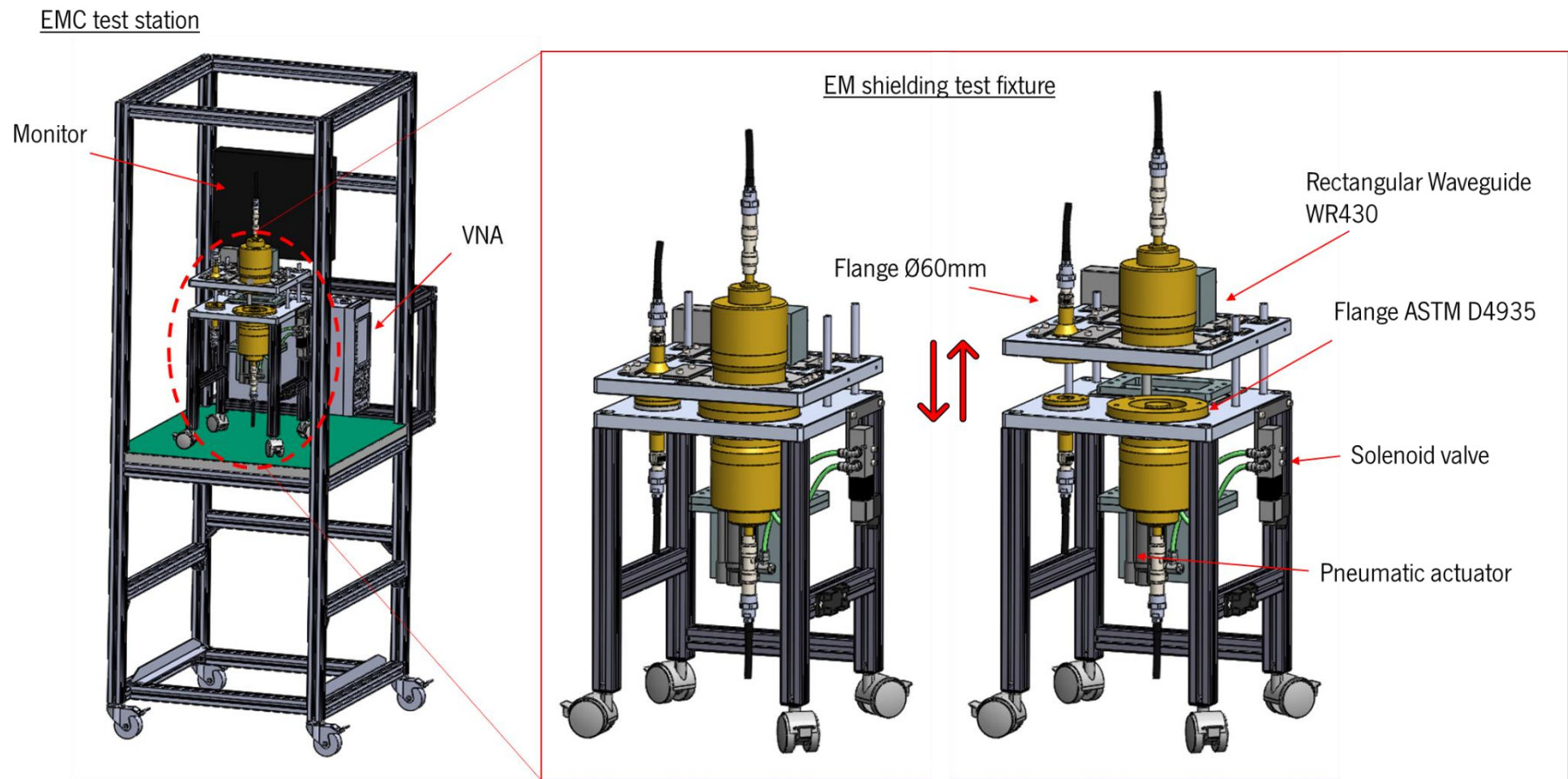


Figure S1. 3D simplified model for the EM shielding apparatus.

**Appendix B.** Supplementary information for the theoretical model.

$$S_{11}(\omega) = \frac{e^{i\frac{\omega}{c}[n_1(d+D)-n_2d]} \left\{ (n_1 + n_2) e^{i\frac{\omega}{c}n_2d} \left[ n_3(n_2 - n_1) \cos\left(\frac{\omega n_3 D}{c}\right) + i(n_3^2 - n_1 n_2) \sin\left(\frac{\omega n_3 D}{c}\right) \right] + (n_1 - n_2) \left[ n_3(n_1 + n_2) \cos\left(\frac{\omega n_3 D}{c}\right) - i(n_1 n_2 + n_3^2) \right] \right\}}{e^{i\frac{\omega}{c}[(n_1+n_2)d+n_1D]} (n_2 - n_1) \left[ n_3(n_2 - n_1) \cos\left(\frac{\omega n_3 D}{c}\right) + i(n_3^2 - n_1 n_2) \sin\left(\frac{\omega n_3 D}{c}\right) \right] - e^{i\frac{\omega}{c}[n_1(d+D)-n_2d]} (n_1 + n_2) \left[ n_3(n_1 + n_2) \cos\left(\frac{\omega n_3 D}{c}\right) - i(n_1 n_2 + n_3^2) \sin\left(\frac{\omega n_3 D}{c}\right) \right]}$$

$$S_{12}(\omega) = \frac{4n_1 n_2 n_3}{(n_1 - n_2) e^{i\frac{\omega}{c}[(n_1+n_2)d+n_1D]} \left[ n_3(n_2 - n_1) \cos\left(\frac{\omega n_3 D}{c}\right) + i(n_3^2 - n_1 n_2) \sin\left(\frac{\omega n_3 D}{c}\right) \right] + n_1 + n_2 e^{i\frac{\omega}{c}[n_1(d+D)-n_2d]} \left[ n_3(n_1 + n_2) \cos\left(\frac{\omega n_3 D}{c}\right) - i(n_1 n_2 + n_3^2) \sin\left(\frac{\omega n_3 D}{c}\right) \right]}$$

$$S_{21}(\omega) = \frac{8n_1 n_2 n_3 e^{-i\frac{\omega}{c}[(n_1-n_3)(d+D)-2n_2d]}}{(n_1 + n_2)(n_1 - n_3)(n_3 - n_2) e^{i\frac{\omega}{c}[(n_2+n_3)d+2n_3D]} + (n_2 - n_1)(n_1 - n_3)(n_2 + n_3) e^{i\frac{\omega}{c}[(3n_2+n_3)d+2n_3D]} + (n_1 - n_2)(n_1 + n_3)(n_2 - n_3) e^{i\frac{\omega}{c}(3n_2+n_3)d} + (n_1 + n_2)(n_1 + n_3)(n_2 + n_3) e^{i\frac{\omega}{c}(n_2+n_3)d}}$$

$$S_{22}(\omega) = \frac{\left\{ n_3(n_1 - n_2)(n_1 + n_2) \left( e^{2i\frac{\omega}{c}n_2d} - 1 \right) \cos\left(\frac{\omega n_3 D}{c}\right) e^{-i\frac{\omega}{c}[(n_1+n_2)d+n_1D]} + 2e^{-i\frac{\omega}{c}n_1(d+D)} \sin\left(\frac{\omega n_3 D}{c}\right) + \left[ n_1(n_2 - n_3)(n_2 + n_3) \sin\left(\frac{\omega n_2 D}{c}\right) + i n_2(n_1 - n_3)(n_1 + n_3) \cos\left(\frac{\omega n_2 D}{c}\right) \right] \right\}}{e^{i\frac{\omega}{c}[(n_1+n_2)d+n_1D]} (n_1 - n_2) \left[ n_3(n_2 - n_1) \cos\left(\frac{\omega n_3 D}{c}\right) + i(n_3^2 - n_1 n_2) \sin\left(\frac{\omega n_3 D}{c}\right) \right] - e^{i\frac{\omega}{c}[n_1(d+D)-n_2d]} (n_1 + n_2) \left[ n_3(n_1 + n_2) \cos\left(\frac{\omega n_3 D}{c}\right) - i(n_1 n_2 + n_3^2) \sin\left(\frac{\omega n_3 D}{c}\right) \right]}$$



## Appendix C. Codes build in *Mathematica 10.2* software.

### HOMOGENEOUS MATERIAL WITH ISOTROPIC AND CONSTANT CONDUCTIVITY

Code for a homogeneous material with isotropic and constant electrical conductivity and permittivity.

```

TM[w_,x_,y_,z_,\[Omega]_]:={{(1/2)*(1+w)*Exp[I*(\[Omega]/c)*(y-x)*z],-(1/2)*(1-w)*Exp[-I*(\[Omega]/c)*(y+x)*z]},{(1/2)*(1-w)*Exp[I*(\[Omega]/c)*(y+x)*z],(1/2)*(1+w)*Exp[-I*(\[Omega]/c)*(y-x)*z]}}
TM[w,x,y,z,\[Omega]]//MatrixForm
(1/2 E^((I (-x+y) z \[Omega])/299792458) (1+w)   -(1/2) E^-((I (x+y) z \[Omega])/299792458) (1-w)
-(1/2) E^((I (x+y) z \[Omega])/299792458) (1-w)   1/2 E^-((I (-x+y) z \[Omega])/299792458) (1+w)
T[w_,u_,n1_,n2_,d_,\[Omega]_]:=TM[w,n1,n2,d/2,\[Omega]].TM[u,n2,n1,-d/2,\[Omega]]
S11[w_,u_,n1_,n2_,d_,\[Omega]_]:=T[w,u,n1,n2,d,\[Omega]][[2,1]]/T[w,u,n1,n2,d,\[Omega]][[2,2]]
S12[w_,u_,n1_,n2_,d_,\[Omega]_]:=1/T[w,u,n1,n2,d,\[Omega]][[2,2]]
S21[w_,u_,n1_,n2_,d_,\[Omega]_]:=T[w,u,n1,n2,d,\[Omega]][[1,1]]-
T[w,u,n1,n2,d,\[Omega]][[1,2]]*T[w,u,n1,n2,d,\[Omega]][[2,1]]/T[w,u,n1,n2,d,\[Omega]][[2,2]]
S22[w_,u_,n1_,n2_,d_,\[Omega]_]:=T[w,u,n1,n2,d,\[Omega]][[1,2]]/T[w,u,n1,n2,d,\[Omega]][[2,2]]
FullSimplify[S11[n2/n1,n1/n2,n1,n2,d,\[Omega]]]
(E^-((I n1 \[Omega])/299792458000)) (-1+E^((I n2 \[Omega])/149896229000)) (-n1+n2) (n1+n2)/(E^((I n2
\[Omega])/149896229000) (n1-n2)^2-(n1+n2)^2)
FullSimplify[S22[n2/n1,n1/n2,n1,n2,d,\[Omega]]]
(E^-((I n1 \[Omega])/299792458000)) (-1+E^((I n2 \[Omega])/149896229000)) (-n1+n2) (n1+n2)/(E^((I n2
\[Omega])/149896229000) (n1-n2)^2-(n1+n2)^2)
(* Note the difference of phase between S11 and S22 when the origin is not in the mid point of the system. It can be moved there
simply by substituting the interval [0,d] by [-d/2,d/2], as shown *)
FullSimplify[S12[n2/n1,n1/n2,n1,n2,d,\[Omega]]]
-(4 E^((I (-n1+n2) \[Omega])/299792458000) n1 n2)/(E^((I n2 \[Omega])/149896229000) (n1-n2)^2-(n1+n2)^2)
FullSimplify[S21[n2/n1,n1/n2,n1,n2,d,\[Omega]]]
-(4 E^((I (-n1+n2) \[Omega])/299792458000) n1 n2)/(E^((I n2 \[Omega])/149896229000) (n1-n2)^2-(n1+n2)^2)

epsilon0:=8.8542*10^-12 (* Permittivity of vacuum in SI units *)
c:=299792458 (* Speed of light in the vacuum in ms^-1 *)
epsilon1r:=1; (* Relative permittivity of outside medium *)
epsilon2r:=2.9; (* Relative permittivity of PC - substitute accordingly *)
n1r:=Sqrt[epsilon1r]; (* Real refraction indices of the different media *)
n2r:=Sqrt[epsilon2r];
sigma0:=250; (* Conductivity of sample in S/m *)
n2c\[Omega]_,sigma0_:=n2r*Sqrt[1+I*(sigma0/(\[Omega]*epsilon0*epsilon2r))]
d:=2*10^-3;(* Thickness of PC in meter *)
ReflectionL[\[Nu]_,d_,sigma0_]:=S11[n2c[2*Pi*\[Nu],sigma0]/n1r,n1r/n2c[2*Pi*\[Nu],sigma0],n1r,n2c[2*Pi*\[Nu],sigma0],d,2
*Pi*\[Nu]]*Conjugate[S11[n2c[2*Pi*\[Nu],sigma0]/n1r,n1r/n2c[2*Pi*\[Nu],sigma0],n1r,n2c[2*Pi*\[Nu],sigma0],d,2*Pi*\[Nu]]];
Plot[ReflectionL[x*10^6,2*10^-3,250],{x,0,3000},PlotStyle->{Blue},AxesOrigin->{0,0},AxesLabel->{"\[Nu] (MHz)","Reflectance"}]

```

```

TransmissionR[\[Nu]_,d_,sigma0_]:=S21[n2c[2*Pi*\[Nu],sigma0]/n1r,n1r/n2c[2*Pi*\[Nu],sigma0],n1r,n2c[2*Pi*\[Nu],sigma0],d,2*Pi*\[Nu]]*Conjugate[S21[n2c[2*Pi*\[Nu],sigma0]/n1r,n1r/n2c[2*Pi*\[Nu],sigma0],n1r,n2c[2*Pi*\[Nu],sigma0],d,2*Pi*\[Nu]]];

Plot[-10*Log10[TransmissionR[x*10^6,2*10^(-3),250]],{x,0,3000},PlotStyle->{Red},AxesOrigin->{0,0},AxesLabel->{"\[Nu] (MHz)", "SE (dB)"}]

Plot[Evaluate@Table[-10*Log10[TransmissionR[x*10^6,2*10^(-3),sigma0]],{sigma0,100,2600,500}],{x,0,3000},PlotStyle->{{Hue[0.6]},Hue[0.2]},Hue[0.4]},Hue[0.6]},Hue[0.8]},AxesOrigin->{0,0},AxesLabel->{"\[Nu] (MHz)", "SE (dB)"}]

Plot[Evaluate@Table[-10*Log10[TransmissionR[x*10^6,y*10^(-4),2500]],{y,2,10,2}],{x,0,3000},PlotStyle->{{Hue[0.6]},Hue[0.8]},Hue[1]},Hue[1.2]},Hue[1.4]},AxesOrigin->{0,0},AxesLabel->{"\[Nu] (MHz)", "SE (dB)"}]

-10*Log10[TransmissionR[1000*10^6,2*10^(-3),2000]]

```

### HOMOGENEOUS MATERIAL WITH ANISOTROPIC AND FREQUENCY-DEPENDENT CONDUCTIVITY

Code for a homogeneous material with anisotropic properties based on the LCR coefficients obtained from the equivalent impedance circuit.

```

TM[w_,x_,y_,z_,\[Omega]_]:=((1/2)*(1+w)*Exp[I*(\[Omega]/c)*(y-x)*z],-(1/2)*(1-w)*Exp[-I*(\[Omega]/c)*(y+x)*z]),{(1/2)*(1-w)*Exp[I*(\[Omega]/c)*(y+x)*z],(1/2)*(1+w)*Exp[-I*(\[Omega]/c)*(y-x)*z]}]

TM[w,x,y,z,\[Omega]]//MatrixForm

(1/2 E^(I (x+y) z \[Omega])/c) (1+w)    -(1/2) E^(-I (x+y) z \[Omega])/c) (1-w)
-(1/2) E^(I (x+y) z \[Omega])/c) (1-w)    1/2 E^(-I (x+y) z \[Omega])/c) (1+w)

T[w_,u_,n1_,n2_,d_,\[Omega]_]:=TM[w,n1,n2,d/2,\[Omega]].TM[u,n2,n1,-d/2,\[Omega]]

S11[w_,u_,n1_,n2_,d_,\[Omega]_]:=T[w,u,n1,n2,d,\[Omega]][[2,1]]/T[w,u,n1,n2,d,\[Omega]][[2,2]]

S12[w_,u_,n1_,n2_,d_,\[Omega]_]:=1/T[w,u,n1,n2,d,\[Omega]][[2,2]]

S21[w_,u_,n1_,n2_,d_,\[Omega]_]:=T[w,u,n1,n2,d,\[Omega]][[1,1]]-
T[w,u,n1,n2,d,\[Omega]][[1,2]]*T[w,u,n1,n2,d,\[Omega]][[2,1]]/T[w,u,n1,n2,d,\[Omega]][[2,2]]

S22[w_,u_,n1_,n2_,d_,\[Omega]_]:=T[w,u,n1,n2,d,\[Omega]][[1,2]]/T[w,u,n1,n2,d,\[Omega]][[2,2]]

FullSimplify[S11[n2/n1,n1/n2,n1,n2,d,\[Omega]]]

(E^(-I (d n1 \[Omega])/c) (-1+E^(2 I d n2 \[Omega])/c) (-n1+n2) (n1+n2))/(E^(2 I d n2 \[Omega])/c) (n1-n2)^2-(n1+n2)^2)

FullSimplify[S22[n2/n1,n1/n2,n1,n2,d,\[Omega]]]

(E^(-I (d n1 \[Omega])/c) (-1+E^(2 I d n2 \[Omega])/c) (-n1+n2) (n1+n2))/(E^(2 I d n2 \[Omega])/c) (n1-n2)^2-(n1+n2)^2)

(* Note the difference of phase between S11 and S22 when the origin is not in the mid point of the system. It can be moved there simply by substituting the interval [0,d] by [-d/2,d/2], as shown *)

FullSimplify[S12[n2/n1,n1/n2,n1,n2,d,\[Omega]]]

-(4 E^(I (d (-n1+n2) \[Omega])/c) n1 n2)/(E^(2 I d n2 \[Omega])/c) (n1-n2)^2-(n1+n2)^2)

FullSimplify[S21[n2/n1,n1/n2,n1,n2,d,\[Omega]]]

-(4 E^(I (d (-n1+n2) \[Omega])/c) n1 n2)/(E^(2 I d n2 \[Omega])/c) (n1-n2)^2-(n1+n2)^2)

epsilon0:=8.8542*10^(-12) (* Permittivity of vacuum in SI units *)
c:=299792458 (* Speed of light in the vacuum in ms^(-1) *)
epsilon1r:=1; (* Relative permittivity of outside medium *)

```

## Appendices

---

```
epsilon2r:=2.9; (* Relative permittivity of PC - substitute accordingly *)
n1r:=Sqrt[epsilon1r]; (* Real refractive indices of the different media *)
d:=1.64*10^(-3); (* Thickness of sample in meter*)
diam:=7*10^(-3); (* Electrode diameter *)
S:=Pi*(diam/2)^2; (* Surface of sample *)
R:=31.893;(* Resistance determined by impedance measurements *)
Ca:=3.02*10^(-11); (* Capacitance determined by impedance measurements *)
tauRC:=R*Ca; (* Decay time determined by impedance measurements *)
gamma:=1; (* Ratio of transverse to longitudinal conductivities measured in DC *)
epsilonop[\[Omega]_]:=((d*tauRC)/(S*R*epsilon0))*(1+I*\[Omega]*tauRC)/(1+\[Omega]^2*tauRC^2);
n2c[\[Omega]_]:=Sqrt[gamma]*Sqrt[epsilonop[\[Omega]]];
ReflectionL[\[Nu]_]:=S11[n2c[2*Pi*\[Nu]]/n1r,n1r/n2c[2*Pi*\[Nu]],n1r,n2c[2*Pi*\[Nu]],d,2*Pi*\[Nu]]*Conjugate[S11[n2c[2*Pi*\[Nu]]/n1r,n1r/n2c[2*Pi*\[Nu]],n1r,n2c[2*Pi*\[Nu]],d,2*Pi*\[Nu]];
Plot[ReflectionL[x*10^6],{x,0,3000},PlotStyle->{Blue},AxesOrigin->{0,0},AxesLabel->{"\[Nu] (MHz)","Reflectance"}, PlotRange->All]
TransmissionR[\[Nu]_]:=S21[n2c[2*Pi*\[Nu]]/n1r,n1r/n2c[2*Pi*\[Nu]],n1r,n2c[2*Pi*\[Nu]],d,2*Pi*\[Nu]]*Conjugate[S21[n2c[2*Pi*\[Nu]]/n1r,n1r/n2c[2*Pi*\[Nu]],n1r,n2c[2*Pi*\[Nu]],d,2*Pi*\[Nu]];
PlotT=Plot[-10*Log10[TransmissionR[x*10^6]],{x,0,3000},PlotStyle->{Red},AxesOrigin->{0,0},AxesLabel->{"\[Nu] (MHz)","SE (dB)"}]
data=Table[{x,Re[-10*Log10[TransmissionR[x*10^6]]]},{x,0,3000, 10}] (*To generate a table with the real part of the function and export it... *)
Export["transmission.txt",data] (* Exports data to a ".txt" file for the document library *)
```

## HETEROGENEOUS MATERIAL WITH ISOTROPIC AND CONSTANT CONDUCTIVITY

Code for a heterogeneous material composed by a two-layer structure with different properties. The first media is defined as a dissipative dielectric with constant permittivity and loss tangent, while the second media is defined as a lossy media with constant and isotropic electrical conductivity. This code is useful for conductive coatings.

```
TM[w_,x_,y_,z_,\[Omega]_]:={{(1/2)*(1+w)*Exp[I*(\[Omega]/c)*(y-x)*z],-(1/2)*(1-w)*Exp[-I*(\[Omega]/c)*(y+x)*z]},{(1/2)*(1-w)*Exp[I*(\[Omega]/c)*(y+x)*z],(1/2)*(1+w)*Exp[-I*(\[Omega]/c)*(y-x)*z]}}
TM[w,x,y,z,\[Omega]]//MatrixForm
(1/2 E^(I ((-x+y) z \[Omega])/c) (1+w)   -(1/2) E^(-I ((x+y) z \[Omega])/c) (1-w)
-(1/2) E^(I ((x+y) z \[Omega])/c) (1-w)   1/2 E^(-I ((-x+y) z \[Omega])/c) (1+w)
T[w_,u_,n1_,n2_,n3_,d_,L_,\[Omega]_]:=TM[w,n1,n3,d+L,\[Omega]].TM[1/(w*u),n3,n2,d,\[Omega]].TM[u,n2,n1,0,\[Omega]]
S11[w_,u_,n1_,n2_,n3_,d_,L_,\[Omega]_]:=T[w,u,n1,n2,n3,d,L,\[Omega]][[2,1]]/T[w,u,n1,n2,n3,d,L,\[Omega]][[2,2]]
S12[w_,u_,n1_,n2_,n3_,d_,L_,\[Omega]_]:=1/T[w,u,n1,n2,n3,d,L,\[Omega]][[2,2]]
S21[w_,u_,n1_,n2_,n3_,d_,L_,\[Omega]_]:=T[w,u,n1,n2,n3,d,L,\[Omega]][[1,1]]-
T[w,u,n1,n2,n3,d,L,\[Omega]][[1,2]]*T[w,u,n1,n2,n3,d,L,\[Omega]][[2,1]]/T[w,u,n1,n2,n3,d,L,\[Omega]][[2,2]]
S22[w_,u_,n1_,n2_,n3_,d_,L_,\[Omega]_]:=T[w,u,n1,n2,n3,d,L,\[Omega]][[1,2]]/T[w,u,n1,n2,n3,d,L,\[Omega]][[2,2]]
FullSimplify[S11[w,n1/n2,n1,n2,n3,d,0,\[Omega]]]
((-1+E^(2 I d n2 \[Omega])/c) (-n1+n2) (n1+n2))/(E^(2 I d n2 \[Omega])/c (n1-n2)^2-(n1+n2)^2)
```

FullSimplify[S22[w,n1/n2,n1,n2,n3,d,0, \[Omega]]]

$$(E^{-((2 d n1 \sqrt{\Omega})/c)} (-1+E^{((2 d n2 \sqrt{\Omega})/c)} (-n1+n2) (n1+n2)))/(E^{((2 d n2 \sqrt{\Omega})/c)} (n1-n2)^2-(n1+n2)^2)$$

(\* Note the difference of phase between S11 and S22 due to the origin not being in the mid point of the system \*)

FullSimplify[S12[w,u,n1,n2,n3,d,0, \[Omega]]]

$$(4 E^{-((d (n1-n2) \sqrt{\Omega})/c)} u)/(-E^{((2 d n2 \sqrt{\Omega})/c)} (-1+u)^2+(1+u)^2)$$

FullSimplify[S21[w,u,n1,n2,n3,d,0, \[Omega]]]

$$-(4 E^{-((d (n1-n2) \sqrt{\Omega})/c)} u)/(E^{((2 d n2 \sqrt{\Omega})/c)} (-1+u)^2-(1+u)^2)$$

FullSimplify[S11[n3/n1,n1/n2,n1,n2,n3,d,L, \[Omega]]]

$$-(2 E^{((d+L) n1-d n2) \sqrt{\Omega}/c} (E^{((2 d n2 \sqrt{\Omega})/c)} (n1+n2) ((-n1+n2) n3 \cos((L n3 \sqrt{\Omega})/c)+(-n1 n2+n3^2) \sin((L n3 \sqrt{\Omega})/c))+(n1-n2) ((n1+n2) n3 \cos((L n3 \sqrt{\Omega})/c)-(-n1 n2+n3^2) \sin((L n3 \sqrt{\Omega})/c)))/(2 E^{((L (n1+d (n1+n2)) \sqrt{\Omega})/c)} (n1-n2) ((-n1+n2) n3 \cos((L n3 \sqrt{\Omega})/c)+(-n1 n2+n3^2) \sin((L n3 \sqrt{\Omega})/c))+E^{((d+L) n1-d n2) \sqrt{\Omega}/c} (n1+n2) ((n1+n2) n3 \cos((L n3 \sqrt{\Omega})/c)-(-n1 n2+n3^2) \sin((L n3 \sqrt{\Omega})/c)))$$

FullSimplify[S22[n3/n1,n1/n2,n1,n2,n3,d,L, \[Omega]]]

$$(2 E^{-((L (n1+d (n1+n2)) \sqrt{\Omega})/c)} ((-1+E^{((2 d n2 \sqrt{\Omega})/c)} (n1-n2) (n1+n2) n3 \cos((L n3 \sqrt{\Omega})/c)+2 E^{((d n2 \sqrt{\Omega})/c)} (n2 (n1-n3) (n1+n3) \cos((d n2 \sqrt{\Omega})/c)+n1 (n2-n3) (n2+n3) \sin((d n2 \sqrt{\Omega})/c)) \sin((L n3 \sqrt{\Omega})/c)))/(2 E^{((L (n1+d (n1+n2)) \sqrt{\Omega})/c)} (n1-n2) ((-n1+n2) n3 \cos((L n3 \sqrt{\Omega})/c)+(-n1 n2+n3^2) \sin((L n3 \sqrt{\Omega})/c))+2 E^{((d+L) n1-d n2) \sqrt{\Omega}/c} (n1+n2) ((n1+n2) n3 \cos((L n3 \sqrt{\Omega})/c)-(-n1 n2+n3^2) \sin((L n3 \sqrt{\Omega})/c)))$$

FullSimplify[S12[n3/n1,n1/n2,n1,n2,n3,d,L, \[Omega]]]

$$(8 n1 n2 n3)/(2 E^{((L (n1+d (n1+n2)) \sqrt{\Omega})/c)} (n1-n2) ((-n1+n2) n3 \cos((L n3 \sqrt{\Omega})/c)+(-n1 n2+n3^2) \sin((L n3 \sqrt{\Omega})/c))+2 E^{((d+L) n1-d n2) \sqrt{\Omega}/c} (n1+n2) ((n1+n2) n3 \cos((L n3 \sqrt{\Omega})/c)-(-n1 n2+n3^2) \sin((L n3 \sqrt{\Omega})/c)))$$

FullSimplify[S21[n3/n1,n1/n2,n1,n2,n3,d,L, \[Omega]]]

$$-(8 E^{-((d n1+L n1-2 d n2-(d+L) n3) \sqrt{\Omega})/c} n1 n2 n3)/(E^{((d (3 n2+n3) \sqrt{\Omega})/c)} (-n1+n2) (n2-n3) (n1+n3)+E^{((2 L n3+d (n2+n3)) \sqrt{\Omega})/c} (n1+n2) (-n1+n3) (-n2+n3)+E^{((2 L n3+d (3 n2+n3)) \sqrt{\Omega})/c} (-n1+n2) (-n1+n3) (n2+n3)-E^{((d (n2+n3) \sqrt{\Omega})/c)} (n1+n2) (n1+n3) (n2+n3))$$

FullSimplify[S22[1,n1/n2,n1,n2,n1,d,L, \[Omega]]]

$$(E^{-((2 d n1 \sqrt{\Omega})/c)} (-1+E^{((2 d n2 \sqrt{\Omega})/c)} (-n1+n2) (n1+n2)))/(E^{((2 d n2 \sqrt{\Omega})/c)} (n1-n2)^2-(n1+n2)^2)$$

epsilon0:=8.8542\*10<sup>-12</sup> (\* Permittivity of vacuum in SI units \*)

c:=299792458 (\* Speed of light in the vacuum in ms<sup>-1</sup> \*)

epsilon1r:=1; (\* Relative permittivity of outside medium \*)

epsilon2r:=1; (\* Relative permittivity of coating \*)

epsilon3r:=2.9; (\* Relative permittivity of polymer \*)

n1r:=Sqrt[epsilon1r]; (\* Real refraction indices of the different media \*)

n2r:=Sqrt[epsilon2r];

n3r:=Sqrt[epsilon3r];

tau30:=0.0051; (\* Loss tangent of polymer at given frequency \*)

omega30:=2\*Pi\*(1\*10<sup>6</sup>); (\* Such given angular frequency \*)

n2c\[Omega]\_,sigma0\_:=n2r\*Sqrt[1+I\*(sigma0/(\[Omega]\*epsilon0\*epsilon2r))]

n3c\[Omega]\_,tau30\_,omega30\_:=n3r\*Sqrt[1+I\*(tau30\*omega30/\[Omega])]

d:=1\*10<sup>-3</sup>; (\* Thickness of coating in meter \*)

L:=2.2\*10<sup>-3</sup>; (\* Thickness of polymer substrate in meter \*)

## Appendices

---

```
ReflectionL[\[Nu]_,d_,sigma0_]:=S11[n3c[2*Pi*\[Nu],tau30,omega30]/n1r,n1r/n2c[2*Pi*\[Nu],sigma0],n1r,n2c[2*Pi*\[Nu],sigma0],n3c[2*Pi*\[Nu],tau30,omega30],d,L,2*Pi*\[Nu]]*Conjugate[S11[n3c[2*Pi*\[Nu],tau30,omega30]/n1r,n1r/n2c[2*Pi*\[Nu],sigma0],n1r,n2c[2*Pi*\[Nu],sigma0],n3c[2*Pi*\[Nu],tau30,omega30],d,L,2*Pi*\[Nu]]];
```

```
Plot[ReflectionL[x*10^6,1*10^(-3),250],{x,0,3000},PlotStyle->{Blue},AxesOrigin->{0,0},AxesLabel->{"\[Nu] (MHz)", "Reflectance"}]
```

```
TransmissionR[\[Nu]_,d_,sigma0_]:=S21[n3c[2*Pi*\[Nu],tau30,omega30]/n1r,n1r/n2c[2*Pi*\[Nu],sigma0],n1r,n2c[2*Pi*\[Nu],sigma0],n3c[2*Pi*\[Nu],tau30,omega30],d,L,2*Pi*\[Nu]]*Conjugate[S21[n3c[2*Pi*\[Nu],tau30,omega30]/n1r,n1r/n2c[2*Pi*\[Nu],sigma0],n1r,n2c[2*Pi*\[Nu],sigma0],n3c[2*Pi*\[Nu],tau30,omega30],d,L,2*Pi*\[Nu]]];
```

```
Plot[-10*Log10[TransmissionR[x*10^6,1*10^(-4),600]],{x,0,3000},PlotStyle->{Red},AxesOrigin->{0,0},AxesLabel->{"\[Nu] (MHz)", "SE (dB)"}]
```

```
Plot[Evaluate@Table[-10*Log10[TransmissionR[x*10^6,10^(-4),sigma0]],{sigma0,100,2600,500}],{x,0,3000},PlotStyle->{{Hue[0]},{Hue[0.2]},{Hue[0.4]},{Hue[0.6]},{Hue[0.8]}},AxesOrigin->{0,0},AxesLabel->{"\[Nu] (MHz)", "SE (dB)"}]
```

```
Plot[Evaluate@Table[-10*Log10[TransmissionR[x*10^6,y*10^(-4),1600]],{y,1,13,3}],{x,0,3000},PlotStyle->{{Hue[0.6]},{Hue[0.8]},{Hue[1]},{Hue[1.2]},{Hue[1.4]}},AxesOrigin->{0,0},AxesLabel->{"\[Nu] (MHz)", "SE (dB)"}]
```

**Appendix D.** Supplementary results to chapter 3.5.

**EM SHIELDING RESULTS**

EMSE was examined across mouldings generated under various injection moulding conditions and positions along the rectangular plate, specifically near the gate and opposite the gate. Table S1, Table S2 and Table S3 provides the average value for the shielding effectiveness measured for M7, M8 and M9 compounds, respectively.

Table S1. Shielding effectiveness measured for the M7 compound, units in dB.

		Frequency (MHz)	30	100	300	500	800	1000	1500	2000	2500	3000	
<b>Near Gate</b>	<b>E01</b>	Average	34.60	34.53	33.30	32.35	31.56	31.01	32.01	35.41	35.54	36.44	
		Std. Dev.	0.21	0.18	0.28	0.27	0.26	0.27	0.39	0.27	0.30	0.28	
	<b>E02</b>	Average	35.44	34.09	32.79	31.97	31.35	30.96	32.33	34.86	35.35	36.63	
		Std. Dev.	0.64	0.36	0.38	0.38	0.45	0.54	0.79	0.41	0.47	0.60	
	<b>E03</b>	Average	39.73	37.75	35.55	34.19	33.12	32.46	33.67	37.71	37.56	38.34	
		Std. Dev.	0.48	0.43	0.40	0.38	0.38	0.42	0.72	0.47	0.50	0.62	
	<b>E04</b>	Average	39.61	37.12	35.76	34.79	34.04	33.64	35.34	38.35	39.00	40.09	
		Std. Dev.	0.79	0.36	0.43	0.43	0.41	0.44	0.52	0.49	0.55	0.50	
	<b>Opposite Gate</b>	<b>E01</b>	Average	36.47	33.69	32.31	31.75	31.41	31.27	33.24	35.22	35.92	37.66
			Std. Dev.	0.48	0.09	0.12	0.12	0.12	0.13	0.15	0.14	0.14	0.14
		<b>E02</b>	Average	35.65	32.89	31.65	31.12	30.87	30.80	32.74	34.02	34.97	36.78
			Std. Dev.	1.61	0.54	0.48	0.51	0.58	0.69	0.85	0.71	0.80	0.88
<b>E03</b>		Average	39.98	36.60	33.99	32.99	32.26	31.90	33.81	36.98	37.48	38.88	
		Std. Dev.	0.95	0.41	0.34	0.30	0.30	0.33	0.51	0.34	0.38	0.43	
<b>E04</b>		Average	40.08	34.94	33.34	32.74	32.42	32.36	34.51	36.74	37.82	39.51	
		Std. Dev.	1.20	0.22	0.13	0.16	0.19	0.22	0.37	0.26	0.24	0.24	

Table S2. Shielding effectiveness measured for the M8 compound, units in dB.

		Frequency (MHz)	30	100	300	500	800	1000	1500	2000	2500	3000
<b>Near Gate</b>	<b>E01</b>	Average	56.89	53.82	52.62	51.83	51.83	52.53	56.98	62.39	65.71	68.64
		Std. Dev.	1.74	0.95	0.80	0.94	1.08	1.19	1.36	1.50	1.67	1.82
	<b>E02</b>	Average	54.91	52.58	52.08	51.62	52.30	53.40	58.11	63.36	67.33	70.90
		Std. Dev.	0.96	0.97	1.18	1.31	1.42	1.50	1.61	1.75	2.08	2.36
	<b>E03</b>	Average	58.12	52.74	51.26	50.66	51.50	52.82	58.20	63.29	66.72	70.39
		Std. Dev.	1.91	0.95	1.75	1.96	2.31	2.60	3.24	3.56	3.80	4.19
	<b>E04</b>	Average	56.53	53.06	51.56	51.07	52.40	54.06	59.88	64.61	68.25	72.29
		Std. Dev.	1.66	0.25	0.91	1.15	1.44	1.57	1.84	2.21	2.53	2.77
<b>Opposite Gate</b>	<b>E01</b>	Average	52.78	48.98	45.41	44.39	45.56	47.12	52.12	54.64	56.98	60.13
		Std. Dev.	1.01	0.84	0.73	0.83	0.92	1.00	1.16	1.26	1.39	1.49
	<b>E02</b>	Average	52.17	49.87	47.71	46.66	47.73	49.27	54.66	58.17	60.89	64.38
		Std. Dev.	3.19	1.39	1.90	1.78	2.03	2.11	2.34	2.99	3.36	3.61
	<b>E03</b>	Average	53.99	48.76	45.33	44.50	45.93	47.64	52.69	54.94	57.32	62.26
		Std. Dev.	1.40	1.69	1.90	1.96	2.49	2.80	3.21	3.45	3.83	4.73
	<b>E04</b>	Average	53.69	49.25	46.53	45.74	47.19	48.97	54.43	57.02	59.71	63.23
		Std. Dev.	2.64	1.57	1.43	1.49	1.82	1.97	2.48	2.83	3.09	3.37

Table S3. Shielding effectiveness measured for the M9 compound, units in dB.

		Frequency (MHz)	30	100	300	500	800	1000	1500	2000	2500	3000	
<b>Near Gate</b>	<b>E01</b>	Average	56.82	58.77	66.17	70.90	75.85	78.83	84.99	91.16	96.31	98.40	
		Std. Dev.	3.03	3.30	2.97	2.66	2.72	2.88	3.01	5.21	7.30	6.72	
	<b>E02</b>	Average	59.25	60.67	65.55	69.27	74.17	77.21	84.59	94.27	97.90	102.97	
		Std. Dev.	1.13	1.06	2.15	2.78	2.72	2.78	2.49	3.31	4.25	3.75	
	<b>E03</b>	Average	59.46	61.28	67.09	71.07	76.28	79.37	86.95	96.20	100.37	105.34	
		Std. Dev.	2.83	2.23	0.92	0.95	1.04	0.93	1.44	1.89	1.49	1.81	
	<b>E04</b>	Average	60.27	61.44	65.29	68.29	73.57	76.82	85.17	92.77	98.68	106.58	
		Std. Dev.	0.72	0.85	1.79	1.87	1.63	1.68	2.00	1.57	1.80	3.41	
	<b>Opposite Gate</b>	<b>E01</b>	Average	59.42	61.46	66.29	69.85	75.20	78.64	85.09	89.73	93.57	99.96
			Std. Dev.	0.86	1.05	2.61	2.30	1.82	1.98	2.77	3.02	3.47	6.96
		<b>E02</b>	Average	59.86	62.26	66.70	70.06	74.40	77.62	85.24	92.53	96.42	97.13
			Std. Dev.	2.86	2.41	3.32	4.06	4.27	4.63	5.56	5.84	3.78	2.92
<b>E03</b>		Average	62.40	64.32	68.47	72.53	78.21	81.81	90.08	98.19	97.93	102.93	
		Std. Dev.	0.69	1.75	1.83	1.11	0.31	0.63	2.06	5.72	1.03	1.75	
<b>E04</b>		Average	59.44	61.40	65.89	69.55	75.77	79.13	87.56	92.21	97.42	102.28	
		Std. Dev.	1.83	3.35	4.74	5.45	5.75	6.15	8.02	4.92	4.34	2.97	

Table S4 to Table S7 provides a comprehensive representation of EMSE variations for both compounds. The data beneath columns labelled “E01 → E02” illustrates the changes in shielding resulting from the increment in melt temperature and injection speed between experiment conditions E01 and E2. Conversely, the data under columns labelled “Near Gate → Opp. Gate” elucidates the variations in shielding attributed to the increased flow path length, reflecting different measurement areas.



Table S4. Effect of processing conditions E01 to E02 and sample position on the EM shielding of the three compounds.

Frequency (MHz)	M7						M8						M9					
	E01 → E02			Near Gate → Opp. Gate			E01 → E02			Near Gate → Opp. Gate			E01 → E02			Near Gate → Opp. Gate		
30	Near Gate	0.84	2.4%	E01	1.87	5.4%	Near Gate	-1.98	-3.5%	E01	-4.11	-7.2%	Near Gate	2.43	4.3%	E01	2.60	4.6%
	Opp. Gate	-0.81	-2.2%	E02	0.22	0.6%	Opp. Gate	-0.61	-1.2%	E02	-2.74	-5.0%	Opp. Gate	0.44	0.7%	E02	0.62	1.0%
100	Near Gate	-0.44	-1.3%	E01	-0.84	-2.4%	Near Gate	-1.24	-2.3%	E01	-4.84	-9.0%	Near Gate	1.90	3.2%	E01	2.68	4.6%
	Opp. Gate	-0.80	-2.4%	E02	-1.20	-3.5%	Opp. Gate	0.89	1.8%	E02	-2.71	-5.2%	Opp. Gate	0.80	1.3%	E02	1.58	2.6%
300	Near Gate	-0.51	-1.5%	E01	-1.00	-3.0%	Near Gate	-0.54	-1.0%	E01	-7.21	-13.7%	Near Gate	-0.62	-0.9%	E01	0.12	0.2%
	Opp. Gate	-0.66	-2.0%	E02	-1.14	-3.5%	Opp. Gate	2.31	5.1%	E02	-4.36	-8.4%	Opp. Gate	0.41	0.6%	E02	1.15	1.8%
500	Near Gate	-0.38	-1.2%	E01	-0.61	-1.9%	Near Gate	-0.21	-0.4%	E01	-7.44	-14.4%	Near Gate	-1.63	-2.3%	E01	-1.05	-1.5%
	Opp. Gate	-0.63	-2.0%	E02	-0.85	-2.7%	Opp. Gate	2.27	5.1%	E02	-4.96	-9.6%	Opp. Gate	0.21	0.3%	E02	0.79	1.1%
800	Near Gate	-0.21	-0.7%	E01	-0.15	-0.5%	Near Gate	0.47	0.9%	E01	-6.27	-12.1%	Near Gate	-1.68	-2.2%	E01	-0.65	-0.9%
	Opp. Gate	-0.54	-1.7%	E02	-0.48	-1.5%	Opp. Gate	2.17	4.8%	E02	-4.57	-8.7%	Opp. Gate	-0.80	-1.1%	E02	0.23	0.3%
1000	Near Gate	-0.04	-0.1%	E01	0.26	0.8%	Near Gate	0.87	1.7%	E01	-5.40	-10.3%	Near Gate	-1.63	-2.1%	E01	-0.20	-0.3%
	Opp. Gate	-0.46	-1.5%	E02	-0.16	-0.5%	Opp. Gate	2.14	4.5%	E02	-4.13	-7.7%	Opp. Gate	-1.02	-1.3%	E02	0.41	0.5%
1500	Near Gate	0.32	1.0%	E01	1.23	3.8%	Near Gate	1.12	2.0%	E01	-4.86	-8.5%	Near Gate	-0.40	-0.5%	E01	0.11	0.1%
	Opp. Gate	-0.49	-1.5%	E02	0.41	1.3%	Opp. Gate	2.54	4.9%	E02	-3.44	-5.9%	Opp. Gate	0.15	0.2%	E02	0.66	0.8%
2000	Near Gate	-0.55	-1.6%	E01	-0.19	-0.5%	Near Gate	0.97	1.6%	E01	-7.75	-12.4%	Near Gate	3.11	3.4%	E01	-1.43	-1.6%
	Opp. Gate	-1.20	-3.4%	E02	-0.84	-2.4%	Opp. Gate	3.54	6.5%	E02	-5.19	-8.2%	Opp. Gate	2.80	3.1%	E02	-1.73	-1.8%
2500	Near Gate	-0.19	-0.5%	E01	0.38	1.1%	Near Gate	1.62	2.5%	E01	-8.73	-13.3%	Near Gate	1.59	1.6%	E01	-2.74	-2.8%
	Opp. Gate	-0.95	-2.6%	E02	-0.38	-1.1%	Opp. Gate	3.91	6.9%	E02	-6.44	-9.6%	Opp. Gate	2.85	3.1%	E02	-1.48	-1.5%
3000	Near Gate	0.19	0.5%	E01	1.22	3.4%	Near Gate	2.27	3.3%	E01	-8.51	-12.4%	Near Gate	4.57	4.6%	E01	1.56	1.6%
	Opp. Gate	-0.88	-2.3%	E02	0.16	0.4%	Opp. Gate	4.26	7.1%	E02	-6.52	-9.2%	Opp. Gate	-2.83	-2.8%	E02	-5.84	-5.7%

Table S5. Effect of processing conditions and sample position on the EM shielding of the three compounds.

Frequency (MHz)	M7						M8						M9					
	E01 → E03			Near Gate → Opp. Gate			E01 → E03			Near Gate → Opp. Gate			E01 → E03			Near Gate → Opp. Gate		
30	Near Gate	5.13	14.8%	E01	1.87	5.4%	Near Gate	1.23	2.2%	E01	-4.11	-7.2%	Near Gate	2.64	4.7%	E01	2.60	4.6%
	Opp. Gate	3.51	9.6%	E03	0.25	0.6%	Opp. Gate	1.21	2.3%	E03	-4.13	-7.1%	Opp. Gate	2.98	5.0%	E03	2.93	4.9%
100	Near Gate	3.21	9.3%	E01	-0.84	-2.4%	Near Gate	-1.08	-2.0%	E01	-4.84	-9.0%	Near Gate	2.51	4.3%	E01	2.68	4.6%
	Opp. Gate	2.91	8.6%	E03	-1.15	-3.0%	Opp. Gate	-0.22	-0.4%	E03	-3.98	-7.5%	Opp. Gate	2.87	4.7%	E03	3.04	5.0%
300	Near Gate	2.25	6.7%	E01	-1.00	-3.0%	Near Gate	-1.36	-2.6%	E01	-7.21	-13.7%	Near Gate	0.92	1.4%	E01	0.12	0.2%
	Opp. Gate	1.68	5.2%	E03	-1.56	-4.4%	Opp. Gate	-0.08	-0.2%	E03	-5.93	-11.6%	Opp. Gate	2.18	3.3%	E03	1.38	2.1%
500	Near Gate	1.84	5.7%	E01	-0.61	-1.9%	Near Gate	-1.17	-2.3%	E01	-7.44	-14.4%	Near Gate	0.17	0.2%	E01	-1.05	-1.5%
	Opp. Gate	1.24	3.9%	E03	-1.21	-3.5%	Opp. Gate	0.11	0.3%	E03	-6.16	-12.2%	Opp. Gate	2.69	3.8%	E03	1.46	2.1%
800	Near Gate	1.55	4.9%	E01	-0.15	-0.5%	Near Gate	-0.32	-0.6%	E01	-6.27	-12.1%	Near Gate	0.44	0.6%	E01	-0.65	-0.9%
	Opp. Gate	0.85	2.7%	E03	-0.85	-2.6%	Opp. Gate	0.37	0.8%	E03	-5.57	-10.8%	Opp. Gate	3.01	4.0%	E03	1.93	2.5%
1000	Near Gate	1.45	4.7%	E01	0.26	0.8%	Near Gate	0.29	0.6%	E01	-5.40	-10.3%	Near Gate	0.53	0.7%	E01	-0.20	-0.3%
	Opp. Gate	0.63	2.0%	E03	-0.56	-1.7%	Opp. Gate	0.51	1.1%	E03	-5.18	-9.8%	Opp. Gate	3.17	4.0%	E03	2.44	3.1%
1500	Near Gate	1.66	5.2%	E01	1.23	3.8%	Near Gate	1.22	2.1%	E01	-4.86	-8.5%	Near Gate	1.96	2.3%	E01	0.11	0.1%
	Opp. Gate	0.57	1.7%	E03	0.14	0.4%	Opp. Gate	0.57	1.1%	E03	-5.51	-9.5%	Opp. Gate	4.99	5.9%	E03	3.13	3.6%
2000	Near Gate	2.30	6.5%	E01	-0.19	-0.5%	Near Gate	0.90	1.4%	E01	-7.75	-12.4%	Near Gate	5.04	5.5%	E01	-1.43	-1.6%
	Opp. Gate	1.76	5.0%	E03	-0.73	-1.9%	Opp. Gate	0.30	0.5%	E03	-8.35	-13.2%	Opp. Gate	8.46	9.4%	E03	1.99	2.1%
2500	Near Gate	2.02	5.7%	E01	0.38	1.1%	Near Gate	1.01	1.5%	E01	-8.73	-13.3%	Near Gate	4.06	4.2%	E01	-2.74	-2.8%
	Opp. Gate	1.56	4.3%	E03	-0.08	-0.2%	Opp. Gate	0.34	0.6%	E03	-9.40	-14.1%	Opp. Gate	4.36	4.7%	E03	-2.44	-2.4%
3000	Near Gate	1.90	5.2%	E01	1.22	3.4%	Near Gate	1.75	2.6%	E01	-8.51	-12.4%	Near Gate	6.94	7.1%	E01	1.56	1.6%
	Opp. Gate	1.22	3.2%	E03	0.54	1.4%	Opp. Gate	2.13	3.5%	E03	-8.13	-11.6%	Opp. Gate	2.97	3.0%	E03	-2.41	-2.3%

Table S6. Effect of processing conditions and sample position on the EM shielding of the three compounds.

Frequency (MHz)	M7						M8						M9					
	E01 → E04			Near Gate → Opp. Gate			E01 → E04			Near Gate → Opp. Gate			E01 → E04			Near Gate → Opp. Gate		
30	Near Gate	5.01	14.5%	E01	1.87	5.4%	Near Gate	-0.36	-0.6%	E01	-4.11	-7.2%	Near Gate	3.45	6.1%	E01	2.60	4.6%
	Opp. Gate	3.61	9.9%	E04	0.47	1.2%	Opp. Gate	0.91	1.7%	E04	-2.84	-5.0%	Opp. Gate	0.02	0.0%	E04	-0.83	-1.4%
100	Near Gate	2.59	7.5%	E01	-0.84	-2.4%	Near Gate	-0.76	-1.4%	E01	-4.84	-9.0%	Near Gate	2.67	4.5%	E01	2.68	4.6%
	Opp. Gate	1.25	3.7%	E04	-2.18	-5.9%	Opp. Gate	0.27	0.6%	E04	-3.81	-7.2%	Opp. Gate	-0.05	-0.1%	E04	-0.04	-0.1%
300	Near Gate	2.46	7.4%	E01	-1.00	-3.0%	Near Gate	-1.05	-2.0%	E01	-7.21	-13.7%	Near Gate	-0.89	-1.3%	E01	0.12	0.2%
	Opp. Gate	1.03	3.2%	E04	-2.42	-6.8%	Opp. Gate	1.12	2.5%	E04	-5.03	-9.8%	Opp. Gate	-0.41	-0.6%	E04	0.60	0.9%
500	Near Gate	2.44	7.5%	E01	-0.61	-1.9%	Near Gate	-0.76	-1.5%	E01	-7.44	-14.4%	Near Gate	-2.61	-3.7%	E01	-1.05	-1.5%
	Opp. Gate	1.00	3.1%	E04	-2.05	-5.9%	Opp. Gate	1.35	3.0%	E04	-5.33	-10.4%	Opp. Gate	-0.30	-0.4%	E04	1.26	1.8%
800	Near Gate	2.48	7.9%	E01	-0.15	-0.5%	Near Gate	0.57	1.1%	E01	-6.27	-12.1%	Near Gate	-2.28	-3.0%	E01	-0.65	-0.9%
	Opp. Gate	1.01	3.2%	E04	-1.62	-4.8%	Opp. Gate	1.63	3.6%	E04	-5.21	-9.9%	Opp. Gate	0.56	0.7%	E04	2.20	3.0%
1000	Near Gate	2.63	8.5%	E01	0.26	0.8%	Near Gate	1.53	2.9%	E01	-5.40	-10.3%	Near Gate	-2.01	-2.6%	E01	-0.20	-0.3%
	Opp. Gate	1.09	3.5%	E04	-1.28	-3.8%	Opp. Gate	1.85	3.9%	E04	-5.08	-9.4%	Opp. Gate	0.50	0.6%	E04	2.31	3.0%
1500	Near Gate	3.33	10.4%	E01	1.23	3.8%	Near Gate	2.90	5.1%	E01	-4.86	-8.5%	Near Gate	0.19	0.2%	E01	0.11	0.1%
	Opp. Gate	1.27	3.8%	E04	-0.83	-2.4%	Opp. Gate	2.31	4.4%	E04	-5.46	-9.1%	Opp. Gate	2.47	2.9%	E04	2.39	2.8%
2000	Near Gate	2.94	8.3%	E01	-0.19	-0.5%	Near Gate	2.22	3.6%	E01	-7.75	-12.4%	Near Gate	1.61	1.8%	E01	-1.43	-1.6%
	Opp. Gate	1.52	4.3%	E04	-1.62	-4.2%	Opp. Gate	2.38	4.4%	E04	-7.59	-11.8%	Opp. Gate	2.47	2.8%	E04	-0.56	-0.6%
2500	Near Gate	3.46	9.7%	E01	0.38	1.1%	Near Gate	2.54	3.9%	E01	-8.73	-13.3%	Near Gate	2.37	2.5%	E01	-2.74	-2.8%
	Opp. Gate	1.91	5.3%	E04	-1.18	-3.0%	Opp. Gate	2.74	4.8%	E04	-8.53	-12.5%	Opp. Gate	3.85	4.1%	E04	-1.26	-1.3%
3000	Near Gate	3.65	10.0%	E01	1.22	3.4%	Near Gate	3.66	5.3%	E01	-8.51	-12.4%	Near Gate	8.19	8.3%	E01	1.56	1.6%
	Opp. Gate	1.85	4.9%	E04	-0.57	-1.4%	Opp. Gate	3.10	5.2%	E04	-9.06	-12.5%	Opp. Gate	2.32	2.3%	E04	-4.31	-4.0%

Table S7. Effect of processing conditions E03 to E04 and sample position on the EM shielding of the three compounds.

Frequency (MHz)	M7						M8						M9					
	E03 → E04			Near Gate → Opp. Gate			E03 → E04			Near Gate → Opp. Gate			E03 → E04			Near Gate → Opp. Gate		
<b>30</b>	Near Gate	-0.12	-0.3%	E03	0.25	0.6%	Near Gate	-1.60	-2.7%	E03	-4.13	-7.1%	Near Gate	0.80	1.3%	E03	2.93	4.9%
	Opp. Gate	0.10	0.3%	E04	0.47	1.2%	Opp. Gate	-0.30	-0.6%	E04	-2.84	-5.0%	Opp. Gate	-2.96	-4.7%	E04	-0.83	-1.4%
<b>100</b>	Near Gate	-0.63	-1.7%	E03	-1.15	-3.0%	Near Gate	0.32	0.6%	E03	-3.98	-7.5%	Near Gate	0.16	0.3%	E03	3.04	5.0%
	Opp. Gate	-1.66	-4.5%	E04	-2.18	-5.9%	Opp. Gate	0.49	1.0%	E04	-3.81	-7.2%	Opp. Gate	-2.92	-4.5%	E04	-0.04	-0.1%
<b>300</b>	Near Gate	0.21	0.6%	E03	-1.56	-4.4%	Near Gate	0.30	0.6%	E03	-5.93	-11.6%	Near Gate	-1.81	-2.7%	E03	1.38	2.1%
	Opp. Gate	-0.65	-1.9%	E04	-2.42	-6.8%	Opp. Gate	1.20	2.6%	E04	-5.03	-9.8%	Opp. Gate	-2.59	-3.8%	E04	0.60	0.9%
<b>500</b>	Near Gate	0.59	1.7%	E03	-1.21	-3.5%	Near Gate	0.41	0.8%	E03	-6.16	-12.2%	Near Gate	-2.78	-3.9%	E03	1.46	2.1%
	Opp. Gate	-0.24	-0.7%	E04	-2.05	-5.9%	Opp. Gate	1.24	2.8%	E04	-5.33	-10.4%	Opp. Gate	-2.98	-4.1%	E04	1.26	1.8%
<b>800</b>	Near Gate	0.93	2.8%	E03	-0.85	-2.6%	Near Gate	0.90	1.7%	E03	-5.57	-10.8%	Near Gate	-2.72	-3.6%	E03	1.93	2.5%
	Opp. Gate	0.16	0.5%	E04	-1.62	-4.8%	Opp. Gate	1.26	2.7%	E04	-5.21	-9.9%	Opp. Gate	-2.45	-3.1%	E04	2.20	3.0%
<b>1000</b>	Near Gate	1.18	3.6%	E03	-0.56	-1.7%	Near Gate	1.24	2.3%	E03	-5.18	-9.8%	Near Gate	-2.55	-3.2%	E03	2.44	3.1%
	Opp. Gate	0.46	1.4%	E04	-1.28	-3.8%	Opp. Gate	1.34	2.8%	E04	-5.08	-9.4%	Opp. Gate	-2.67	-3.3%	E04	2.31	3.0%
<b>1500</b>	Near Gate	1.67	5.0%	E03	0.14	0.4%	Near Gate	1.68	2.9%	E03	-5.51	-9.5%	Near Gate	-1.78	-2.0%	E03	3.13	3.6%
	Opp. Gate	0.70	2.1%	E04	-0.83	-2.4%	Opp. Gate	1.74	3.3%	E04	-5.46	-9.1%	Opp. Gate	-2.52	-2.8%	E04	2.39	2.8%
<b>2000</b>	Near Gate	0.64	1.7%	E03	-0.73	-1.9%	Near Gate	1.32	2.1%	E03	-8.35	-13.2%	Near Gate	-3.43	-3.6%	E03	1.99	2.1%
	Opp. Gate	-0.25	-0.7%	E04	-1.62	-4.2%	Opp. Gate	2.08	3.8%	E04	-7.59	-11.8%	Opp. Gate	-5.99	-6.1%	E04	-0.56	-0.6%
<b>2500</b>	Near Gate	1.45	3.9%	E03	-0.08	-0.2%	Near Gate	1.53	2.3%	E03	-9.40	-14.1%	Near Gate	-1.69	-1.7%	E03	-2.44	-2.4%
	Opp. Gate	0.35	0.9%	E04	-1.18	-3.0%	Opp. Gate	2.40	4.2%	E04	-8.53	-12.5%	Opp. Gate	-0.51	-0.5%	E04	-1.26	-1.3%
<b>3000</b>	Near Gate	1.75	4.6%	E03	0.54	1.4%	Near Gate	1.90	2.7%	E03	-8.13	-11.6%	Near Gate	1.24	1.2%	E03	-2.41	-2.3%
	Opp. Gate	0.63	1.6%	E04	-0.57	-1.4%	Opp. Gate	0.97	1.6%	E04	-9.06	-12.5%	Opp. Gate	-0.65	-0.6%	E04	-4.31	-4.0%

**ELECTRICAL CONDUCTIVITY RESULTS**

The electrical conductivity (EC) was assessed by subjecting specimens to varying levels of compression force applied to the electrodes. Table S8 to Table S12 encompasses the outcomes of the specimens in different positions of all the studied compounds.

Table S8. Measured EC on the specimens produced with E01 and near to the gate. Values are expressed in S/m.

E01 Near Gate F (N)	M7						M8						M9					
	Parallel		Perpendicular		Transversal		Parallel		Perpendicular		Transversal		Parallel		Perpendicular		Transversal	
	Avg.	Std. dev.	Avg.	Std. dev.	Avg.	Std. dev.	Avg.	Std. dev.	Avg.	Std. dev.	Avg.	Std. dev.	Avg.	Std. dev.	Avg.	Std. dev.	Avg.	Std. dev.
20	23.38	4.48	25.71	1.25	5.31	2.04	123.3	1.51	249.96	3.97	2.81	0.05	740.09	153.72	1321.84	497.16	11.69	2.36
40	26.03	3.06	26.98	0.75	6.12	2.31	128.09	1.02	238.94	1.83	3.1	0.04	776.82	209.61	1428.28	504.9	14.19	2.76
60	30.97	6.59	27.78	1.58	6.53	2.54	128.4	0.58	230.39	3.73	3.32	0.02	836.79	235.66	1396.79	433.18	15.22	3.02
80	30.69	5.11	28.33	1.46	6.8	2.49	129.53	0.88	226.73	0.54	3.48	0.02	885.72	278.12	1389.93	519.45	15.95	2.98
100	31.83	4.58	28.95	1.67	6.87	2.48	132.88	2.02	218.39	1.75	3.73	0	935.62	296.31	1368.42	490.64	17.09	3.09
150	32.06	4.93	29.76	2.07	7.37	2.58	157.17	0.79	231.74	1.68	3.95	0.02	918.75	336.92	1331.26	458.83	15.9	2.82
200	33.4	3.36	30.24	2.58	7.67	2.7	156.33	1.34	228.42	2.41	4.48	0.04	922.48	334.85	1319.47	405.75	18.07	3.27

Table S9. Measured EC on the specimens produced with E01 at the opposite to the gate location. Values are expressed in S/m.

E01 Opp. Gate F (N)	M7						M8						M9					
	Parallel		Perpendicular		Transversal		Parallel		Perpendicular		Transversal		Parallel		Perpendicular		Transversal	
	Avg.	Std. dev.	Avg.	Std. dev.	Avg.	Std. dev.	Avg.	Std. dev.	Avg.	Std. dev.	Avg.	Std. dev.	Avg.	Std. dev.	Avg.	Std. dev.	Avg.	Std. dev.
20	35.49	5.71	48.95	4.3	6.74	1.14	n.a.	n.a.	n.a.	n.a.	8.08	0.54	n.a.	n.a.	n.a.	n.a.	16.12	1.9
40	37.59	4.28	47.85	5.69	8.22	1.56	n.a.	n.a.	221.31	9.6	8.72	0.22	n.a.	n.a.	833.46	150.83	19.32	2.07
60	36.75	4.45	48.22	5.34	8.86	1.91	390.84	2.14	228.07	0	8.53	0.58	411.49	220.11	855.22	141.56	13.87	1.97
80	37.78	4.59	48.3	5.78	9.38	1.87	368.22	2.18	226.31	0.44	8.65	0.52	429.77	229.24	864.81	154.36	14.81	1.92
100	38.71	5.12	48.57	6.66	9.37	1.78	394.34	6.8	239.85	2.64	8.24	0.31	516.93	285.09	876.02	144.56	13.38	1.52
150	40.37	5.32	47.52	6.19	10.16	2.13	379.46	1.52	245.56	0.09	8.08	0.43	539.61	293.44	906.13	145.86	13.78	1.81
200	41.13	5.37	48.23	6.23	10.39	2.5	382.76	4.57	259.74	0	12.49	1.77	597.51	283.41	952.09	117.16	12.5	1.37

Table S10. Measured EC on the specimens produced with E04 and near to the gate. Values are expressed in S/m.

E04 Near Gate F (N)	M7						M8						M9					
	Parallel		Perpendicular		Transversal		Parallel		Perpendicular		Transversal		Parallel		Perpendicular		Transversal	
	Avg.	Std. dev.	Avg.	Std. dev.	Avg.	Std. dev.	Avg.	Std. dev.	Avg.	Std. dev.	Avg.	Std. dev.	Avg.	Std. dev.	Avg.	Std. dev.	Avg.	Std. dev.
20	49.79	3.18	49.74	10.99	4.71	1.19	232.06	40.05	253.82	93.46	5.41	3.26	828.91	211.06	1445.94	216.96	18.95	8.11
40	50.21	3.27	55.62	10.72	5.33	1.23	211.55	52.09	258.44	92.34	6.27	3.85	841.77	179.48	1345.53	299.68	21.13	8.91
60	51.82	3.27	57	9.41	5.62	1.62	222.27	58.77	277.58	113.32	6.74	4.18	854.23	157.99	1349.55	390.11	21.42	9.72
80	56.64	3.87	59.32	6.08	5.74	1.51	231.02	70.3	249.98	83.78	7.1	4.6	896.71	151.18	1341.72	456.38	23.29	10.6
100	55.97	4.11	59.22	6.51	5.97	1.18	236.04	75.99	247.44	78.76	7.39	4.81	921.27	99.24	1362.2	448.64	24.49	10.4
150	61.37	6.24	59.19	6.64	6.33	1.14	243.15	80.99	248.43	77.99	7.96	5.62	1002.27	125.94	1358.18	398.84	25.89	11.46
200	63.92	5.43	59.62	6.68	6.65	1.23	245.14	77.03	248.46	79.44	8.53	6.36	1041.12	159.75	1356.64	383.5	27.59	12.83

Table S11. Measured EC on the specimens produced with E04 at the opposite to the gate location. Values are expressed in S/m.

E04 Opp. Gate F (N)	M7						M8						M9					
	Parallel		Perpendicular		Transversal		Parallel		Perpendicular		Transversal		Parallel		Perpendicular		Transversal	
	Avg.	Std. dev.	Avg.	Std. dev.	Avg.	Std. dev.	Avg.	Std. dev.	Avg.	Std. dev.	Avg.	Std. dev.	Avg.	Std. dev.	Avg.	Std. dev.	Avg.	Std. dev.
20	45.5	23.48	66.27	5.21	2.96	0.69	225.97	2.25	564.58	38.86	5.38	1.51	1116.71	178.33	1679.02	366.74	13.44	3.45
40	51	21.93	68.26	5.76	3.64	0.72	268.96	66.93	364.82	147.23	7.43	2.25	1153.04	165.98	1641.67	322.54	22.64	5.67
60	53.95	20.99	70.78	5.22	4.07	0.81	254.03	66.18	345.86	104.18	8.32	3.17	1214.97	124.92	1645.72	281.33	26.85	7.79
80	55.29	17.86	70.73	6.47	4.41	0.9	275.4	58.84	360.8	106.56	9.17	4.19	1233.37	130.68	1670.58	314.61	28.31	9.37
100	57.16	16.92	71.63	6.78	4.64	0.8	288.05	68.41	353.85	94.09	9.39	4.76	1269.19	135.46	1682.36	299.56	28.96	9.84
150	57.94	16.03	72.95	7.97	5.1	0.91	277.72	71.97	359.66	94.75	10.1	4.7	1359.4	103.5	1645.18	240.51	30.66	9.86
200	56.94	17.62	74.58	7.99	5.37	1.03	295.13	92.44	343.51	66.31	14.36	3.62	1407.1	129.74	1664.37	235.7	34.48	13.08

Table S12. Measured EC on all the compounds and sampling positions with an applied compression force of 200 N. Values are expressed in S/m.

Direction	M7			M8			M9		
<b>Parallel</b>	E01   Near Gate	33.40	±3.36	E01   Near Gate	156.33	±1.34	E01   Near Gate	922.48	±334.85
	E01   Opp. Gate	41.13	±5.37	E01   Opp. Gate	382.76	±4.57	E01   Opp. Gate	597.51	±283.41
	E04   Near Gate	63.92	±5.43	E04   Near Gate	245.14	±77.03	E04   Near Gate	1041.12	±159.75
	E04   Opp. Gate	56.94	±17.62	E04   Opp. Gate	295.13	±92.44	E04   Opp. Gate	1407.10	±129.74
<b>Perpendicular</b>	E01   Near Gate	30.24	±2.58	E01   Near Gate	228.42	±2.41	E01   Near Gate	1319.47	±405.75
	E01   Opp. Gate	48.23	±6.23	E01   Opp. Gate	259.74	±0.00	E01   Opp. Gate	952.09	±117.16
	E04   Near Gate	59.62	±6.68	E04   Near Gate	248.46	±79.44	E04   Near Gate	1356.64	±383.50
	E04   Opp. Gate	74.58	±7.99	E04   Opp. Gate	343.51	±66.31	E04   Opp. Gate	1664.37	±235.70
<b>Transversal</b>	E01   Near Gate	7.67	±2.70	E01   Near Gate	4.48	±0.04	E01   Near Gate	18.07	±3.27
	E01   Opp. Gate	10.39	±2.50	E01   Opp. Gate	12.49	±1.77	E01   Opp. Gate	12.50	±1.37
	E04   Near Gate	6.65	±1.23	E04   Near Gate	8.53	±6.36	E04   Near Gate	27.59	±12.83
	E04   Opp. Gate	5.37	±1.03	E04   Opp. Gate	14.36	±3.62	E04   Opp. Gate	34.48	±13.08

Table S13 presents the fluctuations in EC achieved by progressively increasing the compression force from 20 N to 200 N. The table encompasses outcomes for specimens of all the studied compounds.

Table S13. Compression force effect, from 20 N to 200 N, to the measured EC on all the compounds and sampling position. Values are expressed in S/m.

Direction	M7			M8			M9		
<b>Parallel</b>	E01   Near Gate	+10.03	+42,9%	E01   Near Gate	+27.93	+21,8%	E01   Near Gate	+85.69	+10,2%
	E01   Opp. Gate	+5.64	+15,9%	E01   Opp. Gate	-8.08	-2,1%	E01   Opp. Gate	+186.02	+45,2%
	E04   Near Gate	+14.13	+28,4%	E04   Near Gate	+13.08	+5,6%	E04   Near Gate	+212.21	+25,6%
	E04   Opp. Gate	+11.44	+25,1%	E04   Opp. Gate	+69.16	+30,6%	E04   Opp. Gate	+290.39	+26,0%
<b>Perpendicular</b>	E01   Near Gate	+4.53	+17,6%	E01   Near Gate	-10.52	-4,4%	E01   Near Gate	-108.82	-7,6%
	E01   Opp. Gate	-0.72	-1,5%	E01   Opp. Gate	+38.43	+17,4%	E01   Opp. Gate	+118.63	+14,2%
	E04   Near Gate	+9.88	+19,9%	E04   Near Gate	-5.353	-2,1%	E04   Near Gate	-89.30	+6,2%
	E04   Opp. Gate	+8.31	+12,5%	E04   Opp. Gate	-221.07	-39,2%	E04   Opp. Gate	-14.65	-0,9%
<b>Transversal</b>	E01   Near Gate	+2.36	+44,5%	E01   Near Gate	+1.67	+59,7%	E01   Near Gate	+6.39	+54,6%
	E01   Opp. Gate	+3.66	+54,3%	E01   Opp. Gate	+4.41	+54,5%	E01   Opp. Gate	-3.62	-22,5%
	E04   Near Gate	+1.95	+41,4%	E04   Near Gate	+3.12	+57,7%	E04   Near Gate	+8.65	+45,6%
	E04   Opp. Gate	+2.41	+81,6%	E04   Opp. Gate	+8.98	+166,8%	E04   Opp. Gate	+21.04	+156,5%



Table S14 shows the EC variations for the three analysed compounds. These results were obtained with an applied compression force of 200 N. Data placed bellow columns entitled “E01 → E04” indicates the EC variations induced by the increase in melt temperature and injection speed (from E01 to E02). While the data placed bellow columns entitled “Near Gate → Opp. Gate” present the EC variations from the increase in the flow path (different measurement areas).

Table S14. Effect of processing conditions E01 to E04 and sample position on the EC of the three compounds. Measures are expressed in S/m and were taken under a compression force of 200 N.

Direction	M7						M8						M9					
	E01 → E04			Near Gate → Opp. Gate			E01 → E04			Near Gate → Opp. Gate			E01 → E04			Near Gate → Opp. Gate		
Parallel	Near Gate	+30.51	+91.3%	E01	+7.73	+23.1%	Near Gate	+88.82	+56.8%	E01	+226.43	+144.8%	Near Gate	+118.64	+355.2%	E01	-324.97	-973%
	Opp. Gate	+15.81	+38.4%	E04	-6.98	-10.9%	Opp. Gate	-87.63	-22.9%	E04	+49.99	+20.4%	Opp. Gate	+809.59	+1968.4%	E04	365.98	+573%
Perpendicular	Near Gate	+29.38	+97.1%	E01	+17.98	+59.5%	Near Gate	+20.05	+8.8%	E01	+31.32	+13.7%	Near Gate	+37.17	+122.9%	E01	-367.38	-1215%
	Opp. Gate	+26.35	+54.6%	E04	+14.96	+25.1%	Opp. Gate	+83.77	+32.3%	E04	+95.04	+38.3%	Opp. Gate	+712.28	+1476.9%	E04	307.73	+516%
Transversal	Near Gate	-1.02	-13.3%	E01	+2.72	+35.5%	Near Gate	+4.05	+90.5%	E01	+8.01	+178.8%	Near Gate	+9.52	+124.1%	E01	+1,38	+2.1%
	Opp. Gate	-5.02	-48.3%	E04	-1.28	-19.3%	Opp. Gate	+1.87	+15.0%	E04	+5.82	+68.2%	Opp. Gate	+21.98	+211.5%	E04	+0,60	+0.9%

**Appendix E.** Supplementary results to chapter 3.6.

**EXPERIMENTAL WORK**

Table S15. Injection moulding conditions for the CF filled polymer compounds.

<b>Material</b>	<b>DE0026 (PC + 10% CF)</b>				<b>DE003 (PC + 15% CF)</b>				<b>DE006 (PC + 30% CF)</b>			
<b>Experimental Plan</b>	<b>A</b>	<b>B</b>	<b>C</b>	<b>D</b>	<b>A</b>	<b>B</b>	<b>C</b>	<b>D</b>	<b>A</b>	<b>B</b>	<b>C</b>	<b>D</b>
<b>Melt Temperature (°C)</b>	305	305	305	305	305	305	305	305	305	305	305	305
<b>Injection speed (mm/s)</b>	40	40	40	40	40	40	40	40	40	40	40	40
<b>Injection Pressure (bar)</b>	29	33	42	80	30	38	41	85	37	63	47	90
<b>Holding Pressure (bar)</b>	15	15	15	15	15	15	15	15	15	15	15	15
<b>Holding Time (s)</b>	10	10	10	10	10	10	10	10	10	10	10	10
<b>Mould Temperature (°C)</b>	80	80	80	80	80	80	80	80	80	80	80	80
<b>Cooling Time (s)</b>	35	35	35	35	35	35	35	35	35	35	35	35

Table S16. Injection moulding conditions for the SFF filled polymer compounds.

<b>Material</b>	<b>DS0026I (PC + 10% SFF)</b>				<b>DS0036I (PC + 15% SFF)</b>			
<b>Experimental Plan</b>	<b>A</b>	<b>B</b>	<b>C</b>	<b>D</b>	<b>A</b>	<b>B</b>	<b>C</b>	<b>D</b>
<b>Melt Temperature (°C)</b>	305	305	305	305	305	305	305	305
<b>Injection speed (mm/s)</b>	40	40	40	40	40	40	40	40
<b>Injection Pressure (bar)</b>	25	44	33	71	23	45	30	68
<b>Holding Pressure (bar)</b>	15	15	15	15	15	15	15	15
<b>Holding Time (s)</b>	10	10	10	10	10	10	10	10
<b>Mould Temperature (°C)</b>	80	80	80	80	80	80	80	80
<b>Cooling Time (s)</b>	35	35	35	35	35	35	35	35

**EM SHIELDING RESULTS**

The electromagnetic shielding examined across the injection moulded specimens under different processing conditions (A, B, C and D). The average EMSE values for each CF or SSF-filled compound at different frequencies can be seen from Table S17 to Table S21.

Table S17. Shielding effectiveness measured for the DE0026 (PC + 10% CF) compound, units in dB.

Exp. condition	Frequency (MHz)	30	100	300	500	800	1000	1500	2000	2500	3000
<b>A</b>	Average	18.07	11.32	9.74	10.66	12.37	12.96	13.45	14.91	12.03	16.13
	Std. Dev.	0.74	0.30	0.18	0.20	0.17	0.17	0.17	0.19	0.49	0.61
<b>B</b>	Average	15.42	9.38	8.88	10.71	13.25	13.73	14.08	15.59	15.44	18.71
	Std. Dev.	0.26	0.30	0.41	0.43	0.38	0.19	0.32	0.25	0.51	0.26
<b>C</b>	Average	15.25	8.06	5.57	6.08	7.80	8.54	9.44	12.17	11.42	12.92
	Std. Dev.	1.14	0.64	0.27	0.25	0.26	0.22	0.27	0.26	0.23	0.20
<b>D</b>	Average	10.31	4.64	3.88	5.05	7.21	8.18	9.29	12.31	11.60	13.32
	Std. Dev.	0.18	0.09	0.12	0.13	0.13	0.13	0.13	0.11	0.08	0.19

Table S18. Shielding effectiveness measured for the DE003 (PC + 15% CF) compound, units in dB.

Exp. condition	Frequency (MHz)	30	100	300	500	800	1000	1500	2000	2500	3000
<b>A</b>	Average	14.38	9.12	9.45	11.28	13.51	14.26	15.55	14.38	13.86	15.61
	Std. Dev.	2.06	0.95	0.25	0.25	0.26	0.25	0.72	1.30	2.31	1.73
<b>B</b>	Average	14.18	8.59	9.00	11.00	13.63	14.05	15.28	14.75	18.48	15.70
	Std. Dev.	0.47	0.31	0.21	0.19	0.21	0.20	0.67	0.97	1.05	1.18
<b>C</b>	Average	11.25	6.27	6.67	8.36	10.65	11.64	13.86	14.82	15.09	15.63
	Std. Dev.	1.05	0.61	0.29	0.39	0.41	0.37	0.53	1.04	0.87	1.27
<b>D</b>	Average	9.08	5.26	5.96	7.80	10.44	11.93	12.50	14.31	14.13	17.23
	Std. Dev.	0.31	0.19	0.22	0.17	0.16	0.10	0.72	0.70	1.05	0.80

Table S19. Shielding effectiveness measured for the DE006 (PC + 30% CF) compound, units in dB.

Exp. condition	Frequency (MHz)	30	100	300	500	800	1000	1500	2000	2500	3000
<b>A</b>	Average	29.41	24.89	24.61	24.93	25.09	24.70	25.70	27.45	28.82	31.20
	Std. Dev.	4.73	1.23	0.63	0.65	0.51	0.53	1.74	0.78	1.56	0.75
<b>B</b>	Average	18.73	17.54	18.76	20.18	21.20	21.20	22.52	22.45	23.12	25.20
	Std. Dev.	0.82	0.35	0.40	0.26	0.21	0.20	1.51	0.74	0.46	0.72
<b>C</b>	Average	25.65	22.08	21.90	22.76	23.34	23.35	24.29	24.90	25.28	26.86
	Std. Dev.	4.51	0.96	0.96	0.82	0.86	0.87	1.64	1.21	2.86	1.48
<b>D</b>	Average	18.94	17.80	18.35	19.74	20.41	20.68	21.83	22.93	22.90	25.97
	Std. Dev.	1.16	1.20	1.28	0.86	0.88	0.83	1.51	0.61	1.13	0.72

Table S20. Shielding effectiveness measured for the DS0026I (PC + 10% SSF) compound, units in dB.

Exp. condition	Frequency (MHz)	30	100	300	500	800	1000	1500	2000	2500	3000
<b>A</b>	Average	36.73	34.89	33.96	34.27	34.59	34.73	36.18	39.11	38.55	41.67
	Std. Dev.	5.67	2.98	2.40	2.36	2.49	2.57	2.83	3.03	3.42	3.70
<b>B</b>	Average	40.20	39.52	43.40	45.69	48.16	48.83	50.78	54.17	56.42	73.07
	Std. Dev.	1.47	1.02	1.74	1.15	1.45	1.72	1.97	1.88	1.82	2.81
<b>C</b>	Average	30.64	23.88	22.31	22.69	22.65	22.40	21.97	23.07	21.44	23.60
	Std. Dev.	9.29	3.37	1.44	1.15	1.44	1.70	1.81	1.73	1.73	1.83
<b>D</b>	Average	39.16	33.12	25.90	25.56	22.74	22.03	21.67	23.14	21.66	24.71
	Std. Dev.	5.83	2.95	2.63	2.25	1.79	1.68	1.58	1.53	1.58	1.92

Table S21. Shielding effectiveness measured for the DS0036I (PC + 15% SSF) compound, units in dB.

Exp. condition	Frequency (MHz)	30	100	300	500	800	1000	1500	2000	2500	3000
<b>A</b>	Average	49.24	48.56	54.41	58.25	62.40	63.40	67.15	67.81	64.42	64.01
	Std. Dev.	1.92	2.75	3.48	2.24	1.27	0.69	1.11	1.63	1.85	2.60
<b>B</b>	Average	52.28	49.60	58.06	63.10	68.03	67.71	70.26	71.05	66.88	66.58
	Std. Dev.	2.14	2.63	2.88	2.02	1.33	1.38	1.46	0.92	0.86	0.84
<b>C</b>	Average	33.06	34.26	37.61	39.24	40.52	41.47	45.89	53.24	51.76	53.57
	Std. Dev.	4.26	1.49	2.17	2.32	2.98	3.22	2.99	2.07	2.94	2.33
<b>D</b>	Average	45.20	41.58	45.16	48.16	50.01	50.29	50.58	52.60	51.79	60.26
	Std. Dev.	3.79	1.95	3.06	2.47	1.99	1.81	3.28	3.60	3.25	3.06

The normalized shielding (EM shielding divided by the specimen thickness) for each CF or SSF-filled compound at different frequencies can be seen from Table S22 to Table S26.

Table S22. Thickness normalized shielding measured for the DE0026 (PC + 10% CF) compound, units in dB/mm.

Exp. condition	Frequency (MHz)	30	100	300	500	800	1000	1500	2000	2500	3000
<b>A</b>	Average	6.06	3.80	3.27	3.58	4.15	4.35	4.51	5.00	4.04	5.41
	Std. Dev.	0.25	0.10	0.06	0.07	0.06	0.06	0.06	0.06	0.16	0.20
<b>B</b>	Average	5.10	3.10	2.93	3.54	4.38	4.54	4.65	5.15	5.10	6.18
	Std. Dev.	0.09	0.10	0.14	0.14	0.13	0.06	0.11	0.08	0.17	0.09
<b>C</b>	Average	9.57	5.05	3.49	3.81	4.89	5.36	5.92	7.63	7.16	8.10
	Std. Dev.	0.72	0.40	0.17	0.16	0.16	0.14	0.17	0.16	0.14	0.13
<b>D</b>	Average	6.87	3.09	2.58	3.36	4.80	5.45	6.19	8.20	7.73	8.87
	Std. Dev.	0.12	0.06	0.08	0.09	0.09	0.09	0.08	0.07	0.06	0.13

Table S23. Thickness normalized shielding measured for the DE003 (PC + 15% CF) compound, units in dB/mm.

Exp. condition	Frequency (MHz)	30	100	300	500	800	1000	1500	2000	2500	3000
<b>A</b>	Average	4.77	3.02	3.13	3.74	4.48	4.72	5.15	4.77	4.59	5.17
	Std. Dev.	0.68	0.31	0.08	0.08	0.08	0.08	0.24	0.43	0.77	0.57
<b>B</b>	Average	4.60	2.79	2.92	3.57	4.43	4.56	4.96	4.79	6.00	5.10
	Std. Dev.	0.15	0.10	0.07	0.06	0.07	0.06	0.22	0.31	0.34	0.38
<b>C</b>	Average	7.15	3.99	4.24	5.31	6.77	7.40	8.81	9.42	9.59	9.93
	Std. Dev.	0.67	0.39	0.18	0.25	0.26	0.24	0.34	0.66	0.55	0.81
<b>D</b>	Average	5.70	3.30	3.74	4.90	6.56	7.49	7.85	8.98	8.87	10.82
	Std. Dev.	0.19	0.12	0.14	0.10	0.10	0.07	0.45	0.44	0.66	0.50

Table S24. Thickness normalized shielding measured for the DE006 (PC + 30% CF) compound, units in dB/mm.

Exp. condition	Frequency (MHz)	30	100	300	500	800	1000	1500	2000	2500	3000
<b>A</b>	Average	9.72	8.23	8.14	8.24	8.29	8.17	8.50	9.08	9.53	10.31
	Std. Dev.	1.56	0.41	0.21	0.22	0.17	0.17	0.58	0.26	0.52	0.25
<b>B</b>	Average	5.57	5.21	5.58	6.00	6.30	6.30	6.70	6.67	6.88	7.49
	Std. Dev.	1.97	1.84	1.96	2.11	2.22	2.22	2.40	2.36	2.42	2.64
<b>C</b>	Average	14.25	12.27	12.16	12.64	12.96	12.97	13.49	13.83	14.04	14.92
	Std. Dev.	5.65	4.35	4.31	4.47	4.58	4.58	4.83	4.91	5.21	5.31
<b>D</b>	Average	11.26	10.58	10.91	11.74	12.13	12.29	12.98	13.63	13.62	15.44
	Std. Dev.	0.69	0.71	0.76	0.51	0.52	0.49	0.90	0.36	0.67	0.43

## Appendices

Table S25. Thickness normalized shielding measured for the DS0026I (PC + 10% SSF) compound, units in dB/mm.

Exp. condition	Frequency (MHz)	30	100	300	500	800	1000	1500	2000	2500	3000
<b>A</b>	Average	12.11	11.50	11.19	11.30	11.40	11.45	11.93	12.89	12.71	13.74
	Std. Dev.	1.87	0.98	0.79	0.78	0.82	0.85	0.93	1.00	1.13	1.22
<b>B</b>	Average	13.19	12.97	14.24	14.99	15.80	16.02	16.66	17.77	18.51	23.97
	Std. Dev.	0.48	0.33	0.57	0.38	0.48	0.56	0.65	0.62	0.60	0.92
<b>C</b>	Average	19.37	15.10	14.11	14.35	14.32	14.16	13.89	14.59	13.55	14.93
	Std. Dev.	5.88	2.13	0.91	0.73	0.91	1.08	1.15	1.09	1.09	1.16
<b>D</b>	Average	26.42	22.34	17.47	17.24	15.34	14.86	14.62	15.61	14.61	16.67
	Std. Dev.	3.93	1.99	1.77	1.52	1.21	1.13	1.07	1.03	1.07	1.30

Table S26. Thickness normalized shielding measured for the DS0036I (PC + 15% SSF) compound, units in dB/mm.

Exp. condition	Frequency (MHz)	30	100	300	500	800	1000	1500	2000	2500	3000
<b>A</b>	Average	16.31	16.09	18.03	19.30	20.68	21.01	22.25	22.47	21.34	21.21
	Std. Dev.	0.64	0.91	1.15	0.74	0.42	0.23	0.37	0.54	0.61	0.86
<b>B</b>	Average	17.16	16.28	19.06	20.71	22.33	22.22	23.06	23.32	21.95	21.85
	Std. Dev.	0.70	0.86	0.94	0.66	0.44	0.45	0.48	0.30	0.28	0.28
<b>C</b>	Average	20.45	21.20	23.27	24.28	25.07	25.66	28.39	32.94	32.02	33.14
	Std. Dev.	2.63	0.92	1.34	1.44	1.84	1.99	1.85	1.28	1.82	1.44
<b>D</b>	Average	28.14	25.89	28.11	29.99	31.14	31.31	31.49	32.75	32.24	37.52
	Std. Dev.	2.36	1.22	1.90	1.54	1.24	1.13	2.04	2.24	2.02	1.90

The specific shielding (EM shielding divided by the specimen density) for each CF or SSF-filled compound at different frequencies can be seen from Table S27 to

S31.

Table S27. Specific shielding measured for the DE0026 (PC + 10% CF) compound, units in dB.cm<sup>3</sup>/g.

Exp. condition	Frequency (MHz)	30	100	300	500	800	1000	1500	2000	2500	3000
<b>A</b>	Average	14.90	9.28	7.95	8.67	10.08	10.57	10.97	12.18	9.85	13.22
	Std. Dev.	0.56	0.24	0.18	0.19	0.17	0.17	0.17	0.18	0.48	0.54
<b>B</b>	Average	12.60	7.64	7.25	8.76	10.89	11.25	11.56	12.80	12.65	15.28
	Std. Dev.	0.26	0.13	0.17	0.14	0.15	0.07	0.10	0.09	0.40	0.12
<b>C</b>	Average	12.73	6.70	4.53	4.91	6.29	6.90	7.62	9.85	9.26	10.52
	Std. Dev.	0.69	0.51	0.26	0.22	0.22	0.17	0.22	0.20	0.19	0.18
<b>D</b>	Average	8.45	3.81	3.18	4.14	5.91	6.71	7.60	10.07	9.50	10.89
	Std. Dev.	0.18	0.09	0.10	0.12	0.11	0.12	0.10	0.09	0.07	0.14

Table S28. Specific shielding measured for the DE003 (PC + 15% CF) compound, units in dB.cm<sup>3</sup>/g.

Exp. condition	Frequency (MHz)	30	100	300	500	800	1000	1500	2000	2500	3000
<b>A</b>	Average	11.95	7.51	7.58	9.08	10.88	11.48	12.36	11.90	10.45	12.49
	Std. Dev.	1.77	0.81	0.18	0.17	0.19	0.17	0.52	1.11	1.65	1.35
<b>B</b>	Average	11.58	7.02	7.12	8.81	10.97	11.33	11.82	12.45	14.15	13.35
	Std. Dev.	0.32	0.21	0.18	0.18	0.16	0.13	0.14	0.11	0.47	0.18
<b>C</b>	Average	9.09	5.11	5.37	6.77	8.62	9.41	11.00	12.13	12.07	12.79
	Std. Dev.	0.96	0.44	0.03	0.15	0.19	0.17	0.47	0.83	0.85	1.16
<b>D</b>	Average	7.44	4.36	4.79	6.36	8.50	9.65	9.75	11.95	10.83	14.29



## Appendices

	Std. Dev.	0.19	0.06	0.07	0.10	0.10	0.05	0.08	0.07	0.04	0.19
--	-----------	------	------	------	------	------	------	------	------	------	------

Table S29. Specific shielding measured for the DE006 (PC + 30% CF) compound, units in dB.cm<sup>3</sup>/g.

Exp. condition	Frequency (MHz)	30	100	300	500	800	1000	1500	2000	2500	3000
<b>A</b>	Average	23.21	19.14	18.81	19.04	19.13	18.81	19.36	20.80	21.71	23.69
	Std. Dev.	3.85	1.09	0.40	0.49	0.27	0.20	1.20	0.38	1.00	0.39
<b>B</b>	Average	14.39	13.39	14.26	15.45	16.24	16.21	16.92	17.40	17.67	19.50
	Std. Dev.	0.55	0.23	0.26	0.21	0.18	0.13	1.14	0.62	0.29	0.65
<b>C</b>	Average	19.71	16.64	16.34	17.11	17.52	17.54	18.00	18.72	18.63	20.15
	Std. Dev.	4.00	0.68	0.48	0.54	0.56	0.59	1.14	1.04	2.45	1.34
<b>D</b>	Average	14.50	12.93	13.27	14.62	15.16	15.38	15.82	17.20	16.85	19.89
	Std. Dev.	0.54	0.39	0.41	0.35	0.31	0.29	0.23	0.28	0.36	0.34

Table S30. Specific shielding measured for the DS0026I (PC + 10% SSF) compound, units in dB.cm<sup>3</sup>/g.

Exp. condition	Frequency (MHz)	30	100	300	500	800	1000	1500	2000	2500	3000
<b>A</b>	Average	29.97	28.66	28.13	28.46	28.83	28.98	30.28	32.72	32.41	35.01
	Std. Dev.	5.41	2.60	1.79	1.58	1.51	1.53	1.59	1.68	1.95	2.17
<b>B</b>	Average	32.66	32.31	35.52	37.33	39.53	40.22	41.89	44.65	46.16	58.80
	Std. Dev.	1.46	0.59	1.76	1.10	1.25	1.43	1.68	1.43	1.02	1.15
<b>C</b>	Average	23.04	18.41	17.78	18.26	18.30	18.12	17.70	18.52	17.23	18.94
	Std. Dev.	8.39	2.68	1.22	0.94	1.18	1.42	1.41	1.21	1.16	1.23
<b>D</b>	Average	30.27	26.73	20.77	20.33	18.17	17.61	17.33	18.52	17.34	19.82
	Std. Dev.	4.69	2.75	2.42	1.94	1.58	1.47	1.39	1.36	1.40	1.73

S31. Specific shielding measured for the DS0036I (PC + 15% SSF) compound, units in dB.cm<sup>3</sup>/g.

Exp. condition	Frequency (MHz)	30	100	300	500	800	1000	1500	2000	2500	3000
<b>A</b>	Average	38.84	38.84	43.22	45.80	49.22	50.12	52.97	53.63	51.09	50.89
	Std. Dev.	1.73	2.03	2.82	2.11	0.99	0.43	1.04	1.49	1.64	2.30
<b>B</b>	Average	41.62	39.29	46.31	50.20	53.92	53.73	55.95	56.28	53.05	52.66
	Std. Dev.	1.71	2.17	2.48	1.86	1.24	1.31	1.34	0.85	0.61	0.65
<b>C</b>	Average	25.32	26.86	29.73	30.96	32.04	32.90	36.55	41.72	39.89	41.79
	Std. Dev.	3.78	1.21	2.01	2.00	2.63	2.76	2.33	1.55	1.70	1.30
<b>D</b>	Average	35.62	32.47	34.72	37.36	38.87	39.11	39.06	40.56	39.96	47.11
	Std. Dev.	3.58	1.53	1.89	2.02	1.57	1.40	2.68	2.92	2.61	2.71

The DC electrical conductivity (EC) for each CF-filled compound and SS-filled compounds can be seen in Table S32 and

Table S33, respectively.

Table S32. Measured EC on CF-filled compounds with an applied compression force of 200 N. Values are expressed in S/m.

Direction		DE0026 (PC + 10% CF)		DE003 (PC + 15% CF)		DE006 (PC + 30% CF)			
<b>Parallel</b>	A	1.15E-01	± 1.99E-02	A	4.55E-02	± 1.09E-02	A	3.34	± 0.46
	B	5.06E-03	± 1.68E-03	B	4.01E-02	± 1.14E-02	B	4.03	± 0.31
	C	2.06E-01	± 3.40E-02	C	2.47E-01	± 3.75E-02	C	8.28	± 0.55
	D	3.04E-02	± 1.23E-02	D	1.44E-01	± 1.02E-02	D	4.30	± 0.19
<b>Perpendicular</b>	A	1.13E-01	± 4.65E-02	A	4.21E-02	± 1.19E-02	A	2.05	± 0.19
	B	4.38E-03	± 1.22E-03	B	3.29E-02	± 4.24E-03	B	3.54	± 0.62
	C	2.11E-01	± 5.14E-02	C	2.25E-01	± 2.90E-02	C	9.48	± 0.80
	D	4.22E-02	± 1.81E-02	D	1.18E-01	± 6.46E-02	D	4.84	± 0.15
<b>Transversal</b>	A	1.23E-02	± 1.30E-03	A	8.16E-03	± 6.07E-04	A	0.25	± 0.03

## Appendices

B	7.26E-04	± 7.37E-05	B	6.01E-03	± 1.19E-03	B	0.80	± 0.05
C	2.65E-02	± 3.92E-04	C	2.79E-02	± 9.33E-04	C	0.44	± 0.04
D	4.21E-03	± 4.41E-05	D	1.20E-02	± 1.90E-03	D	0.31	± 0.04

Table S33. Measured EC on SSF-filled compounds with an applied compression force of 200 N. Values are expressed in S/m.

Direction	DS0026I (PC + 10% SSF)			DS0036I (PC + 15% SSF)		
<b>Parallel</b>	A	2.52	± 0.78	A	25.03	± 5.54
	B	3.65	± 0.84	B	9.01	± 2.05
	C	2.37	± 1.47	C	40.73	± 16.59
	D	2.02	± 0.84	D	17.83	± 7.77
<b>Perpendicular</b>	A	2.93	± 1.20	A	21.20	± 2.74
	B	5.81	± 3.01	B	14.08	± 4.63
	C	1.72	± 0.51	C	24.38	± 8.02
	D	2.73	± 0.99	D	11.63	± 6.04
<b>Transversal</b>	A	0.53	± 0.21	A	1.29	± 0.51
	B	0.88	± 0.20	B	1.98	± 0.76
	C	0.68	± 0.13	C	0.94	± 0.28
	D	0.46	± 0.15	D	0.42	± 0.12

Table S34. Electrical conductivity anisotropic ratio (L/T).

Direction	DE0026 (PC + 10% CF)		DE003 (PC + 15% CF)		DE006 (PC + 30% CF)		DS0026I (PC + 10% SSF)		DS0036I (PC + 15% SSF)	
<b>Parallel / Perpendicular</b>	A	1.02	A	1.08	A	1.63	A	0.86	A	1.18
	B	1.16	B	1.22	B	1.14	B	0.63	B	0.64
	C	0.97	C	1.10	C	0.87	C	1.38	C	1.67
	D	0.72	D	1.22	D	0.89	D	0.74	D	1.53
<b>Parallel / Transversal</b>	A	9.40	A	5.58	A	13.09	A	4.74	A	19.42
	B	6.97	B	6.67	B	5.05	B	4.15	B	4.55
	C	7.76	C	8.85	C	18.66	C	3.50	C	43.45
	D	7.23	D	11.92	D	13.89	D	4.43	D	42.72

<b>Perpendicular / Transversal</b>	A	9.22	A	5.16	A	8.03	A	5.50	A	16.44
	B	6.03	B	5.48	B	4.44	B	6.61	B	7.10
	C	7.96	C	8.066	C	21.37	C	2.54	C	26.00
	D	10.02	D	10.87	D	15.62	D	6.00	D	27.87

The complex and frequency dependent properties were characterized by analysing the material impedance assuming an equivalent LCR circuit model for the material under test. The measured Inductance (L), Capacitance (C) and Resistance (R) values for each fibre-filled compound is shown in Table S35. The complex and frequency dependent permittivity ( $\epsilon'_{r}$  and  $\epsilon''_{r}$ ) were obtained from the equivalent impedance model and the corresponding real part of the frequency-dependent electrical conductivity ( $\sigma'_{Z}$ ) in the through-thickness direction (or transversal) was calculated according to the methodology described in section 3.3.4. The anisotropic characteristic for the frequency-dependent electrical conductivity was estimated by applying a ratio of proportionality between the longitudinal and transversal DC measures (Table S34) obtaining the longitudinal conductivity ( $\sigma'_{XY}$ ) which can be used to estimate the electromagnetic shielding of the specific material and compared to the experimental data. A resume for the measured properties at 1 GHz is shown in Table S36 for the CF-filled compounds. Measures for the SSF-filled materials were not reliable due to possible measurement errors from the DC apparatus and the unadjusted equivalent impedance circuit for the ferromagnetic nature of the stainless-steel fibres. Hence, this analysis was taken exclusively for the CF-filled materials

Table S35. LCR coefficients measured by the impedance analyser.

		<b>DE0026 (PC + 10% CF)</b>			<b>DE003 (PC + 15% CF)</b>			<b>DE006 (PC + 30% CF)</b>			<b>DS0026I (PC + 10% SSF)</b>			<b>DS0036I (PC + 15% SSF)</b>		
<b>Exp. condition</b>		<b>R</b>	<b>C</b>	<b>L</b>	<b>R</b>	<b>C</b>	<b>L</b>	<b>R</b>	<b>C</b>	<b>L</b>	<b>R</b>	<b>C</b>	<b>L</b>	<b>R</b>	<b>C</b>	<b>L</b>
<b>A</b>	Average	4.96	4.42E-12	2.60E-09	3.15	4.59E-12	2.94E-09	13.30	1.14E-11	4.31E-09	11.31	1.15E-11	4.38E-09	12.55	4.79E-11	4.46E-09
	Std. Dev.	0.23	7.51E-14	2.29E-11	0.08	2.83E-14	2.01E-11	0.87	7.08E-13	2.81E-11	4.14	5.45E-12	3.50E-10	4.18	5.88E-11	3.74E-10
<b>B</b>	Average	3.01	4.18E-12	2.62E-09	3.60	4.63E-12	2.97E-09	12.93	1.06E-11	4.41E-09	21.75	2.47E-11	3.23E-09	16.65	1.67E-11	3.70E-09
	Std. Dev.	0.14	3.26E-14	1.85E-11	0.17	1.46E-13	4.62E-11	0.79	6.45E-13	2.05E-11	9.24	1.37E-11	1.09E-09	8.20	7.17E-12	1.01E-09
<b>C</b>	Average	5.34	4.91E-12	3.12E-09	4.37	5.17E-12	3.59E-09	15.78	1.84E-11	4.44E-09	7.32	7.76E-12	4.43E-09	17.60	3.73E-11	4.26E-09

## Appendices

	Std. Dev.	0.44	1.33E-13	4.11E-11	0.04	6.04E-14	3.07E-11	0.71	1.55E-12	4.04E-11	0.90	6.54E-13	2.67E-10	5.03	8.82E-12	1.12E-09
<b>D</b>	Average	3.28	4.68E-12	3.13E-09	4.66	5.15E-12	3.52E-09	17.81	2.09E-11	4.38E-09	3.63	5.45E-12	4.22E-09	14.93	2.17E-11	4.41E-09
	Std. Dev.	0.10	9.17E-14	4.62E-11	0.13	2.05E-14	8.04E-12	0.96	1.82E-12	3.82E-11	0.54	8.79E-14	1.90E-10	4.29	1.36E-11	6.31E-10

The complex and frequency dependent permittivity ( $\epsilon' r$  and  $\epsilon'' r$ ) were obtained from the equivalent impedance model and the corresponding real part of the frequency-dependent electrical conductivity ( $\sigma' Z$ ) in the through-thickness direction (or transversal) was calculated according to the methodology described in section 3.3.4. The anisotropic characteristic for the frequency-dependent electrical conductivity was estimated by applying a ratio of proportionality between the longitudinal and transversal DC measures (Table S34) obtaining the longitudinal conductivity ( $\sigma' XY$ ) which can be used to estimate the electromagnetic shielding of the specific material and compared to the experimental data. A resume for the measured properties at 1 GHz is shown in Table S36 for the CF-filled compounds. Measures for the SSF-filled materials were not reliable due to possible measurement errors from the DC apparatus and the unadjusted equivalent impedance circuit for the ferromagnetic nature of the stainless-steel fibres. Hence, this analysis was taken exclusively for the CF-filled materials.

Table S36. Resume table from the impedance analysis at 1 GHz for the CF-filled compounds.

Exp. condition	CF wt%	Zeq  ( $\Omega$ )	$\epsilon' r$	$\epsilon'' r$	$\sigma' Z$ (S/m)	DC $\sigma$ ratio	$\sigma' XY$ (S/m)	SE from $\sigma' Z$ (dB)	SE from $\sigma' XY$ (dB)	Experimental SE (dB)
<b>A</b>	10	20.31	37.79	5.21	0.29	4	1.16	4.12	13.08	12,96
	15	16.55	40.79	3.71	0.21	5	1.03	4.43	15.29	14,26
	30	18.67	53.4	50.79	2.83	10	28.26	9.6	24.68	24,70
<b>B</b>	10	21.81	37.19	2.94	0.16	5	0.82	3.9	14.6	13,73
	15	16.17	43.49	4.56	0.25	5	1.27	5.12	16.09	14,05
	30	18.1	54.87	47.21	2.63	6	15.76	9.45	21.39	21,20
<b>C</b>	10	13.93	22.53	3.72	0.21	6	1.24	1	8.26	8,54
	15	9.34	23.95	3.4	0.19	9	1.7	1.02	11.55	11,64
	30	24.88	20.84	37.73	2.1	20	41.99	4.56	23.36	23,35
<b>D</b>	10	14.72	20.60	1.99	0.11	7	0.78	0.64	8.04	8,18
	15	9.96	24.51	3.7	0.21	9	1.85	1.13	11.95	11,93
	30	26.66	16.24	37.54	2.09	15	31.33	4.55	21.07	20,68

**Appendix G.** Supplementary results to chapter 4.2.

**EM SHIELDING RESULTS**

The average shielding measured along the frequency band between 30 MHz and 3 GHz, as a function of the amount of printed CF layers is depicted in Table S44.

Table S37. Average shielding effectiveness measured for the printed composites, units in dB.

	<b>Onyx (0 CF)</b>	<b>1 CF</b>	<b>2 CF</b>	<b>4 CF</b>	<b>6 CF</b>	<b>8 CF</b>	<b>10 CF</b>	<b>12 CF</b>	<b>14 CF</b>
<b>SE</b>	3.15	18.02	46.21	50.05	50.48	57.84	61.83	65.05	69.83
<b>Deviation</b>	0.91	5.04	8.52	7.13	5.75	4.55	5.62	5.09	4.69

The average normalized shielding (SE divided by the specimen thickness) and the adjusted normalized shielding for the total CF thickness (SE divided by the effective CF layer thickness (CFt)) measured along the frequency band between 30 MHz and 3 GHz, as a function of the amount of printed CF layers is depicted in Table S38.

Table S38. Thickness normalized SE measured for the printed composites, units in dB.

	<b>Onyx (0 CF)</b>	<b>1 CF</b>	<b>2 CF</b>	<b>4 CF</b>	<b>6 CF</b>	<b>8 CF</b>	<b>10 CF</b>	<b>12 CF</b>	<b>14 CF</b>
<b>SE/t</b>	1.59	9.02	23.03	24.90	25.26	28.70	30.43	32.12	34.43
<b>Deviation</b>	0.46	2.52	4.25	3.54	2.88	2.26	2.76	2.51	2.31
<b>SE/ CFt</b>		144.18	184.82	100.09	67.31	57.84	49.47	43.37	39.90
<b>Deviation</b>		40.30	34.06	14.25	7.67	4.55	4.49	3.39	2.68

The average specific shielding (SE divided by the material density) measured along the frequency band between 30 MHz and 3 GHz, as a function of the amount of printed CF layers is depicted in Table S39.

Table S39. Average specific shielding measured for the printed composites, units in dB.

	<b>Onyx (0 CF)</b>	<b>1 CF</b>	<b>2 CF</b>	<b>4 CF</b>	<b>6 CF</b>	<b>8 CF</b>	<b>10 CF</b>	<b>12 CF</b>	<b>14 CF</b>
<b>Specific SE</b>	2.76	15.85	39.79	44.08	44.51	51.51	55.16	58.84	60.71
<b>Deviation</b>	0.80	4.43	7.33	6.28	5.07	4.06	5.01	4.60	4.07

The shielding by absorption, reflection, and total shielding as a function of the amount of printed CF layers is depicted in Table S40, Table S41 and Table S42, respectively.

Table S40. Shielding by absorption measured for printed composites, units in dB.

<b>MHz</b>	<b>Onyx (0 CF)</b>	<b>1 CF</b>	<b>2 CF</b>	<b>4 CF</b>	<b>6 CF</b>	<b>8 CF</b>	<b>10 CF</b>	<b>12 CF</b>	<b>14 CF</b>
<b>200</b>	4.64	19.89	40.70	42.67	44.22	47.48	50.16	49.91	55.14
<b>400</b>	1.24	18.30	43.80	46.85	49.83	51.71	54.15	53.84	55.38
<b>600</b>	0.79	17.85	48.47	52.74	59.58	54.06	54.85	54.70	59.02
<b>800</b>	0.78	19.52	59.35	58.50	52.78	52.45	54.85	56.78	62.81
<b>1000</b>	-0.75	18.53	44.75	46.67	46.67	51.66	56.02	58.45	60.29
<b>1200</b>	-0.50	18.92	40.14	44.99	46.88	51.87	58.66	60.17	65.31
<b>1400</b>	0.04	14.61	37.13	39.91	42.75	49.25	54.71	57.21	61.77
<b>1600</b>	0.90	13.18	38.12	40.77	45.23	50.50	55.96	58.27	63.17
<b>1800</b>	0.52	10.94	33.90	38.03	42.42	48.64	53.49	56.28	61.49
<b>2000</b>	-0.91	9.73	30.06	35.78	40.84	47.49	52.13	54.52	58.69
<b>2200</b>	-0.31	9.34	27.77	35.77	39.50	45.22	49.60	53.20	58.45
<b>2400</b>	0.22	9.20	29.07	33.07	37.40	42.81	45.67	48.41	53.41
<b>2600</b>	-0.36	9.58	27.78	32.74	37.44	42.91	45.65	48.43	54.36
<b>2800</b>	-0.67	9.07	24.87	31.45	34.42	40.97	42.88	46.98	53.65
<b>3000</b>	0.06	8.09	21.60	28.12	30.03	36.92	38.47	44.30	50.95
<b>Average</b>	0.38	13.78	36.50	40.54	43.33	47.60	51.15	53.43	58.26
<b>Deviation</b>	1.31	4.43	9.78	8.08	7.17	4.75	5.49	4.61	4.11

Table S41. Shielding by reflection measured for the printed composites, units in dB.

<b>MHz</b>	<b>Onyx (0 CF)</b>	<b>1 CF</b>	<b>2 CF</b>	<b>4 CF</b>	<b>6 CF</b>	<b>8 CF</b>	<b>10 CF</b>	<b>12 CF</b>	<b>14 CF</b>
<b>200</b>	-2.82	-0.45	-0.22	1.45	-2.61	1.48	1.95	4.24	4.35
<b>400</b>	0.75	1.71	2.91	3.44	-0.43	4.45	4.96	6.70	7.50
<b>600</b>	1.45	4.24	5.05	5.36	1.58	6.10	6.58	8.10	8.46
<b>800</b>	1.61	4.97	5.99	6.50	3.49	7.38	7.92	9.29	9.92
<b>1000</b>	3.19	7.61	10.98	8.53	5.47	9.09	9.22	10.18	9.78
<b>1200</b>	3.33	5.35	7.64	7.18	4.66	8.18	8.47	9.14	9.21
<b>1400</b>	2.97	6.13	11.18	10.61	9.14	11.42	12.18	12.23	12.96
<b>1600</b>	2.42	4.49	8.40	8.78	6.48	9.80	9.82	10.24	10.08
<b>1800</b>	3.04	4.15	10.97	10.73	9.18	11.51	11.74	12.12	12.00
<b>2000</b>	4.58	3.52	13.09	12.03	10.45	12.66	13.00	14.76	14.38
<b>2200</b>	4.04	3.05	12.84	10.06	9.14	11.67	11.06	13.51	12.15
<b>2400</b>	3.61	2.95	9.31	10.55	9.16	11.28	11.77	12.92	13.42
<b>2600</b>	4.37	2.98	9.06	9.91	7.89	10.07	10.07	11.00	11.15
<b>2800</b>	5.15	3.24	10.05	9.62	8.49	10.29	10.76	11.41	11.38
<b>3000</b>	5.47	3.01	10.84	10.41	9.20	11.63	12.53	12.93	13.45
<b>Average</b>	2.88	3.80	8.54	8.35	6.09	9.13	9.47	10.58	10.68
<b>Deviation</b>	2.00	1.83	3.60	2.90	3.86	3.02	2.98	2.69	2.55



Table S42. Total shielding effectiveness measured for the printed composites, units in dB.

<b>MHz</b>	<b>Onyx (0 CF)</b>	<b>1 CF</b>	<b>2 CF</b>	<b>4 CF</b>	<b>6 CF</b>	<b>8 CF</b>	<b>10 CF</b>	<b>12 CF</b>	<b>14 CF</b>
<b>200</b>	1.82	19.44	40.48	44.13	41.61	48.96	52.10	54.16	59.50
<b>400</b>	1.99	20.01	46.71	50.29	49.40	56.15	59.11	60.54	62.88
<b>600</b>	2.25	22.09	53.51	58.10	61.16	60.15	61.43	62.80	67.48
<b>800</b>	2.39	24.49	65.34	65.00	56.27	59.83	62.77	66.08	72.73
<b>1000</b>	2.44	26.14	55.73	55.21	52.14	60.75	65.23	68.64	70.07
<b>1200</b>	2.84	24.27	47.79	52.18	51.54	60.05	67.13	69.30	74.52
<b>1400</b>	3.01	20.74	48.30	50.52	51.89	60.67	66.89	69.44	74.73
<b>1600</b>	3.32	17.67	46.52	49.55	51.71	60.30	65.78	68.51	73.25
<b>1800</b>	3.57	15.09	44.88	48.76	51.60	60.16	65.23	68.40	73.49
<b>2000</b>	3.67	13.24	43.15	47.81	51.29	60.16	65.12	69.28	73.07
<b>2200</b>	3.73	12.39	40.61	45.83	48.64	56.90	60.66	66.71	70.60
<b>2400</b>	3.83	12.15	38.38	43.61	46.56	54.09	57.44	61.33	66.84
<b>2600</b>	4.02	12.56	36.84	42.65	45.33	52.98	55.73	59.43	65.51
<b>2800</b>	4.48	12.31	34.92	41.07	42.91	51.26	53.64	58.39	65.02
<b>3000</b>	5.52	11.10	32.45	38.52	39.23	48.54	50.99	57.23	64.40
<b>Average</b>	3.26	17.58	45.04	48.88	49.42	56.73	60.62	64.02	68.94
<b>Deviation</b>	0.98	5.05	8.32	6.68	5.47	4.31	5.33	4.99	4.62

## Appendix H. Supplementary results to chapter 4.3.

### EM SHIELDING RESULTS

EMSE was examined for multiple graphene-based inks painted on a silicone substrate. Table S43, and corresponding graph in Figure S2, provides the average value for the measured SE in all the specimens.

Table S43. Average shielding effectiveness measured for the graphene inks, units in dB.

MHz	100	300	500	800	1000	1500	2000	2500	3000	Average	Std. Dev.
<b>G1</b>	-0.02	0.05	0.08	0.11	0.11	0.14	0.13	0.13	0.16	0.10	0.06
<b>G2</b>	0.52	0.58	0.58	0.56	0.58	0.62	0.61	0.85	0.63	0.61	0.09
<b>G3</b>	13.96	12.19	11.70	11.21	11.40	11.11	11.39	13.10	10.20	11.80	1.13
<b>G4</b>	7.91	8.00	7.69	7.33	7.15	6.76	6.49	6.97	7.20	7.28	0.51
<b>G5</b>	10.40	10.38	10.20	9.99	9.79	9.49	9.49	10.10	10.60	10.05	0.40
<b>G6</b>	14.58	8.60	7.61	7.03	6.98	7.02	6.89	8.44	9.17	8.48	2.44
<b>G6+Ni</b>	7.90	3.11	2.48	2.19	2.12	2.28	2.16	3.27	5.31	3.42	1.96
<b>G6+Zn</b>	9.84	4.88	4.21	3.85	3.82	3.94	3.84	5.09	6.61	5.12	1.99

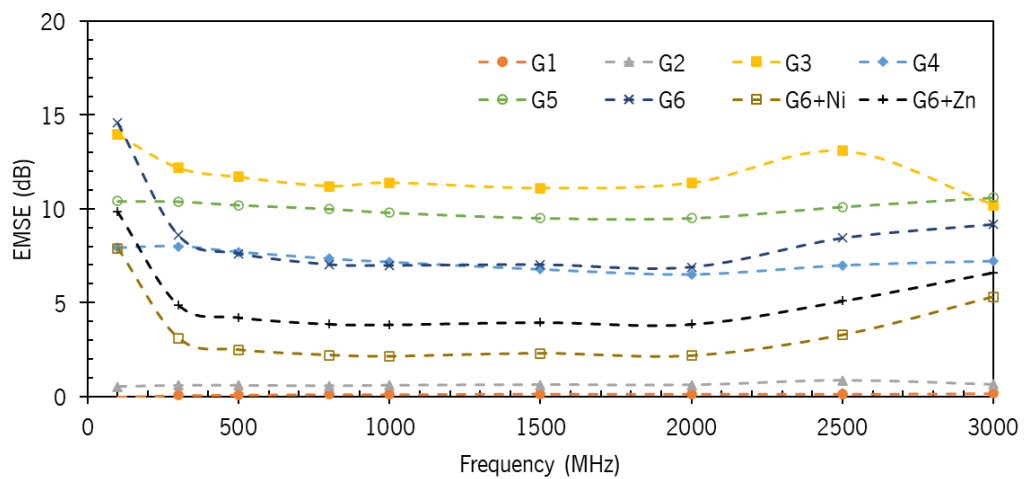


Figure S2. Average shielding effectiveness measured for the graphene inks, units in dB.

## Appendices

A study regarding the effect of incremental graphene layers on the specimens SE was achieved, exhibiting the average results from Table S44, and corresponding graph in Figure S3. An analysis of the logarithmic regression was conducted and is included in the graph.

Table S44. SE measured with the increase of graphene layers, units in dB

MHz	100	300	500	800	1000	1500	2000	2500	3000	Average	Std. Dev.
<b>Silicone</b>	2.41	0.40	0.15	0.24	0.13	2.68	0.18	-0.94	5.67	1.21	2.03
<b>1</b>	3.38	1.30	1.03	1.09	1.00	4.07	1.38	5.17	6.29	2.75	2.04
<b>2</b>	5.55	3.04	2.73	2.68	2.66	5.48	3.43	11.01	6.89	4.83	2.79
<b>3</b>	6.46	3.79	3.45	3.40	3.39	5.95	4.30	12.36	7.29	5.60	2.93
<b>5</b>	10.34	7.15	6.72	6.58	6.66	8.74	8.06	16.48	9.59	8.93	3.14
<b>7</b>	12.67	9.27	8.81	8.67	8.79	10.66	10.58	18.18	11.44	11.01	3.02
<b>10</b>	15.00	11.41	10.91	10.74	10.90	12.58	12.90	19.98	13.33	13.08	2.94
<b>15</b>	17.24	13.60	13.15	13.09	13.33	14.85	15.89	22.82	16.10	15.56	3.10
<b>17</b>	18.59	14.89	14.45	14.40	14.69	16.11	17.40	24.74	17.39	16.96	3.29
<b>20</b>	19.10	15.44	15.04	15.04	15.58	16.86	18.24	26.55	18.13	17.78	3.63
<b>25</b>	19.93	16.35	16.02	16.12	16.54	18.11	19.64	29.57	19.35	19.07	4.25
<b>30</b>	20.86	17.27	16.97	20.30	18.02	19.67	20.94	27.10	20.50	20.18	3.02
<b>31</b>	25.47	21.46	20.80	20.47	20.74	21.97	22.84	30.61	22.21	22.95	3.25
<b>35</b>	26.99	22.93	22.30	21.98	22.34	22.92	24.37	30.97	23.55	24.26	2.94
<b>40</b>	26.87	22.91	22.31	22.03	22.49	23.10	24.59	31.01	23.96	24.36	2.91
<b>42</b>	27.73	23.72	23.13	22.92	23.52	24.46	25.66	32.25	25.05	25.38	2.98

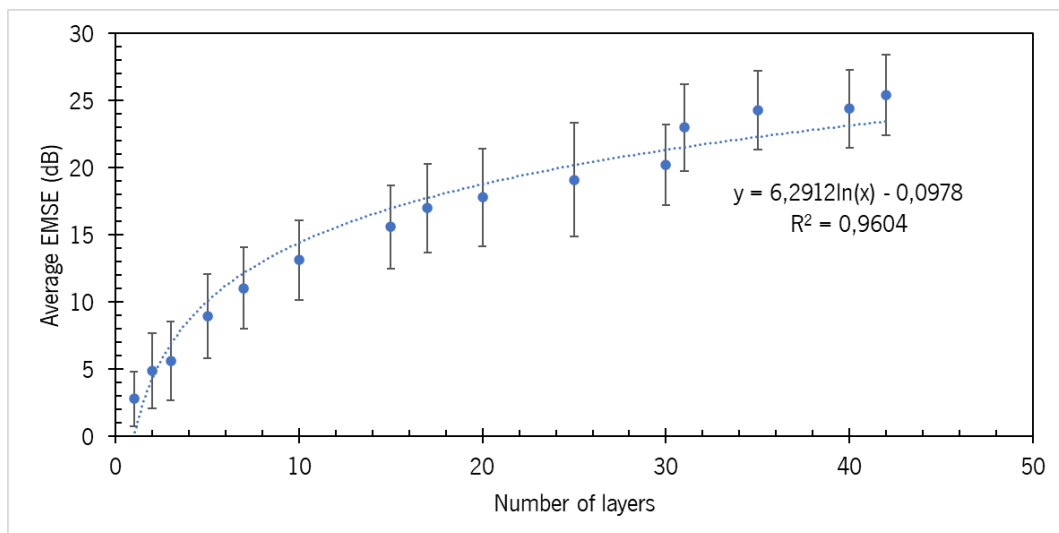


Figure S3. EMSE properties with the increase of graphene layers with adjusted logarithmic regression.

A theoretical study to characterize the SE through the silicon substrate coated with graphene was achieved. The analysis was conducted varying the material thickness and conductivity and the obtained results are show in Table S45, and corresponding Figure S4.

Table S45. Estimated EM shielding for graphene coatings with a given thickness and constant conductivity.

Conductivity (S/m)	50 μm	100 μm	200 μm	500 μm	1000 μm
10	0.79	1.50	2.78	5.76	9.18
50	3.35	5.76	9.19	15.11	20.34
100	5.76	9.19	13.55	20.34	25.96
150	7.64	11.64	16.44	23.58	29.38
200	9.19	13.55	18.61	25.94	31.85
250	10.50	15.12	20.34	27.79	33.82
300	11.50	16.44	21.78	29.32	35.45
400	13.55	18.61	24.10	31.76	38.11
600	16.44	21.78	27.44	35.24	42.13
800	18.61	24.10	29.85	37.76	45.27
1000	20.34	25.93	31.73	39.74	47.94
1500	23.58	29.31	35.19	43.46	53.44
2000	25.93	31.73	37.66	46.24	57.94

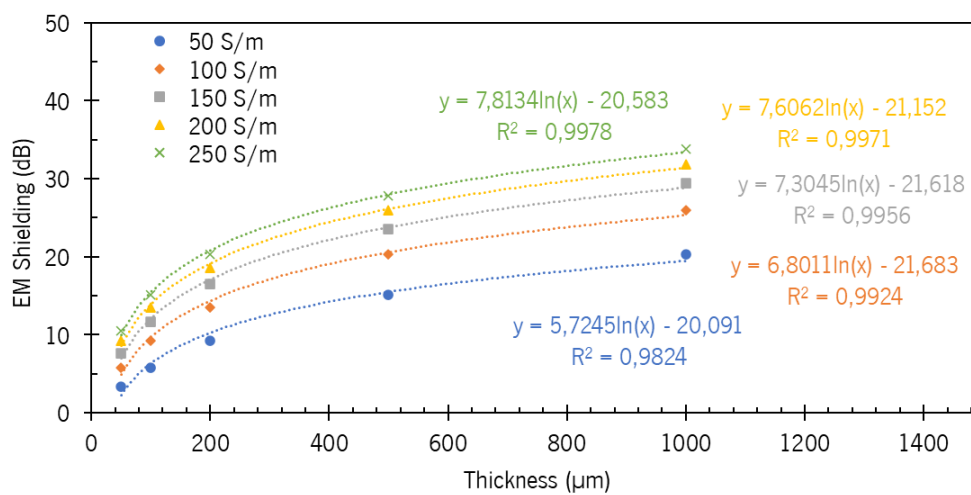


Figure S4. Effect of the layer thickness on the EM shielding of graphene coating with constant conductivity, with corresponding logarithmic trend equation.